MICROPHYSICAL-DYNAMICAL PROCESSES AND INTERACTIONS IN A PRECIPITATING CUMULUS CELL MODEL

by

MAN KONG YAU

S.B., Massachusetts Institute of Technology
(1971)

S.M., Massachusetts Institute of Technology
(1973)

SUBMITTED IN
PARTIAL FULFILLMENT
OF THE REQUIREMENTS FOR THE
DEGREE OF DOCTOR OF SCIENCE
at the
MASSACHUSETTS INSTITUTE OF
TECHNOLOGY
May,1977

Signature of Author.....
Department of Meteorology, May 31, 1977.

Certified by.....
Thesis Supervisor

Accepted by.....
Chairman, Departmental Committee
on Graduate Students

WITHDRAWN
FROM
MIT LIBRARIES
JUN 21 1977

MICROPHYSICAL-DYNAMICAL PROCESSES AND INTERACTIONS IN A PRECIPITATING CUMULUS CELL MODEL

by
MAN KONG YAU

Submitted to the Department of Meteorology on 31 May 1977
in Partial Fulfillment of the Requirements for
the Degree of Doctor of Science

ABSTRACT

This study is concerned with the microphysical-dynamical interactions in a cumulus cloud and the effects of cumulus activities on the atmosphere. The three principal components of the investigation are: (1)development of a practical microphysical parameterization scheme which allows explicit calculation of the drop-size spectra;(2) analysis of the role of perturbation pressure by simple analytic models; (3) development and application of a two-cylinder model which allows sensitivity tests on the major microphysical and dynamical processes.

The microphysical parameterization scheme developed is much simpler than the full stochastic technique yet includes realistically the major microphysical processes. The growth of cloud droplets is bypassed but evolution of the drop-size spectrum and the effect of differential fallspeeds are allowed by the growth of rain and graupel particles in a total of 25 size categories. The processes included are condensation,melting, evaporation, accretion, collection, breakup, freezing, riming, and deposition. Experiments with the scheme in the context of a kinematic updraft indicate comparable results to those of a stochastic model in warm rain development. Sensitivity tests point out the existence of a negative feedback mechanism between the autoconversion and accretion processes, the important contribution of rain-rain interactions in the evolution of drop-size spectra, and the essential role of impaction breakup as a limiting mechanism for drop growth.

The effect of perturbation pressure is clarified by analytic solutions of the anelastic pressure equation. Qualitative results from simple sinusoidal forcings indicate that the buoyancy- and drag-induced perturbation pressure forces oppose the forcing but may be important in supporting a negatively buoyant updraft. The dynamic pressure is found to be a response to the Bernoulli effect and the centrifugal force due to the rotation of the air. Quantitative assessment of the role of perturbation pressure with more realistic forcings by the Green's functions method shows that the pressure force is of the same order of magnitude as the buoyancy and drag and must therefore be included for realistic simulation of cumulus processes.

A time-dependent two-cylinder model is formulated which incorporates the practical microphysical parameterization. Perturbation pressure is calculated explicitly by a Fourier Bessel series expansion. Numerical experiments with the model on the microphysical-dynamical interactions show that precipitation loading near the cloud base appears to be responsible for the initiation of the downdraft while evaporation from falling small drops can significantly enhance downdraft development. Strong subsidence in the environment leads to earlier dissipation of the cloud as a result of the transport of downward momentum and the drying of the environment on adiabatic descent. Inclusion of the ice phase leads to a deeper cloud as a result of the added buoyancy from latent heats released in the freezing of water drops and depositional growth of ice particles. Perturbation pressure is found to smooth the steep velocity gradient near the cloud top, extend the region of detrainment, suppress the intensity of convection, but may prolong cloud life time by supporting the updraft near the cloud base. Strong entrainment has been demonstrated to be a major dissipative process and the model responds readily to the temperature and humidity distributions of the ambient atmosphere.

Analysis of the moisture and heat budgets shows that in the cloud column, condensation is the major heat source and evaporation a major heat sink. The vertical transports moisten the air aloft but condensation and entrainment of drier air from the environment deplet the moisture supply in the lower portion. In the environment, evaporative cooling exceeds the warming due to detrainment of cloudy air but adiabatic warming by subsidence offsets much of the cooling effect. Detrainment of water vapor and the evaporation of cloud droplets moisten the air aloft but subsidence drying causes a net drying effect below.

The model is applied to a computation of cumulus transports of mass and heat. Comparison of the present results at Boston in the month of July with those obtained by Houze (1973) indicates that the two models give comparable total heat transports in the region of the cloud column. The level of maximum heat transport is noticeably lower in the present computation.

Thesis Supervisor: Pauline M. Austin
Title: Senior Research Associate

ACKNOWLEDGEMENTS

The author would like to express his sincere gratitude to his principal advisor, Dr. Pauline M. Austin, for her guidance and encouragement during the development of this thesis. Without her kindness and support, this thesis would never have been written. The critical comments and advice of Professor Frederick Sanders are also gratefully acknowledged.

The author had the good fortune to have frequent disscussions with Professor Yoshi. Ogura during his stay as Visiting Professor in the Fall of 1975 and the Spring of 1976 at M.I.T. He also benefitted from disscussions with Dr. Edwin Kessler and Professor Eugenia Kalnay de Rivas. Professor David Randall was kind to read the manuscript and offered helpful comments.

Appreciation is extended to Mr. Loren Nelson for providing the stochastic collection program and to Mr. Neil Gordon for some stimulating discussions. Mr. Steven Ricci helped to draft the figures. Mr. Lancelot Tin, the author's brother-in-law provided some financial assistance.

Finally, the author thanks his wife, Fernina, for typing the thesis and for the love, understanding, and encouragement she has provided.

This research has been supported by NOAA under grant no. 04-5-022-1 and the National Science Foundation under grant no. DES75-14135.

TABLE OF CONTENTS

TITLE	1
ABSTRACT	2
ACKNOWLEDGEMENTS	4
TABLE OF CONTENTS	5
LIST OF TABLES	8
LIST OF FIGURES	9
CHAPTER ONE. INTRODUCTION	17
1.1. Background	17
1.2. Statement of problem	19
CHAPTER TWO. THE MICROPHYSICAL PROCESSES	21
2.1. Problems in including microphysics in dynamic models	21
2.2. Formulation of a model of microphysical processes	22
2.2.1 Introduction	22
2.2.2 Continuity equations	24
2.2.3 The microphysical processes	26
2.3. Comparison of present model with other schemes	36
2.3.1 Model equations	36
2.3.2 Intitial conditions and computation methods	39
2.3.3 Results	40
2.4. Sensitivity tests	42
2.5. Summary	45
CHAPTER THREE. ANALYSIS OF PERTURBATION PRESSURE	47
3.1. Background	47
3.2. Derivation of the anelastic pressure equation	51
3.3. Analytic solutions for structurally simple forcing functions	53
3.3.1 Form of the forcing functions	53
3.3.2 Solutions of the pressure equations	56
3.4. Green's function solutions for more realistic forcings	67
3.4.1 More realistic forcing functions	67
3.4.2 Method of solution	67
3.4.3 Pressure responses	70
3.4.4 Negative buoyancy and perturbation pressure	73
3.5. Summary	74
CHAPTER FOUR. FORMULATION OF A TWO-CYLINDER MODEL	75
4.1. General description	75
4.2. Basic equations	76

CHAPTER FOUR cont'd

4.3. Equations for the two-cylinder model 78
4.3.1 Averaged equations for velocities, potential temperature, and water substances 78
4.3.2 Determination of horizontally averaged perturbation pressure 86
4.4. Specification of experiment and numerical methods 91
4.5. Specification of radius for the inner and outer cylinder 94

CHAPTER FIVE. INTERACTION OF MICROPHYSICAL AND DYNAMICAL PROCESSES IN THE TWO-CYLINDER MODEL 98
5.1. Introduction 98
5.2. General behavior of the model 101
5.3. Effect of compensatory current in the environment 108
5.4. Effect of evaporation on downdraft initiation and development 110
5.5. Effect of ice phase 111
5.6. Effects of microphysical parameterization 112
5.7. Effect of perturbation pressure 116
5.8. Effect of cloud radius and entrainment 117
5.9. Effect of initial conditions 118
5.10. Effect of parameters in numerical scheme 120
5.11. Summary 121

CHAPTER SIX. EFFECT OF CUMULUS CONVECTION ON THE ENVIRONMENT 123
6.1. Introduction 123
6.2. Equations for time-integrated effects of cumulus 125
6.2.1 Heat and moisture budget 125
6.2.2 Formulas for mass and heat fluxes 128
6.3. Effect of cumulus 129
6.3.1 Computations with idealized sounding 129
6.3.2 Monthly transports at Boston in July 133
6.3.3 Computations with a mean Marshall Islands Sounding 138
6.4. Sensitivity test for heat flux calculations 139
6.5. Summary 140

CHAPTER SEVEN. CONCLUSION 142

FIGURES 147

APPENDIX 2.1 CONDENSATION AND EVAPORATION OF CLOUD DROPLETS 222

APPENDIX 2.2 GROWTH MODES AND MELTING OF GRAUPEL 224

APPENDIX 2.3 COMPUTATION OF SPECTRAL TRANSFER TERM 228

APPENDIX 3.1 DERIVATION OF GREEN'S FUNCTIONS 233

APPENDIX 4.1 STABILITY ANALYSIS FOR INTERNAL GRAVITY WAVE MOTION 238

APPENDIX 4.2 FINITE DIFFERENCE EQUATIONS AND SEQUENCE OF COMPUTATION 243

LIST OF SYMBOLS 247a

BIOGRAPHICAL NOTE 248

REFERENCES 249

LIST OF TABLES

TABLE		PAGE
2.1	Size categories for hydrometeors	23
2.2	Fraction of drops of radius R frozen at temperature T°c	35
2.3	Sensitivity tests performed	43
3.1	Forcing functions	68
3.2	Maximum values of forcing and induced pressure force	72
5.1	Summary of experiments	100
5.2	Comparison of results from E2 and E6	115
6.1	Extent of data sample	135
6.2	Comparison between computed and mean observed echo-top height	137
6.3	Sensitivity of H_T to microphysical parameterization, cloud radius, and radii ratio	140a

LIST OF FIGURES

Figure		Page
2.1	The microphysical processes in the P model.	147
2.2	Radius(r_s) of satellite drops produced by impaction of drops of radii R and R'.	148
2.3	The initial droplet spectrum for model S.	148
2.4	The kinematic updraft profile.	148
2.5	Comparison of liquid water for model S, P, and K.	149
2.6	Comparison of surface rainfall intensity for models S, K, and P.	150
2.7	Comparison of radar reflectivities at 400 m and 3200 m.	150
2.8	The evolution of raindrop size spectra for models S and P at 18, 22, and 26 minutes.	151
2.9	Effect of varying autoconversion rate K on surface rainfall intensity in model P.	152
2.10	Effect of varying autoconversion threshold a on surface rainfall intensity in model P.	152
2.11	Effect of varying K on rain dropsize spectra in model P.	153
2.12	Effect of varying a on rain dropsize spectra in model P.	153
2.13	Effect of varying autoconversion rate K and autoconversion threshold a on radar reflectivity in model P.	154
2.14	Effect of rain-rain interaction on time evolution of radar reflectivity factor and dropsize spectrum.	155
2.15	Effect of variable coalescence efficiency and satellites on rainfall intensity.	155
2.16	Effect of variable coalescence efficiency and satellites on radar reflectivity profile.	156

Figure		Page
2.17	Effect of variable coalescence efficiency and satellites on dropsize spectra.	156
A1	Transfer of hydrometeor water between categories.	157
A2	Comparison of cloud and rain density at 400 m and 3200 m computed by the EM and FD methods.	158
A3	Comparison of surface rainfall intensity computed by FD and EM methods.	158
A4	Comparison of dropsize spectra at 16, 20 and 24 minutes computed by FD and EM methods.	159
A5	Comparison of radar reflectivity factor computed by FD and EM methods.	160
3.1	Vertical section of buoyancy forcing.	161
3.2	Same as Fig. 3.1 except for drag forcing Q_1.	161
3.3	Same as Fig. 3.1 except for drag forcing Q_2.	161
3.4	Vertical section of horizontal velocity u.	161
3.5	Vertical section of vertical velocity w.	162
3.6	Streamfunction in arbitrary units.	162
3.7	Vertical section of non-dimensional perturbation pressure induced by buoyancy forcing.	162
3.8	Vertical section of vertical pressure gradient force induced by buoyancy forcing.	162
3.9	Vertical section of net vertical acceleration $g(\theta'/\theta_o)-c_p\theta_o(\partial\pi_\theta/\partial z)$.	163
3.10	Vertical section of horizontal pressure force induced by buoyancy forcing.	163
3.11	Vertical section of non-dimensional perturbation pressure induced by drag forcing Q_1.	163

Figure		Page
3.12	Same as Fig. 3.11 except for drag forcing Q_2.	163
3.13	Drag forces $-gQ_{1,2}$, drag pressure forces $C_p\theta_o\frac{\partial \Pi'_{Q_{1,2}}}{\partial z}$, and $-gQ_{1,2} - C_p\theta_o\frac{\partial \Pi_{Q_{1,2}}}{\partial z}$ at the central axis.	164
3.14	The natural coordinate system.	164
3.15	Vertical section of kinetic energy per unit mass.	165
3.16	Vertical section of squared vorticity.	165
3.17	Vertical section of non-dimensional perturbation pressure induced by kinetic energy forcing.	165
3.18	Vertical section of non-dimensional pressure induced by vorticity forcing.	165
3.19	Vertical section of dynamic perturbation pressure.	166
3.20	Vertical perturbation pressure force induced by dynamic forcing at the central axis.	166
3.21	Vertical section of non-dimensional buoyancy perturbation pressure for $S_z=2\times10^{-5}m^{-1}$.	166
3.22	Comparison of horizontal profiles for u and w in the case of axi- and slab-geometry.	166
3.23	Vertical section of non-dimensional perturbation pressure induced by buoyancy forcing.	167
3.24	Same as Fig. 3.23 except for slab-symmetric geometry.	167
3.25	Vertical section of non-dimensional perturbation pressure induced by dynamic forcing for axi-symmetric geometry.	167
3.26	Same as Fig. 3.25 except for slab-symmetric geometry.	167

Figure		Page
3.27	Vertical section of non-dimensional pressure induced by drag forcing.	168
3.28	Same as Fig. 3.27 except for slab-symmetric geometry.	168
3.29	Vertical section of vertical buoyancy perturbation pressure gradient force for axi-symmetry geometry.	168
3.30	Vertical section of vertical buoyancy perturbation pressure gradient force for slab-symmetric geometry.	168
3.31	Same as Fig. 3.29 except for vertical dynamic perturbation pressure gradient force.	169
3.32	Same as Fig. 3.30 except for vertical dynamic perturbation pressure gradient force.	169
3.33	Same as Fig. 3.29 except for vertical drag perturbation pressure gradient force.	169
3.34	Same as Fig. 3.30 except for vertical drag perturbation pressure gradient force.	169
3.35	Buoyancy and buoyancy pressure force at the central axis.	170
3.36	Drag and drag pressure force at the central axis.	170
3.37	Vertical advection and dynamic pressure force at the central axis.	170
3.38	Effect of perturbation pressure force on negative buoyancy.	171
3.39	Vertical section of non-dimensional perturbation pressure induced by buoyancy forcing in eq.(3.49)	171
3.40	Vertical section of vertical pressure gradient force induced by forcing in eq.(3.49) in cm sec^{-2}.	171
4.1	Basic configuration of the two-cylinder model.	172

Figure		Page
4.2	Idealized sounding used to represent the base state atmosphere.	172
4.3	The staggered-grid system.	173
4.4	Relation of σ and heat transport H_T.	174
B1	The grid system for stability analysis of internal gravity wave motion.	174a
5.1	Time-height cross-section of vertical velocity $\bar{w}_a$ in the inner cylinder for experiment E1.	175
5.2	Same as Fig. 5.1 except for potential temperature deviation $\bar{\theta}'_a$.	176
5.3	Same as Fig. 5.1 except for rain water content $\bar{q}_{ra}$.	177
5.4	Time variation of surface rainfall intensity in the inner cylinder for experiment E1.	178
5.5	Vertical distribution of relative humidity in the inner cylinder for E1 at 35 minutes.	178
5.6	Radial velocity at the edge of the inner cylinder at 10,20, and 30 minutes for experiment E1.	179
5.7	Rainfall spectra in the inner cylinder near the cloud base and the cloud top at 30,35,40, and 50 minutes for E1.	180
5.8	Same as Fig. 5.1 except for radar reflectivities.	181
5.9	Analysis of forces in the vertical momentum equation (4.23) in the inner cylinder at 15,20,25, and 30 minutes for experiment E1.	182
5.10	Analysis of water budget in the environment, the cloud column, and the whole integration domain for experiment E1.	183
5.11	Same as Fig. 5.1 except for experiment E2.	184
5.12	Same as Fig. 5.2 except for experiment E2.	185

Figure		Page
5.13	Same as Fig. 5.3 except for experiment E2.	186
5.14	Comparison of surface rainfall intensity for experiments E1 and E2.	187
5.15	Same as Fig. 5.7 except for experiment E2.	188
5.16	Same as Fig. 5.8 except for experiment E2.	189
5.17	Same as Fig. 5.10 except for experiemnt E2.	190
5.18	Same as Fig. 5.1 except for experiment E3.	191
5.19	Same as Fig. 5.1 except for experiment E4.	192
5.20	Same as Fig. 5.2 except for experiment E4.	193
5.21	Comparison of the vertical velocity in the inner cylinder for the case with and without ice phase.	194
5.22	Comparison of the potential temperature deviation in the inner cylinder for the case with and without the ice phase.	195
5.23	Comparison of cloud, cloud ice, and rain water content in the inner cylinder at 30 minutes for E5 and E1.	196
5.24	Same as Fig. 5.1 except for experiment E6.	197
5.25	Same as Fig. 5.2 except for experiment E6.	198
5.26	Same as Fig. 5.3 except for experiment E6.	199
5.27	Same as Fig. 5.8 except for experiment E6.	200
5.28	Comparison of rain intensity and cumulative rainfall for model P and model K micro-physical parameterization.	201
5.29	Same as Fig. 5.10 except for experiment E6.	202
5.30	Same as Fig. 5.1 except for experiment E7.	203
5.31	Same as Fig. 5.2 except for experiment E7.	204
5.32	Same as Fig. 5.8 except for experiment E7.	205

Figure		Page
5.33	Comparison of radial velocity at the edge of the inner cylinder at 10,20,and 30 min. for experiments E6 and E7.	206
5.34	Effect of varying the cloud radius on maximum $\bar{W}_a$,$\bar{\theta}'_a$,$\bar{q}_{ca}$,$\bar{q}_{ra}$,$\bar{Z}_a$,rainfall intensity, and cumulative rainfall in the inner cylinder.	207
5.35	Effect of varying the amplitude of velocity impulse W_o on maximum $\bar{W}_a$, $\bar{\theta}'_a$, $\bar{q}_{ca}$, $\bar{q}_{ra}$, and $\bar{Z}_a$ in the inner cylinder.	209
5.36	Effect of humidity impulse on maximum $\bar{W}_a$,$\bar{\theta}'_a$, $\bar{q}_{ca}$,$\bar{q}_{ra}$,and $\bar{Z}_a$ in the inner cylinder.	210
5.37	Effect of environmental temperature lapse rate on maximum $\bar{W}_a$,$\bar{\theta}'_a$,$\bar{q}_{ca}$,$\bar{q}_{ra}$, and $\bar{Z}_a$ in the inner cylinder.	211
5.38	Effect of varying the environmental humidity stratification on maximum $\bar{W}_a$,$\bar{\theta}'_a$,$\bar{q}_{ca}$,$\bar{q}_{ra}$,and $\bar{Z}_a$ in the inner cylinder.	212
5.39	Effect of varying the time step δ t on maximum $\bar{W}_a$,$\bar{\theta}'_a$,$\bar{q}_{ca}$,$\bar{q}_{ra}$, and $\bar{Z}_a$ in the inner cylinder.	213
5.40	Effect of varying the space increment δ z on maximum $\bar{W}_a$,$\bar{\theta}'_a$,$\bar{q}_{ca}$,$\bar{q}_{ra}$, and $\bar{Z}_a$in the inner cylinder.	214
6.1	Factors contributing to the temperature change in the cloud for a cloud life-time of one hour.	215
6.2	Factors contributing to the temperature change in the environment for a cloud life-time of one hour.	215
6.3	Factors contributing to the moisture change in the cloud for a cloud life-time of one hour.	216
6.4	Factors contributing to the moisture change in the environment for a cloud life-time of one hour.	216

Figure		Page
6.5	Mass flux per unit area integrated over a cloud life-time of one hour.	217
6.6	Heat flux per unit area integrated over a cloud life-time of one hour.	217
6.7	Average monthly mass transport by cumulus clouds at Boston for the month of July.	218
6.8	Average monthly sensible heat transport by cumulus clouds at Boston for the month of July.	218
6.9	Monthly mean sounding for Majuro, Marshall Islands in July, 1975.	219
6.10	Mass flux per unit area integrated over a cloud life-time of one hour with the sounding in fig. 6.9.	220
6.11	Heat flux per unit area integrated over a cloud life-time of one hour with the sounding in fig. 6.9.	220
6.12	Effect of microphysical parameterization on time-integrated heat flux for a cloud life-time of 70 minutes.	221
6.13	Effect of cloud radius on time-integrated heat flux for a cloud life-time of 70 min.	221
6.14	Effect of radii ratio σ on time-integrated heat flux for a cloud life-time of 70 min. Model P microphysics used.	221

CHAPTER ONE

INTRODUCTION

1.1 Background

In the past, meteorological events on different scales have been investigated separately, but it is now recognized that significant interactions occur along the whole spectrum of atmospheric circulations. As a consequence, many current investigations are geared toward understanding of interactions between different scales. In view of the role of cumulus convection as a mechanism for vertical transports and as a source of energy through the release of latent heat, a full comprehension of the cumulus processes is particularly significant.

The microphysical dynamical interactions within a cumulus cell and the effect of cumulus convection on the larger scale environment constitute two major aspects in the understanding of cumulus processes. The first mode of interaction is effected through the formation and distribution of precipitation. The latent heats of condensation, sublimation, fusion, and evaporation, the water loading and precipitation fallout, together with entrainment and ambient wind combine into a complex feedback system to regulate the life cycle of the whole cloud. Further complication is added by the role of perturbation pressure, which not only affects the dynamics through the pressure gradient force, but also influences the rate of condensation by the functional dependence of saturation vapor density on pressure.

(Ogura and Phillips, 1962).

Investigation of microphysical-dynamical interactions by laboratory and synoptic analysis techniques is difficult because of the disparity in scale between microphysical phenomena and air circulations. Thus most of the interactive studies are through numerical models. However, the limitation of present-generation computers have forced most studies to emphasize either the dynamics or the microphysics. Compensating current and perturbation pressure are neglected in models with complex microphysics. (Danielsen et al, 1972; Ogura and Takahashi, 1973; Silverman and Glass, 1973). Other two- and three-dimensional models (e.g. Takeda, 1971; Orville, 1968; Schlesinger, 1973a, 1975; Wilhelmson, 1974) treat the dynamics more fully but of necessity adopt a highly simplified microphysical parameterization scheme. The slab-symmetric model of Clark (1973), though fairly complete in warm rain microphysics and dynamics in a non-shear environment, is of limited usefulness because of the constraint on the number of experiments which can be performed economically.

Interaction of cumulus clouds with the environment is accomplished through the release of latent heat and transport of moisture and enthalpy through detrainment and subsidence warming. The role of cumulus convection in the formation of hurricanes and the initiation of development of extratropical cyclones have been established (Charney and Eliassen, 1964; Tracton, 1973). Cumulus transports have been obtained from

diagnostic studies of large-scale variables (Ogura and Cho, 1973; Arakawa and Schubert, 1974) and in a more direct manner from radar and detailed rainfall measurements (Austin and Houze, 1973). However, estimates which have been made to date are crude; the uncertainties stem largely from lack of precise knowledge about the microphysical-dynamical coupling, the efficiency of precipitation, and the entrainment mechanism.

1.2 Statement of problem

This thesis studies the microphysical-dynamical interactions and transports of mass and heat associated with cumulus cells. The approach is through development and use of an axi-symmetric two-cylinder model which includes all the major microphysical and dynamical processes. On account of the axi-symmetric geometry assumed, the effect of wind shear is not considered.

The microphysical scheme is developed in Chapter 2. To allow for evolution of drop-size spectrum and the effect of differential fall velocities, rain and graupel particles develop in a total of twenty-five size categories. The scheme is much simpler than the full stochastic technique yet compares favorably with a stochastic treatment for warm rain development in a kinematic updraft.

The role of perturbation pressure is clarified in Chapter 3. Analytic solutions of the anelastic pressure equation for simple forcings are obtained. Results indicate that the pertur-

bation pressure force opposes the buoyancy in a cumulus cloud but may be important in supporting a negatively buoyant updraft near the surface.

The formulation of the two-cylinder model forms the subject of Chapter 4. The model incorporates the microphysical scheme developed in Chapter 2 with explicit pressure calculations by Fourier Bessel series expanison. The radius of the inner cylinder is specified from observational information of the dimensions of cumulus cells. The radius of the outer cylinder which represents the cloud environment is determined from the hypothesis that cumulus clouds achieve the most efficient heat transport in the region of convection. Chapter 5 deals with microphysical and dynamical interactions in the model. The effects of evaporation, water load, size-distribution of precipitation particles, ice phase, perturbation pressure, and entrainment on the life history of the cell are examined.

Finally, Chapter 6 contains an investigation of the effects of cumulus on the heat and moisture budgets of the atmosphere. The model is applied to a study of cumulus transports of mass and heat at Boston for the month of July. Sensitivity of the heat flux computations to variations of model parameters is also explored.

CHAPTER TWO

THE MICROPHYSICAL PROCESSES

2.1 Problems in including microphysics in dynamic models

It is recognized that a complete description of the microphyscis in a cumulus cloud requires consideration of the activation of cloud condensation nuclei (Fitzgerald, 1973), diffusional growth by condensation, stochastic collision and coalescence of cloud and rain drop-size particles (Berry, 1967; Leighton and Rogers, 1974), drop breakup (Srivastava, 1971; List and Gillespie, 1976), ice particle nucleation, growth of ice crystals by sublimation and aggregation, as well as stochastic collection in the growth of graupel and hail (Young, 1974a, 1974b; Cotton, 1972; Danielsen et al, 1972; Scott and Hobbs, 1977). However, diffusional growth of a population of drops and the stochastic nature of the collection processes within a dynamic framework necessitates explicit calculation of supersaturation and the spectral distribution function of the number of drops. The amount of computation would strain the capacity of the most modern computers.

A simpler model is therefore needed. Kessler (1969) proposed a parameterization scheme which partitioned all water substance into cloud and precipitation. The latter is assumed to follow the Marshall-Palmer distribution at all times and to fall with a single effective fall velocity at a given level. Interaction between cloud and rain is formulated upon the concept

of autoconversion and accretion.

While Kessler's work significantly advanced the understanding of microphysical-kinematical interactions, certain limitations inherent in its simplicity have not been fully explored. In the first place, the Marshall-Palmer distribution may give a good estimate for average distributions representing a large number of samples in many storms, but considerable departure from it occurs in individual cases (Mason and Andrews, 1960). Secondly, since the vertical transport of precipitation particles is related directly to the differential fall velocities, a neglect of this aspect leads to improper distribution of hydrometeors which may in turn affect the circulation dynamics.

2.2 Formulation of a model of microphysical processes

2.2.1 Introduction

To remove the restriction imposed by Kessler's scheme, a model which is relatively simple compared with the full stochastic treatment is proposed. The growth of cloud droplets is bypassed but variations in fallspeeds are taken into account by the growth of rain and graupel particles in a total of 25 size-categories (Table 2.1). The major processes included are in fig. 2.1.

The validity of the present model is established by comparison of computations with other models in section 2.3. Sensitivity tests in section 2.4 give insight into the role of autoconversion, coalescence efficiency, accretion, and

Table 2.1

SIZE CATEGORIES FOR HYDROMETEORS

Type of hydrometeors	Range δR (cm)	Median radius R (cm)	Fall velocity V ($m\ sec^{-1}$)
Cloud	0-0.002	0.001	0.01
Rain and graupel categories			
1	0.002-0.008	0.005	0.23
2	0.008-0.04	0.025	1.95
3	0.04-0.07	0.055	4.10
4	0.07-0.1	0.085	5.74
5	0.1-0.13	0.115	6.91
6	0.13-0.16	0.145	7.73
7	0.16-0.19	0.175	8.29
8	0.19-0.22	0.205	8.66
9	0.22-0.25	0.235	8.90
10	0.25-0.28	0.265	9.06
11	0.28-0.34	0.31	11.50
12	0.34-0.46	0.40	13.00
13	0.46-0.7	0.58	15.7
14	0.7-1.18	0.94	20.0
15	1.18-2.14	1.66	26.6

In the model, 10 categories of raindrops are allowed while graupel categories extend from 1 to 15.

satellite drops in the formation of precipitation.

2.2.2 Continuity equations

Vapor $\rho_0 q_v$, cloud water $\rho_0 q_c$, cloud ice $\rho_0 \hat{q}_c$, rain water $\rho_0 q_r$, and graupel $\rho_0 \hat{q}_r$ densities are governed by the following set of continuity equations.

Continuity for vapor

$$\frac{\partial}{\partial t}(\rho_0 q_v) + \nabla \cdot (\rho_0 q_v \vec{u}) = -P1 + P2C + P2R + P2G - P3I - P3G \tag{2.1}$$

The microphysical processes are described in section 2.2.3.

Continuity for cloud

$$\frac{\partial}{\partial t}(\rho_0 q_c) + \nabla \cdot (\rho_0 q_c \vec{u}) = P1 - P2C - P4 - P5 - P8C + P9I - P10C \tag{2.2}$$

Continuity for cloud ice

$$\frac{\partial}{\partial t}(\rho_0 \hat{q}_c) + \nabla \cdot (\rho_0 \hat{q}_c \vec{u}) = P3I + P8C - P9I \tag{2.3}$$

Continuity for rain

$$\begin{aligned} \frac{\partial}{\partial t}(\rho_0 q_r) + \nabla \cdot (\rho_0 q_r \vec{u}) + \frac{\partial}{\partial z}(\rho_0 q_r V) = & -\delta R \frac{\partial}{\partial R}\left(\rho_0 q_r \frac{\dot{R}}{\delta R}\right) \\ & - P2R + P4 + P5 \\ & + P6 + P7 - P8R \\ & + P9G - P10R \end{aligned} \tag{2.4}$$

where $\rho_0 q_r$ is the rain density of the category with a median radius R and range δR. The first term on the right represents spectral shifting of drops from one size category to another as a result of the change in radius R by the microphysical

processes. The derivation of this term can be regarded as a divergence in a four-dimensional space with coordinates X,Y,Z, and R. Since the appearance of large drops is crucial for the fast development of the drop-size spectrum, a special technique developed by Egan and Mahoney (1971) is used to compute this term. The technique involves calculations of the first and second moments of the distribution and eliminates much of the numerical spreading associated with simple finite differencing.

Following Kessler (1969), it is assumed that vapor, cloud water,and cloud ice follow the three-dimensional motions of the wind while rain and graupel particles share only its horizontal motions but fall with a terminal velocity V relative to the air.

Continuity for graupel

$$\frac{\partial}{\partial t}(\rho_0 \hat{q}_r) + \nabla\cdot(\rho_0 \hat{q}_r \vec{u}) + \frac{\partial}{\partial z}(\rho_0 \hat{q}_r V) = -\delta R \frac{\partial}{\partial R}\left(\rho_0 \hat{q}_r \frac{\dot{R}}{\delta R}\right) - P2G + P3G + P8R - P9G + P10C + P10R \qquad (2.5)$$

The terminal velocities of raindrops are taken from measurements by Davies reported by Best (1950). The formulas suggested for an I.C.A.N. atmosphere are:

$$V = \begin{cases} 1.216 \times 10^{6} R^{2} e^{0.0191 z} & ; \quad R < 25\mu \\ 191 \left\{ 1 - e^{\left[-\left(\frac{20R}{0.316}\right)^{1.754} \right]} \right\} e^{0.029 z} & ; \quad 25\mu \leq R < 150\mu \\ 934 \left\{ 1 - e^{-\left(\frac{20R}{1.77}\right)^{1.147}} \right\} e^{0.0405 z} & ; \quad R \geq 150\mu \end{cases} \tag{2.6}$$

where Z is the height in km.

Graupel particles with a radius $\leq$ 0.265 cm are assumed to fall with the same fallspeed as raindrops. For larger graupel, the equation by Mason (1971) is used.

$$V = \left(\frac{8}{3} \frac{\rho_g}{\rho_o} \frac{g}{C_D} R \right)^{1/2} \tag{2.7}$$

where ρ_g , the density of the graupel, is taken as 0.9 g cm^{-3} and C_D is the drag coefficient with a numerical value of 0.55 (English, 1973).

2.2.3 The microphysical processes

Condensation (P1) and evaporation of cloud (P2C)

Clark (1973) computed the nucleation of cloud droplets from a spectrum of condensation nuclei and their subsequent growth by diffusion in a dynamic model. The cloud dynamics resulting from this detailed treatment of nucleation and condensation are found not to deviate substantially from that of a bulk physical model where all supersaturated vapor condenses instantaneously. In view of this finding, condensation and evaporation of cloud droplets in the present model will be computed from the

dynamic effect alone. Modification of supersaturation mixing ratio through the release of latent heat in a manner proposed by Asai (1965) is adopted. The procedure is described in Appendix 2.1.

It is further assumed that condensation contributes only to the growth of cloud droplets. Actually precipitation particles do grow by condensation, but the growth rate in terms of fractional increase in mass is relatively small and neglect of this effect should not appreciably change the result.

Evaporation of rain (P2R) and wet graupel (P2G)

If evaporation of cloud droplets still leaves the air subsaturated, evaporation of raindrops and wet graupel particles are allowed to occur. The equations from Mason (1971) and English (1973) give

$$P2R = \frac{-4\pi R(S-1)\left(1+0.21\,Re^{1/2}\right)N(R)}{\frac{L_v}{\mathcal{K}T}\left(\frac{L_v}{R_v T}-1\right)+\frac{R_v T}{D\,e_s(T)}} \tag{2.8}$$

$$P2G = -2\pi R\hat{N}\left(2.0+0.844\chi\,Re^{1/2}\right)D(\rho_{vc}-\rho_{vs}) \tag{2.9}$$

where χ is a numerical factor which is assumed 0.7 for a spherical graupel on the basis of experimental data by Macklin (1963).

Depositional growth of cloud ice (P3I) and graupel (P3G)

Cloud ice and graupel particles are assumed to be spherical in shape. Their growths by deposition are given by

Byers (1965) and English (1973) as

$$P3I = \frac{4\pi r (S_i - 1) \hat{N}_i(r)}{\frac{L_s}{K_T}\left(\frac{L_s}{R_v T} - 1\right) + \frac{R_v T}{D e_i(T)}} \tag{2.10}$$

$$P3G = 2\pi R \hat{N}(R) \left(2.0 + 0.844 X R_e^{1/2}\right) D(\rho_{vc} - \rho_{vs}) \tag{2.11}$$

Autoconversion (P4)

Autoconversion is the process of stochastic collection of cloud droplets to form raindrop-size particles. Kessler's (1969) linear relationship gives

$$\begin{aligned} P4 &= K(\rho_0 q_c - a) \quad ; \ \rho_0 q_c > a \\ &= 0 \quad ; \text{ otherwise} \end{aligned} \tag{2.12}$$

where K and a represent respectively a prescribed rate of autoconversion and an autoconversion threshold.

In the present model autoconversion is assumed to produce only small raindrops centered at 50 μ radius. The assumption appears to be justified from the nature of the collection process which produces a natural break in the number density around a radius of 40 μ (Berry and Reinhart, 1973). Based on the nature of the collection kernel, Berry and Reinhart suggested that 50 μ is an appropriate division between rain and cloud droplets.

A simple linear formula for autoconversion is used instead of the more complicated relations derived by Berry (1968) and Cotton (1972). Silverman and Glass (1973) obtained similar cloud development in a one-dimensional time-dependent model with either Kessler's or Berry's autoconversion formulation.

Accretion (P5), collection of rain (P6), and riming (P10C,P10R)

Accretion of cloud by rain and graupel particles can be simulated by the continuous collection process. Hence

$$P5 = \sum_{R>r} N(R)\,\pi(R+r)^2\,[V(R)-V(r)]\,E(R,r)\,\rho_0\,q_c \qquad (2.13)$$

$$P10C = \sum_{R>r} \hat{N}(R)\,\pi(R+r)^2\,[V(R)-V(r)]\,\hat{E}(R,r)\,\rho_0\,q_c \qquad (2.14)$$

where E(R,r) is the collection efficiency.

Raindrops of radius R collect smaller water drops but are depleted by coalescence with larger rain and graupel particles. Therefore,

$$P6 = \sum_{R>R'} N(R)\,\pi(R+R')^2\,[V(R)-V(R')]\,E(R,R')\,\rho_0\,q_r(R') - \sum_{R'>R} N(R')\,\pi(R+R')\,[V(R')-V(R)]\,E(R',R)\,\rho_0\,q_r(R) \qquad (2.15)$$

and

$$P10R = \sum_{R'>R} \hat{N}(R')\,\pi(R'+R)^2\,[V(R')-V(R)]\,\hat{E}(R',R)\,\rho_0\,q_r(R) \qquad (2.16)$$

The collection efficiency E(R,R') is the product of collision $E_1(R,R')$ and coalescence $E_2(R,R')$ efficiencies. An average collection efficiency of 0.8 is assumed for cloud droplets based on data from Mason (1971). The collision efficiency for raindrops is one but the coalescence efficiency from Brazier-Smith et al (1973) is used. The form is

$$E_2(R,R') = \frac{120^* f(R/R')}{5\,R'\,\rho_w U^2}$$

where f(R/R') is a dimensionless factor given by

$$f(R/R') = f(\gamma) = \frac{[1+\gamma^2-(1+\gamma^3)^{2/3}][1+\gamma^3]^{11/3}}{\gamma^6(1+\gamma)^3} \qquad (2.17)$$

Experimental results from Macklin and Bailey (1968) indicated that the collection efficiency of smooth spheres and artificial hailstones decreases with an increase in radius. The value can be as low as 0.2 for a stone with a radius of 4 cm. However, English (1973) compared the growth of hailstones in a modelled updraft using a collection efficiency of unity and the one given by Macklin and Bailey. The difference in the final diameter of hailstones from using the two different collection efficiencies was found to be small for stones less than 1.25 cm in radius. Since the largest graupel in the present model is 1.66 cm, a collection efficiency of unity is assumed.

Not all the supercooled water collected by the graupel freezes as latent heat is released by the freezing process. The determination of the amount of freezing follows.

Growth mode of graupel and melting (P9G, P9I)

The heat transfer between an ice particle and its environment determines whether wet or dry growth is possible. Since a wet graupel reflects electromagnetic waves like a water drop, the growth mode of graupel is important in computing the radar reflectivity factor and therefore must be determined explicitly. Experimental results (Vali, 1968) indicate that cloud ice occurs only at a very low temperature and would be unimportant for graupel growth throughout a major portion of the cloud. As a result collection of cloud ice by wet graupel will be neglected.

Cloud ice is assumed to melt instantaneously above 0°c, but the determination of the growth mode and the melting of the ice core of graupel particles are from the heat transfer equations of English (1973) modified for a graupel with a portion of unfrozen water on its surface. The details of the calculation are in Appendix 2.2.

Breakup (P7)

The problem of drop breakup by aerodynamic instability on free fall was studied by Komayabasi (1964) and Srivastava (1971). The expression for the probability of breakup and the size distribution of the fragments are:

$$P(R) = 2.94 \times 10^{-7} \exp(34R) \quad (\text{sec}^{-1}) \tag{2.18}$$

$$Q(R,R') = \frac{436.1}{R} \exp(-7\,R'/R) \quad (\text{cm}^{-1}) \tag{2.19}$$

Equation (2.18) indicates that instantaneous breakup is negligible for drops less than 2.5 mm. In the present model water drops $\geq$ 2.65 mm radius break up instantaneously and are redistributed according to (2.19).

A second breakup mechanism which has recently been found to be of greater importance is that of impaction. Experimental studies by Whelpdals and List (1971), Spengler and Gokhale (1973), Brazier-Smith et al (1972), and McTaggert-Cowan and List (1975) indicated that a varity of modes of breakup often result when raindrops collide. In general, impaction results in distributions of water masses which peak around the original radii of the parent drops. But the inclusion of the formation of satellites appears to play a role in shaping the size distribution of precipitation (Young, 1975); List and Gillespie, (1976).

To include the effects of drop breakup and the formation of satellites, the simple model of Brazier-Smith et al (1973) is adopted. Each collision between drops of masses X(R) and X(R') is assumed to produce three satellites drops of radius r_s and mass $\frac{0.04\,X(R)\,X(R')}{X(R)+X(R')}$, contributed equally by the

colliding pair. Fig. 2.2 depicts the sizes of the satellite drops produced and indicates the dominant role of the smaller drops in the resulting sizes of the satellites.

The number of collisions, $\tilde{N}(R,R')$ that occur between drops of radius R and R' are

$$\tilde{N}(R,R') = \pi (R+R')^2 E_1(R,R') N(R) N(R') [V(R) - V(R')]$$

The number of separations $\tilde{N}_S(R,R')$ is given by

$$\tilde{N}_S(R,R') = \tilde{N}[1 - E_2(R,R')]$$

Therefore the masses lost in each category of radius R and R' are $\tilde{N}_S \left[\frac{0.06\, X(R)\, X(R')}{X(R) + X(R')}\right]$ and the mass of satellites produced is

$\tilde{N}_S \left[\frac{0.12\, X(R) X(R')}{X(R) + X(R')}\right]$

The combined effect of instability and impaction breakup gives:

$$\begin{aligned} P7 = & -\rho_0 q_r(R) P(R) + \sum_{R'>R} \rho_0 q_r(R') P(R') Q(R,R') \delta R' \\ & - \sum_{R>R'} \tilde{N}_S(R,R') \left[\frac{0.06 X(R) X(R')}{X(R)+X(R')}\right] \\ & + \sum_{R'} \sum_{R''} \tilde{N}_S(R',R'') \left[\frac{0.12\, X(R') X(R'')}{X(R')+X(R'')}\right] \delta_{r_s,R} \end{aligned} \qquad (2.20)$$

where $\delta_{r_s,R}$ is a Dirac delta function.

The first two terms on the right of (2.20) represent in-

stantaneous breakup and the third and fourth term are the effect due to impaction.

Freezing (P8C, P8R)

The exact mechanism for the initiation of the ice phase is still poorly understood. Young (1974a)examined ice particle multiplication mechanisms and proposed a model of ice phase nucleation based on contact nucleation. However, no direct measurement of contact nuclei is available and the exact mechanism for this process remains controversial (Fukuta, 1975; Cooper, 1975). In view of this situation, a highly simplified model based on freezing of raindrops is used. Sensitivity tests will give insight into the freezing processes.

Based on Vali's (1968) observation of the freezing of water drops formed from bulk precipitation samples, Danielsen et al (1972) suggested that the fraction of drops F of volume v frozen at temperature T°c is

$$F = 1 - \exp[-v K_1(T)]$$

where

$$K_1 = 1.47\{\exp[-0.68(T+7)]-1\}; \text{ for } T < -7°c$$

$$= 0 \qquad ; \text{ for } T > -7°c$$

(2.21)

This fraction as a function of temperature and median radius is listed in Table 2.2.

Table 2.2

FRACTION OF DROPS OF RADIUS R FROZEN AT TEMPERATURE T°c

T°C \ R	.001	.005	.025	.055	.085	.115	.145	.175	.205	.235	.265 (cm)
-10	4.5×10^{-8}	5.1×10^{-6}	6.4×10^{-4}	6.8×10^{-3}	2.5×10^{-2}	6.1×10^{-2}	.12	.20	.30	.41	.53
-15	1.4×10^{-6}	1.8×10^{-4}	2.2×10^{-2}	.21	.58	.88	.98	1	1	1	1
-20	4.3×10^{-5}	5.3×10^{-3}	.49	1	1	1	1	1	1	1	1
-25	1.3×10^{-3}	.15	1	1	1	1	1	1	1	1	1
-30	3.7×10^{-2}	.99	1	1	1	1	1	1	1	1	1
-35	.68	1	1	1	1	1	1	1	1	1	1
-40	1	1	1	1	1	1	1	1	1	1	1
-45	1	1	1	1	1	1	1	1	1	1	1

For simplicity, frozen drops are assumed to ramain spherical with a density of 1 g cm^{-3}. Freezing occurs whenever the fraction of graupel masses to the total rain and graupel masses in a particular category is less than F. This assumption gives

$$PSR = \frac{1}{\delta t}\left\{\rho_0 \hat{q}_r(R)\exp[-\nu K_1(T)] + \rho_0 q_r(R)[1-\exp(-\nu K_1(T))]\right\} \tag{2.22}$$

$$PSC = \frac{1}{\delta t}\left\{\rho_0 \hat{q}_c(r)\exp[-\nu K_1(T)] + \rho_0 q_c(r)[1-\exp(-\nu K_1(T))]\right\}$$

Equation (2.22) refers to an average rate in a time step δt .

2.3 Comparison of present model with other schemes

The present microphysical model differs from the Kessler parameterization and stochastic method mainly in the assumption about autoconversion and the calculation of the collection processes. As such, it will be tested in a situation where these processes are included. Specifically, the effects of the initiation of warm rain in a one-dimensional kinematic updraft are compared. For the stochastic method, the formulation by Nelson (1971) is used. Comparisons between Kessler's and the present scheme are made under identical conditions as are in Nelson (1971).

2.3.1 Model equations

Stochastic model (model S)

The evolution of the number density distribution function given by Nelson is

$$\frac{\partial}{\partial t}[f\langle x\rangle dx] = -\frac{\partial}{\partial z}[(w+V) f\langle x\rangle dx]$$
$$+ \int_{x_0}^{x/2} f\langle x\rangle [f\langle x_c\rangle dx_c] \Phi(x_c, x') dx'$$
$$= \int_{x_0}^{x_m} f\langle x\rangle [f\langle x\rangle dx] \Phi(x, x') dx'$$
$$+ \int_{x}^{x_m} f\langle x'\rangle \Psi(x, x') dx'$$
$$- \frac{1}{x}\int_{x_0}^{x} [f\langle x\rangle dx] x' \Psi(x', x) dx' \qquad (2.23)$$

where $f\langle x\rangle dx$ is the number density distribution function taken over mass X; Xc=X-X'; X_o and X_m are respectively the smallest and largest drops considered; the collection and breakup kernels are given by $\Phi(x,x')$ and $\Psi(x,x')$.

Vertical droplet transport is represented by the first term on the right. The second term is the creation of X drops by coalescence of X' and X-X' drops. Drops of mass X are depleted by coalescence with X' drops in the third term. The fourth term is the effect of breakup of X' drops to yield fragments of mass X. The last term denotes the breakup of X drops.

Kessler's model (model K)

For future reference in Chapter 4, the general three-dimensional equations are described. Only the one-dimensional case without condensation and evaporation is used in this chapter.

The continuity equations for cloud and rain are:

$$\frac{\partial}{\partial t}(\rho_0 q_c) + \nabla\cdot(\rho_0 q_c \vec{u}) = P1 - P2C - AC - CC \qquad (2.24)$$

$$\frac{\partial}{\partial t}(\rho_0 q_r) + \nabla_H\cdot(\rho_0 q_r \vec{u}_H) + \frac{\partial}{\partial z}[\rho_0 q_r (V_0 + w)] = AC + CC - EVP \qquad (2.25)$$

P1 and P2C have the same meaning as in the last section, namely, condensation and evaporation of cloud. Autoconversion (AC) is assumed to produce precipitation particles following the Marshall-Palmer distribtuion. Accretion of cloud (CC), evaporation of raindrops (EVP), and fallspeed of the median diameter drop (V_o) are formulated by Kessler (1969) as

$$CC = 9.28\ \rho_0 q_c (\rho_0 q_r)^{7/8} \exp(kz/2) \qquad (2.26)$$

$$EVP = 4.3\ \rho_0 q_c (\rho_0 q_r)^{13/20} \qquad (2.27)$$

$$V_0 = 2.864\ (\rho_0 q_r)^{1/8} \exp(kz/2) \qquad (2.28)$$

where $k = 0.96 \times 10^{-6}\ cm^{-1}$

Present model (model P)

Equations (2.2) and (2.4) restricted to one-dimensional advection, collection, spectral shifting, autoconversion, and instantaneous breakup become

$$\frac{\partial}{\partial t}(\rho_0 q_c) + \frac{\partial}{\partial z}(\rho_0 q_c w) = - P4 - P5 \tag{2.29}$$

$$\frac{\partial}{\partial t}(\rho_0 q_r) + \frac{\partial}{\partial z}[\rho_0 q_r (w+V)] = -\delta R \frac{\partial}{\partial R}\left(\rho_0 q_r \frac{\dot{R}}{\delta R}\right) + P4 + P6 + P7 + P5 \tag{2.30}$$

However, no graupel particles and impaction breakup effects are included in the P5, P6, and P7 processes. For the computation of radar reflectivity factors, the following relations are used:

$$Z = 5.69\,(\rho_0 q_r)^{7/4} \quad (\text{mm}^6\ \text{m}^{-3}) \tag{2.31}$$

(model K)

and

$$Z = \sum_k N(R)\,(2R)^6 \tag{2.32}$$

(model P)

2.3.2 Intitial conditions and computation methods

The vertical dimension in the domain is represented by 10 space levels. In accordance with the initial condition used by Nelson (1971), a cloud water content of 0.8 g m^{-3} is specified at levels 2 to 10 for models P and K. Level 1 is retained as a rainout accumulator to conserve the total mass within the system.

For the stochastic model, an initial droplet spectrum normalized to a liquid water content of 0.8 g m^{-3} is specified. The spectrum is obtained from observation data of Braham et al (1957) in tropical cumuli without radar echoes. This initial spectrum is depicted in fig. 2.3.

To better resolve the small drops, the integrals for the coalescence and breakup terms in model S is solved by representing masses on a logarithmic scale with a total of 61 categories. The smallest drop has a radius of 4μ. The detail of the computation can be found in Nelson (1971).

Finite difference solution of the spectral shifting term $\delta R \frac{\partial}{\partial R}(\rho_0 q_r \frac{\dot{R}}{\delta R})$ in model P indicates too much numerical spreading in the evolution of the dropsize spectra. Accordingly, a method by Egan and Mahoney (1971) is used. This method computes the moments of the water content and is in Appendix 2.3.

The updraft profile used in the calculations is shown in fig. 2.4. The vertical transport terms are solved by a forward upstream method with δt =20 sec and δz =400 m. Reduction of δt to half this value shows no significant changes in the results.

2.3.3 Results

The evolution of the liquid water content, surface rainfall rate, radar reflectivity profile, and dropsize spectra are compared for the three models. The liquid

water content near the cloud base and cloud top (fig. 2.5) shows a local accumulation of liquid water above the updraft maximum on account of vertical transport in the early stage of the cloud. A peak total liquid water content of 4.2 g m^{-3} developed near the cloud top in model S while 3 g m^{-3} of cloud water is shown in model P at a time of 7 min. The temporary accumulation zone leads to rapid coalescence growth producing particles large enough to fall against the updraft. The arrival of rain at the cloud base is marked by the increase of rain water content after 15 minutes (model P).

In comparison, model K develops precipitation earlier both near the top and base of the cloud. This is a reflection of the assumed Marshall-Palmer distribution which gives a higher growth rate and large fall velocity of raindrops during the early stage of precipitation development. However, earlier depletion of cloud water and precipitation fallout leads to much less rain water near the cloud base in a later time.

Surface rainfall rate (fig. 2.6) and reflectivity profiles (fig. 2.7) showed similar results for models P and S. Model K produced an earlier rainfall maximum and a lower peak radar reflectivity factor. In the S and P models, radar reflectivity factor at the cloud base increases at a rate of 8 dbz min^{-1} from 13 to 17 minutes. This rate is consistent with observations by Saunders (1965) made on tropical cumuli.

The evolution of rain drop-size spectrum for models S and P at 18, 22, and 26 minutes is shown in fig. 2.8. The models predict rain to begin at the surface with the arrival of relatively large drops. Except for a slight scarcity of drops around 500 μ radius at the cloud base and a narrower spectrum at 18 minutes, model P is seen to agree well with the result from the stochastic model.

The realism of the one-dimensional stochastic model in simulation of the warm rain process has been discussed by Nelson (1971). He concluded that despite its simplicity and the neglect of horizontal divergence the model gives results consistent with the observed liquid water content and the onset of rain in tropical cumuli. The present microphysical scheme has been shown to give comparable results in terms of liquid water content, rainfall rate, radar reflectivity profiles, size-spectra of raindrops and is therefore to be preferred over the stochastic scheme on account of the smaller volume of computations required. Further sensitivity tests for the P model follow.

2.4 Sensitivity tests

The sensitivity tests that have been performed are listed in Table 2.3.

Effect of autoconversion rate and threshold

Figs. 2.9-2.13 indicate that the development of preci-

Table 2.3

SENSITIVITY TESTS PERFORMED

Process	Quantity	Tests
autoconversion	autoconversion rate(K)	$K=10^{-2}$ sec
		$K=10^{-3}$ sec
		$K=10^{-4}$ sec
	autoconversion threshold(a)	$a=0$ g m^{-3}
		$a=0.7$ g m^{-3}
collection (rain-rain)	self collection of rain particles	self collection of rain particles allowed
		self collection of rain particles not allowed
	coalescence efficiency $E_2(R,R')$ and satellite drops	$E_2(R,R')=1$, no satellite drops
		$E_2(R,R')$ from Brazier-Smith et al (1973), no satellite drops
		$E_2(R,R')$ from Brazier-Smith et al (1973), with satellite drops

pitation is relatively insensitive to changes in a and K. It should be pointed out that the combined effect of autoconversion and collection is responsible for growth of precipitation in this model. The {increase / decrease} of the rate of the autoconversion process {decreases / increases} the cloud water content which in turn {decreases / increases} the accretion rate for cloud droplets. Thus a negative feedback mechanism is involved and the development of precipitation is not greatly affected.

It is probable that this insensitivity would be modified if condensation, evaporation, and horizontal divergence were included. Nevertheless, model P is expected to be less sensitive to the autoconversion process than the K model. The reason is that in the former case, autoconversion produces only small raindrops centered at 50 μ radius.

Effect of rain-rain interaction

The importance of rain-rain interaction is illustrated in fig. 2.14. Suppression of this effect leads to a much slower growth process with negligible rainfall at the surface. The maximum size of the particles at cloud base is limited to 300 μ and the radar reflectivity factor never exceeds 25 dbz. This demonstrates that the process of accretion of only cloud drops is inadequate to explain the observed size spectrum. Raindrop interactions stand out as a major mechanism in the development of precipitation.

Effect of a variable coalescence efficiency and satellite drops

Rainfall rate, drop-size spectra, and radar reflectivity

factor for a variable coalescence efficiency are shown in fig. 2.15-2.17. Comparison with the results using a unit coalescence efficiency demonstrates the role of impaction breakup as a limiting mechanism for the growth of large drops. The narrower drop-size spectrum causes a delay of the onset of rainfall and a smaller maximum rainfall rate. Radar reflectivity factor near the cloud base is generally smaller. A difference of 6 dbz appears at a time of 21 minutes.

Rainfall rate and radar reflectivity factor calculations are relatively insensitive to the formation of satellite drops. The major effect of satellites is seen to increase the spectral number density for drops less than 500 μ radius at 50 minutes.

2.5 Summary

A simple microphysical model has been developed in this chapter. Despite its simplicity, the model is able to give results comparable to those of a stochastic method for development of warm rain in a one-dimensional kinematic updraft. Sensitivity tests appear to indicate a negative feedback mechanism in the autoconversion and accretion processes. Rain-rain interaction has been demonstrated to be of great importance in the development of precipitation drop-size spectrum and impaction breakup imposes limitation on drop growth. Incorporation of the model into a dynamic

framework will be made in Chapter 4 to study the microphysical-dynamical interactions in a cumulus cloud.

CHAPTER THREE

ANALYSIS OF PERTURBATION PRESSURE

3.1 Background

Since the earlier days of the parcel and slice methods, considerable progress has been made in the modelling of convective phenomena on the cumulus scale. The plume and bubble models (e.g. Levine, 1959;Squires and Turner, 1962) incorporated the entrainment concept of Stommel (1947) and Austin (1948). More elaborate one-dimensional models (e.g. Simpson and Wiggert, 1969) have been proved to be a useful tool in weather modification studies especially in field experiments.

A major assumption made in the dynamic structure of these models is that the pressure inside the cloud adjusts instantaneously to that of the environment. Convection is driven by the classical Archimedian buoyancy and any effects which might arise as a result of possible deviation of the pressure from that of the environment are ignored. This assumption, although an oversimplification, has not been seriously challenged until recent years. The reason lies partly in the difficulty of including perturbation pressure in simple models and partly in the incomplete information on the nature of the perturbation pressure forces given by earlier observations (e.g. The Thunderstorm Project, 1949).

The impetus for the recognition of the importance of perturbation pressure comes from a number of recent observations.

On the basis of a balloon sounding taken inside the updraft of an active severe storm, Barnes (1970) reported an excess hydrostatic pressure of 3 mb at a level of 6 km and a pressure deficit of 1 mb near the cloud base. As is pointed out by Davies-Jones and Ward (1971), Barnes corrected only for the dynamic pressure effect in deriving the pressure-height relations; some of the excess pressure might well be accounted for by liquid water drag and entrainment mixing. Nevertheless, it is reasonable to expect that a real excess of 1-2 mb can occur at 6 km (Barnes, 1971).

Observations by Marwitz (1973) provided an indirect indication of the role of perturbation pressure forces. Radar tracking of 21 slow-fall chaff packets which rise in the weak echo region of eight Colorado storms revealed that the inflow air often has its origin near the surface. The air is, however, negatively buoyant below the cloud base in seven cases. An important deduction is that most storms develop a substantial pressure perturbation. The horizontal pressure gradient accelerates the low-level inflow toward the center of the updraft while a vertical pressure gradient transports the negatively buoyant surface air to a level above cloud base where it gains positive buoyancy.

A large number of observations on the same phenomenon have since been reported by Davies-Jones (1974, 1975). In certain cases, air with a virtual temperature 10°c colder than the

environment still accelerates upward. The mechanism must be dynamic in nature and perturbation pressure forces appear to offer a plausible explanation.

Theoretical investigations of the perturbation pressure effect have been carried out through qualitative arguments, simple analytic models, and numerical experiments. Bleeker and Andre (1950) discussed the observed surface pressure associated with thunderstorms in terms of the lifting of pressure surfaces in the upper part of a convective column and the divergence and convergence of the air that result. Van Thullenar (1960) argued from a hypothetical sounding of the cloud and environment that substantial hydrostatic pressure, different from the environment, might build up inside the cloud. Sanders (1975) discussed qualitatively the pressure response from different modes of forcing on the basis of the anelastic pressure equation (Ogura and Phillips, 1962).

Simple analytic models of the perturbation pressure forced by buoyancy forcing have been solved by Young (1972) and Gordon (1975). The latter demonstrated that perturbation pressure gradient force may support the negatively buoyant air in convective storms found in observations. However, these investigations are limited to only one aspect of the forcing mechanism and the profiles of the forcing functions which can yield analytic solutions are highly restricted.

Numerical cloud models which solve for the pressure explicitly

(e.g. Arnason and Greenfield, 1968; Soong and Ogura, 1973; Schlesinger, 1973a,1973b, 1975; Wilhelmson,1974) typically show that the pressure force acts against the buoyancy. Of particular interest is the numerical experiment by Wilhelmson and Ogura (1972) which pointed out that the perturbation pressure is an order of magnitude smaller than that which scale analysis (Ogura and Phillips, 1962) has indicated. They therefore concluded that the dependence of temperature on perturbation pressure may be neglected in the calculation of saturation vapor pressure in deep convection. However, a major drawback of these complicated models is that they often add little insight in understanding the physics underlying the processes. Furthermore, numerical models impose an artificial lateral pressure boundary condition and a unique solution of the perturbation pressure equation cannot be obtained (Ogura and Charney, 1960).

The purpose of this chapter is to analyze the effect of the perturbation pressure in a comprehensive manner by means of analytic techniques. As a basis for the investigation, the anelastic pressure equation is derived in section 3.2. Simple sinusoidal forcing functions are then used to obtain analytic solutions in section 3.3. These forcing functions might lack a certain degree of realism but are instructive in demonstrating the essential physical properties of the pressure responses. More realistic forcing functions are then specified in section 3.4 and the general solutions are obtained by Green's functions.

3.2 Derivation of the anelastic pressure equation

Ogura and Phillips (1962) obtained by scale analysis a set of equations for inviscid flow suitable for the study of small-scale convection in a non-rotating atmosphere. The equation of motion modified to include non-isentropic base-state potential temperature distributions is given by Wilhelmson and Ogura (1972) as

$$\underbrace{\frac{\partial \vec{u}}{\partial t}}_{\text{inertial term}} + \underbrace{\vec{u}\cdot\nabla\vec{u}}_{\text{inertial term}} = \underbrace{-c_p\theta_0\nabla\pi'}_{\text{pressure gradient force}} + \underbrace{g\left(\frac{\theta'}{\theta_0} + 0.61\,q_v'\right)\hat{k}}_{\text{thermal and water vapor buoyancy}} \underbrace{- gQ\hat{k}}_{\text{hydrometeor drag}} \qquad (3.1)$$

where $\theta_0(z)$ is the base state potential temperature for a hydrostatic atmosphere; θ', π', q_v' denote respectively the perturbation potential temperature, non-dimensional pressure, and water vapor content from the base state; Q is the mixing ratio of all hydrometeors. It will be assumed that falling hydrometeor particles reach their terminal velocities at once and the drag force is therefore equal to the sum of their weights.

Ogura and Phillips (1962) showed that for shallow convection, the velocity field is non-divergent;

$$\nabla\cdot\vec{u} = 0 \qquad (3.2)$$

but for the case of deep convection the continuity equation takes the following form.

$$\nabla\cdot(\rho_0\vec{u}) = 0 \qquad (3.3)$$

where ρ_0 is the density of the base state atmosphere. An

important consequence of (3.2) and (3.3) is that the time rate of change of density does not appear and sound waves are filtered out.

For simplicity, equation (3.2) will be used. The anelastic pressure equation in this case can be obtained by taking the divergence of (3.1) and utilizing (3.2). The result turns out to be

$$c_p \nabla\cdot(\theta_0 \nabla\pi') = -\nabla\cdot(\vec{u}\cdot\nabla\vec{u}) + g\frac{\partial}{\partial z}\left(\frac{\theta'}{\theta_0} + 0.61 q_v'\right) - g\frac{\partial Q}{\partial z} \qquad (3.4)$$

Equation (3.4) indicates that the pressure perturbation responds instantaneously to the forcing on the right; within the accuracy of the anelastic approximation.

Following Wilhelmson and Ogura (1972) the first term on the right of (3.4) is termed dynamic, the second buoyancy, and the third drag. Since the equation is linear in π', the response to the various components of forcing can be split into the corresponding component equations. Thus

$$c_p \nabla\cdot(\theta_0 \nabla\pi'_\theta) = g\frac{\partial}{\partial z}\left(\frac{\theta'}{\theta_0} + 0.61 q_v'\right) \qquad (3.5)$$

$$c_p \nabla\cdot(\theta_0 \nabla\pi'_Q) = -g\frac{\partial Q}{\partial z} \qquad (3.6)$$

$$c_p \nabla\cdot(\theta_0 \nabla\pi'_m) = -\nabla\cdot(\vec{u}\cdot\nabla\vec{u}) \qquad (3.7)$$

where π'_m, π'_θ, π'_Q are respectively the perturbation pressure corresponding to the dynamic, buoyancy, and drag forcings.

In the analysis that follows, motions will be limited vertically by two parallel fixed boundaries separated by a distance H. The top and bottom boundaries are rigid with the free-slip condition. Then

$$\frac{\partial \vec{u}_H}{\partial z} = 0 \,, \quad w = 0 \qquad \text{at } z=0 \text{ and } z=H$$
$$\theta' = 0 \,, \quad q_v' = 0 \tag{3.8}$$

The pressure boundary conditions follow from (3.1) and (3.8), that is

$$c_p \theta_0 \frac{\partial \pi'}{\partial z} = -g Q \qquad \text{at } z=0$$
$$\frac{\partial \pi'}{\partial z} = 0 \qquad \text{at } z=H \tag{3.9}$$

3.3 Analytic solutions for structurally simple forcing functions

3.3.1 Form of the forcing functions

Simple sinusoidal functions are specified for the potential temperature perturbation, hydrometeor water content, updraft velocity, and horizontal inflow. The functions are chosen for their simplicity so that physical insight can be gained without

undue complexity in mathematical analysis.

For the pressure response to buoyancy and drag forcings, three-dimensional solutions can be readily obtained. The dynamic forcing is however non-linear in the velocity fields. In order to avoid mathematical complications, motions will be restricted to the X-Z plane and solutions to equation (3.7) are obtained for the case of slab geometry.

The potential temperature perturbation is specified to have the form:

$$\theta' = \hat{\theta} \sin(nz) \cos(lx) \cos(my) \qquad (3.10)$$

where $n = \frac{\pi}{H}$, $l = \frac{\pi}{L_1}$, $m = \frac{\pi}{L_2}$. L_1 and L_2 are horizontal dimensions of the cloud; H is the vertical extent of the updraft; $\hat{\theta}$ is the amplitude.

To simplify the calculations, θ' is assumed to include the effect of water vapor buoyancy. A value of 1°c is used for $\hat{\theta}$ in accordance with observed buoyancy found in small cumuli (Malkus, 1954). The vertical section of $g(\theta'/\theta_0)$ at y=0 (hereafter called vertical section) is depicted in fig. 3.1.

As is indicated in the figure, negative buoyancy exists outside the cloud and the negative amplitude is larger than that which might be expected from evaporation of water vapor as a result of mixing near the cloud edge. But this unrealistic

feature however should not affect the qualitative conclusions.

To model non-precipitating and precipitating cloud, two profiles for Q are used. Q_1 represents the water content profile in a non-precipitating cumulus. Q_2 has a maximum at the ground to simulate the effect of precipitation reaching the surface. The two profiles are written as

$$Q_1 = \hat{Q} \sin(nz) \cos(lx) \cos(my) \tag{3.11}$$

$$Q_2 = \hat{Q} \left[\frac{1+\cos(nz)}{2}\right] \cos(lx) \cos(my) \tag{3.12}$$

where the amplitude $\hat{Q}$ has a value of 1 g kg^{-1}. The profiles for $-gQ_1$ and $-gQ_2$ are in figs. 3.2-3.3.

It is recognized that (3.11) and (3.12) do not conform to any physical forcing outside the cloud, since negative water content does not exist. This inconsistency will be removed by the use of a top-hat profile in section 3.4. In the meantime the sinusoidal forcings can at least be treated formally as a single harmonic in a series expansion for Q.

The updraft velocity in the X-Z plane is given by

$$w = \hat{W} \sin(nz) \cos(lx) \tag{3.13}$$

By assuming slab-symmetry, the horizontal velocity can be calculated from the continuity equation. Thus

$$u = -\left(\frac{n}{l}\right) \hat{W} \sin(lx) \cos(nz) \tag{3.14}$$

Warner (1970) obtained measurements of updraft velocities in cumulus cloud with a depth ranging from 0.7 to 4 km. Based on his findings, a value of 5 m sec^{-1} is chosen for $\hat{W}$. The u and w velocities and the streamfunction are shown in figs. 3.4-3.6.

3.3.2 Solutions of the pressure equations

Solutions to equations (3.5), (3.6), and (3.7) are obtained for a constant base state potential temperature. This simplification will later be shown to be valid as the effect of the stability factor $S_z = \frac{1}{\theta_0}\frac{\partial \theta_0}{\partial z}$ on perturbation pressure is slight under normal atmospheric conditions.

Perturbation pressure from buoyancy forcing

By substituting θ' from (3.10), equation (3.5) becomes

$$c_p \nabla^2 \pi'_\theta = \frac{g\hat{\theta}}{\theta_0^2} n \cos(nz) \cos(lx) \cos(my) \tag{3.15}$$

A solution for π'_θ in the form

$$\pi'_\theta = \hat{\pi}'_\theta \cos(nz) \cos(lx) \cos(my) \tag{3.16}$$

can be obtained by substituting (3.16) into (3.15) and equating the coefficient of the same harmonic. Hence

$$\pi'_\theta = -\frac{g}{c_p \theta_0^2} \frac{n\hat{\theta}}{(l^2+m^2+n^2)} \cos(nz) \cos(lx) \cos(my) \tag{3.17}$$

The associated pressure forces are

$$-c_p\theta_0 \frac{\partial \pi'_\theta}{\partial z} = -\frac{g}{\theta_0}\frac{n^2\hat{\theta}}{(l^2+m^2+n^2)} \sin(nz)\cos(lx)\cos(my) \quad (3.18)$$

$$-c_p\theta_0 \frac{\partial \pi'_\theta}{\partial x} = -\frac{g}{\theta_0}\frac{nl\hat{\theta}}{(l^2+m^2+n^2)} \cos(nz)\sin(lx)\cos(my) \quad (3.19)$$

$$-c_p\theta_0 \frac{\partial \pi'_\theta}{\partial y} = -\frac{g}{\theta_0}\frac{nm\hat{\theta}}{(l^2+m^2+n^2)} \cos(nz)\sin(lx)\sin(my) \quad (3.20)$$

Fig. 3.7 shows the vertical section of π'_θ . A high pressure center is located inside the cloud above the level of maximum buoyancy and a low pressure dome lies directly underneath. The vertical pressure gradient force (fig. 3.8) acts downward and opposes the buoyancy in the region of the updraft. The total acceleration illustrated in fig. 3.9 reveals a net upward acceleration inside the cloud and a downward acceleration outside. The circulation is completed by the horizontal perturbation gradient force which induces inflow in the lower half of the cloud and outflow in the upper portion (fig. 3.10). The picture is reminiscent of a ring vortex.

Further deductions regarding the effect of the horizontal scale and geometry of the cloud can be obtained from equations (3.18)-(3.20). By letting L_1 and $L_2 \longrightarrow \infty$, the pressure forces become

$$-c_p\theta_0 \frac{\partial \pi'_\theta}{\partial z} = -\frac{g}{\theta_0}\hat{\theta}\sin(nz)\cos(lx)\cos(my)$$

$$= -g\frac{\theta'}{\theta_0}$$

$$\frac{\partial \pi'_\theta}{\partial x} = \frac{\partial \pi'_\theta}{\partial y} = 0$$

Thus the $\left\{\begin{matrix}\text{vertical}\\\text{horizontal}\end{matrix}\right\}$ pressure gradient force $\left\{\begin{matrix}\text{increases}\\\text{decreases}\end{matrix}\right\}$ with an increase in horizontal scale. The cloud becomes hydrostatic for an infinite horizontal extent.

If L_2 is allowed to become large in (3.18)-(3.20), then

$$-c_p\theta_0 \frac{\partial \pi'_\theta}{\partial z} = -\frac{g}{\theta_0}\frac{n^2\hat{\theta}}{(l^2+n^2)}\sin(nz)\cos(lx)$$

$$-c_p\theta_0 \frac{\partial \pi'_\theta}{\partial x} = -\frac{g}{\theta_0}\frac{nl\hat{\theta}}{(l^2+n^2)}\cos(nz)\sin(lx)$$

$$\frac{\partial \pi'_\theta}{\partial y} = 0$$

The cloud in this case becomes two dimensional and since the X and Z components of the pressure force have larger magnitudes than in the three-dimensional case, the effect of perturbation pressure will be more pronounced for a slab model than for a

three- dimensional one.

Pressure response to drag forcing

For a non-precipitating cloud, the pressure boundary condition remains homogeneous and the same procedure as is used in the case of the buoyancy forcing can be employed to obtain the perturbation pressure. For a precipitating cloud, a homogeneous solution for (3.6) will be determined which together with the particular solution satisfies the boundary condition (3.9).

Substituting (3.12) into (3.6) together with the expansion of $\pi'_\alpha = \hat{\pi}_\alpha(z)\cos(lx)\cos(my)$, an equation for $\hat{\pi}_\alpha(z)$ is obtained as

$$\frac{d^2\hat{\pi}_\alpha(z)}{dz^2} - (l^2+m^2)\hat{\pi}_\alpha = \frac{g}{c_p\theta_0}\hat{Q}\frac{n}{2}\sin(nz) \qquad (3.21)$$

The solution to (3.21) is

$$c_p\hat{\pi}_\alpha(z) = C_1\sinh(l^2+m^2)^{1/2}z + C_2\cosh(l^2+m^2)^{1/2}z$$

$$- \frac{g}{\theta_0}\hat{Q}\frac{n}{2(l^2+m^2+n^2)}\sin(nz) \qquad (3.22)$$

Where the constant C_1 and C_2 must be determined from the boundary conditions.

Figs. 3.11-3.12 compare the vertical sections of π'_α corresponding to the two forcings represented by (3.11) and (3.12). For a non-precipitating cloud, a high pressure area develops below the level of maximum water content and a low pressure area

develops above. In the precipitating case, the low pressure area is shifted to the middle portion of the cloud and an intense high forms near the surface (fig. 3.12).

The drag and pressure forces at the central axis depicted in fig. 3.13 indicate that in general the pressure force opposes the drag of the hydrometeors. This force is especially large near the ground for a precipitating cloud. The large gradient is required to satisfy the hydrostatic condition at the surface. The magnitude of the pressure forces should not be taken too seriously; as is mentioned previously the forcing functions are not realistic outside the cloud region.

Pressure response to dynamic forcing

By means of vector identities, equation (3.7) can be put into the following form:

$$c_p \theta_0 \nabla^2 \pi_m' = -\underbrace{\nabla^2\left(\frac{\vec{u}\cdot\vec{u}}{2}\right)}_{\text{kinetic energy forcing}} + \underbrace{\vec{\omega}\cdot\vec{\omega} - \vec{u}\cdot(\nabla\times\vec{\omega})}_{\text{vorticity forcing}} \qquad (3.23)$$

where $\vec{\omega}$ is the vorticity given as

$$\vec{\omega} = \nabla \times \vec{u} \qquad (3.24)$$

A significant aspect of (3.23) is that the perturbation pressure is the response to kinetic energy and vorticity forcings. Before proceeding to the solution of (3.23), some results can be anti -

cipated by an approximate analysis of the equation of motion.

If a steady state solution is assumed and the buoyancy and drag forces are neglected, (3.1) reduces to

$$\vec{u} \cdot \nabla \vec{u} = -c_p \theta_0 \nabla \pi'_m \tag{3.25}$$

The left hand side can be further expanded to give

$$\nabla \left(\frac{\vec{u} \cdot \vec{u}}{2} \right) + \vec{\omega} \times \vec{u} = -c_p \theta_0 \nabla \pi'_m \tag{3.26}$$

By taking the dot product of $\vec{u}$ or $\vec{\omega}$ with (3.26), the Bernoulli equation results; that is

$$\frac{\vec{u} \cdot \vec{u}}{2} + c_p \theta_0 \pi'_m = \text{CONSTANT} \tag{3.27}$$

along a streamline or vortex line.

Equation (3.27) represents the conversion of kinetic and potential energies (in this case by perturbation pressure). Thus along a streamline or a vortex line, low pressure areas will be found in regions of high kinetic energy and high pressure areas in regions of low kinetic energy.

Further insight can be gained by casting (3.26) in a natural coordinate system depicted in fig. 3.14. For simplicity, a slab-symmetric circulation in the X-Z plane is assumed. With the air-speed V along the direction of the streamline $\hat{s}$, the vorticity can be shown (see e.g. Holton, 1972) to be

$$\vec{\omega} = \left(-\frac{\partial V}{\partial n} + \frac{V}{R_s} \right) \hat{k} \tag{3.28}$$

where n is along the normal direction and R_s is the radius of

curvature.

By using (3.28), (3.26) can be expressed as

$$\frac{\partial}{\partial n}\left(\frac{V^2}{2}\right)\hat{n} + \frac{\partial}{\partial s}\left(\frac{V^2}{2}\right)\hat{s} + \left(-\frac{\partial V}{\partial n} + \frac{V}{R_s}\right)V\hat{n}$$

$$= -c_p\theta_0\frac{\partial \Pi'_m}{\partial n}\hat{n} - c_p\theta_0\frac{\partial \Pi'_m}{\partial s}\hat{s} \qquad (3.29)$$

where the direction $\hat{s}$ is along the motion of the fluid.

For a constant θ_0, the tangential and normal components of (3.29) are respectively

$$\frac{\partial}{\partial s}\left(\frac{V^2}{2} + c_p\theta_0\,\Pi'_m\right) = 0 \qquad (3.30)$$

and

$$\frac{V^2}{R_s} = -c_p\theta_0\frac{\partial \Pi'_m}{\partial n} \qquad (3.31)$$

Thus Bernoulli's equation is recovered in (3.30) and (3.31) becomes the statement of the balance of the centrifugal and perturbation pressure forces.

Equation (3.31) shows that a low pressure area is located to the {right / left} of the direction of motion for {clockwise / counterclockwise} rotation. Furthermore, the perturbation pressure force normal to the direction of the flow increases with a decrease in the radius of curvature. Therefore in a cumulus cloud where the circulation resembles that of a ring vortex, a low center would be found near the cloud edge at the level of maximum vertical velocity. The strong rotation of the air at that level

causes a large centrifugal force which balances the perturbation pressure gradient.

The solution to (3.23) is more meaningful when the effects of kinetic energy and vorticity forcing are separated. In two-dimensions, the component equations are:

$$c_p \theta_0 \left(\frac{\partial^2}{\partial x^2} + \frac{\partial^2}{\partial z^2}\right) \pi'_{m_1} = \underbrace{-\frac{1}{2}\left(\frac{\partial^2}{\partial x^2} + \frac{\partial^2}{\partial z^2}\right)(u^2+w^2)}_{-\nabla^2 K.E.} \tag{3.32}$$

$$c_p \theta_0 \left(\frac{\partial^2}{\partial x^2} + \frac{\partial^2}{\partial z^2}\right) \pi'_{m_2} = \underbrace{\left(\frac{\partial w}{\partial x}\right)^2 + \left(\frac{\partial u}{\partial z}\right)^2 - 2\frac{\partial u}{\partial z}\frac{\partial w}{\partial x}}_{\vec{\omega}\cdot\vec{\omega}} + \underbrace{u\left(\frac{\partial^2}{\partial x^2} + \frac{\partial^2}{\partial z^2}\right)u + w\left(\frac{\partial^2}{\partial x^2} + \frac{\partial^2}{\partial z^2}\right)w}_{-\vec{u}\cdot\nabla\times\vec{\omega}} \tag{3.33}$$

With u and w as in (3.13) and (3.14), the solution to (3.32) and (3.33) can be shown to be

$$c_p \theta_0 \pi'_{m_1} = -\frac{\hat{W}^2}{8l^2}\left[(l^2-n^2)\cos(2lx) - (l^2-n^2)\cos(2nz) - (l^2+n^2)\cos(2lx)\cos(2nz)\right] \tag{3.34}$$

$$c_p \theta_0 \pi'_{m_2} = \frac{1}{8}\left(\frac{l^2+n^2}{l^2}\right)\hat{W}^2\left[\cos(2lx)+\cos(2nz) - \cos(2lx)\cos(2nz)\right] \tag{3.35}$$

Vertical sections of kinetic energy and squared vorticity are shown in figs. 3.15-3.16. Two general observations can be

made with the comparison of pressure responses in figs. 3.17-3.18.

(1) Centers of $\begin{Bmatrix}\text{maximum}\\ \text{minimum}\end{Bmatrix}$ kinetic energy are also centers of $\begin{Bmatrix}\text{low}\\ \text{high}\end{Bmatrix}$ perturbation pressure in accordance with the Bernoulli effect.

(2) The centers of maximum squared vorticity correspond to center of low pressure off the center of the cloud. This is the result of the balance of the centrifugal and perturbation pressure forces.

The total perturbation pressure due to dynamic forcing is the sum of (3.34) and (3.35), that is

$$c_p \theta_0 \pi'_m = \frac{\hat{W}^2}{4}\left[\left(\frac{n}{\ell}\right)^2 \cos(2\ell x) + \cos(2nz)\right] \tag{3.36}$$

The corresponding vertical pressure force is given by

$$-c_p \theta_0 \frac{\partial \pi'_m}{\partial z} = \frac{\hat{W}^2}{2}\, n \sin(2nz) \tag{3.37}$$

which is independent of the horizontal scale.

Cross-sections of π'_m and the vertical pressure force at the central axis are plotted in figs. 3.19-3.20. Two high pressure areas occur respectively at cloud top and base. A low is situated off center as is discussed above. The pressure force is upward in the lower part of the cloud and downward near the cloud top.

It is also of interest to note that π'_m in (3.36) is proportional to the square of the updraft velocity. Hence similar pressure response will occur for up and downdraft having similar

configurations and the perturbation pressure due to dynamic forcing will be most important for vigorous storms.

Effect of stratification of the atmosphere

The above analysis assumes a constant base state potential temperature. The real atmosphere, however, is usually stably stratified. The effect of the stratification of potential temperature will be examined to determine its role in affecting the magnitude of the perturbation pressure. Specifically, (3.5) will be solved by allowing for a non-zero but constant stability factor $S_z = \frac{1}{\theta_0}\frac{\partial \theta_0}{\partial z}$

In terms of S_z, (3.5) can be written as

$$C_p\left[\nabla^2 \pi'_\theta + S_z \frac{\partial \pi'_\theta}{\partial z}\right] = g\left[\frac{\partial \theta^*}{\partial z} + S_z \theta^*\right] \tag{3.38}$$

where $\theta^* = \frac{\theta'}{\theta_0^2}$ and is assumed to have the following form

$$\theta^* = \theta_1 \sin(nz)\cos(lx)\cos(my) \tag{3.39}$$

where $\theta_1 = \frac{\hat{\theta}}{\textcircled{H}^2}$; $\hat{\theta}$ is 1°c; $\textcircled{H}$, a mean potential temperature, has a value of 296°k.

Equation (3.38) is solved by expanding π'_θ into

$$\pi'_\theta = \hat{\pi}(z)\cos(lx)\cos(my) \tag{3.40}$$

With θ^* and π'_θ as defined in (3.39) and (3.40), (3.38) gives an equation for $\hat{\pi}$ as

$$C_p\left[\frac{d^2\hat{\pi}}{dz^2} + S_z\frac{d\hat{\pi}}{dz}\right] - (l^2+m^2)\hat{\pi} = g\theta_1[n\cos(nz) + S_z\sin(nz)] \tag{3.41}$$

A particular solution to (3.41) is

$$\hat{\pi}_p = a_1 \cos(nz) + a_2 \sin(nz)$$

where a_1 and a_2 are determined by comparing coefficients.

The homogeneous solution is given by

$$\hat{\pi}_H = b_1 e^{\alpha z} + b_2 e^{\gamma z}$$

with α , γ being the solutions of

$$q^2 + S_z q - (l^2+m^2) = 0$$

The total $\hat{\pi}$ can be written as

$$\hat{\pi} = b_1 e^{\alpha z} + b_2 e^{\gamma z} + a_1 \cos(nz) + a_2 \sin(nz) \qquad (3.42)$$

where the constants b_1 and b_2 are determined from the boundary conditions $\frac{d\hat{\pi}}{dz}$ =0 at z=0 and z=H.

The value of Sz for the atmosphere is on the order of $10^{-5}m^{-1}$ (e.g. Jordan, 1958). π'_θ calculated with an Sz of $2x10^{-5}m^{-1}$ is shown in fig. 3.21. Comparison with fig. 3.7 where Sz=0 indicates that the effect of stratification on computing the perturbation pressure is slight. The difference in the magnitude of the pressure for the two cases is less than 1 per cent. Similar conclusions are expected for the drag and dynamic parts of the perturbation pressure.

3.4 Green's function solutions for more realistic forcings

3.4.1 More realistic forcing functions

Some quantitative aspects of the role of perturbation pressure are investigated with forcing functions having more realistic variations in the horizontal plane. The base state potential temperature is assumed constant in view of the conclusion from the analysis performed in the last section. For simplicity, the problem will be solved in axi and slab geometries. The forms of the forcing functions used are listed in Table 3.1.

The vertical profiles are simple sinusoidal functions used in section 3.4. For the horizontal variations, a Gaussian profile is used for the buoyancy and a top-hat profile for the drag. The horizontal profiles of the velocity fields plotted in fig. 3.22 indicate that to satisfy continuity over an infinite plane, the geometries impose constraints on the magnitude of the compensating current outside the cloud. For the slab-geometry, a much larger compensating current is required to balance the upward mass transport accomplished by the updraft. The amplitudes $\hat{\theta}$, $\hat{Q}$, and $\hat{W}$ are respectively $1^{o}c$, 1 g kg^{-1} and 5 m sec^{-1} as in the last section.

3.4.2 Method of solution

Green's function solution will be developed for equations (3.5), (3.6), (3.7). The method will be illustrated for the axi-symmetric case and the same procedure applies for a slab model.

The general form of (3.5), (3.6), (3.7) is

Table 3.1

FORCING FUNCTIONS

Geometry of cloud / Type of forcing	Axisymmetry	Slab-symmetry
Buoyancy θ'	$\hat{\theta}\, e^{-(r/a)^2} \sin(nz)$	$\hat{\theta}\, e^{-(x/a)^2} \sin(nz)$
Drag Q	$\hat{Q} \sin(nz), 0<r\leq a$ $0 \quad , a<r$	$\hat{Q} \sin(nz), 0<x\leq a$ $0 \quad , a<x$
vertical velocity W	$\hat{W}\,(1-(r/a)^2)e^{-(r/a)^2} .\sin(nz)$	$\hat{W}\,(1-(x/a)^2)e^{-0.5(x/a)^2} .\sin(nz)$
horizontal velocity u	$-\hat{W}\,(r/2)\, e^{-(r/a)^2} .\cos(nz)$	$-\hat{W}\, x\, e^{-0.5(x/a)^2} .\cos(nz)$

a is the radius of the cloud.

r is in the radial direction.

$$\frac{1}{r}\frac{\partial}{\partial r}\left(r\frac{\partial \pi'}{\partial r}\right) + \frac{\partial^2 \pi'}{\partial z^2} = \mathcal{F} \qquad (3.43)$$

where $\mathcal{F}$ is a general forcing function and r is the distance in the radial direction.

The top and bottom boundary conditions are

$$\frac{\partial \pi'}{\partial z} = 0 \qquad \text{at } z=0 \text{ and } z=H$$

For the lateral boundary conditions, it is demanded that

$$\frac{\partial \pi'}{\partial r} = 0 \qquad \text{at } r=0, \text{ and}$$

$$\pi' = 0 \qquad \text{as } r \to \infty$$

The homogeneous boundary conditions allow expansion of the perturbation pressure in a Fourier cosine series of form

$$\pi' = \sum_k \pi_k(r) \cos(knz) \qquad (3.44)$$

Substituting (3.44) into (3.43) gives

$$\sum_k \left[\frac{1}{r}\frac{d}{dr}\left(r\frac{d\pi_k}{dr}\right) - (kn)^2 \pi_k\right] \cos(knz) = \mathcal{F} \qquad (3.45)$$

By means of the orthogonal properties of the cosine functions, the individual Fourier mode is found to satisfy:

$$\frac{1}{r}\frac{d}{dr}\left(r\frac{d\Pi_0}{dr}\right) = \frac{1}{H}\int_0^H \mathcal{F}\,dz = F_0 \tag{3.46}$$

$$\frac{1}{r}\frac{d}{dr}\left(r\frac{d\Pi_k}{dr}\right) - (kn)^2\,\Pi_k = \frac{2}{H}\int_0^H \mathcal{F}\cos(knz)\,dz = F_k \quad , k \neq 0 \tag{3.47}$$

Π_0 is obtained by direct integration while Π_k is solved by using Green's function.

With the appropriate Green's function derived in Appendix 3.1, the pressure modes are computed as

$$\Pi_k(r) = \int_0^\infty G^k(\xi, r)\,\xi\,F_k(\xi)\,d\xi \tag{3.48}$$

where $G^k(\xi, r)$ is the Green's function for the k^{th} mode. The method of evaluation of (3.48) also appears in the same appendix.

3.4.3 Pressure responses

Vertical sections of the perturbation pressures and pressure gradient forces for the two geometries are compared in figs. 3.23-3.34. The pressure responses in general agree with the qualitative picture developed in section 3.3. The buoyancy- and drag- induced pressure forces oppose the prescribed forcing. It is of interest to point out that in the slab model, the low pressure center induced by the dynamic forcing (fig. 3.26) is directly over the edge of the cloud and has a larger absolute magnitude than the highs at the top and bottom of the domain. The opposite is true for the axi-symmetric case and the low center is displaced toward the central axis (fig. 3.25).

Quantitative assessment of the magnitudes of the different

pressure forces can best be made from the vertical profiles at the central axis shown in figs. 3.35-3.37. The peak values of the forcing and the induced pressure forces from these figures are listed in Table 3.2. As anticipated, the pressure forces are larger in the slab geometry; being two to three time as large as the values in the axi-symmetric case. Since convection is often initiated by a buoyancy impulse in numerical models, this difference in pressure forces can partly explain the less vigorous cloud development for slab models reported by Murray (1970) and Soong and Ogura (1973).

Table 3.2 indicates that the pressure forces induced by drag and buoyancy account for 25-50% of the magnitude of the forcing. The dynamic pressure force almost cancels the effect of vertical advection in the slab geometry but is much smaller for the axi-symmetric cloud. The vertical advection tends to place the maximum velocity near the top of the cloud as is generally indicated in one-dimensional models where the effect of perturbation pressure is ignored. It is shown that the dynamic pressure force acts to augment the buoyancy in the lower half of the cloud and opposes motion in the upper half of the updraft (fig. 3.37). This force plays an important role in lessening the strong velocity gradient near the cloud top and tends to lower the level of maximum velocity as has recently been observed (e.g. Marwitz, 1973).

Table 3.2

MAXIMUM VALUES OF FORCING AND INDUCED PRESSURE FORCE

Type of force	Max. force per unit mass (cm sec^{-2})	Max. perturbation pressure force per unit mass (cm sec^{-2})	
		Axisymmetry	slab-symmetry
Buoyancy $g(\theta'/\theta_o)$	+3.3	-0.88	-1.56
Drag $-gQ$	-0.98	+0.30	+0.52
Velocity advection $\bar{u}.\nabla\bar{u}$	+0.98 (max.) -0.98 (min.)	-0.32 +0.32	-0.89 +0.89

3.4.4 Negative buoyancy and perturbation pressure

To determine the role of perturbation pressure in supporting a negatively buoyant updraft, the following form of the buoyancy perturbation is used:

$$\theta' = [\hat{\theta}_1 \sin(nz) + \hat{\theta}_2 \sin(2nz)] e^{-r^2/a^2} \quad (3.49)$$

The buoyancy force corresponding to $\hat{\theta}_1$=0.54 and $\hat{\theta}_2$=-0.6 at the central axis is shown in fig. 3.38. A negative acceleration of 0.8 cm sec^{-2} occurs at a height of 700 m.

A significant change in the perturbation pressure and pressure force fields is depicted in figs. 3.39-3.40. The low pressure center previously situated at the ground is now at 1.6 km. A positive pressure perturbation at the surface induces an upward acceleration below 1.4 km. This force acts to oppose the downward acceleration of the negatively buoyant air.

The sum of buoyancy and pressure force as a function of cloud radius is also plotted in fig. 3.38. An important aspect is that the net acceleration below 1.4 km becomes less downward with the increase in cloud radius. The acceleration becomes completely upward at a radius of 2.5 km giving an aspect ratio (ratio of height to diameter of a cloud) of 0.8.

The aspect ratio obtained appears to be less than is generally observed in cumulus clouds (e.g. Betts, 1973) indicating that the other parts of the perturbation pressure would also be of importance. In particular, the pressure force induced

by dynamic forcing generally acts upward near the ground and if the prevailing shear is such that the drag force of the hydrometeors does not interfere directly with the updraft near the surface, then the acceleration of negatively buoyant air in the lower portion of the cloud by the induced perturbation forces becomes a distinct possibility.

3.5 Summary

A comprehensive analysis of the role of perturbation pressure has been made in this chapter. The buoyancy and drag induced perturbation pressure has been shown to oppose the forcing but can also be instrumental in supporting a negatively buoyant updraft. The dynamic pressure effect has been explained in terms of energy conservation similar to the Bernoulli effect and also in terms of the balance between the centrifugal and perturbation pressure forces. As the pressure force is of the same order of magnitude as the buoyancy and drag, the neglect of this aspect in any cloud models is certainly not justified. A model will be developed in the next chapter where perturbation pressure is calculated in an explict manner.

CHAPTER FOUR

FORMULATION OF A TWO-CYLINDER MODEL

4.1 General description

This chapter describes the formulation of a two-cylinder model which will be used for the purpose of studying the micro-physical-dynamical interactions in a cumulus cloud in Chapter 5 and the investigation of cumulus transports in Chapter 6. A unique feature of the model lies in the inclusion of an explicit calculation of perturbation pressure and the effect of compensatory current in the cloud environment. To make allowance for comparison of results using different microphysical systems, two versions of the model are developed. The first version used Kessler's parameterization scheme (model K) and the second follows the detailed microphysical system (model P) discussed in Chapter 2.

The geometry of the model consists of two concentric columns. For simplicity, the radii for the inner and outer columns, denoted respectively by a and b, are assumed constant with height and time. The inner column is the cloud region which comprises an area of active convection. Compensatory currents occur in the outer cylinder to satisfy the requirement of the continuity of air. The basic configuration is depicted in fig. 4.1.

It is recognized that the assumption of a constant radius

imposes restrictions on the generality of the model. However, the Thunderstorm Project indicated that the average thunderstorm cell does resemble a rising cylindrical column. The radius of the cloud remains essentially constant with height except in the region of the anvil near the cloud top. Slight expansion of the cloud takes place in the mature and dissipating stages of the thunderstorm. Therefore, to a first approximation, it appears that the assumption of a constant radius is justifiable and should not affect the gross feature of the simulated convective element.

The inner radius a is specified from information obtained in visual and radar observations of convective cells. Unfortunately, direct measurements are not available on the dimension of the region of subsidence associated with a convective updraft. To overcome this difficulty, a lower bound for the outer radius will be obtained from the hypothesis that cumulus clouds achieve the most efficient vertical transports of heat. Further sensitivity tests on the effect of varying b are made in Chapter 5.

4.2 Basic equations

The equations governing vertical motion, continuity of air, perturbation pressure, and continuity of water substances in deep convection are derived in Chapter 2 and 3. They are summaried beolw for ease of reference.

Vertical equation of motion

$$\frac{\partial w}{\partial t} + \frac{1}{\rho_0} \nabla.(\rho_0 w \vec{u}) = -C_p \theta_0 \frac{\partial \pi'}{\partial z} + g B - g Q \qquad (4.1)$$

where $$B = \left(\frac{\theta'}{\theta_0} + 0.61 q_v' \right)$$

Continuity equation for air

$$\nabla. (\rho_0 \vec{u}) = 0 \qquad (4.2)$$

Pressure equation

$$C_p \nabla. (\rho_0 \theta_0 \nabla \pi') = - \nabla.(\rho_0 \vec{u}.\nabla \vec{u}) + \frac{\partial}{\partial z}(\rho_0 g B) - \frac{\partial}{\partial z}(\rho_0 g Q) \qquad (4.3)$$

Continuity equations for vapor, cloud, cloud ice, rain, and graupel

$$\frac{\partial q_v}{\partial t} + \frac{1}{\rho_0} \nabla.(\rho_0 q_v \vec{u}) = \Phi_v \qquad (4.4)$$

$$\frac{\partial q_c}{\partial t} + \frac{1}{\rho_0} \nabla. (\rho_0 q_c \vec{u}) = \Phi_c \qquad (4.5)$$

$$\frac{\partial \hat{q}_c}{\partial t} + \frac{1}{\rho_0} \nabla. (\rho_0 \hat{q}_c \vec{u}) = \hat{\Phi}_c \qquad (4.6)$$

$$\frac{\partial q_r}{\partial t} + \frac{1}{\rho_0} \nabla_H. (\rho_0 q_r \vec{u}_H) + \frac{1}{\rho_0} \frac{\partial}{\partial z} [\rho_0 q_r (w + V)] = \Phi_r \qquad (4.7)$$

$$\frac{\partial \hat{q}_r}{\partial t} + \frac{1}{\rho_0} \nabla_H \cdot (\rho_0 \hat{q}_r \vec{u}_H) + \frac{1}{\rho_0} \frac{\partial}{\partial z} [\rho_0 \hat{q}_r (w + V)] = \hat{\Phi}_r \qquad (4.8)$$

The potential temperature equation is a statement of the first law of thermodynamics with form

$$\frac{\partial \theta}{\partial t} + \frac{1}{\rho_0} \nabla \cdot (\rho_0 \theta \vec{u}) = SS \tag{4.9}$$

In equations (4.4)-(4.9), Φ_v, Φ_c, $\hat{\Phi}_c$, Φ_r, and $\hat{\Phi}_r$ are the microphysical processes formulated in Chapter 2; SS represents the heating and cooling terms associated with latent heat exchange in condensation, evaporation, deposition, freezing, and melting. More detailed description of these terms appears in a following section.

4.3 Equations for the two-cylinder model

4.3.1 Averaged equations for velocities, potential temperature, and water substances

Horizontally averaged equations are developed in a manner described by Asai and Kasahara (1967). For simplicity, the cloud is assumed to possess symmetry about the central axis. The averages for a variable A in the inner column in cylindrical coordinates are:

$$\overline{A}_a = \frac{1}{\pi a^2} \int_0^{2\pi} \int_0^a A\, r\, dr\, d\lambda$$

$$\tilde{A}_a = \frac{1}{2\pi} \int_0^{2\pi} A\, d\lambda \quad , \text{ at } r=a \tag{4.10}$$

$$A_a' = A - \overline{A}_a \quad , \quad A_a'' = A - \tilde{A}_a$$

where λ is the azimuthal angle.

Similar averages for the outer cylinder can be written as

$$\bar{A}_b = \frac{1}{\pi(b^2-a^2)} \int_0^{2\pi} \int_a^b A\, r\, dr\, d\lambda$$

$$\tilde{A}_b = \frac{1}{2\pi} \int_0^{2\pi} A\, d\lambda \text{ , at r=b} \qquad (4.11)$$

$$A_b' = A - \bar{A}_b \text{ , } A_b'' = A - \tilde{A}_b$$

The general form for (4.1), (4.4)-(4.9) is

$$\frac{\partial A}{\partial t} + \frac{1}{\rho_o} \nabla_H \cdot (\rho_o A \vec{u}_H) + \frac{1}{\rho_o} \frac{\partial}{\partial z} (\rho_o A \mathcal{W}) = SS \qquad (4.12)$$

where SS is the source and sink terms, $\mathcal{W} = w$ for θ, q_v, q_c, and $\hat{q}_c$; and $\mathcal{W} = w+V$ for q_r and $\hat{q}_r$. The averaging procedure will be illustrated for (4.12).

With the aid of (4.10) and (4.11), (4.12) becomes

$$\frac{\partial \bar{A}_a}{\partial t} + \frac{2}{a}(\bar{A}_a \tilde{u}_a + \widetilde{A_a'' u_a''}) + \frac{1}{\rho_o} \frac{\partial}{\partial z} \left[\rho_o (\bar{A}_a \bar{w}_a + \overline{A_a' w_a'}) \right] = \overline{SS}_a \qquad (4.13)$$

for the inner cylinder, and

$$\frac{\partial \bar{A}_b}{\partial t} + \frac{2}{(b^2-a^2)} \left[b(\tilde{A}_b \tilde{u}_b + \widetilde{A_b'' u_b''}) - a(\tilde{A}_a \tilde{u}_a + \widetilde{A_a'' u_a''}) \right] \qquad (4.14)$$

$$+ \frac{1}{\rho_o} \frac{\partial}{\partial z} \left[\rho_o (\bar{A}_b \bar{w}_b + \overline{A_b' w_b'}) \right] = \overline{SS}_b$$

for the outer cylinder.

The horizontal velocities $\tilde{u}_a$ and $\tilde{u}_b$ at the edge of the cylinders and the vertical velocities $\bar{w}_a$ and $\bar{w}_b$ in the respective columns are constrained by the continuity equation

(4.2). By integrating (4.2) over the circular areas with radius a and b, the velocities $\tilde{u}_a$, $\tilde{u}_b$, $\bar{w}_a$, and $\bar{w}_b$ can be shown to be related by

$$\frac{2}{a}\tilde{u}_a + \frac{1}{\rho_0}\frac{\partial}{\partial z}(\rho_0 \bar{w}_a) = 0 \tag{4.15}$$

$$\frac{2}{a}\tilde{u}_b + \frac{1}{\rho_0}\frac{\partial}{\partial z}(\rho_0 w_0) = 0 \tag{4.16}$$

where $$w_0 = \frac{1}{\pi b^2}\int_0^{2\pi}\int_0^b w r\, dr\, d\lambda$$

$$\sigma^2 \bar{w}_a + (1-\sigma^2)\bar{w}_b = w_0 \tag{4.17}$$

where $$\sigma = \frac{a}{b}$$

W_0 represents the effect of larger scale forcing on the cumulus cloud. In the absence of forcing $W_0=0$ and the inflow from the outer cylinder, $\tilde{u}_b$, also vanishes.

Following Asai and Kasahara, the vertical eddy flux terms, $\overline{A_a' w_a'}$ and $\overline{A_b' w_b'}$; and the lateral eddy fluxes in the environment $\widetilde{u_b'' A_b''}$ are neglected. The turbulent entrainment in the cloud, denoted by $\widetilde{u_a'' A_a''}$, is determined from the eddy exchange hypothesis. Thus

$$\widetilde{u_a'' A_a''} = \frac{\nu}{a}(\bar{A}_a - \bar{A}_b) \tag{4.18}$$

where the eddy exchange coefficient ν , assumed the same for all variables, is proportional to $\left|\frac{\partial w}{\partial r}\right|$ across the lateral boundary of the cloud (Kuo, 1962). Therefore

$$\nu = \alpha^2 a \left| \bar{w}_a - \bar{w}_b \right| \tag{4.19}$$

where α^2 is an empirical constant usually assigned a value of 0.1 (Ogura and Takahashi, 1971; Holton, 1973) in agreement with the steady-state jet models.

The variable $\tilde{A}_a$, which represents the effect of dynamic entrainment, is assumed to have the environmental value for inflow into the inner cylinder but takes on the value characteristic of the cloud whenever detrainment occurs. This is

$$\begin{aligned} \tilde{A}_a &= \bar{A}_b \quad \text{if} \quad \tilde{u}_a < 0 \\ \tilde{A}_a &= \bar{A}_a \quad \text{if} \quad \tilde{u}_a > 0 \end{aligned} \tag{4.20}$$

With the aid of equations (4.15) and (4.18)-(4.20), (4.13)-(4.14) for a closed circulation reduce to the following:

$$\frac{\partial \bar{A}_a}{\partial t} + \frac{2}{a}\tilde{u}_a \tilde{A}_a + \frac{2\alpha^2}{a}\left|\bar{w}_a - \bar{w}_b\right|(\bar{A}_a - \bar{A}_b) + \frac{1}{\rho_0}\frac{\partial}{\partial z}\left[\rho_0 \bar{A}_a \bar{w}_a'\right] = \overline{SS_a} \tag{4.21}$$

$$\frac{\partial \bar{A}_b}{\partial t} - \frac{2a}{(b^2-a^2)}\tilde{A}_a \tilde{u}_a - \frac{2\alpha^2 a \left|\bar{w}_a - \bar{w}_b\right|}{(b^2-a^2)}(\bar{A}_a - \bar{A}_b) + \frac{1}{\rho_0}\frac{\partial}{\partial z}\left[\rho_0 \bar{A}_b \bar{w}_b'\right] = \overline{SS_b} \tag{4.22}$$

Hence the horizontally averaged equations corresponding to (4.1), (4.2), (4.4)-(4.9), (4.17) are

$$\frac{\partial \bar{\omega}_a}{\partial t} + \frac{2}{a}\tilde{u}_a\tilde{\omega}_a + \frac{2\alpha^2}{a}|\bar{\omega}_a - \bar{\omega}_b|(\bar{\omega}_a - \bar{\omega}_b) + \frac{1}{\rho_0}\frac{\partial}{\partial z}[\rho_0 \overline{w_a w_a}]$$

$$= -c_p\theta_0\frac{\partial \overline{\pi_a'}}{\partial z} + g\bar{B}_a - g\bar{Q}_a \qquad (4.23)$$

$$\sigma^2 \bar{\omega}_a + (1-\sigma^2)\bar{\omega}_b = 0 \qquad (4.24)$$

$$\frac{\partial}{\partial t}\begin{bmatrix} \overline{q_{va}'} \\ \overline{q_{ca}} \\ \overline{\hat{q}_{ca}} \\ \overline{q_{ra}} \\ \overline{\hat{q}_{ra}} \\ \overline{\theta_a'} \end{bmatrix} + \frac{2}{a}\tilde{u}_a \begin{bmatrix} \tilde{q}_{va} \\ \tilde{q}_{ca} \\ \tilde{\hat{q}}_{ca} \\ \tilde{q}_{ra} \\ \tilde{\hat{q}}_{ra} \\ \tilde{\theta}_a \end{bmatrix} + \frac{2\alpha^2}{a}|\bar{\omega}_a - \bar{\omega}_b| \begin{bmatrix} \bar{q}_{va} - \bar{q}_{vb} \\ \bar{q}_{ca} - \bar{q}_{cb} \\ \hat{\bar{q}}_{ca} - \hat{\bar{q}}_{cb} \\ 0 \\ 0 \\ \bar{\theta}_a - \bar{\theta}_b \end{bmatrix}$$

$$+ \frac{1}{\rho_0}\frac{\partial}{\partial z}\begin{bmatrix} \rho_0 & \overline{q_{va}} & \overline{\omega_a} \\ \rho_0 & \overline{q_{ca}} & \overline{\omega_a} \\ \rho_0 & \overline{\hat{q}_{ca}} & \overline{\omega_a} \\ \rho_0 & \overline{q_{ra}} & (\overline{\omega_a}+V) \\ \rho_0 & \overline{\hat{q}_{ra}} & (\overline{\omega_a}+V) \\ \rho_0 & \overline{\theta_a} & \overline{\omega_a} \end{bmatrix} = \begin{bmatrix} \overline{\Phi}_{va} \\ \overline{\Phi}_{ca} \\ \overline{\hat{\Phi}}_{ca} \\ \overline{\Phi}_{ra} \\ \overline{\hat{\Phi}}_{ra} \\ \overline{SS}_a \end{bmatrix} \qquad (4.25)$$

$$\frac{\partial}{\partial t}\begin{bmatrix} \overline{q_{rb}} \\ \overline{q_{cb}} \\ \overline{\hat{q}_{cb}} \\ \overline{q_{rb}} \\ \overline{\hat{q}_{rb}} \\ \overline{\theta_b'} \end{bmatrix} - \frac{2a\tilde{u}_a}{(b^2-a^2)}\begin{bmatrix} \tilde{q}_{ra} \\ \tilde{q}_{ca} \\ \tilde{\hat{q}}_{ca} \\ \tilde{q}_{ra} \\ \tilde{\hat{q}}_{ra} \\ \theta_a \end{bmatrix} - \frac{2a\alpha^2|\bar{w}_a-\bar{w}_b|}{(b^2-a^2)}\begin{bmatrix} \overline{q_{ra}}-\overline{q_{rb}} \\ \overline{q_{ca}}-\overline{q_{cb}} \\ \overline{\hat{q}_{ca}}-\overline{\hat{q}_{cb}} \\ 0 \\ 0 \\ \overline{\theta_a}-\overline{\theta_b} \end{bmatrix} + \frac{1}{\rho_0}\frac{\partial}{\partial z}\begin{bmatrix} \rho_0 & \overline{q_r} & \overline{w_b} \\ \rho_0 & \overline{q_{cb}} & \overline{w_b} \\ \rho_0 & \overline{\hat{q}_{cb}} & \overline{w_b} \\ \rho_0 & \overline{q_{rb}}(\overline{w_b}+V) & \\ \rho_0 & \overline{\hat{q}_{rb}}(\overline{w_b}+V) & \\ \rho_0 & \overline{\theta_b} & \overline{w_b} \end{bmatrix}$$

$$= \begin{bmatrix} \overline{\Phi_{rb}} \\ \overline{\Phi_{cb}} \\ \overline{\hat{\Phi}_{cb}} \\ \overline{\Phi_{rb}} \\ \overline{\hat{\Phi}_{rb}} \\ \overline{SS_b} \end{bmatrix} \qquad (4.26)$$

where the effect of turbulent mixing on rain and graupel particles are neglected.

Some physical interpretation can be assigned to different terms in (4.23). Thus the second and the fourth term on the left give the effects of dynamic entrainment and vertical advection; the third term is the effect of turbulent entrainment. It is of interest to point out that both the dynamic and turbulent entrainment terms are inversely proportional to the radius of the cloud a. Therefore the effect of the mixing processes is most important for small clouds. Similar physical interpretations can be made of the terms on the left hand side of (4.25) and (4.26).

The microphysical processes $\overline{\Phi}$, and the heating and cooling term $\overline{SS}$, for model P microphysics are:

$$\bar{\Phi}_v = \frac{1}{\rho_0}\left[-P1 + P2C + P2R + P2G - P3I - P3G\right]$$

$$\bar{\Phi}_c = \frac{1}{\rho_0}\left[P1 - P2C - P4 - P5 - P8C + P9I - P10C\right]$$

$$\bar{\hat{\Phi}}_c = \frac{1}{\rho_0}\left[P3I + P8C - P9I\right]$$

$$\bar{\Phi}_r = \frac{1}{\rho_0}\left[-P2R + P4 + P5 + P6 + P7 - P8R + P9G - P10R\right]$$

$$\bar{\hat{\Phi}}_r = \frac{1}{\rho_0}\left[-P2G + P3G + P8R - P9G + P10C + P10R\right]$$

$$\overline{SS} = \frac{1}{\rho_0}\left[\frac{L_v}{c_p\bar{T}}\left(P1 - P2C - P2R - P2G\right)\right.$$

$$+\frac{L_s}{c_p\bar{T}}\left(P3I + P3G\right)$$

$$\left.+\frac{L_f}{c_p\bar{T}}\left(P8C + P8R - P9I - P9G + P10C + P10R\right)\right]$$

(4.27)

where L_v, L_s, and L_f are respectively the latent heats of condensation, sublimation, and fusion. All processes are calculated for the mean quantities following the manner discussed in Chapter 2.

For a warm rain process, terms involving the ice phase vanish and $\overline{SS}$ reduces to only one term on its right. For a model with parameterized microphysics (model K), $\bar{\Phi}_v$, $\bar{\Phi}_c$, and $\bar{\Phi}_r$ becomes

$$\bar{\Phi}_v = \frac{1}{\rho_0}\left[-P1 + P2C + 4.3\,\rho_0\,\bar{q}_c\,(\rho_0\bar{q}_r)^{13/20}\right]$$

$$\bar{\Phi}_c = \frac{1}{\rho_0}\left[P1 - P2C + K(\rho_0\bar{q}_c - a) - 928\,\rho_0\,\bar{q}_c\,(\rho_0\bar{q}_r)^{7/8}e^{kz/2}\right]$$

$$\bar{\Phi}_r = \frac{1}{\rho_0}\left[-4.3\,\rho_0\,\bar{q}_c\,(\rho_0\bar{q}_r)^{13/20} + K(\rho_0\bar{q}_c - a) + 928\,\rho_0\,\bar{q}_c\,(\rho_0\bar{q}_r)^{7/8}e^{\frac{kz}{2}}\right] \quad (4.28)$$

For both the P and K models, the autoconversion rate K and the autoconversion threshold a are respectively 10^{-3} sec^{-1} and 1 g m^{-3}.

The vertical boundaries are assumed rigid and free-slip, that is

$$\left.\begin{aligned} \frac{\partial \rho_0 \tilde{u}_a}{\partial z} &= 0 \\ \bar{w}_a = \bar{w}_b &= 0 \end{aligned}\right\} \quad \text{at } z=0 \text{ and } z=H \qquad (4.29)$$

As will be shown later, a staggered grid system is used to obtained finite difference solutions of the two-cylinder model. With velocities defined at the sides of a grid cell

and $\bar{\theta}'$, $\bar{q}_v'$, $\bar{q}_c$, $\hat{\bar{q}}_c$, $\bar{q}_r$, and $\hat{\bar{q}}_r$ defined at its center, no explicit boundary conditions are required for equations (4.25) and (4.26). For the computation of perturbation pressure and surface rainfall rate, rain and graupel contents at the surface are obtained by linear extrapolation.

4.3.2 Determination of horizontally averaged perturbation pressure

The horizontally averaged perturbation pressure required in the vertical momentum equation (4.23) and the thermodynamic equations (4.25) and (4.26) are obtained by an explicit solution of the anelastic pressure equation. In cylinderical coordinates (4.3) becomes

$$c_p \rho_0 \theta_0 \frac{1}{r}\frac{\partial}{\partial r}\left(r\frac{\partial \pi'}{\partial r}\right) + \frac{\partial}{\partial z}\left(\rho_0 \theta_0 \frac{\partial \pi'}{\partial z}\right) = -\frac{1}{r}\left[\frac{\partial^2}{\partial r^2}(r\rho_0 u^2) + 2\frac{\partial}{\partial r}\frac{\partial}{\partial z}(r\rho_0 uw) + \frac{\partial^2}{\partial z^2}(r\rho_0 w^2)\right] + \frac{\partial}{\partial z}(\rho_0 g B) - \frac{\partial}{\partial z}(\rho_0 g Q)$$

$$= \mathcal{F} \qquad (4.30)$$

With rigid and free-slip boundary conditions at the top and bottom boundaries and no inflow at r=b, the boundary conditions for (4.30) are

$$\frac{\partial \pi'}{\partial r} = 0 \qquad \text{at } r=0 \text{ and } r=b$$

$$\frac{\partial \pi'}{\partial z} = 0 \qquad \text{at } z=H \tag{4.31}$$

$$c_p \theta_0 \frac{\partial \pi'}{\partial z} = -gQ \quad \text{at } z=0$$

The lateral boundary condition in (4.31) can be satisfied by expansion of the perturbation pressure in a Fourier Bessel series given as

$$\pi' = \sum_k \pi_k(z) J_0(\mu_k r) \tag{4.32}$$

where μ_k is the solution of

$$J_1(\mu_k b) = 0$$

J_0 and J_1 are respectively the Bessel functions of the first kind of order zero and one.

Substituting (4.32) into (4.30) and making use of the orthogonal properties of the Bessel functions, the zeroth and k^{th} mode equations result

$$c_p \frac{\partial}{\partial z}\left(\rho_0 \theta_0 \frac{\partial \pi_0}{\partial z}\right) = \frac{2}{b^2}\int_0^b \mathcal{F}\, dr$$

$$c_p\left[\frac{\partial}{\partial z}\left(\rho_0\theta_0\frac{\partial \Pi_k}{\partial z}\right)-\rho_0\theta_0\mu_k^2\Pi_k\right]=\frac{2}{b^2J_0^2(\mu_k b)}\int_0^b r\,J_0(\mu_k r)\,\mathcal{F}\,dr\,,\quad k\neq 0 \tag{4.33}$$

In order to solve (4.33), it is assumed that the vertical velocity, potential temperature, and water substances can be represented by a top-hat profile with magnitudes equal to that of the horizontally averaged quantities in the inner and outer cylinders. The quantities used to evaluate $\mathcal{F}$ are listed below.

Quantity	Inner cylinder	Outer cylinder
w	$\overline{w}_a$	$\overline{w}_b$
B	$\overline{B}_a=\left(\frac{\overline{\theta}'_a}{\theta_0}+0.61\,\overline{q}'_{va}\right)$	$\overline{B}_b=\left(\frac{\overline{\theta}'_b}{\theta_0}+0.61\,\overline{q}'_{vb}\right)$
Q	$\overline{Q}_a=\left(\overline{q}_{ca}+\hat{q}_{ca}+\overline{q}_{ra}+\hat{q}_{ra}\right)$	$\overline{Q}_b=\left(\overline{q}_{cb}+\hat{q}_{cb}+\overline{q}_{rb}+\hat{q}_{rb}\right)$
u	$\frac{r}{a}\,\tilde{u}_a$	$\left(\frac{b^2-r^2}{ar}\right)\left(\frac{\sigma}{1-\sigma^2}\right)\tilde{u}_a$

where the horizontal velocity, u, is calculated from (4.2) and (4.15).

With u, w, B, and Q defined above, (4.33) can be simplified to

$$\begin{aligned} c_p\frac{\partial}{\partial z}\left(\rho_0\theta_0\frac{\partial \Pi_a}{\partial z}\right) &= g\frac{\partial}{\partial z}\rho_0\left[\sigma^2\overline{B}_a-(1-\sigma^2)\overline{B}_b\right] \\ &\quad \text{buoyancy forcing} \\ &\quad -g\frac{\partial}{\partial z}\rho_0\left[\sigma^2\overline{Q}_a+(1-\sigma^2)\overline{Q}_b\right] \\ &\quad \text{drag forcing} \\ &\quad -\left(\frac{\sigma^2}{1-\sigma^2}\right)\frac{\partial^2}{\partial z^2}\left(\rho_0\overline{w}_a\overline{w}_a\right) \\ &\quad \text{dynamic forcing} \end{aligned} \tag{4.34}$$

$$C_p\left[\frac{\partial}{\partial z}\left(\rho_0\theta_0\frac{\partial \pi_k}{\partial z}\right) - \rho_0\theta_0\mu_k^2\pi_k\right] =$$

$$\frac{2aJ_1(\mu_k a)}{b^2\mu_k J_0^2(\mu_k b)}\, g\left[\underbrace{\frac{\partial}{\partial z}\rho_0(\bar{B}_a - \bar{B}_b)}_{\text{buoyancy forcing}} - \underbrace{\frac{\partial}{\partial z}\rho_0(\bar{Q}_a - \bar{Q}_b)}_{\text{drag forcing}}\right]$$

$$- \underbrace{\left[\frac{1}{\rho_0}\left(\frac{\partial \rho_0 \bar{w}_a}{\partial z}\right)^2\alpha_k + \frac{\partial}{\partial z}\left(\bar{w}_a\frac{\partial \rho_0 \bar{w}_a}{\partial z}\right)\beta_k + \frac{\partial}{\partial z}\left(\rho_0\bar{w}_a\frac{\partial \bar{w}_a}{\partial z}\right)\gamma_k\right]}_{\text{dynamic forcing}} ; \; k\neq 0 \qquad (4.35)$$

where α_k, β_k, and γ_k are functions of σ and μ_k.

The boundary conditions are now

$$C_p\theta_0\frac{\partial \pi_0}{\partial z} = -g\left[\sigma^2\bar{Q}_a + (1-\sigma^2)\bar{Q}_b\right]$$

$$C_p\theta_0\frac{\partial \pi_k}{\partial z} = -\frac{2aJ_1(\mu_k a)}{\mu_k b^2 J_0^2(\mu_k b)}\, g\left[\bar{Q}_a - \bar{Q}_b\right] \; ; \text{ at } z=0$$

$$\text{and } \frac{\partial \pi_0}{\partial z} = \frac{\partial \pi_k}{\partial z} = 0 \qquad \text{at } z=H \qquad (4.36)$$

Ogura and Charney (1962) showed that for Neumann boundary conditions, the solution to the anelastic pressure equation can be determined only up to an arbitrary constant. This non-uniqueness of solution is reflected in the degeneracy of the zeroth mode equation (4.34). In the present model, this constant is set to zero resulting in the vanishing of the horizontally averaged perturbation pressure at the upper boundary.

The horizontally averaged perturbation pressure is obtained by applying the averaging operators in (4.10) and (4.11) to (4.32). The result is

$$\bar{\pi}_a' = \pi_0 + \frac{2}{a}\sum_k \frac{J_1(\mu_k a)}{\mu_k}\pi_k(z)$$

$$\bar{\pi}_b' = (\pi_0 - \sigma^2\bar{\pi}_a')/(1-\sigma^2) \qquad (4.37)$$

In passing, it should be mentioned that two previous attempts have been made to incorporate perturbation pressure in a simple cloud model. Lee (1971) assumed a Gaussian profile for all variables to arrive at an equation for the amplitude of the perturbation pressure. Unfortunately the set of equations obtained imposes a severe restriction of a constant mass flux at all levels in the vertical. Holton (1973) assumed a single mode expansion for the perturbation pressure in the radial direction and derived a horizontally averaged pressure equation for a one-dimensional cloud model. Since the other modes are neglected, this method is only a first approximation to the solution of the anelastic pressure equation.

Equations (4.23)-(4.38), (4.34), (4.35) and (4.37) form a closed system. Because of the non-linearity of the equations, solutions are obtained numerically. The specification of the experiment and the description of numerical methods follow.

4.4 Specification of experiment and numerical methods

Environmental conditions

Idealized temperature and humidity profiles are adopted for investigating the general properties of the model and the study of microphysical-dynamical interactions in Chapter 5. The temperature profile depicted in fig. 4.2 shows a temperature of 26°c at the surface and decreases upward at 9.8°c km^{-1} to the cloud base which is set at 875 m. Above the cloud base, a lapse rate of 6°c km^{-1} is imposed unless stated otherwise.

At and beyond 13 km an isothermal layer blocks strong interaction of the upper boundary with the cumulus tower in severe convection. The relative humidity profile in the same figure indicates an increase from 70% at the surface to saturatiion at the cloud base. Thereafter a decrease of 5.5% km^{-1} is assumed. A minimum of 30% occurs at higher levels.

The idealized sounding is similar to the one used by Ogura and Takahashi(1971) in a one-dimensional cloud model which simulated quite realistically the life cycle of a thunderstorm cell. The temperature lapse rate resembles the 1200 GMT mean Albany sounding in July, 1975 but the relative humidity is substantially higher than the mean Albany sounding.

Initial conditions

Observational evidence and theoretical reasoning indicate that humidity perturbation is to be preferred over potential temperature perturbation in the initiation of con-

vection in cloud models (Murray, 1971). Therefore in the present study, a combination of velocity and humidity impulses is used. The velocity at the initial time is specified as

$$\bar{w}_a = W_0 \sin^2\left(\frac{\pi z}{H_0}\right), \text{ for } z \leq 2 \text{ km}$$
$$\bar{w}_a = \bar{w}_b = 0 \quad , \text{ otherwise} \tag{4.38}$$

where H_0=2 km; W_0 usually has a magnitude of 1 m sec^{-1}. In the region of the velocity impulse and above the cloud base, the air is assumed saturated.

Finite difference scheme

To minimize truncation error and to express the continuity equation in a more natural manner, a staggered grid system is used. Velocity fields are defined at the edges of the grid box and all other variables at the center of the cell (fig. 4.3). The vertical advection equations (4.23), (4.25) and (4.26) are written in conservation form and the modified upstream method (Soong and Ogura, 1973) is used to obtain their numerical solutions. The modified upstream method linearly conserved the advected quantities so that special devices, such as the 'hole filling' technique (Clark, 1973), are not required to eliminate negative hydrometeor water contents in the advection calculation.

It should be mentioned that the modified upstream scheme is similar to the upstream differencing in being first order accurate, stable, but diffusive. Molenkamp (1968) showed that the pseudo-diffusion for the upstream method is almost

as large as the explicit eddy diffusion for small scale atmospheric circulations. On the other hand, quite realistic results have been obtained in cloud simulations using this scheme (e.g. Orville, 1968; Schlesinger, 1973a; Ogura, 1962). Orville and Sloan (1970) compared a second-order method (Crowley, 1968) against the forward upstream technique and found the results concerning the formation and evolution of the cloud in a slab-symmetric model quite similar. As the effect of explicit turbulent diffusion is not the major object of study in this thesis, the modified upstream scheme is considered adequate for the present purpose.

Forward time differencing is usually coupled to the upstream space differencing scheme. Unfortunately, Wilhelmson (1974) found amplifying internal gravity waves in a three-dimensional primitive equation thunderstorm model using the forward upstream and forward-modified upstream methods. This amplification appears to be primarily due to the use of centered space differencing for the pressure derivatives together with forward time differencing for the velocity and potential temperature time derivatives. Linear stability analysis indicates this arrangement to be unconditionally unstable for all wave lengths (Wilhelmson, 1974).

In order to avoid the spurious amplification, the velocity fields in the present model are computed at half time steps and the resulting values are then used to advect the various

quantities from time step n to n+1. Linear stability analysis for internal gravity wave motion using this modification shows that the scheme is conditionally stable by certain restrictions on the time steps. The analysis is presented in Appendix 4.1.

The zeroth mode pressure equation (4.34) is solved by simple marching. Solutions to (4.35) can be obtained efficiently by the 'double-sweep' method (Richtmyer, 1967). The detailed finite difference equations for the whole model and the sequence of computations appear in Appendix 4.2.

Unless stated otherwise, the height of the integration domain is 15 km, δz = 250 m and δt = 10 sec. δz and δt as chosed satisfies the Courant-Friedrich-Lewy linear stability criterion.

$$\delta t \leq \frac{\delta z}{|\bar{w} + V|} \tag{4.39}$$

4.5 Specification of radius for the inner and outer cylinder

Empirical evidence and radar measurements are used to specify the radius of the updraft radius. Observations on small trade wind cumuli often reveal a horizontal dimension less than 2 km (Malkus, 1954). Based on RHI data, the Thunderstorm Project reported that for Ohio thunderstorms, the horizontal extent of the echo is comparable to its vertical extent. The typical dimension ranges from 20,000-30,000 ft. Austin and Houze (1972) found that convective cells in general give small intense radar echoes corresponding to an area of

10 km^2. Since precipitation may fall over an area larger than that of the updraft, horizontal dimensions of radar echoes are expected to exceed the updraft dimension. Thus in most cases, it appear reasonable to assume an updraft radius of 1-2 km. A value of a=1.5 km is used in this thesis.

To determine the dimension of the subsiding region, a hypothesis by Asai and Kasahara (1967) is adopted ------- convection that actually occurs will maximize the vertical heat transport and hence becomes a most efficient generator of kinetic energy. Specifically, a σ is sought which maximizes the heat transport H_T defined as

$$H_T = \sigma^2 \int_0^\tau \int_0^H c_p \rho_0 \bar{w}_a \bar{T}_a' \, dz \, dt + (1-\sigma^2) \int_0^\tau \int_0^H c_p \rho_0 \bar{w}_b \bar{T}_b' \, dz \, dt \qquad (4.40)$$

where $\bar{T}'$ is the deviation of temperature from that of the base state environment, τ is the life time of the cloud. Some justification of this hypothesis will be given a posteriori.

In order to calculate H_T for different values of a, σ, and Γ, a number of numerical experiments are performed using the two-cylinder model with Kessler's parameterized microphysics. To impose the condition that the total kinetic energy per unit area of the initial motion does not depend on the parameters σ or a, the initial velocity perturbation is assumed to have a form

$$w = w_0 \sin^2\left(\frac{\pi z}{H_0}\right) \left(\frac{a_0 \sigma_0}{a \sigma}\right) \left(\frac{1-\sigma^2}{1-\sigma_0^2}\right)^{1/2} \qquad (4.41)$$

where σ_0 =0.1, a_0 = 1 km.

It can be shown that the total kinetic energy per unit area computed from (4.41) is independent of a and σ .

Fig. 4.4 depicts the curves for the heat transport per unit area in the case of Γ =6°c km^{-1}, a=1.5 km, and τ =1 hr. H_T reaches a maximum at σ = 0.3. A slight shift to larger σ is indicated for a=1.0 km and H_T peaks at σ =0.4 for Γ =7°c km^{-1}. The cut-off for small σ is caused by the increase in the area of convection (b increases with σ when a is kept the same). The cut-off at larger values of σ is attributable to the stabilizing effect of the compensatory current whose magnitude increases with increasing σ . For a more unstable atmosphere represented by Γ =7°c km^{-1}, the effect of the compensatory current is less important and a shift of the H_T maximum toward a larger value of σ results.

A σ of 0.3-0.4 corresponds to a ratio of 0.1-0.19 between the areas of rising and sinking motions respectively. Observations on cumulus clouds show that active cumulus updrafts cover several per cent of the area under investigation (Malkus, 1961). Bjerknes (1938) showed theoretically that conditional instability favors infinitely small areas of rising motion and the largest areas of sinking motion if friction and entrainment effects are neglected. Charney (1971) demonstrated that in order for energy to be released in a hydrostatic at-

mosphere for saturated adiabatic ascent and dry adiabatic descent, the area of rising motion cannot exceed 20% of the area undergoing subsidence. Hence the value of σ determined from the hypothesis of maximum heat transport appears to be in good agreement with these findings. A σ of 0.32 will be used for most of the computations. In view of the conclusions by Bjerknes, sensitivity tests will be performed for smaller values of σ .

CHAPTER FIVE

INTERACTION OF MICROPHYSICAL AND DYNAMICAL PROCESSES IN THE TWO-CYLINDER MODEL

5.1 Introduction

Interactions between precipitation physics and cloud dynamics constitute a complicated feedback process. The interplay is effected largely through the formation,dissolution, and redistribution of hydrometeors. The latent heats of condensation, sublimation, fusion, and evaporation released in the formation of cloud, rain, and ice particles serve as heat sources and sinks, The water loading, precipitation fallout, and entrainment of enviromental air feed back into the dynamics to regulate and control the life cycle of the cloud. Indications of these relationship have been noted in observations. The diluting effect of entrainment on cloud growth was discussed by Austin (1948). Byers and Braham (1949) attributed the initiation of downdraft in the mature stage of a thunderstorm to the drag of precipitation particles and evaporative cooling below cloud base. The importance of the ice phase in cloud development is indicated by AgI seeding experiments (Simpson et al, 1970). In some cases, explosive growth of the seeded cloud occurs through the instantaneous release of latent heat. A number of numerical studies have also emphasized the role of evaporation, water load, and microphysical parame-

terization in the simulation of the life cycle of a precipitating element (e.g. Das, 1964; Srivastava, 1967; Murray and Koenig, 1972; Silverman and Glass, 1973). However, as is pointed out in Chapter 1, because of the extreme complexity of the processes and the range of scales involved, the development of a cumulus cell cannot be completely modeled. The two-cylinder model developed in Chapter 4 is itself highly simplified, but numerical experiments and sensitivity tests should provide useful estimates of the relative importance of different effects and the probable consequences of various assumptions or over-simplifications.

This chapter presents results on a series of experiments using the two-cylinder model. The focus is on the effect of the interaction of the microphysical and dynamical processes on the evolution of a convective element. Hence the important role of cumulus clouds as a transporter for mass, heat, and moisture will be discussed separately in Chapter 6.

Table 5.1 summaries the experiments performed. The results of experiment 1 and 2 (E1 and E2) will be discussed in detail to illustrate the general property of the model and the effect of compensatory current in the environment. E3 and E4 address the question of the relation of evaporation to the development of the downdraft circulation. The ice phase is examined in E5 while E6 investigates the effect of different microphysical parameterization schemes. It will be shown that

Table 5.1

SUMMARY OF EXPERIMENTS

Expt.	cloud radius (a)	$\sigma = \frac{\sigma}{a}$	evaporation of rain	limit of rain spectra	ice phase	model for microphysics	π'	W_o	impulse saturated above cloudbase	lapse rate above base	R.H. at base	δt	δz	n
	(km)							(m/s)		(°c/km)	(%)	(sec)	(m)	
E1	1.5	.16	Y	N	N	P	Y	1	Y	6	100	10	250	10
E2	1.5	.32	Y	N	N	P	Y	1	Y	6	100	10	250	10
E3	1.5	.32	N	N	N	P	Y	1	Y	6	100	10	250	10
E4	1.5	.32	N	Y[1]	N	P	Y	1	Y	6	100	10	250	10
E5	1.5	.16	N	N	Y	P	Y	1	Y	6	100	10	250	10
E6	1.5	.32	N	N	N	K	Y	1	Y	6	100	10	250	10
E7	1.5	.32	N	N	N	K	N	1	Y	6	100	10	250	10
E8	1.0	.32	N	N	N	K	Y	1	Y	6	100	10	250	10
E9	2.0	.32	N	N	N	K	Y	1	Y	6	100	10	250	10
E10	1.5	.32	N	N	N	K	Y	0.2	Y	6	100	10	250	10
E11	1.5	.32	N	N	N	K	Y	1	N	6	100	10	250	10
E12	1.5	.32	N	N	N	K	Y	1	Y	7	100	10	250	10
E13	1.5	.32	N	N	N	K	Y	1	Y	6	90	10	250	10
E14	1.5	.32	N	N	N	K	Y	1	Y	6	100	5	250	10
E15	1.5	.32	N	N	N	K	Y	1	Y	6	100	20	250	10
E16	1.5	.32	N	N	N	K	Y	1	Y	6	100	10	500	10
E17	1.5	.32	N	N	N	K	Y	1	Y	6	100	10	250	20

Y= process included
N= process excluded
P= model P microphysics formulated in Chapter 2
K= Kessler's microphysical parameterization
n= number of modes used in computing π'
1 maximum raindrop size limited to 850μ
— parameter tested
b radius of outer cylinder

the treatment of microphysics has important consequence in the water budget and radar reflectivity distributions. E7 demonstrates the effect of neglecting the perturbation pressure in the life history of the cloud. E8 and E9 reveal changes in cloud properties as a function of cloud radius and hence entrainment rate. Finally the sensitivity of the model to various parameters in the initial conditions and computation scheme are studied in E10-17. Unless specified otherwise, the idealized sounding and initial perturbation in section 4.4 are used in the computations.

5.2 General behavior of the model——— case of σ =0.16(E1)

The time-height cross-sections for the vertical velocity $\bar{w}_a$, potential temperature deviation $\bar{\theta}'_a$ and precipitation water content $\bar{q}_{ra}$ in the inner column are shown in figs. 5.1-5.3. The release of latent heat of condensation, evident from the positive potential temperature deviation in the major part of the cloud, results in rapid increase of vertical velocity up to 25 min. A cold cap, however, appears just above the cloud top in response to dry adiabatic ascent through the conditionally unstable atmosphere. A minimum $\bar{\theta}'_a$ of -2°c occurs at 28 minutes at 7 km. Gravitational oscillatory behavior of the solution appears near the upper part of the domain.

Precipitation developes rapidly. A maximum value of 6.7 g kg^{-1} is found at 3 km. The precipitation loading acts

against the buoyancy to weaken the updraft after 25 min. Further growth of precipitation particles produces raindrops with a substantial fallspeed to fall against the updraft. The arrival of precipitation below the cloud base where the updraft is relatively weak coupled with the evaporative cooling of water drops initiates the downdraft near the surface at 28 min. The downdraft increases in intensity and extends rapidly upward reaching a maximum of -2.9 m sec^{-1} at 33 min. A rain gush with precipitation rate up to 130 mm hr^{-1} follows shortly after (fig. 5.4).

The relative humidity profile at 35 min (fig. 5.5) indicates the downdraft to be subsaturated despite heavy rainfall. Evidently the rate of evaporation of rain drops is too slow to counteract the increase in saturation mixing ratio from the warming of the air on adiabatic descent. Such phenomenon, known as the 'humidity dip', has been reported in the Thunderstorm Project and studied theoretically by Kambunova and Ludlam (1966) and Das and Subba Rao (1972).

The adiabatic warming of the air in the downdraft gives rise to a second updraft at 40 min. However, no substantial growth of the cloud results. Gravity waves begin to dominate over the whole domain after 45 min. The whole life cycle of the cloud is limited to about 40 min.

The radial velocity at the edge of the inner cylinder (fig. 5.6) indicates inflow of ambient air in the lower portion of the cloud at 10 and 20 min. The strongest inflow is located

near the lower boundary with a magnitude of 4 m sec^{-1}. When compared with the inflow, the outflow is of comparable magnitude but spreads throughout a deeper layer in the upper part of the cloud. During the mature stage at 30 min., outflow from the downdraft takes place near the surface and the main region of entrainment is lifted to a region between 3 to 5.5 km.

The evolution of drop-size distribution and radar reflectivity

Fig. 5.7 depicts the evolution of the precipitation drop-size distribution at the cloud base and near the cloud top. The Marshall-Palmer (MP) distribution corresponding to the same liquid water content is also plotted for comparison. Shortly after the onset of rain at the surface at 30 min. the spectrum near the cloud top is narrow and unimodal. Autoconversion appears to be efficient in producing a large number of small drops while coalescence growth extends the distribution into the region of larger radius. At 35 minutes a bi-modal spectrum appears at the cloud base as a result of the continued growth by the coalescence process. The second modal radius is centered at 1250 μ . Comparison with the MP distribution reveals that the computed spectrum has more drops in the range between 1200 μ - 2300 μ , but fewer drops at other ranges. As the precipitation falls out and the updraft weakens at 40 min. the distribution gradually narrows. The computed spectrum at 50 min near the cloud base follows fairly closely

the corresponding MP distribution for drops with radius $r < 1300\,\mu$. But as is the case with all distributions near the cloud top, the computed spectrum exhibits fewer drops as the radius increases.

List and Gillespie (1976) have demonstrated from a numerical model that collision induced breakup can be an efficient mechanism in limiting the size of raindrops in warm rain. They concluded that large drops (of diameter 5-6 mm) observed in cold rain originate from melting ice particles. Therefore, the computed drop-size distribution would be expected to broaden if a significant amount of ice particles were present.

The radar reflectivity profile computed from the evolving drop-size distribution is shown in fig. 5.8. For convenience of discussion, the minimum detectable signal, which of course depends on the radar and the range of the target, is assumed a value of 10 dbz. The reflectivities then are detectable at 15 minutes at a height of 2 km. The profile first spreads vertically and then rapidly downward. The maximum computed reflectivity is 58 dbz. It is interesting to note that the region of maximum reflectivity corresponds to the region of high liquid water content and overlaps areas of both up and down circulations.

Analysis of terms in the vertical velocity equation

To determine the factors which contribute most importantly

the formation of the downdraft, the different forces in equation (4.23) are analysed in fig. 5.9. For the sake of discussion, the different forces are termed as:

Buoyancy: $g\left(\frac{\bar{\theta}'_a}{\theta_0} + 0.61\bar{q}'_{va}\right)$

Drag: $-g\bar{Q}_a$

Dynamic entrainment and vertical advection : $-\left[\frac{1}{\rho_0}\frac{\partial \rho_0 \bar{w}_a \bar{w}_a}{\partial z} + \frac{2}{a}\tilde{u}_a\tilde{w}_a\right]$

Perturbation pressure gradient : $-c_p\theta_0\frac{\partial \bar{\pi}'_a}{\partial z}$

Turbulent entrainment : $-\frac{2\alpha^2}{a}|\bar{w}_a - \bar{w}_b|(\bar{w}_a - \bar{w}_b)$

As is indicated in the figure, the buoyancy is the most important force throughout a major portion of the cloud at 15 min. The peak amplitude amounts to 8.8 cm sec^{-2} at 2.3 km. A region of negative buoyancy is located above the cloud top as a result of adiabatic cooling of the air on ascent. The perturbation pressure force opposes the buoyancy above a height of 1.2 km. Near the cloud base a positive pressure force tends to offset the negative acceleration brought about by vertical advection and dynamic entrainment of subsiding air in the environment. In comparison, the liquid water drag is smaller than both the buoyancy and pressure forces. The level of maximum water load coincides with that of maximum buoyancy resulting in a decrease in the intensity of the updraft circulation. A similar distribution of the forces is depicted at 20 min. The liquid water drag is however

larger and is below the level of maximum buoyancy. The effect of turbulent entrainment remains quite negligible.

The perturbation pressure force weakens below the cloud base as the cloud rises. At 25 min. this force seems to oppose the drag force at 2.75 km and the buoyancy force at higher levels. The liquid water drag gradually shifts its peak downward with the falling of precipitation particles. Finally at 30 min, the water load overcomes the resistance of the pressure forces below the cloud base and the downdraft is initiated near the surface. Since the breakdown of the updraft occurs near the ground and not in the region of maximum water load at a higher level, it appears that the precipitation process, which results in the fallout of precipitation into a region with relatively small upward motion, plays an important role in downdraft initiation. The evaporation of rain drops results in a region of negative buoyancy near the ground. But as its magnitude is smaller than the liquid water drag in this region, the effect of evaporation is of secondary importance in initiating the downdraft. Further investigation on how evaporation might affect downdraft development is reported in E3 and E4.

The role of perturbation pressure force in opposing the buoyancy and supporting the updraft near and below the cloud base found in E1 is in agreement with the results of recent two-dimensional models. Soong and Ogura (1973) estimated

that the pressure force cancels about half the buoyancy at the level of maximum vertical motion during the mature stage of the simulated cloud. Schlesinger (1973b) showed that the vertical pressure gradient force is significantly hydrostatic and opposes the buoyancy throughout the domain of integration. Therefore, as is conjectured in Chapter 3, it can be concluded that the pressure force is an important part of the cloud dynamics. The effect of neglecting this force in the life history of a cumulus cloud will be demonstrated in E 7.

Water budget

The water budget integrated over the volume of the cloud (radius a), the environment (radius b), and the total computation domain (radius a+b) is displayed in fig. 5.10. In the region of the cloud, condensation produces cloud droplets at an early stage. The autoconversion process gives rise to precipitation particles which accrete a large portion of the cloud water content. Rainfall reaches the surface after about 25 min. and the evaporation of precipitation near the surface and in the unsaturated downdraft becomes evident. Most of the rain has fallen to the surface by 50 min.

In comparison, evaporation is much larger in the environment. The detrainment of cloud and precipitation water into the relatively dry ambient air results in instantaneous evaporation of all detrained cloud water. Because of the finite evaporation rate, part of the detrained rain water is able to

reach the ground. Thus evaporation of detrained liquid water accounts for a major part of the evaporative process. The cumulative rainfall in the environment is about half that of the updraft column.

The total water budget for the entire region indicates that of the 142 units of condensate formed 71 units finally reach the surface and 71 units are evaporated. The efficiency of the cloud, defined as the ratio of surface precipitation to the total condensation, is thus 50 per cent.

5.3 Effect of compensatory current in the environment (E2)

The parameter σ relates the velocity in the environment $\bar{W}_b$, to the updraft velocity $\bar{W}_a$ through equation (4.24). Since σ is less than unity, the absolute magnitude of $\bar{W}_b$ increases with an increase in σ. Direct calculation gives $\bar{W}_b=-0.026\ \bar{W}_a$ for $\sigma=0.16$ and $\bar{W}_b=-0.114\ \bar{W}_a$ for $\sigma=0.32$. During the developing and mature stage of the cloud, the velocity in the cloud is upward, and downward compensatory currents occur in the environment. The subsiding air influences the cellular circulation in two ways. In the first place, the direct mixing of downward momentum decreases the strength of the updraft and hence the rate of condensation. Secondly, adiabatic warming and drying of the environmental air and the subsequent mixing inside the cloud through the mechanism of dynamic and turbulent entrainment reduces the

amount of vapor that can be condensed. Comparison of results for the two different values of σ demonstrates the importance of these processes.

The time-height cross-section of $\bar{W}_a$ and $\bar{\theta}'_a$ for σ =0.32 are depicted in figs. 5.11 and 5.12. When compared with figs. 5.1 and 5.2, the effect of stronger subsidence is shown to suppress cloud growth. The maximum velocity in the present case is smaller and the downdraft appears earlier near the surface. The downdraft possesses a larger amplitude due to the mixing of the cloud with the stronger downward moving air in the environment. The potential temperature responds to the adiabatic warming to give a larger value at 32 min.

The slower updraft has direct consequence to the distribution of precipitation. The rainwater content has a smaller value of 4 g kg^{-1} (fig. 5.13). Although rainfall begins earlier, the maximum rainfall rate is less than a third of the maximum value in the case of σ =0.16 (fig. 5.14).

The evolving raindrop-size spectra in fig. 5.15 indicates a narrow distribution and the spectrum near the cloud top is bimodal at 30 min. A depletion of very small drops is noted in the size spectrum at 50 min. This effect is attributable to the stronger evaporation in the drier air caused by the stronger downdraft. Similar to the case for σ =0.16 (fig. 5.7), the computed spectrum shows relatively few drops in the range of large radius. The liquid water contents are

smaller and the size distributions are narrower than the case for σ =0.16; as a result the radar reflectivities are smaller than the previous case (fig. 5.8 and fig. 5.16).

The water budget in fig. 5.17 shows that condensation in the case of σ =0.32 is about half that of σ =0.16. However, the ratio of evaporation to condensation is greater both in the cloud and the environment. Accordingly, the total evaporation exceeds the precipitation in the whole area of convection. Of the 75 units of water condensed, 25.5 units reaches the surface and 48.5 units are evaporated. The efficiency decreases to 34 per cent.

5.4 Effect of evaporation on downdraft initiation and development (E3 and E4)

The force analysis performed in section 5.2 indicates that evaporation of falling precipitation may be of secondary importance for the initiation of a downdraft. However, the computed drop-size spectra for E1 and E2 consistently show fewer drops of radius $< 500\ \mu$ than the corresponding MP distribution. To further confirm the lesser role of evaporation in downdraft initiation and to explore the effect of the presence of small drops on the development of the downdraft, E3 and E4 were run. Evaporation of raindrops is suppressed in E3 while in E4 drops larger than 850 μ are assumed to break up completely into drops centered at 550 μ ,

thereby enhancing the evaporation process.

Time-height cross-section of $\bar{W}_a$ for E3 and sections of $\bar{W}_a$ and $\bar{\theta}'_a$ for E4 are shown in figs. 5.18-5.20. The velocity field for the case without evaporation reveals no substantial difference from the case with the evaporation of precipitation particles (fig. 5.11). However, the downdraft in E4 (fig. 5.19) is stronger and has a longer duration. The much enhanced evaporation from the presence of many small drops resulted in a substantial negative potential temperature near the surface and $\bar{\theta}'_a$ reaches -1.5^{o}c at 37 min. Therefore, at least in the present model, evaporation is not important for the initiation of the downdraft but the presence of small drops can significantly enhance downdraft development.

5.5 Effects of ice phase (E5)

The vertical velocity and potential temperature deviation for E5 which includes the effect of the ice phase are depicted in figs. 5.21-5.22. The corresponding curves for E1 where no freezing occurs are plotted for comparison.

No substantial difference in $\bar{W}_a$ and $\bar{\theta}'_a$ occurs in the two experiments at 25 minutes. Freezing of cloud and raindrops has just commenced and the amounts are too small to render appreciable changes. However, rapid increase of $\bar{\theta}'_a$ takes place between 4.5 to 7 km (fig. 5.22) at 30 minutes in E5. As a results the vertical velocity in E5 increases and is larger than that for

El above 4.3 km. The cloud grows taller by about 1 km. Similar behavior is also shown at 35 minutes.

The mechanism for the increase of potential temperature and buoyancy is demonstrated by the profiles for cloud water, cloud ice, and rain water contents at 30 minutes (fig. 5.23). With the inclusion of ice phase, a considerable amount of cloud ice is present above 5 km. The latent heat of fusion involved in the freezing of water drops and the latent heat of sublimation in the depositional growth of ice particles provide an additional heat source at the upper domain of the cloud. The graupel content for this simulation is however quite small and causes no substantial changes in the radar reflectivity, rainfall rate, and rain drop-size distribution.

It should be pointed out that the ice phase formulation in the model is crude and freezing commences at a high level in the case of the idealized sounding used. Therefore further experimentation is required to determine how the growth and fallout of graupel particels would affect the distributions of radar reflectivity, rainfall rate, and drop-size spectra.

5.6 Effects of microphysical parameterization (E6)

Kessler's parameterization scheme (model K) represents an ingenious attempt to simplify the complexity of the microphysical processes. By assuming a MP distribution with a constant parameter N_o, the microphysics for cloud and rain can be summaried in two continuity equations. Although the

procedure reduces tremendously the amount of computations, the basic assumption of a fixed distribution may produces undesirable consequences in the computations involving growth and distribution of hydrometeors. The validity of Kessler's scheme therefore must be examined by comparison of results with a model where the dropsize spectrum develops in an explicit manner. Experiment E2 and E6 provide such a comparison.

Before discussing the results from E6, some of the consequences from Kessler's basic assumptions are analysed. First, the fallspeed of the median volume diameter drop derived from the MP distribution (eq. 2.28) is a weak function of the precipitation water content. Fall velocities on the order of 2 to 3 m sec^{-1} are associated with the presence of only a minute amount of liquid water. In actual storms, during the early stage of precipitation growth, the autoconversion process produces small drops with negligible terminal velocities. Hence the advective speed and accretion rate computed from Kessler's formulation are likely to give an overestimation of realistic values. The second consequence arises from the assumption of a constant N_o. Under natural conditions, whenever evaporation occurs, it depletes quickly the number of small drops and N_o is expected to decrease. Hence Kessler's formulation overestimates the rate of the evaporation process.

Figs. 5.24-5.29 present sections of $\overline{W}_a$, $\overline{\theta}'_a$, $\overline{q}_{ra}$, $\overline{Z}_a$ and the graphs of the rainfall rate and water budget for E6. The major differences in the dynamic, thermodynamic, and microphysical variables between E2 and E6 are summarized in Table 5.2.

The effect of the larger fall velocity in Kessler's scheme during the early stage of cloud growth is revealed from a comparison of surface rainfall (fig. 5.28) and radar reflectivity profiles (figs. 5.16 and 5.27). In E6, the onset of surface precipitation is 3 min earlier and the radar reflectivity originates at a lower level. These effects are the results of a larger accretion rate for model K microphysics which causes rapid depletion of cloud water and a rise in the rain amount before 20 min (fig. 5.29). At the same time the faster fallout leads to less accumulation of rainfall aloft (figs. 5.26 and 5.13) and earlier onset of the downdraft (fig. 5.24).

The longer duration of the downdraft and the more pronounced negative potential temperature deviation near the surface (fig. 5.25) reflect the effect of a more rapid rate of evaporation in Kessler's scheme. The minimum $\bar{\theta}'_a$ reaches -1.5°c at 30 min. A similar picture is also illustrated in the water budget in fig. 5.29 where a large part of the precipitation is evaporated from the environment and a smaller portion of the rain accumulates in the cloud region. As a result, the ratio of evaporation to condensation is larger for E6 and the efficiency of the cloud decreases.

The radar reflectivity profile in fig. 5.27 shows a stronger reflectivity aloft when compared with that in E2 (fig. 5.16). It has been shown that the dropsize distribution in E2 near the cloud top is narrower than the corresponding MP spectrum. The dominant role of large drops in affecting the distribution of radar reflectivity is thus demonstrated.

Inspection of Table 5.2 indicates that the microphysical

Table 5.2

COMPARISON OF RESULTS FROM E2 AND E6

Experiment	E2	E6
Microphysical parameterization	Model P	Model K
Max. updraft ($m\ sec^{-1}$)	6.67	6.72
Max. downdraft ($m\ sec^{-1}$)	-3.43	-3.58
Time of onset of downdraft (min)	23	22
Max. cloud top (km)	6	6
Max. $\bar{\theta}'_a$ (°K)	2.96	2.91
Min. $\bar{\theta}'_a$ in downdraft (°K)	-0.36	-1.54
Total condensation (arbitrary units)	75	72
ratio of cumulative rainfall over condensation	0.34	0.17
ratio of evaporation over condensation	0.66	0.83
Time of onset of rain at surface(min)	24	21
Max. rainfall intensity ($mm\ hr^{-1}$)	35.9	18.3
Max. radar reflectivity (dbz)	48.3	49.4

parameterization has relatively little effect to the dynamical and thermodynamical processes except near the ground. The water budget and the precipitation rate, however, vary considerably from that of the more detailed parameterization (model P). In view of the fact that the dynamical and thermodynamical behavior of the simulated cloud is similar for the two microphysical schemes, the two-cylinder model with model K microphysics will be used for the rest of the sensitivity tests because of the large saving in computations.

5.7 Effect of perturbation pressure (E7)

To determine the effect of perturbation pressure on cloud evolution, E7 was run with the perturbation pressure set to zero. Sections of $\overline{W}_a$, $\overline{\theta}'_a$, and $\overline{q}_{ra}$ are illustrated in figs. 5.30-5.32. The corresponding sections in E6 (figs. 5.21-5.23) are used for comparison.

Exclusion of the perturbation pressure field results in a tight gradient of $\overline{W}_a$ near the top of the cloud. The growth of the cloud is more rapid and the maximum $\overline{W}_a$ climbed to 7.3 m sec^{-1} at 18 min. However, without the supporting effect of the perturbation pressure force near the surface, the cloud is more susceptible to the dissipating effect of the precipitation processes and the downdraft forms at 13 min. Although confined to a shallow larger, the downdraft cuts off the moisture supply and the cloud dissipated at

32 min. Because the life history is shortened, less condensation takes place and a corresponding decrease in the maximum value of $\bar{\theta}'_a$ and $\bar{q}_{ra}$ occurs.

The radial velocity fields at three different times are compared in fig. 5.33. Without the perturbation pressure, the inflow region extends to a great depth. On the other hand, the outflow region is confined to a shallow layer near the cloud top and next to the ground. The outflow velocity in strong, with a maximum amplitude exceeding 12 m sec^{-1}.

Perturbation pressure therefore acts both to suppress and to help cloud growth. The maximum updraft weakens and the velocity gradient is smoothed near the cloud top. Detrainment now takes place throughout a deep layer. However, the pressure force is generally positive near the surface and acts to prolong the life history of the cloud by its protective role against the downward drag of the precipitation.

5.8 Effect of cloud radius and entrainment (E8 and E9)

The dimension of a cloud affects both the strength of the entrainment processes and the perturbation pressure force. The dynamic and turbulent entrainment terms formulated in the two-cylinder model bear an inverse relation to the cloud radius. The analysis in Chapter 3 has shown that the perturbation pressure force increases with an increase in the dimension of the updraft. It appears likely that for small clouds, the entrainment processes may be a more dominant

mechanism. In the case of larger clouds, the pressure force would play a leading role. To investigate the relative importance of these two effects, three clouds with radii at 1, 1.5, and 2 km and a σ of 0.32 are simulated. Results for the maximum values of $\overline{W}_a$, $\overline{\theta}'_a$, $\overline{q}_{ca}$, $\overline{q}_{ra}$, precipitation rate, $\overline{z}_a$, and cumulative rainfall amount are depicted in fig. 5.34.

In general, the amplitude of the various quantities increase with an increase in radius. The increase in more pronounced for a radius change from 1 to 1.5 km. $\overline{q}_{ra}$, precipitation rate, and cumulative rainfall are almost doubled. $\overline{\theta}'_a$ increase from 2.2°c to 2.8°c. Smaller changes are shown for an increase of radius from 1.5 to 2 km. A point to note is that except for a lag in time, very little change in the maximum amplitude of $\overline{W}_{a\ max}$ occurs. These results suggest that for clouds with a radius $<$ 1.5 km, entrainment is an important dissipative process. The pressure force may become progressively more important as the radius exceeds 1.5 km.

5.9 Effect of initial conditions (E10-E17)

The environmental temperature and humidity profiles, and an initial impulse are required as initial conditions for the cumulus cloud model. The sensitivity of the model to the initial impulse is investigated in E10 and E11. W_o, the amplitude of the velocity perturbation, is reduced from 1 m sec^{-1} to 0.2 m sec^{-1} in E10. The humidity impulse is completely suppressed in E11.

The results displayed in figs. 5.35 and 5.36 show that reducing the strength of the initial impulse delays the development of the cloud by 5 min. The overall characteristic of the cloud in terms of the maximum velocity, potential temperature deviation, radar reflectivity, as well as cloud and rain water contents are insensitive to the imposed changes. Therefore for a relatively humid atmosphere as is exemplified by the idealized sounding in fig. 4.2, a smaller initial impulse only delays the evolution of the convective element.

The atmospheric stratification of temperature and humidity has a large influence on cloud growth. Fig. 5.37 from E12 shows that the cloud properties respond readily to a steeper lapse rate of 7°c km^{-1}. $\overline{W}_{a\ max}$ increase to 13.7 m sec^{-1}, $\overline{\theta}'_a$ climbs to 6.1 °K, and $\overline{q}_{ra}$ reaches a value of 8 g kg^{-1}. The moisture content of the atmosphere, particularly near the cloud base and in the subcloud layer also appear to be crucial for the growth of a deep cloud. The humidity profile for E13 increases linearly from 70% at the ground to 90% to the cloud base, and decreases at a rate of 5.5% km^{-1} thereafter. With this change in the humidity profile, the cloud grows only to 4 km. The amplitudes of $\overline{W}_a$, $\overline{\theta}'_a$, $\overline{q}_{ca}$, $\overline{q}_{ra}$, and $\overline{Z}_a$ are considerably reduced as is illustrated in fig. 5.38.

It is probably true that this sensitivity to the moisture distribution may be caused in part by the simple structure of the two-cylinder model. The cloud column is not protected from the drier air from the environment. Dynamic and turbulent entrainment fed in the drier air directly resulting in a depletion

of moisture available for condensation. On the other hand, the importance of moisture stratification to cloud development is also bore out by observations. From an investigation of Ohio thunderstorms in the Thunderstorm Project, Braham(1952) noted that thunderstorms will not develop unless there is locally more moisture than is indicated by the mean Ohio sounding for thunderstorm days. He suggested that a pre-thunderstorm period of convection which continually transports water upward from the lower levels, might provide a mechanism for the local enhancement of moisture.

5.10 Effect of parameters in numerical scheme (E14-E17)

Effect of varying the time step δt, and space increment δz, are shown in figs. 5.39-5.40. The solution is relatively insensitive to a variation in δt from 5 to 20 sec. A larger δz of 500 m decreases the amplitude of all cloud variables. Molenkamp (1968) showed that the pseudo-diffusion coefficient associated with the forward upstream differencing scheme for a one-dimensional advection equation is of the form

$$\gamma = \frac{1}{2}|w|\left(1 - \left|w\frac{\delta t}{\delta z}\right|\right)\delta z \qquad (5.1)$$

So that for a fixed $\left|w\frac{\delta t}{\delta z}\right|$ satisfying the linear stability criteria, the solution becomes more diffusive with a larger space increment. The result of E16 is consistent with this finding.

No substantial changes in the solutions occur when the number of modes used to calculate π' is increased from 10 to 20 in E17. It appears that 10 modes is sufficient for the values of the radius a and σ used in the experiment.

5.11 Summary

The microphysical and dynamical interactions in a precipitating cumulus cloud have been investigated by a series of experiments with the two-cylinder model. Water loading has been shown to be the major factor for the initation of the downdraft while evaporation from falling small drops can significantly enhance the downdraft development. An increase in the subsidence rate in the environment which occurs when the percentage of cell area occupied by the updraft is increased, leads to earlier dissipation of the cloud as a result of the transport of downward momentum and the drying of the air in the environment through adiabatic descent. The latent heats of fusion and sublimation released in the freezing of cloud and rain water contents and during the depositional growth of ice particles increase the buoyancy in the upper region of the cloud and resulted in a higher cloud top. Comparison of Kessler's parameterization with a more detailed microphysical formulation indicates that using different schemes has relatively little effect on the dynamics and thermodynamics of the

cloud but causes significant changes in the water budget and the distribution of radar reflectivity. Perturbation pressure acts to smooth the strong velocity gradient near the cloud top, extending the region of detrainment, suppress the intensity of convection, and to prolong cloud life time by supporting the updraft near the cloud base. Strong entrainment has been found to be a major dissipative process and the model performance is found sensitive to the temperature and humidity distributions of the ambient atmosphere. Finally, the sensitivity of the model to parameters in the numerical scheme has also been explored.

CHAPTER SIX

EFFECT OF CUMULUS CONVECTION ON THE ENVIRONMENT

6.1 Introduction

The importance of the effect of cumulus convection on the larger scale circulation has now been generally recognized. Diagnostic studies from larger scale observations (e.g. Yanai, 1973; Ogura and Cho, 1973; Nitta, 1975) have shown that the detrainment from cumulus clouds cools and moistens the environment but the cumulus-induced subsidence causes large-scale warming and drying. These results further suggest the coexistence of shallow and tall clouds which might be important in maintaining the structure of the large-scale temperature and humidity fields in the tropical atmosphere.

A different approach which deduces the cumulus transports of mass, heat, and momentum from detailed rainfall measurements was due to Austin and Houze (1973). They related the lifting in a cumulus cell to the precipitation which it produces and derived formulas expressing the entrainment and temperature excess in terms of the cell depth and precipitation amounts. Houze (1973) applied the model to a climatological study of cumulus transports and concluded that transports by cumulus clouds are of the same order of magnitude as other large-scale vertical fluxes during at least one season of the year.

However, the results of the above investigations depend on the choice of a cloud model. The one-dimensional, steady-state entraining plume which has often been used in diagnostic studies possesses a number of shortcomings. The life cycle of the cloud is not included, the effect of the downdraft is incorporated with debatable assumptions (e.g. Houze and Leary, 1976; Johnson, 1976; Nitta, 1977), and the microphysical parameterizations are extremely crude.

A more sophisticated time-dependent model might overcome some of the above difficulties. Lopez (1973) developed a one-dimensional Lagrangian model to study the effect of cumulus in the heat and moisture budget of the environment using a mean cumulus cloud population. Soong and Ogura (1976) used a two-dimensional axi-symmetric model to deduce the size distribution of clouds which is required to maintain the observed large-scale temperature and humidity profiles in an undisturbed period during BOMEX. A similiarity between these two studies is that a mean sounding is used and the cloud population is generated by varying the strength of the initial impulse.

In this chapter, the effect of cumulus convection and the associated mass and heat transports will be explored using the two-cylinder model with model K microphysics. The effects of an isolated convective element on the heat and moisture budget in the cloud and in the environment during its entire life history are first examined. The model is then applied to study the

monthly transports of mass and heat by an ensemble of cumulus clouds at Boston in the month of July. In contrast to the approach of Lopez or Soong and Ogura where a mean sounding is used, the present method computes the transports from individual storms passing over an observing station on different days. The transports from these cells normalized to the observed rainfall amount are summed to give a total transport over an extended period. The approach is essentially the same as Houze (1973) but a more sophisticated model is used in the present study.

The equations for the heat and moisture budgets, and calculations of mass and heat fluxes are presented in section 6.2. The effects of the cumulus are analyzed in section 6.3. Sensitivity tests for the heat flux calculations are in section 6.4.

6.2 Equations for time-integrated effects of cumulus

6.2.1 Heat and moisture budget

Let the operators $\langle\ \rangle_a$ and $\langle\ \rangle_b$ be defined as

$$\langle F\rangle_a = \int_\tau F_a\, dt$$

$$\langle F\rangle_b = \int_\tau F_b\, dt \qquad (6.1)$$

where $F_{a,b}$ is any function in the cloud and in the environment respectively and τ is the life time of the cloud.

By applying (6.1) to the potential temperature and water vapor deviation equations in (4.25), (4.26) and using (4.15), the equations for the vertical distribution of time-integrated heat and moisture budgets become

$$\langle \Delta\theta \rangle_a = \langle -\bar{w}_a \frac{\partial \bar{\theta}_a}{\partial z} \rangle_a + \langle \epsilon_\theta \rangle_a + \frac{L}{c_p \bar{\pi}_a} \langle C \rangle_a - \frac{L}{c_p \bar{\pi}_a} \langle E_c \rangle_a - \frac{L}{c_p \bar{\pi}_a} \langle E_r \rangle_a \tag{6.2}$$

vertical advection; entrainment and detrainment; condensation; evap. of cloud; evap. of rain

$$\langle \Delta\theta \rangle_b = \langle -\bar{w}_b \frac{\partial \bar{\theta}_b}{\partial z} \rangle_b + \langle \epsilon_\theta \rangle_b + \frac{L}{c_p \bar{\pi}_b} \langle C \rangle_b - \frac{L}{c_p \bar{\pi}_b} \langle E_c \rangle_b - \frac{L}{c_p \bar{\pi}_b} \langle E_r \rangle_b \tag{6.3}$$

$$\langle \Delta q_v \rangle_a = \langle -\bar{w}_a \frac{\partial \bar{q}_{va}}{\partial z} \rangle_a + \langle \epsilon q_v \rangle_a - \langle C \rangle_a + \langle E_c \rangle_a + \langle E_r \rangle_a \tag{6.4}$$

$$\langle \Delta q_v \rangle_b = \langle -\bar{w}_b \frac{\partial \bar{q}_{vb}}{\partial z} \rangle_b + \langle \epsilon q_v \rangle_b - \langle C \rangle_b + \langle E_c \rangle_b + \langle E_r \rangle_b \tag{6.5}$$

where

$$\langle \Delta\theta \rangle_a = \int_\tau \frac{\partial \bar{\theta}'_a}{\partial t}\, dt$$

$$\langle \Delta\theta \rangle_b = \int_\tau \frac{\partial \bar{\theta}'_b}{\partial t}\, dt$$

$$\langle \epsilon_\theta \rangle_a = -\int_\tau \frac{2}{a}\left[\tilde{u}_a(\tilde{\theta}_a - \bar{\theta}_b) + \alpha^2 |\bar{\omega}_a - \bar{\omega}_b|(\bar{\theta}'_a - \bar{\theta}'_b)\right] dt$$

$$\langle \epsilon_\theta \rangle_b = \int \frac{2a}{(b^2-a^2)}\left[\tilde{u}_a(\tilde{\theta}_a - \bar{\theta}_b) + \alpha^2 |\bar{\omega}_a - \bar{\omega}_b|(\bar{\theta}'_a - \bar{\theta}'_b)\right] dt$$

where $\tilde{\theta}_a = \bar{\theta}'_a$ when $\tilde{u}_a > 0$,

and $\tilde{\theta}_a = \bar{\theta}'_b$ when $\tilde{u}_a \leqslant 0$

$$\langle C \rangle_a = \int_\tau (P1)_a\, dt$$

$$\langle C \rangle_b = \int_\tau (P1)_b\, dt$$

$$\langle E_c \rangle_a = \int_\tau (P2C)_a\, dt$$

$$\langle E_c \rangle_b = \int_\tau (P2C)_b\, dt$$

$$\langle E_r \rangle_a = \int_\tau (P2R)_a\, dt$$

$$\langle E_r \rangle_b = \int_\tau (P2R)_b\, dt$$

(6.6)

Equations (6.2)-(6.5) indicate that vertical advection, entrainment/detrainment, condensation, and evaporation are the four processes contributing to the modification of the atmosphere by cumulus clouds. In particular, subsidence ($\bar{\omega}_b < 0$) warms and dries the environment when $\frac{\partial \bar{\theta}_b}{\partial z} > 0$ and $\frac{\partial \bar{q}_{vb}}{\partial z} < 0$.

In the computations to be presented in section 6.3 the term on the left and the last four terms on the right hand side of equations (6.2)-(6.5) are computed explicitly. The term for the vertical advection is then obtained as a residue.

6.2.2 Formulas for mass and heat fluxes

The upward mass transport by updrafts (M_u) and the downward mass transport by downdrafts (M_d) inside the cloud are given by

$$M_u = \int_\tau \rho_0 \bar{\omega}_a \, dt \quad ; \quad \bar{\omega}_a > 0 \tag{6.7}$$

$$M_d = \int_\tau \rho_0 \bar{\omega}_a \, dt \quad ; \quad \bar{\omega}_a < 0 \tag{6.8}$$

The corresponding sensible heat fluxes by up and downdrafts are

$$H_u = c_p \int_\tau \rho_0 \bar{\omega}_a (\bar{T}_a - T_0) dt \; ; \; \bar{\omega}_a > 0 \tag{6.9}$$

$$H_d = c_p \int_\tau \rho_0 \bar{\omega}_a (\bar{T}_a - T_0) dt \; ; \; \bar{\omega}_a < 0 \tag{6.10}$$

The heat flux in the environment, H_e, is defined as

$$H_e = c_p \int_\tau \rho_0 \bar{\omega}_b (\bar{T}_b - T_0) dt \tag{6.11}$$

where $\bar{T}_a$, $\bar{T}_b$, and T_0 are respectively the temperatures in the cloud, the environment, and the base state atmosphere.

6.3 Effects of cumulus

6.3.1 Computations with idealized sounding

Heat and moisture budget

The mechanisms whereby cumulus activities affect the heat and moisture budgets of the atmosphere are analyzed from the result of experiment E12 listed in Table 5.1. Convection is initiated by a velocity perturbation in an idealized base-state stratification. The source and sink terms in the potential temperature and water vapor deviation equations are integrated in time through a cloud life-time τ of 1 hr.

Factors contributing to the temperature change in the cloud region (inner cylinder) are depicted in fig. 6.1. Condensation, $\frac{L}{c_p \bar{\pi}_a} \langle c \rangle_a$, produces heating from the cloud-base at 875 m to a height of 6 km. The maximum heating is located around 2 km. Entrainment of environmental air, $\langle \epsilon_\theta \rangle_a$, gives a slight warming effect when the whole life history of the cloud is considered. The air in the environment is of course colder than that of the updraft during the early stage of cloud development. But as convection proceeds, the air in the environment sudsides and warms. Entrainment of this warmer air into the cloud results in a net warming effect. Two regions of warming brought about by the advection term, $\langle -\bar{w}_a \frac{\partial \bar{\theta}_a}{\partial z} \rangle$, occur respectively in the subcloud layer and around 6 km. The warming in the upper region is caused by the slight sinking of air near the cloud top while warming in the subcloud layer is

attributable to the descent of the air in the downdraft.

The vertical transport term counteracts a major part of the warming from 700 m to 6 km. Evaporation of cloud water, $\frac{-L}{c_p \bar{\pi}_a} \langle E_c \rangle_a$, cools the air in the upper region while evaporation of raindrops, $\frac{-L}{c_p \bar{\pi}_a} \langle E_r \rangle_a$, contributes significantly to the cooling below 3 km and particularly in the subcloud layer.

The net 1 hr temperature change in the cloud region, $\langle \Delta\theta \rangle_a$, is plotted on the same figure but on a different horizontal scale. A net warming occurs from 500 m to 5 km and a net cooling results above 5 km and below 500 m. It appears that condensation in a cumulus updraft represents the major contribution in warming a large part of the atmosphere in the region where convection occurs. Evaporation of cloud and rain water plays an important role in cooling the air near the cloud and in the subcloud layer.

The effect of cumulus on the temperature change in the environment is revealed in fig. 6.2. Subsidence, represented by the term $\langle -\bar{w}_b \frac{\partial \bar{\theta}_b}{\partial z} \rangle_b$, is by far the largest contribution to the warming of the air in the environment. Detrainment of cloud air, $\langle \epsilon_\theta \rangle_b$, warms the air from 500 m to 6 km; but its magnitude amounts to only about a third of that caused by subsidence.

Evaporation of detrained cloud water, $\frac{-L}{c_p \bar{\pi}_b} \langle E_c \rangle_b$ produces the largest cooling in the region from the cloud base to a level slightly over 6 km. In comparison, evaporative cooling from

the raindrops, $\frac{L}{c_p \bar{\pi}_b} \langle E_r \rangle_b$, is smaller but is the dominant contribution below the cloud base. A slight cooling from detrainment is noted below 500 m and above 6 km; probably the result of cold outflow from the downdraft and cold air detrained near the cloud top.

The net temperature change in the environment $\langle \Delta\theta \rangle_b$ is similar to that in the cloud column. Since evaporative cooling exceeds the warming from detrainment, the evironment would be cooled if the effect of subsidence were not taken into account. The result of the model computation suggests that subsidence warming offsets much of the cooling in the region from 0.5 to 5 km. As a result, the atmosphere is warmed in this region but cooled in the area around the cloud top and near the surface.

Fig. 6.3 shows the factors which contribute to the moisture budget in the cloud column. Condensation, $\langle C \rangle_a$, and entrainment, $\langle E_{q_v} \rangle_a$, serve as moisture sinks above the cloud base. Downward transport, $\langle -\bar{w}_a \frac{\partial \bar{q}_{va}}{\partial z} \rangle_a$, from the downdraft apparently depletes the moisture below the cloud base. The most important moisture source is the vertical transport of water vapor. The evaporation of rain, $\langle E_r \rangle_a$, is important near the ground. The role of evaporation of cloud droplets, $\langle E_c \rangle_a$, as a moisture source is negligible except near the cloud top.

The profile of $\langle \Delta q_v \rangle_a$ depicted in the same figure indicate a net moistening above 3.2 km and a net drying below. Vertical transport dominates over entrainment and condensation in the upper region. However, below 3.2 km, the combined effects of

condensation and entrainment exceed the effects of vertical transport and evaporation from rain and cloud water. The net drying in the subcloud layer is mainly due to the transport process but is modified by the evaporation of rain drops.

The moisture change in the environment is shown in fig. 6.4. Evaporation from detrained cloud water, $\langle E_c \rangle_b$, and detrainment of water vapor from the cloud column, $\langle \epsilon_{q_v} \rangle_b$, are the two major contributions to the moistening of the environment. Evaporation of raindrops, $\langle E_r \rangle_b$, provides an additional moisture source. But its magnitude is smaller except below the cloud base. Subsidence, $\left\langle -\bar{\omega}_b \frac{\partial \bar{q}_{v_b}}{\partial z} \right\rangle_b$, represents by far the largest moisture sink in the environment and dries the air at all levels with a maximum effect at a height of 2.6 km.

The overall moisture change in the environment, $\langle \Delta q_v \rangle_b$, as a result of cumulus convection indicates a net moistening aloft and a net drying below. Evaporation of cloud water and detrainment of water vapor is largely responsible for the moistening. Subsidence is the main drying agent while downward transport in the downdraft further dries the air near the surface.

Mass and heat fluxes

The vertical distribution of the mass flux integrated over the life cycle of the simulated cloud is shown in fig. 6.5. M_u increases with height up to 1.5 km and decreases thereafter. M_d exhibits a minimum slightly below the cloud base.

The total downward mass flux, obtained by integrating M_d through the whole depth of the cloud, amounts to 30% of the total upward mass transport. Hence the downdraft circulation can contribute quite significantly to the mass flux in a precipitating cloud column.

The heat fluxes by up and downdraft are plotted in fig.6.6. H_u shows a maximum of 5.5×10^9 ergs cm^{-2} at 2.7 km. A slight negative heat transport is located above 5.6 km as a result of the penetration of air into the stably stratified atmosphere. The downdraft transports sensible heat downward at all levels above 0.5 km. Cooling of the air by the evaporation of falling precipitation gives rise to a positive H_d near the surface. In comparison, the heat flux in the environment by compensatory currents, H_e, is an order of magnitude smaller than the transports by the convective up and downdrafts.

6.3.2 Monthly transports at Boston in July

To use the present cell model for computing the effect of cumulus activities for a specific area and time interval one needs to know, or assume, the number of cells which occurred, their heights and dimensions and the characteristics of the environment in which they were embedded. The time-integrated effects of the individual cells are computed and added to yield the over-all effect. As an example, the mass and heat transports are computed for a unit area in the vicinity of Boston for the month of July. The data base is essentially the same as that used by Houze (1973) and the results are compared with his.

Table 6.1 lists the days when cellular convection occurred, the time of precipitation, the mean radar echo-top height, and the precipitation amount. Precipitation was measured by rain gauges at West Concord, 30 km west of Boston. Echo-top heights were estimated from the Range Height Indicators (RHI) of the MIT radars. On the days when radar records were missing, the seasonally averaged echo-top height determined by Houze (1972) is assumed to be representative.

Radiosonde observation which are required to describe the environment are available only for 0000 GMT and 1200 GMT at Albany, NY; Portland, Maine; and Nantucket, Mass. Soundings prior to, during, and after the time of passage of a storm at West Concord are used as input to the model. The sounding that results in a cloud with top closest to the mean echo-top height is taken to be representative of the cell environment.

Austin and Houze (1972) found that cells are usually embedded in mesoscale precipitation areas. As such, the environment surrounding the cell is assumed saturated. The temperature sounding below the mean lifting condensation level at 1 km is modified by extrapolation along the dry adiabat. In some cases unrealistically high values of θ_e results from this procedure and the extrapolation is then made along the moist adiabat.

An initial impulse, the cloud radius, and the dimension of the outer cylinder representing the environment must be specified. A velocity perturbation given by (4.38) is used

Table 6.1

EXTENT OF DATA SAMPLE

Cases	Date	Time of precipitation (EST)	Mean echo-top height (km)	Measured celluar precipitation (cm)
1	July 9,1962	1100-1450	9	1.97
2	July 23,1962	1900-2000	7.5	0.14
3	July 26,1962	1400-1550	7	0.28
4	July 3,1963	0100-0200	7.5	0.02
5**	July 8,1963			
(a)		0200-0400	5	0.29
(b)		1500-1750	11	1.67
6	July 18,1963	1600-1650	12	0.02
7	July 30,1963	0500-0550	7.5	0.49
8	July 12,1969	1300-1500	12	0.25
9	July 13,1969	0300-0430	7.5*	0.02
10	July 29,1969	0600-1510	9.5	0.65
11	July 30,1969	0800-2010	7.5*	2.0

* seasonal mean echo-top height

** In case 5, echo-top height increased substantially in the afternoon.

to initiate the convection. The exact dimension of the updraft however, cannot be determined from radar measurements as the relation between updraft dimension and reflectivity distribution is still unclear. To overcome this difficulty, an average cell radius of 1.5 km is assumed but the calculated transport is normalized by the ratio of the computed to the measured precipitation amount. Sensitivity tests in sections 5.8 and 6.4 indicate that both the computed heat transport and the cumulative rainfall increase with an increase in cloud radius but at slightly different rates. Therefore, the arbitrariness in prescribing the radius would be partially compensated by the normalization procedure. A σ of 0.32 is used in accordance with the hypothesis of maximum heat transport discussed in Chapter 4.

Mass and heat transports by up and downdrafts are calculated for each of the case in Table 6.1 using a sounding representative of the cell environment. The transports are summed for each storm. The arithmetic mean for the months of July in the three years then gives the average monthly transport for July. To reduce the amount of computations involved, a coarser resolution of δt =20 sec and δz =500 m was used.

Comparisons between the computed and observed echo-tops are listed in Table 6.2. For clouds with tops below 9 km the agreement between the computed and observed heights is good. The model however tends to underpredict clouds with

Table 6.2

COMPARISON BETWEEN COMPUTED AND MEAN OBSERVED ECHO-TOP HEIGHT

Cases	'representative' sounding used		mean echo-top height (km)	computed cloud top (km)
	station	time of ascent		
1	14764	7/9/62 1200Z	9	9.25
2	14764	7/24/62 0000Z	7.5	8.75
3	14764	7/26/62 1200Z	7	6.25
4	14756	7/3/63 1200Z	7.5	7.75
5				
(a)	14764	7/8/63 1200Z	5	4.25
(b)	14764	7/9/63 0000Z	11	7.75
6	14756	7/19/63 0000Z	12	9.75
7	14756	7/30/63 0000Z	7.5	9.25
8	14764	7/12/69 1200Z	12	8.75
9	14735	7/13/69 0000Z	7.5*	7.25
10	14764	7/29/69 1200Z	9.5	6.75
11	14735	7/31/69 0000Z	7.5*	7.75

* seasonal mean echo-top height

tops above 9 km. A partial explanation of the descrepency may be found in the neglect of ice phase in the present computation. The latent heats of fusion and sublimation are expected to be important in clouds that rise to great heights.

The average monthly mass transport curves are shown in fig. 6.7. Maximum upward transport occurs at 2.5 km but considerable mass transport still takes place above 6 km. The transport by the downdraft is smaller but certainly not negligible. The integrated downdraft transport is about one fourth of that accomplished by the updraft.

The sensible heat transports by the up and downdraft depicted in fig. 6.8 indicate a much larger transport by the updrafts. Comparison with the heat transport curve obtained by Houze (1973) reveals that the total heat transport computed from the two models is of comparable magnitude. The major difference lies in the level of maximum transport which occurs at 3.3 km in the present study but is at 6 km in the computation by Houze. This effect is probably due to the fact that the maximum mass transport was placed near the cloud top in the model of Austin and Houze (1973). The heat flux in the environment by compensatory currents is negative but is much smaller than the fluxes in the cloud region.

6.3.3 Computations with a mean Marshall Islands Sounding

To investigate the variation in cumulus transports in a different geographic location, a monthly mean sounding for Majuro , Marshall Islands in July 1975 is used as input for

the model. The sounding is published in Climatological Data, National Summary by the National Climate Center of NOAA. and is plotted in fig. 6.9. For the model computations, the humidity in the environment is assumed saturated above the lifting condensation level (LCL). The relative humidity at the ground is assumed 75% and increases linearly to saturation value at the LCL.

The mass transports (fig. 6.10) shows a similar profile to the average monthly transports of Boston (fig. 6.7). Two relative maxima occur respectively at 1.7 and 3.5 km. The heat flux profile by the updraft (fig. 6.11) is bimodal and the magnitude is considerable above 4 km. The transport by the downdraft shows a positive value below 0.5 km.

An experiment was also run with the humidity profile as indicated in fig. 6.9. In this case only a shallow cloud developed and the heat and mass transports were relatively small.

6.4 Sensitivity test for heat flux calculations

The sensitivity of the model to the microphysical parameterization, cloud radius, and radii ratio in computing the heat transports is explored with the idealized sounding plotted in fig. 4.2. Fig. 6.12 shows that in the convective updraft, the model P microphysics results in a larger upward heat transport below 3 km. In the subcloud layer, the upward heat flux associated with Kessler's schemes is much larger than that of the more detailed formulation.

The heat flux calculations in the cloud column is sensitive to the variations in cloud radius (fig. 6.13) and the radii ratio (fig. 6.14). In general, H_u and H_d increase with an increase in the radius of the cloud. Although H_u indicates a larger value for a smaller σ of 0.16, the total integrated heat flux per unit area throughout the domain of convection calculated from (4.40) actually shows a decrease when σ varies from 0.32 to 0.16 (Table 6.3).

6.5 Summary

This chapter examines the effects of cumulus convection on the heat and moisture budgets of the atmosphere and the cumulus transports of heat and mass. Condensation is found to be a major heat source and evaporation a major heat sink in the region of the updraft column. In the environment, evaportive cooling exceeds the warming due to detrainment of cloudy air but adiabatic warming by subsidence offsets much of the cooling effect.

Examination of the moisture budget reveals that vertical transport moistens the air aloft in the cloud. Condensation and entrainment of drier air from the environment deplete the moisture supply in the lower portion of the cloud column. On the other hand, the environment is moistened by the detrained water vapor and evaporation of cloud droplets aloft while subsidence drying causes a net drying effect below.

Table 6.3

SENSITIVITY OF H_T TO MICROPHYSICAL PARAMETERIZATION, CLOUD RADIUS, AND RADII RATIO

Microphysical parameterization	cloud radius (km)	radii ratio	H_T (arbitrary unit)
model P	1.5	0.32	1
model p	1.5	0.16	0.76
model K	1.0	0.32	0.58
model K	1.5	0.32	0.9
model K	2.0	0.32	1.15

Comparison of the mass and heat transports at Boston in July computed by the present model with those obtained by Houze (1973) indicates that the two models give comparable total heat transports in convective updrafts. The level of maximum heat flux is however much lower in the present computation. Comparison of the transports at Boston with those calculated from a mean sounding at Majuro, Marshall Islands shows larger transports aloft in the latter case.

CHAPTER SEVEN

CONCLUSION

This study is concerned with the microphysical-dynamical interactions in a cumulus cloud and the effects of cumulus activities on the atmosphere. The approach is through development and use of a two-cylinder model which allows sensitivity tests on the major microphysical and dynamical processes. The study is carried out in three major steps.

First, a microphysical parameterization scheme is developed and tested in the context of a kinematic updraft. Explicit evolution of the drop-size spectrum and the effect of differential fallspeeds are allowed by the growth of rain and graupel particles in a total of 25 size categories. Despite its simplicity, the scheme gives results comparable to those of a stochastic model in warm rain development. Sensitivity tests indicate the existence of a negative feedback mechanism between the autoconversion and accretion processes, the important contribution of rain-rain interactions in the evolution of drop-size spectrum, and the essential role of impaction breakup as a limiting mechanism for drop growth.

Second, the effect of perturbation pressure is clarified by a simple analytic model. The buoyancy and drag induced perturbation pressure has been shown to oppose the forcing but may be important in supporting a negatively buoyancy updraft. The dynamic pressure is found to be a response to the Bernoulli effect and the centri-

fugal force due to rotation of the air. The pressure force is of the same order of magnitude as the buoyancy and drag and its neglect would lead to qualitative and quantitative errors in cloud simulation.

Lastly, a two-cylinder model is formulated which includes the microphysical scheme developed in the first step of the study. Perturbation pressure is incorporated explicitly by a Fourier Bessel series expansion and the area occupied by compensating currents in the outer cylinder is determined from the hypothesis that cumulus cells achieve the most efficient heat transport. Numerical experiments with the model on the microphysical-dynamical interactions show that precipitation loading near the cloud base appears to be responsible for the initiation of the downdraft while evaporation from falling small drops can significantly enhance downdraft development. Strong subsidence in the environment leads to earlier dissipation of the cloud as a result of the transport of downward momentum and the drying of the environment on adiabatic descent. Inclusion of the ice phase leads to a deeper cloud as a result of the added buoyancy from the latent heats released in the freezing of water drops and depositonal growth of ice particles. Perturbation pressure is found to smooth the steep velocity gradient near the cloud top, extend the region of detrainment, suppress the intensity of convection, but may prolong cloud life time by supporting the updraft near the cloud base. Strong entrainment has been demonstrated to be a major dissipative process and the model responds

readily to the temperature and humidity distributions of the ambient atmosphere.

The effects of cumulus activities in the cloud column and in the environment can be summaried as:

(1) In the cloud column

Condensation is the major heat source and evaporation a major heat sink. The vertical transports moisten the air aloft but condensation and entrainment of drier air from the environment deplet the moisture supply in the lower portion.

(2) In the environment

Evaporative cooling exceeds the warming due to detrainment of cloudy air but adiabatic warming by subsidence offsets much of the cooling effect. Detrainment of water vapor and the evaporation of cloud droplets moisten the air aloft but subsidence drying causes a net drying effect below.

The model is also applied to a computation of cumulus transports of mass and heat. Comparison of the present results at Boston in the month of July with those obtained by Houze (1973) indicates that the two models give comparable total heat transports. The level of maximum heat transport is noticeably lower in the present computation.

Further research with the model should be directed toward:

(a) Comparison with actual observations

The model has demonstrated its usefulness in understanding the complicated processes in a cumulus cloud. Further use of the model as an operational tool must await extensive tests with

observations. Since in-cloud measurements of temperature and liquid water contents are difficult to obtain, a practical comparison can be made with the distribution of radar reflectivities, echo-top height, rainfall rate and amount. Information of this type is readily available from radar and rain-gauge measurements. As the model is sensitive to the temperature and humidity distribution of the ambient atmosphere, soundings close to the time of the onset of convection should be used.

It is recognized that the present model treats the ice phase rather crudely and does not include the effect of mesoscale organization and wind shear which are generally observed to be associated with cumulus activities. Therefore the computed results may not be satisfactory under these conditions and further studies as outline in section (c) should be conducted.

(b) Computations of cumulus transports

The model can be applied to compute the cumulus transports of heat, mass, and moisture in places where the distribution of cloud population, echo-heights, and precipitation amounts are available (e.g. during GATE). The radius of the cloud, the radii ratio σ, and the initial impulse might have to be varied to generate a cloud population similar to those observed. This method has certain advantage over the steady-state entraining plume used in diagnostic studies as the effect of the cloud life cycle, the perturbation pressure, and the precipitation physics are represented in a more realistic manner.

(c) Further refinement of the model

Further refinement of the model should be aimed at

1) exploration of the role of mesoscale organization either as a mechanism for lifting or moisture enhancement.
2) clarifying the effect of the wind shear.
   Since the model cannot include wind shear directly, two and three-dimensional kinematic models can be used to elucidate the relations between air motion and the distribution of radar reflectivities. Such relations would serve as a guide for interpretation of results or suggest modifications for the two-cylinder model.
3) further study on the ice phase effect including the variations in the rate of freezing and the growth of ice crystals.

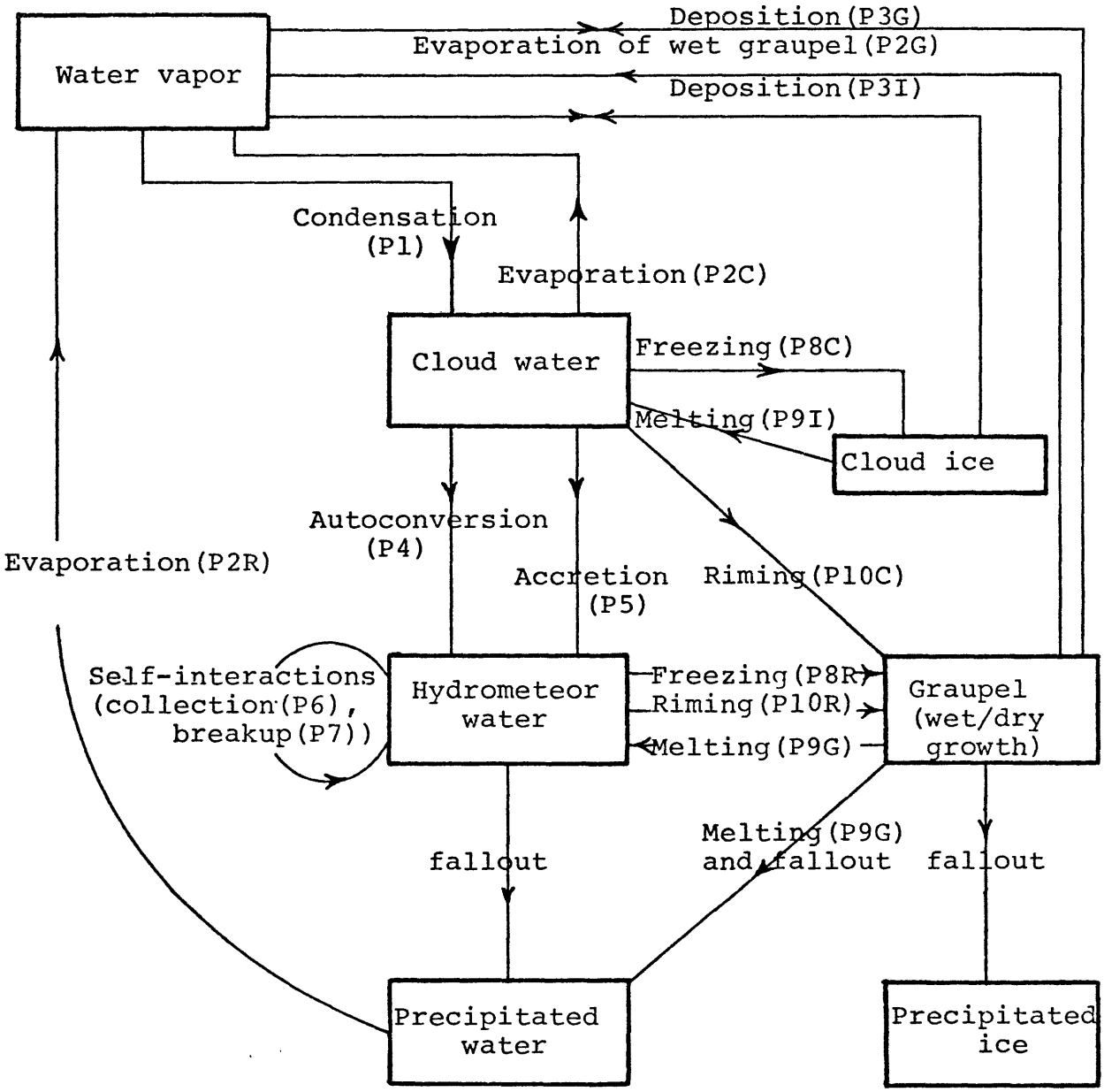


Fig. 2.1. The microphysical processes in the P model. Precipitated water and precipitated ice refer to rain and graupel particles that fall out of the cloud. Refer to text for P1,P2C....etc.

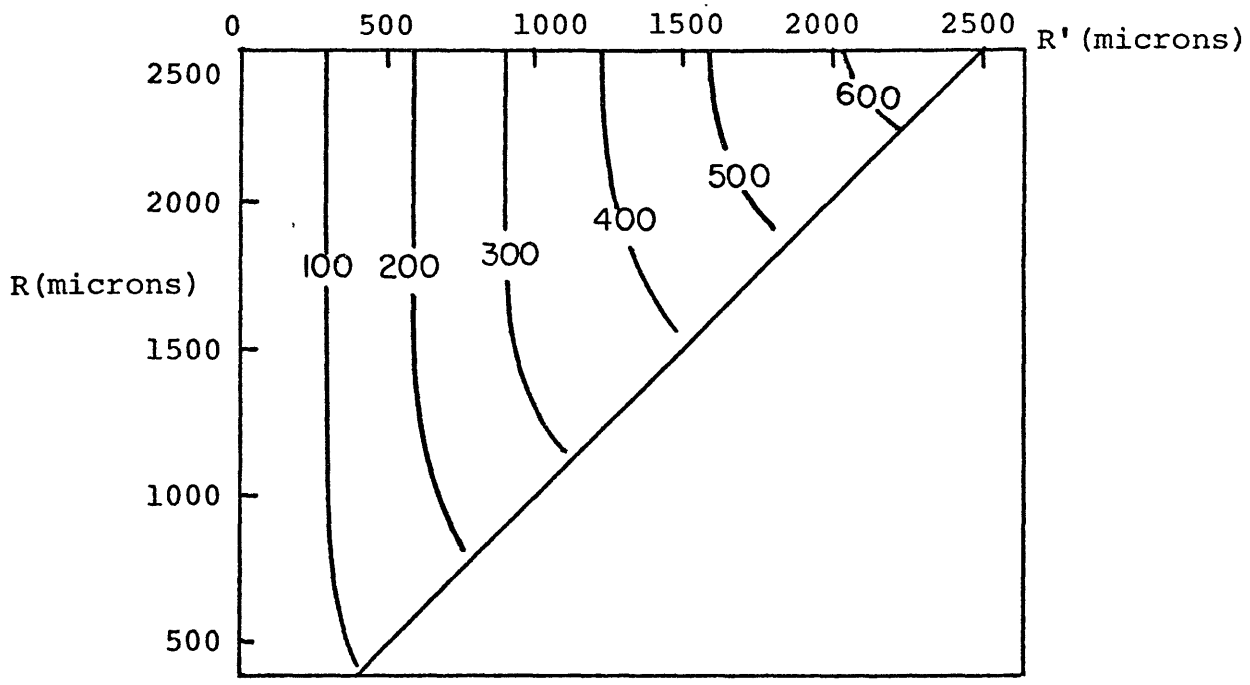


Fig. 2.2. Radius(r_s) of satellite drops produced by impaction of drops of radii R and R' (R > R'). The contours of r_s are in microns.

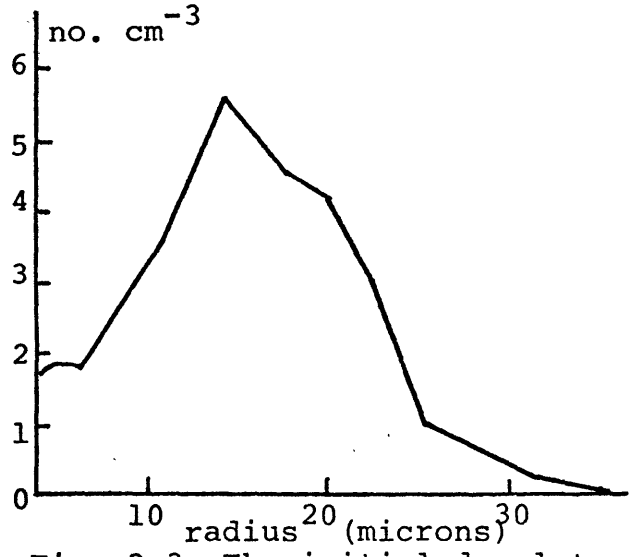


Fig. 2.3. The initial droplet spectrum for model S.

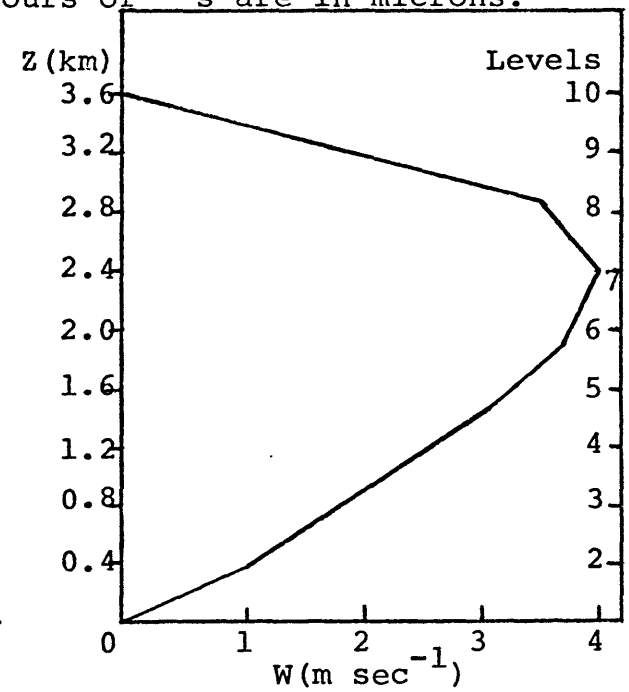


Fig. 2.4. The kinematic updraft profile.

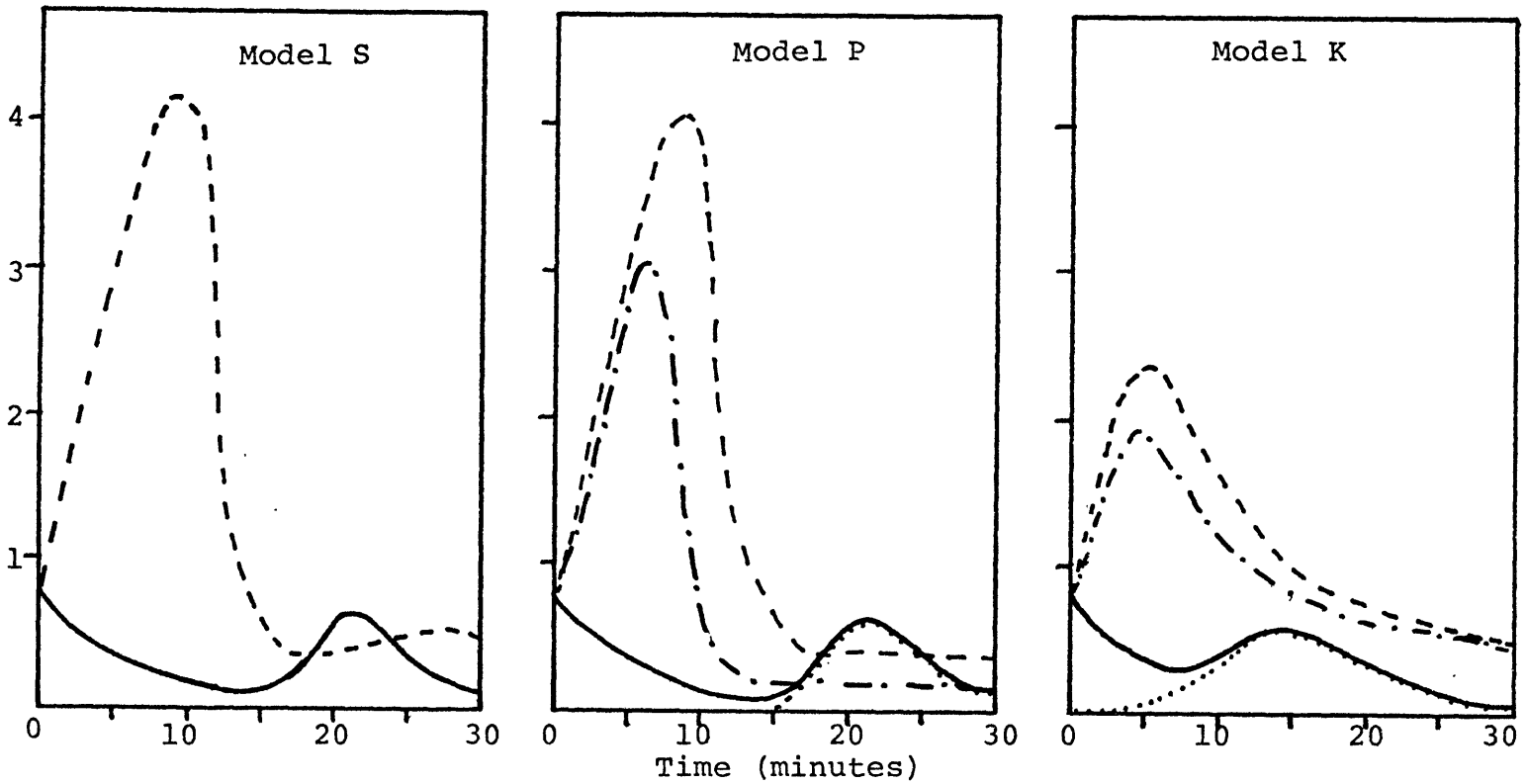


Fig. 2.5. Comparison of liquid water for model S,P, and K.Cloud + rain water at 400 m ———, at 3200 m – – – – –
Cloud water at 3200 m for models P and K —.—.—.
Rain water at 400 m for models P and K .....

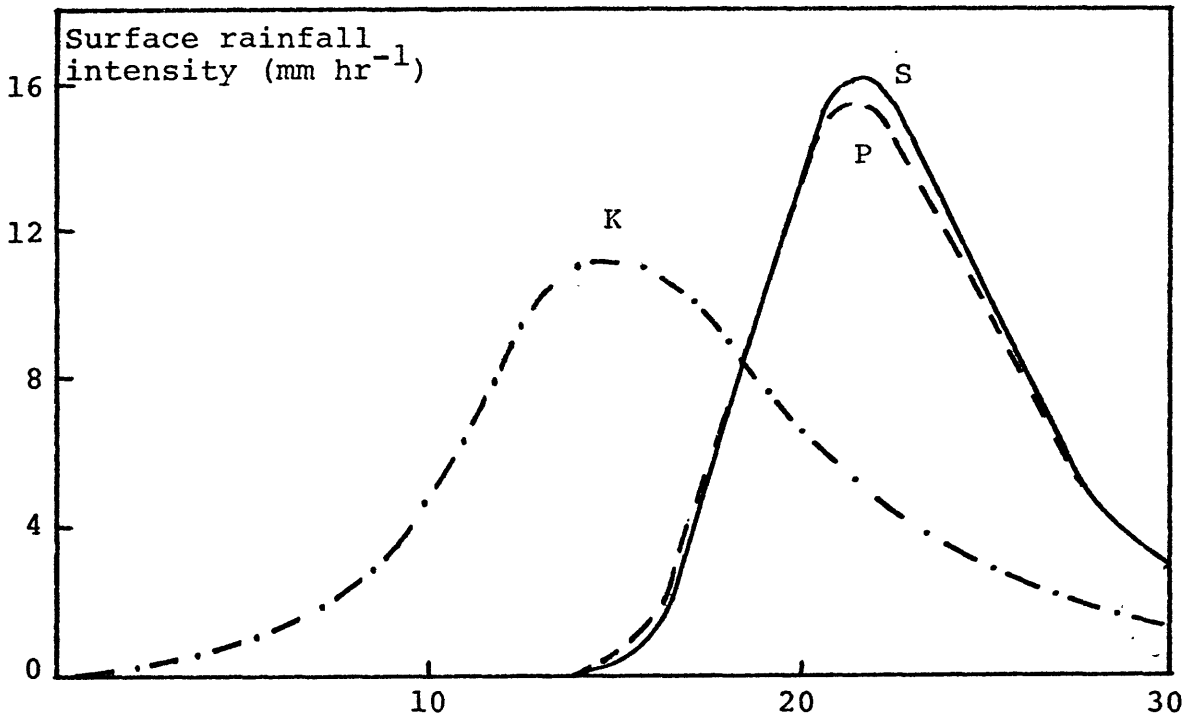


Fig. 2.6. Comparison of surface rainfall intensity for models S, K, and P. a=0.5 g m^{-3} K=10^{-3} sec^{-1}

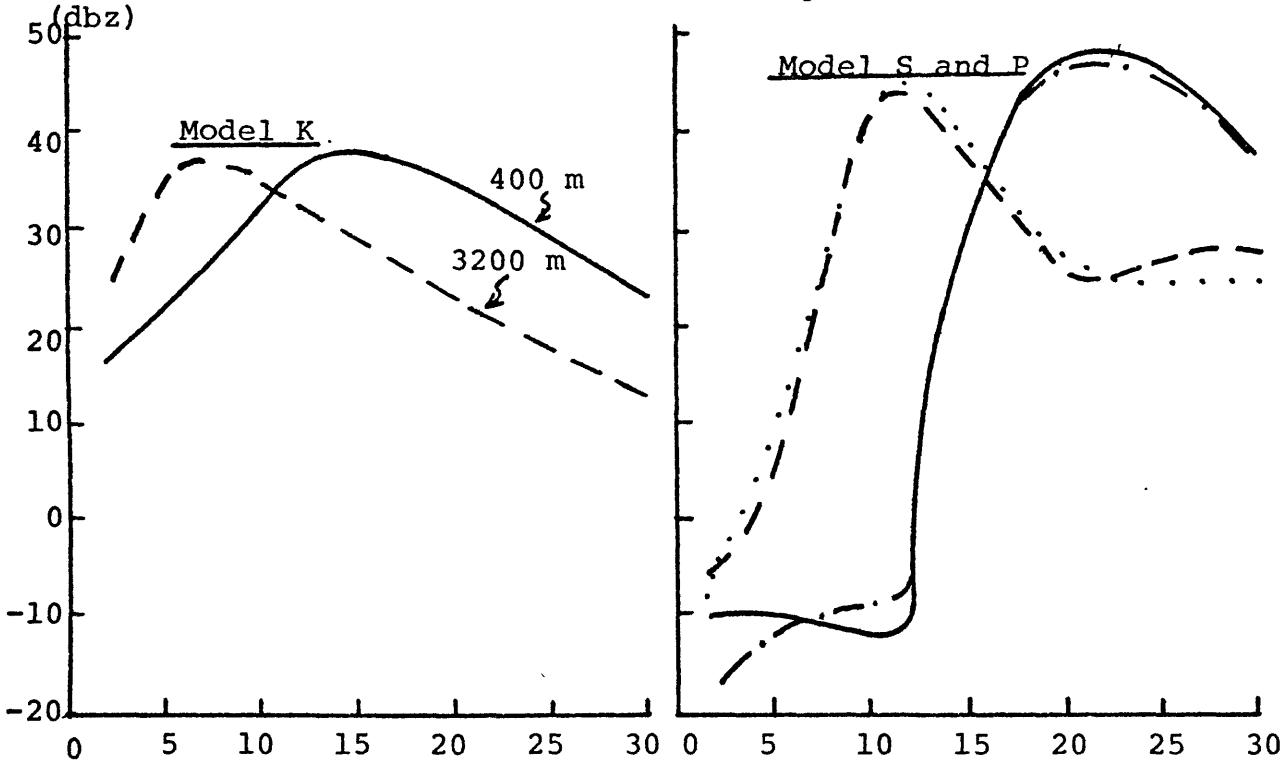


Fig. 2.7. Comparison of radar reflectivities at 400 m and 3200 m. model S, at 400 m ——, 3200 m — — — model P, 400 m — ·— ·—·, 3200 m .....

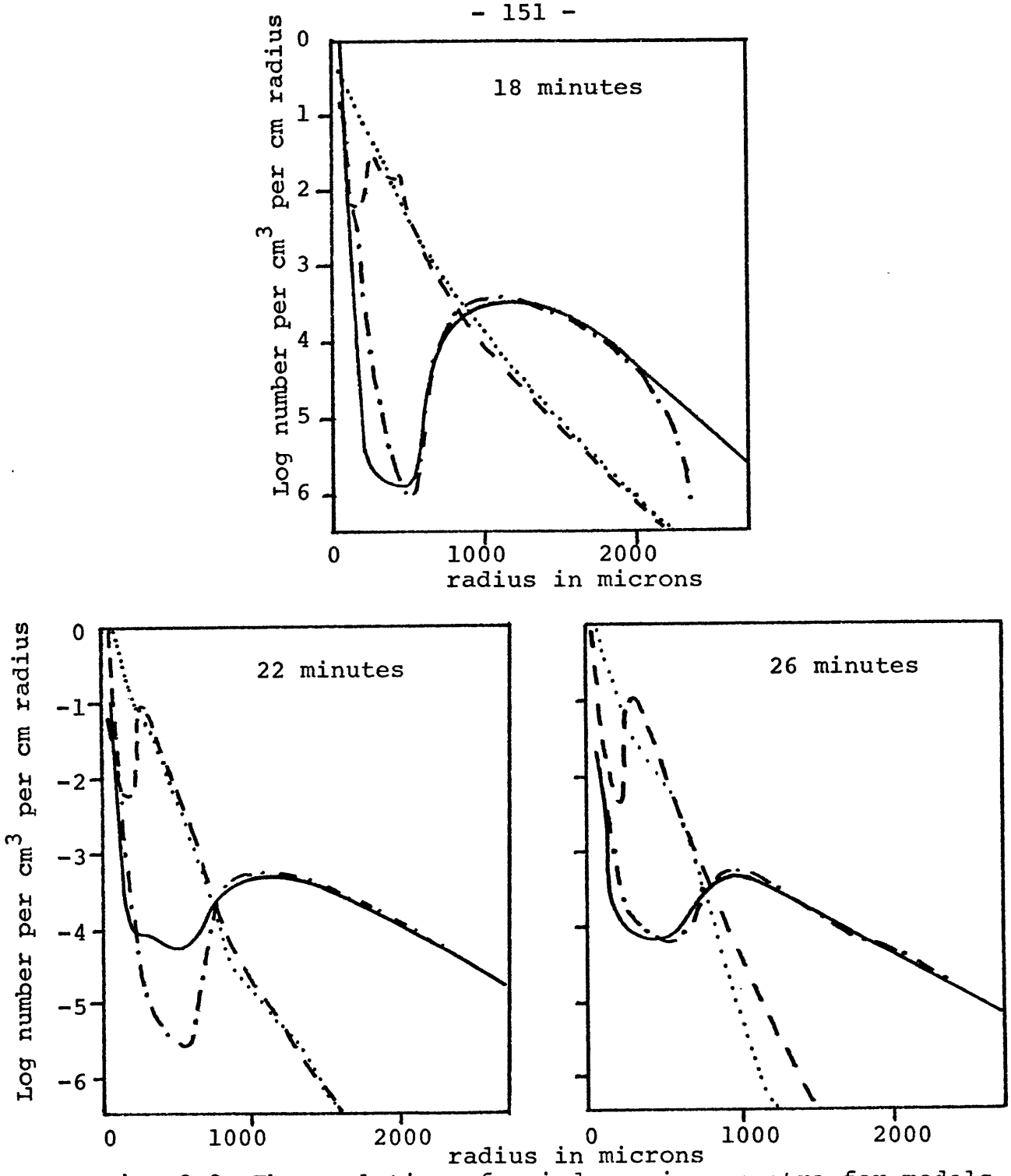


Fig. 2.8. The evolution of raindrop size spectra for models S and P at 18, 22, and 26 minutes.
Model S spectrum at 400 m ——, 3200 m _ _ _,
Model P spectrum at 400 m __.__.__., 3200 m .....

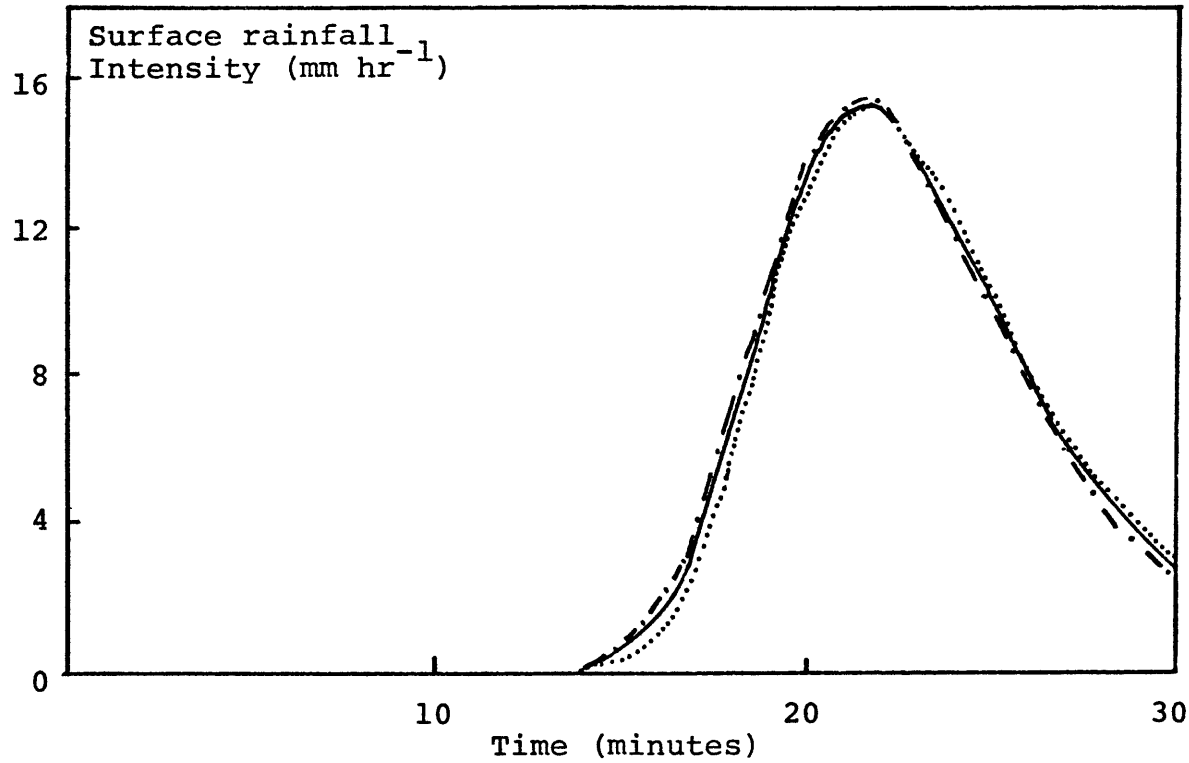


Fig. 2.9. Effect of varying autoconversion rate K_1 in Model P. $K=10^{-4}sec^{-1}$ ....., $K=10^{-2}$ sec^{-1} —.—., $K=10^{-3}$ sec^{-1} ————.

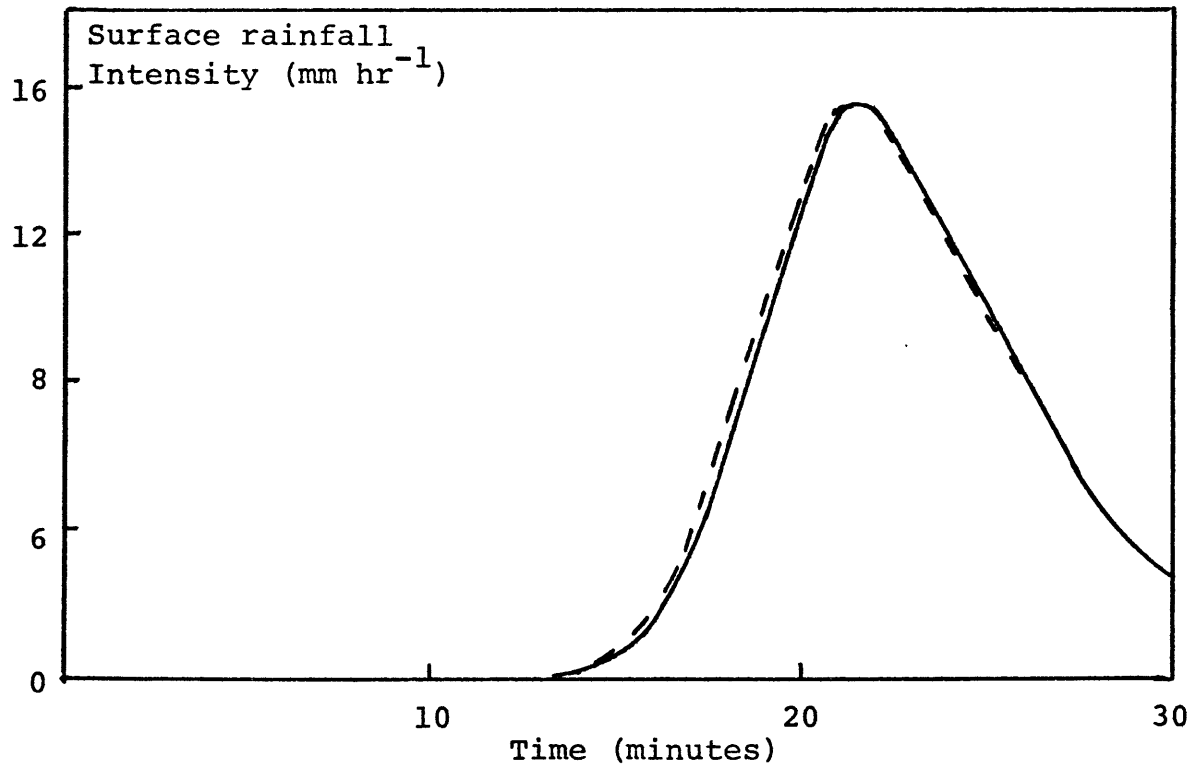


Fig. 2.10. Effect of varying autoconversion threshold a in Model P. a=0 g m^{-3} — — —, a=0.7 g m^{-3} ————.

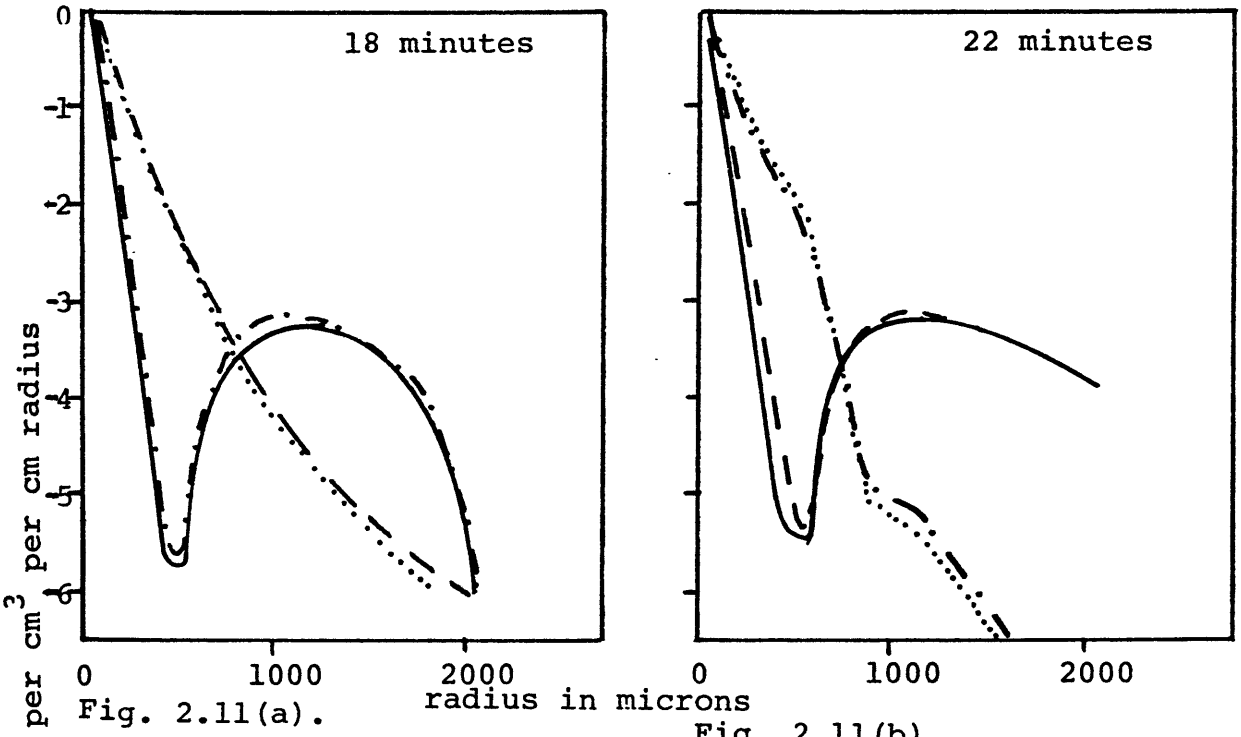


Fig. 2.11(a).

Fig. 2.11(b).

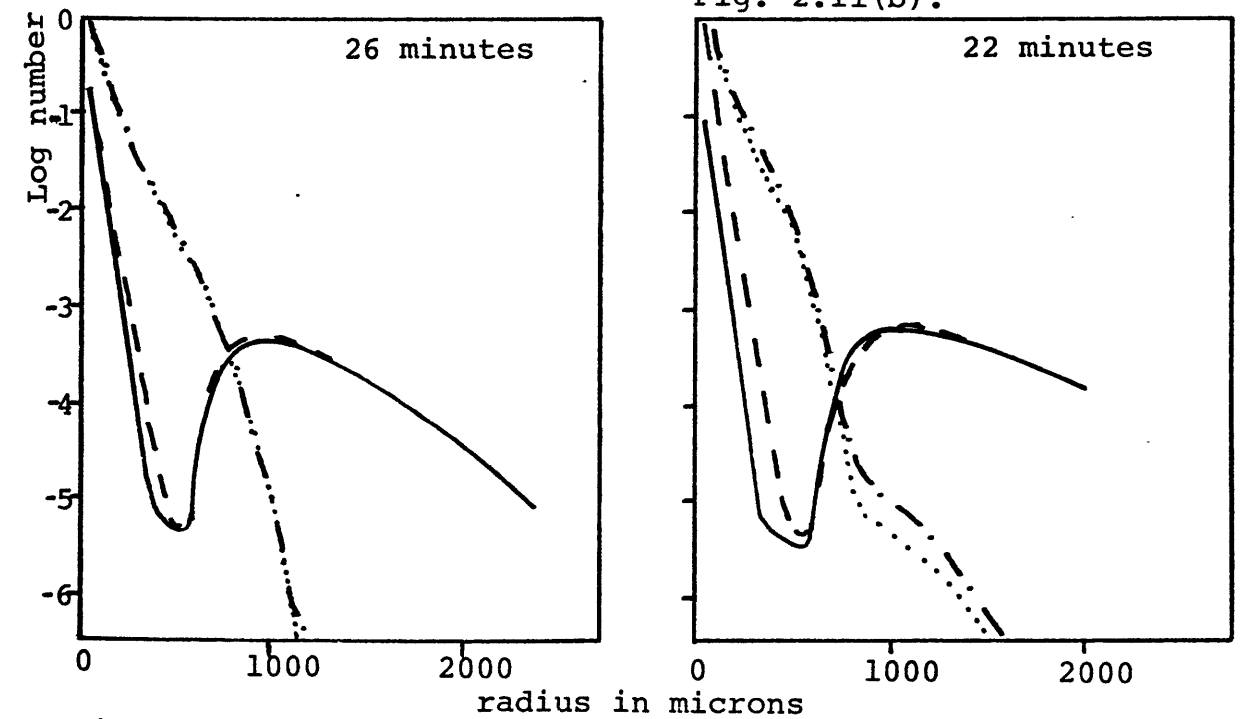


Fig. 2.11(c). Effect of varying K on rain dropsize spectra in Model P.
Spectrum at 400 m, $K=10^{-3}sec^{-1}$ ——
$K=10^{-2}sec^{-1}$ – – –
Spectrum at 3200 m,
$K=10^{-3}sec^{-1}$.—.—.
$K=10^{-2}sec^{-1}$ .....

Fig. 2.12. Effect of varying a on rain dropsize spectra in Model P.
Spectrum at 400 m,
$a=0.7$ g m^{-3} ——
$a=0$ g m^{-3} – – –
Spectrum at 3200 m,
$a=0.7$ g m^{-3} —.—.—.
$a=0$ g m^{-3} .....

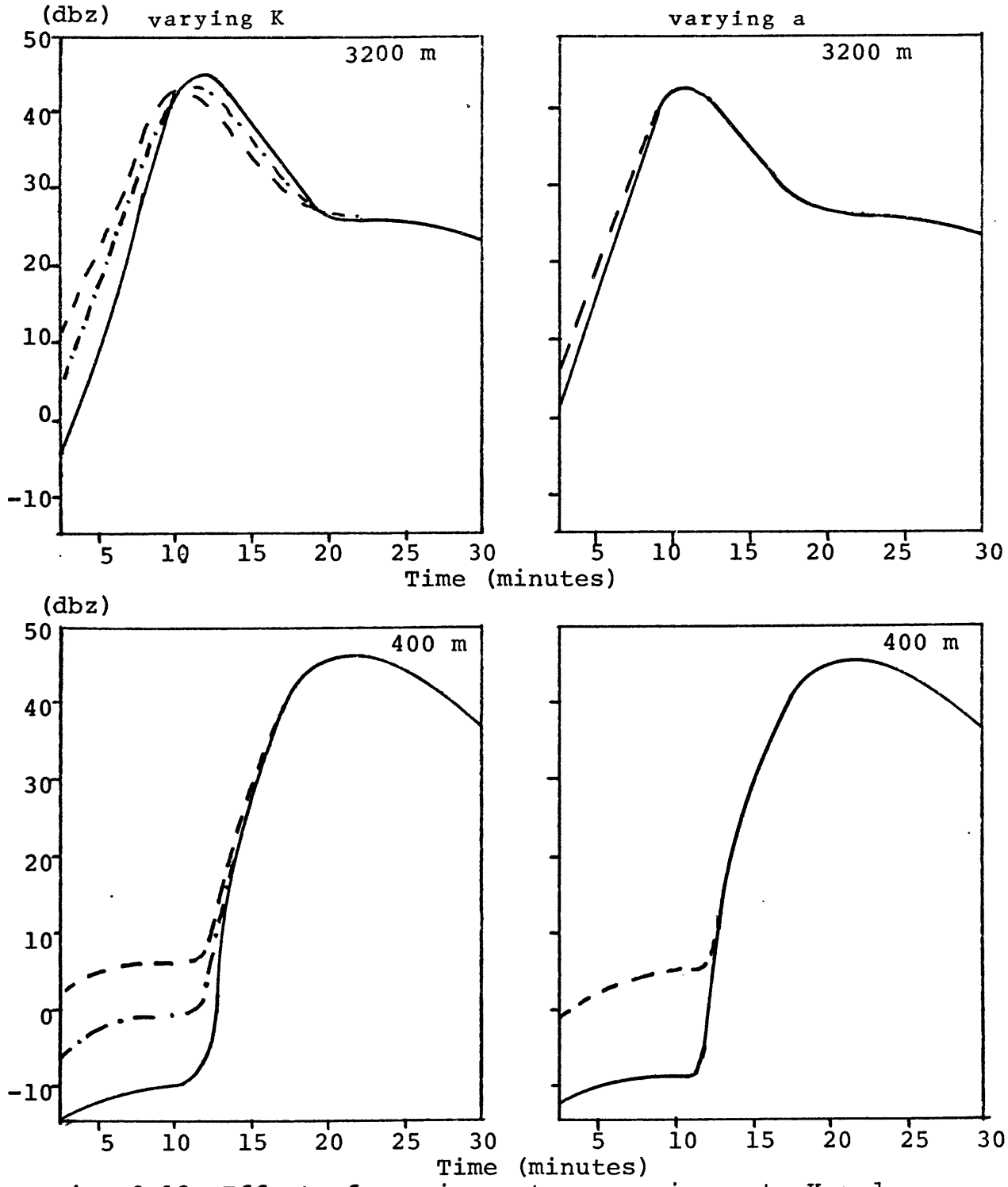


Fig. 2.13. Effect of varying autoconversion rate K and autoconversion threshold a on radar refectivity in Model P. $K=10^{-4}sec^{-1}$ ——, $K=10^{-3}sec^{-1}$ —.—.—, $K=10^{-2}sec^{-1}$ — — —. a=0 g m^{-3} — — —, a=0.7 g m^{-3} ——.

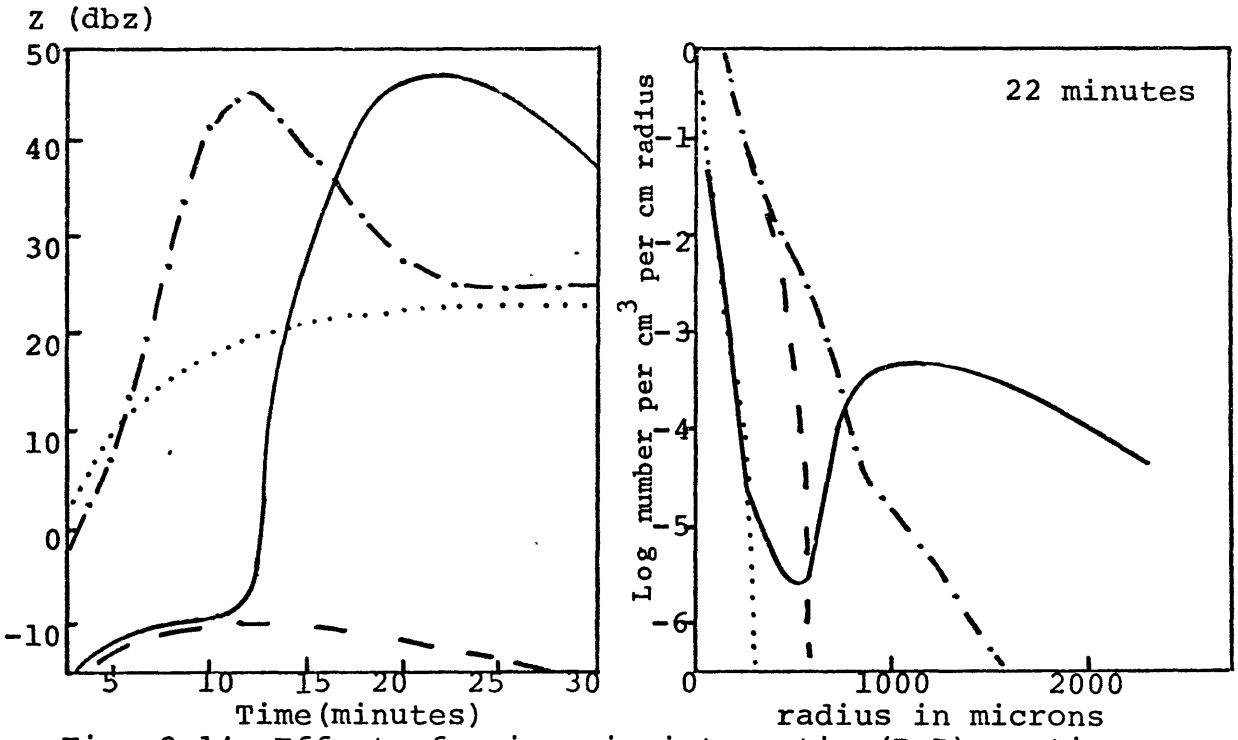


Fig. 2.14. Effect of rain-rain interaction(R-R) on time evolution of radar reflectivity factor (Z) and dropsize spectrum. Z at 400 m,with R-R———, no R-R—— ——.Z at 3200 m, with R-R-.-.-.-.,no R-R..... Dropsize spectrum at 400 m, with R-R———, no R-R.....;at 3200m,with R-R-.-.-,no R-R—— ——.

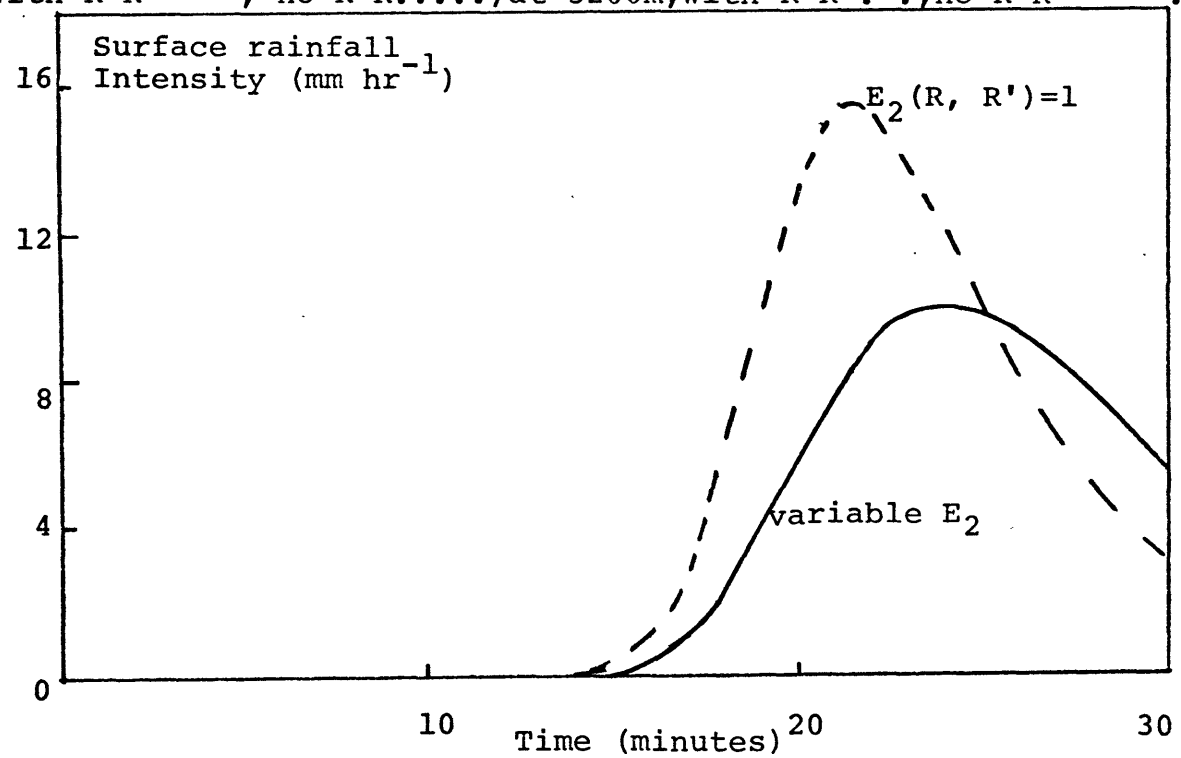


Fig. 2.15. Effect of variable coalescence efficiency on rainfall intensity. The case with satellite drops and variable coalesence efficiency shows no difference from the solid curve.

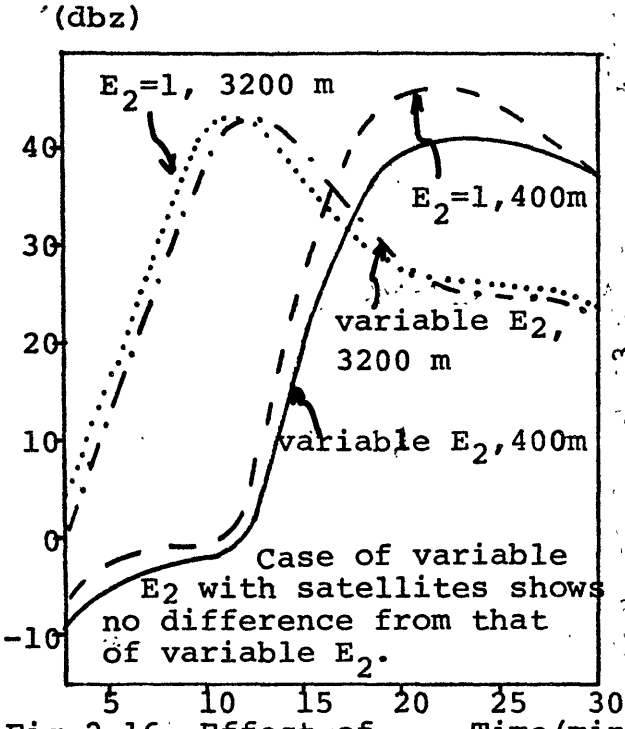


Fig.2.16. Effect of variable E_2 and satellites on radar reflectivity profile(Z).

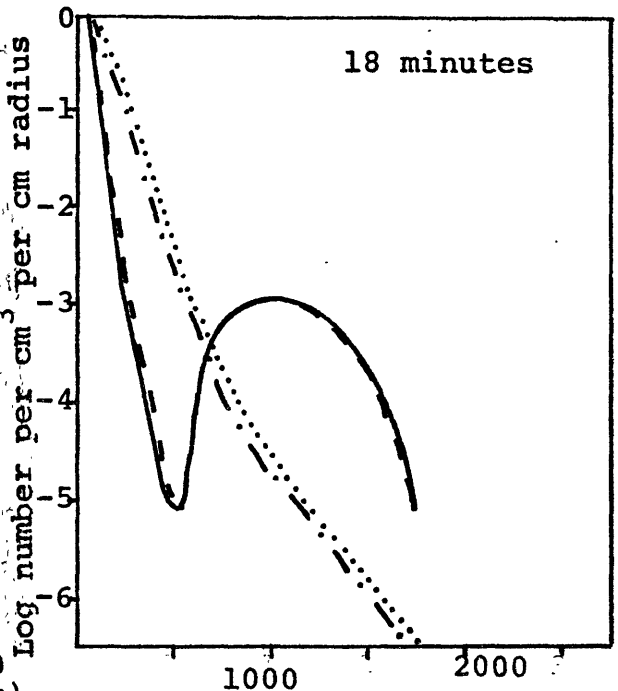


Fig. 2.17(a)

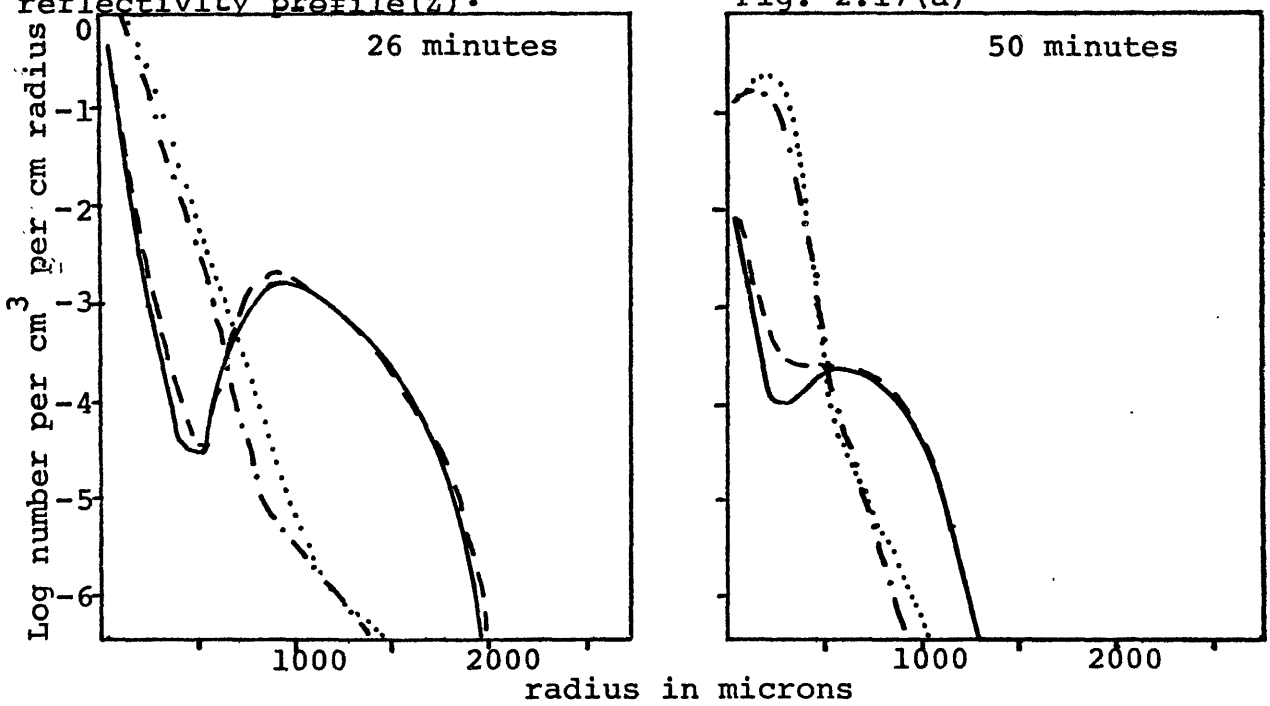


Fig. 2.17(b). Effect of variable coalescence efficiency and satellites on dropsize spectra. Spectrum at 400 m for variable E_2 without satellites————, with satellites— — —. Spectrum at 3200 m for variable E_2 without satellites-.-.-., with satellites.....

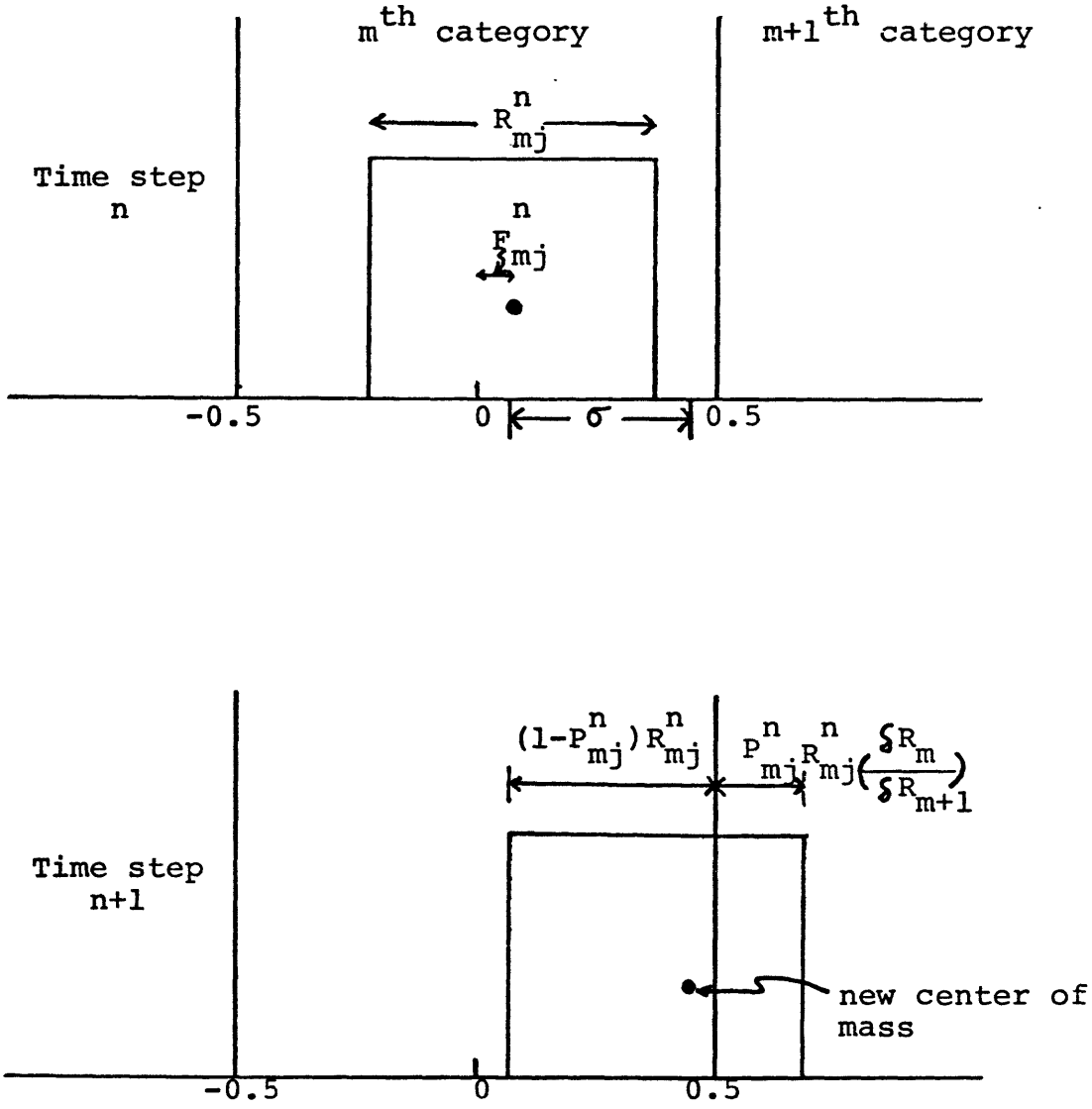


Fig. A1. Transfer of hydrometeor water between categories.

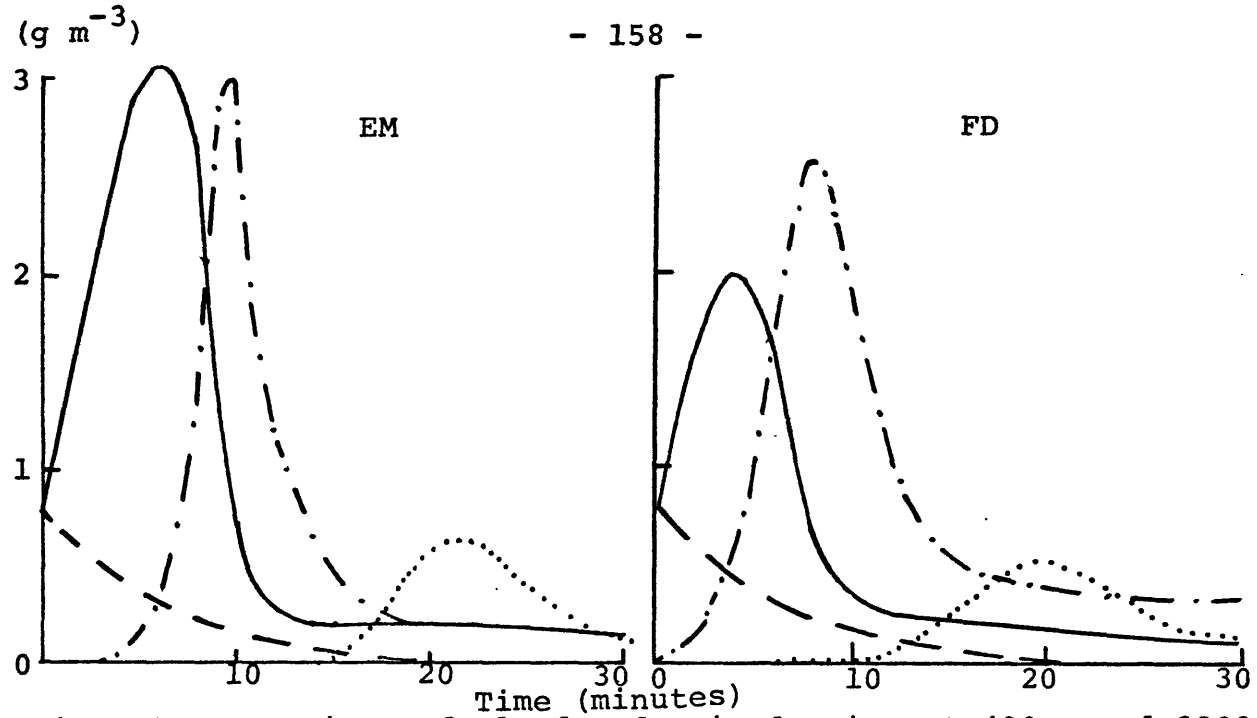


Fig. A2. Comparison of cloud and rain density at 400 m and 3200 m computed by the EM and FD methods. Cloud density at 400 m – – –, at 3200 m ———. Rain density at 400 m ...., at 3200 m —.—.—.

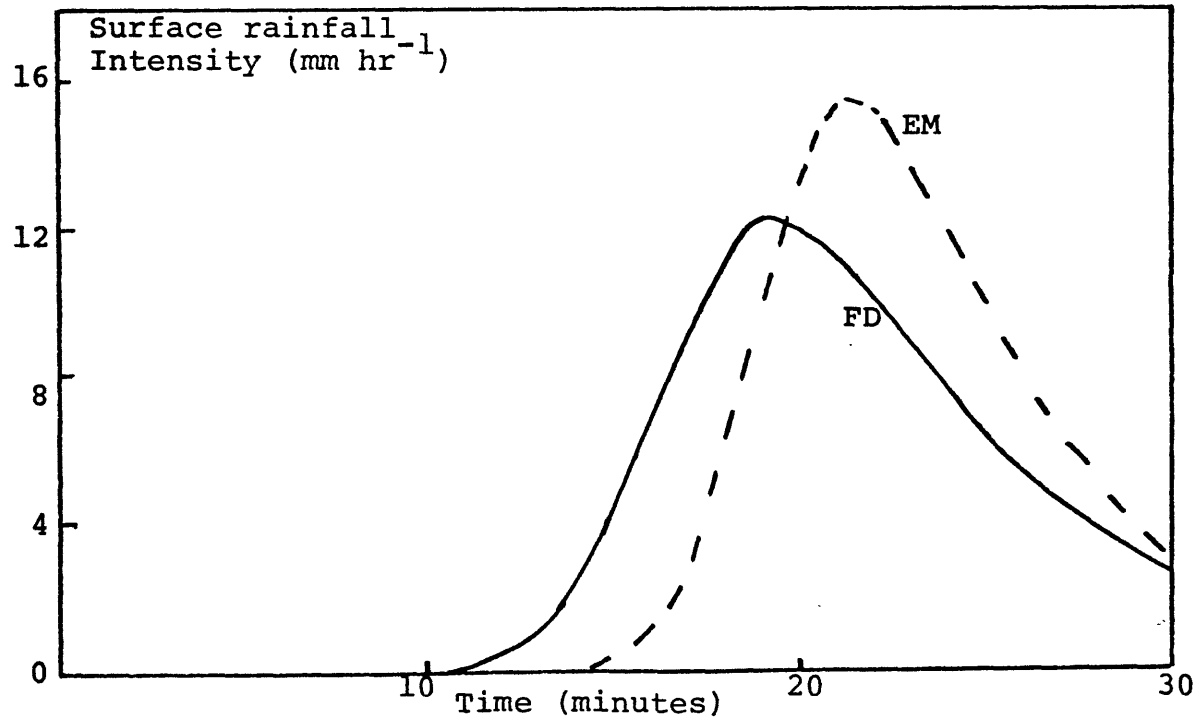


Fig. A3. Comparison of surface rainfall intensity computed by FD and EM methods

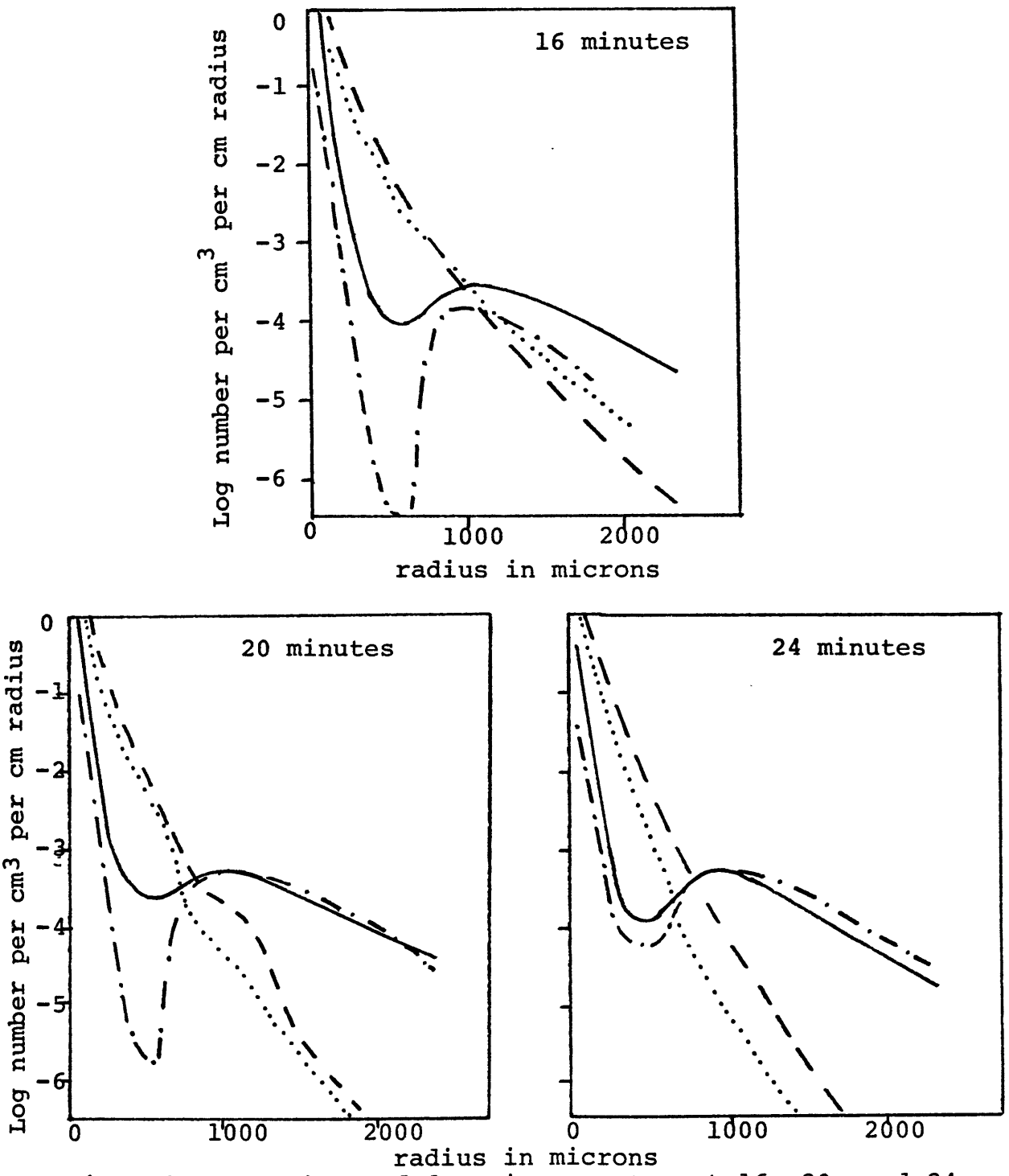


Fig. A4. Comparison of dropsize spectra at 16, 20, and 24 minutes computed by FD and EM methods. Spectrum at 400 m by FD ——, by EM —.—.—. Spectrum at 3200 m by FD — — —, by EM .....

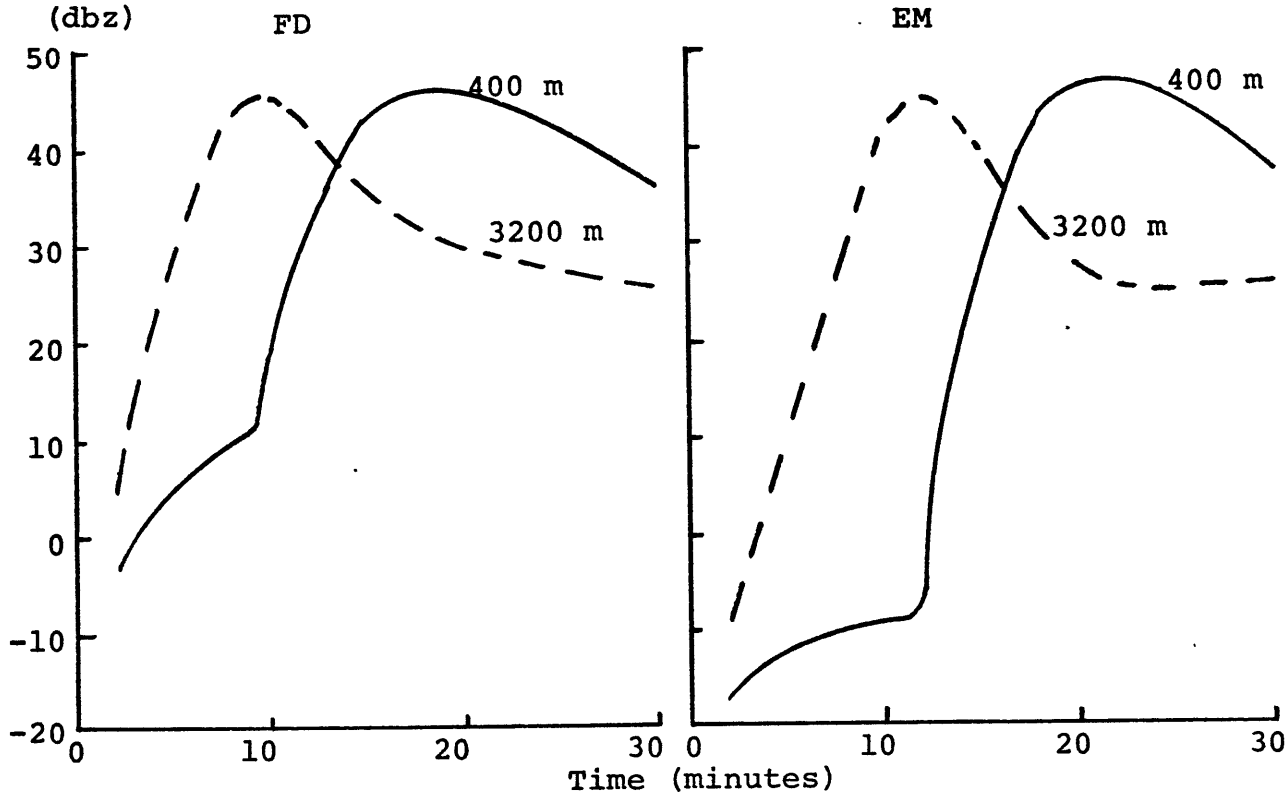


Fig. A5. Comparison of radar reflectivity factor computed by FD and EM methods.

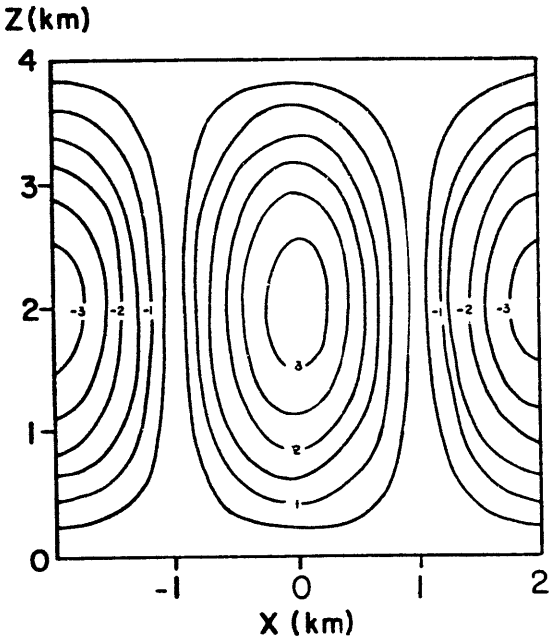


Fig. 3.1. Vertical section of buoyancy forcing. The contour interval is 0.5 cm sec^{-2}. H=4 km, L_1=1 km.

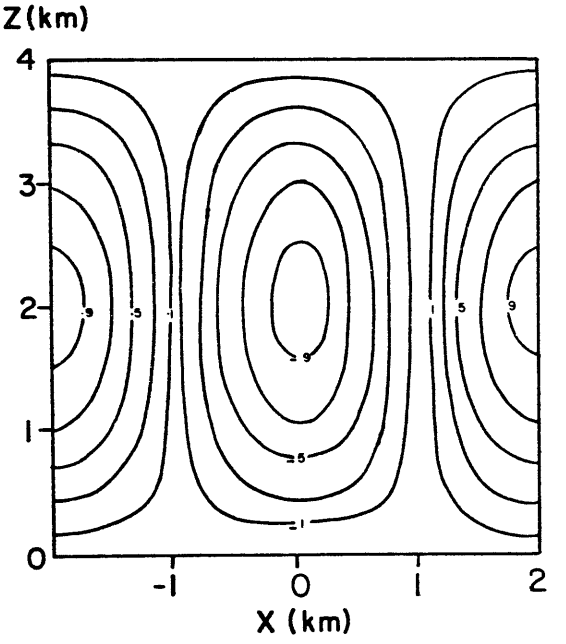


Fig. 3.2. Same as Fig. 3.1 except for drag forcing Q_1. The contour interval is 0.3 m sec^{-2}.

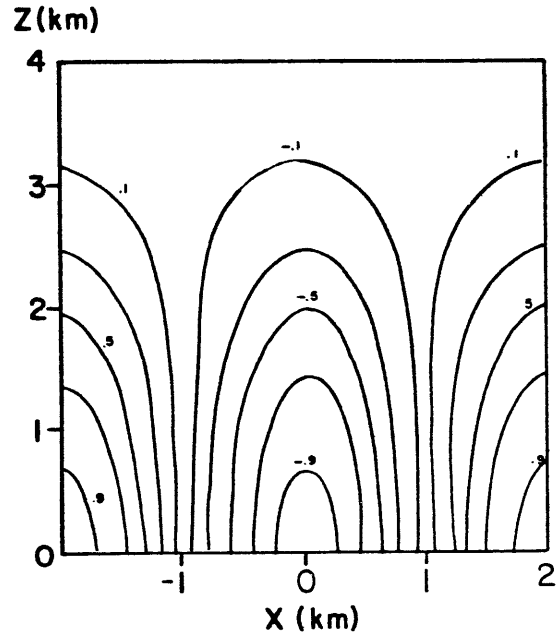


Fig. 3.3. Same as Fig. 3.1 except for drag forcing Q_2. The contour interval is 0.3 m sec^{-2}.

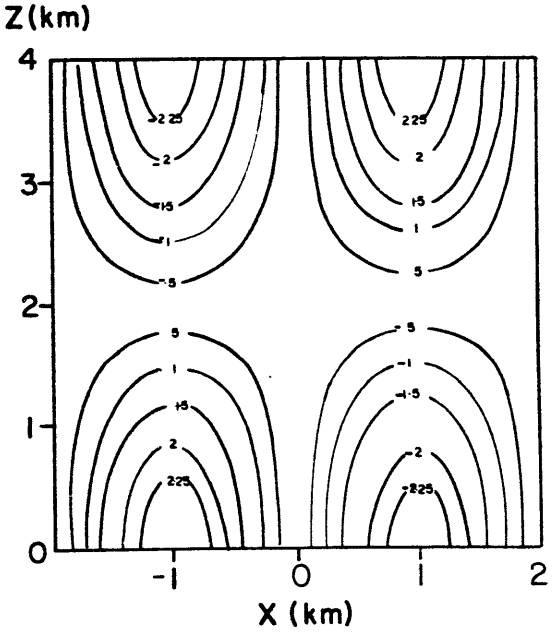


Fig. 3.4. Vertical section of horizontal velocity u . H=4 km, L_1=1 km. The contours are in $m\ sec^{-1}$.

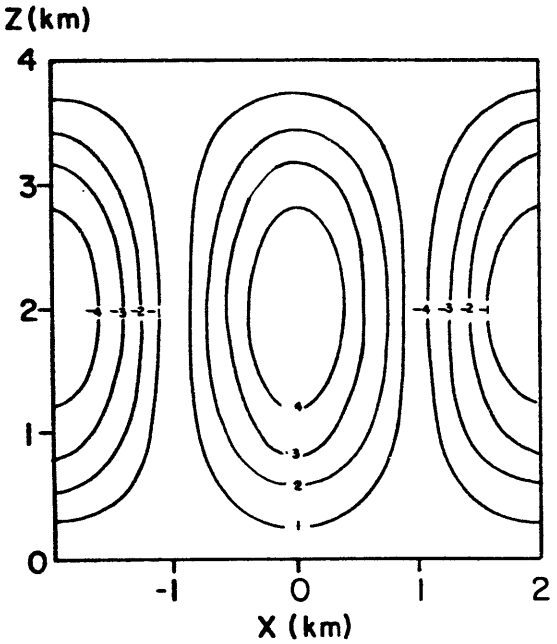


Fig. 3.5.Vertical section of vertical velocity w. H=4 km, L_1=1 km.The contour interval is 1 m sec^{-1}.

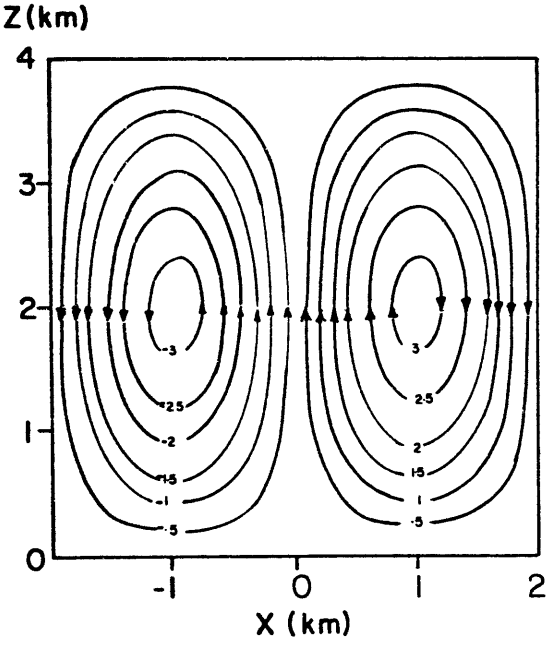


Fig. 3.6. Streamfunction in arbitrary units. H=4 km, L_1=1 km.

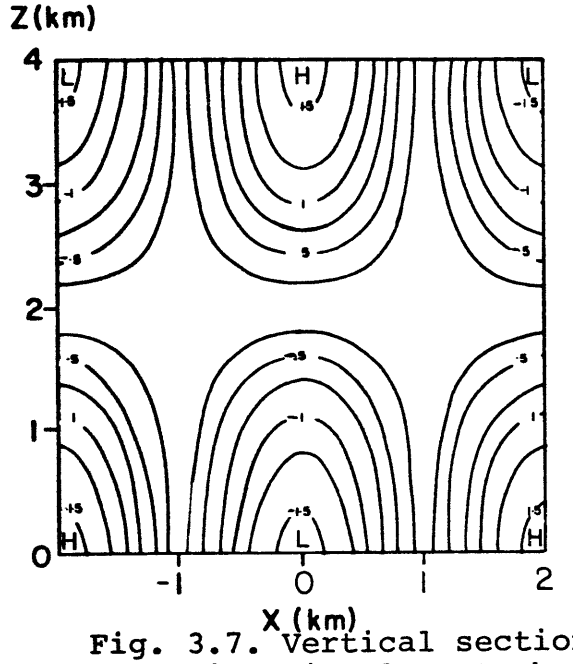


Fig. 3.7. Vertical section of non-dimensional perturbation pressure induced by buoyancy forcing. The contour interval is $0.5xi0^{-5}$.H= 4 km, L_1=1 km.

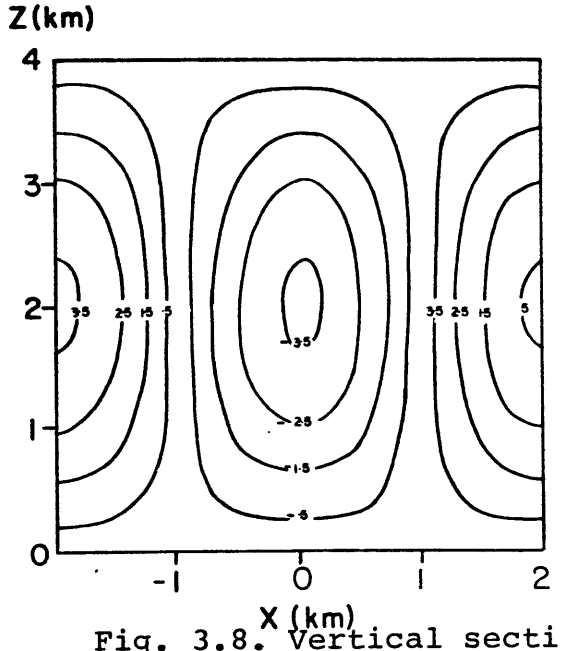


Fig. 3.8. Vertical section of vertical pressure gradient force induced by buoyancy forcing. The contour interval is 0.1cm sec^{-2}. H=4 km, L_1=1 km.

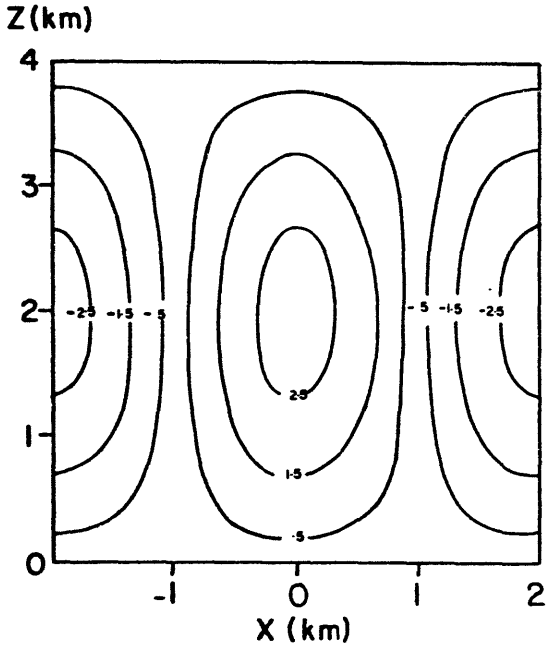


Fig. 3.9. Vertical section of net vertical acceleration $g(\theta'/\theta_o)-C_p\theta_o(\partial\pi'/\partial z)$. The contour interval is 1cm sec^{-2}.

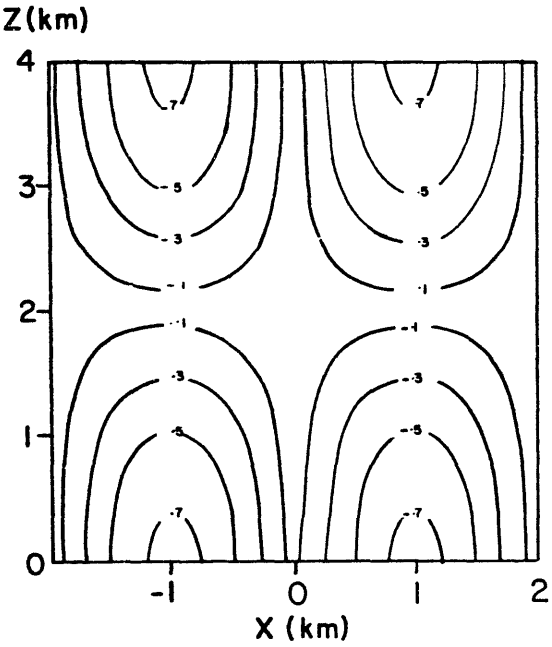


Fig. 3.10. Vertical section of horizontal pressure force induced by buoyancy forcing in cm sec^{-2}.

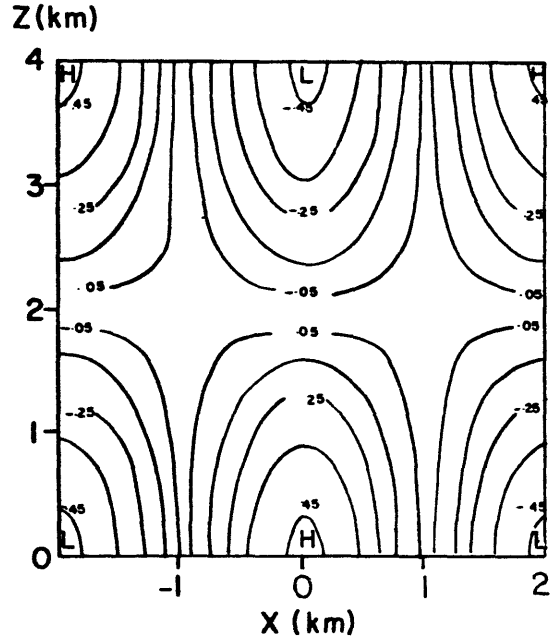


Fig. 3.11. Vertical section of non-dimensional perturbation pressure induced by drag forcing Q_1. The contour interval is 0.1×10^{-5}.

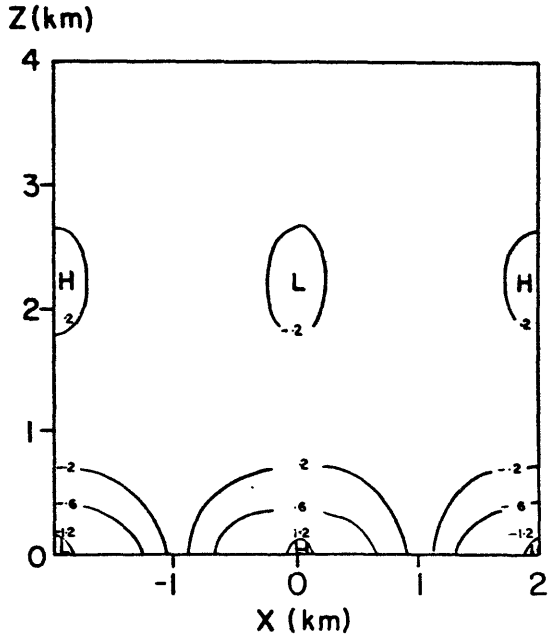


Fig. 3.12. Same as Fig. 3.11 except for drag forcing Q_2. The contours are in unit of 10^{-5}.

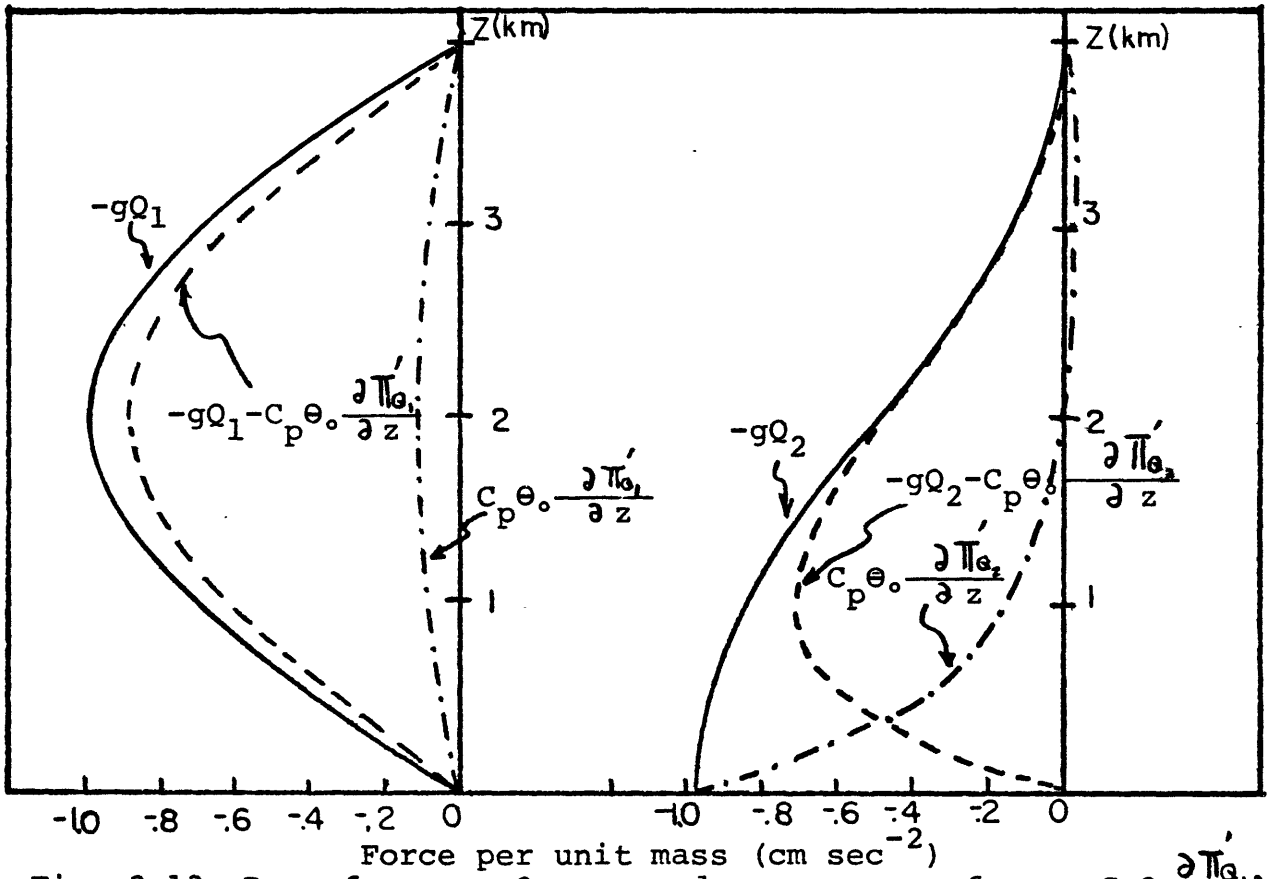


Fig. 3.13. Drag forces $-gQ_{1,2}$, drag pressure forces $C_p\theta_o\frac{\partial \pi'_{\theta_{1,2}}}{\partial z}$ and $-gQ_{1,2}-C_p\theta_o\frac{\partial \pi'_{\theta_{1,2}}}{\partial z}$ at the central axis.

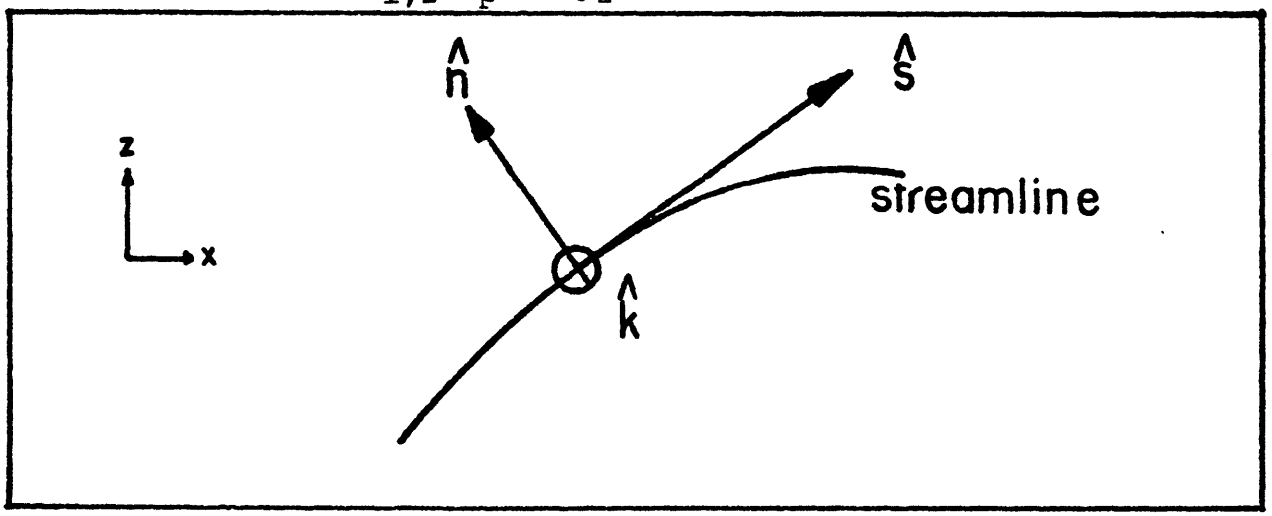


Fig. 3.14. The natural coordinate system. $\hat{s}$ is the unit vector along the direction of the flow. $\hat{n}$ is the unit vector normal to the direction of the flow in the X-Z plane. $\hat{k}$ is the unit vector in the direction perpendicular to $\hat{s}$ and $\hat{n}$ (i.e. out of the plane of the figure)

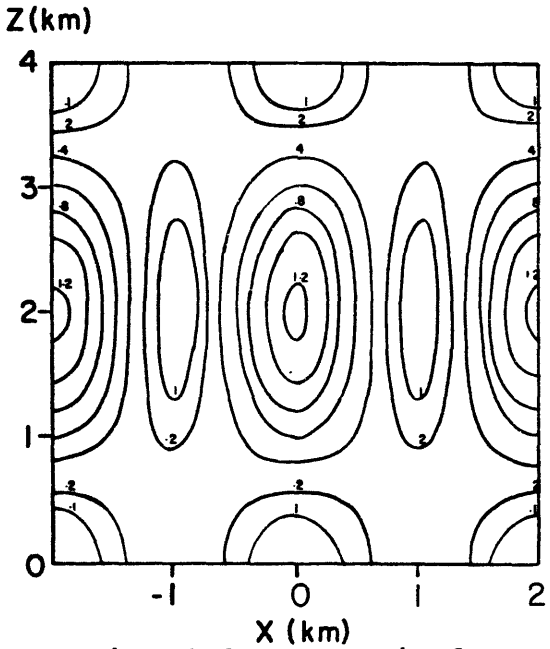


Fig. 3.15. Vertical section of kinetic energy per unit mass in units of 10^5 cm^2 sec^{-2}. H=4 km, L_1=1 km.

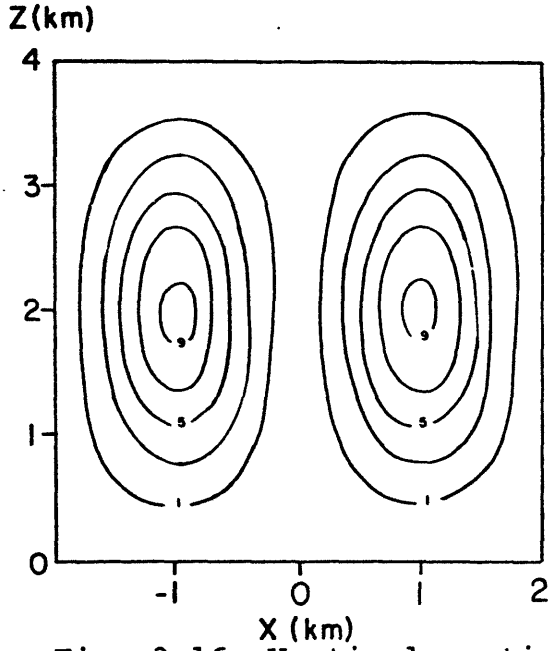


Fig. 3.16. Vertical section of squared vorticity in units of 10^{-5} sec^{-2}. H=4km, L_1=1 km.

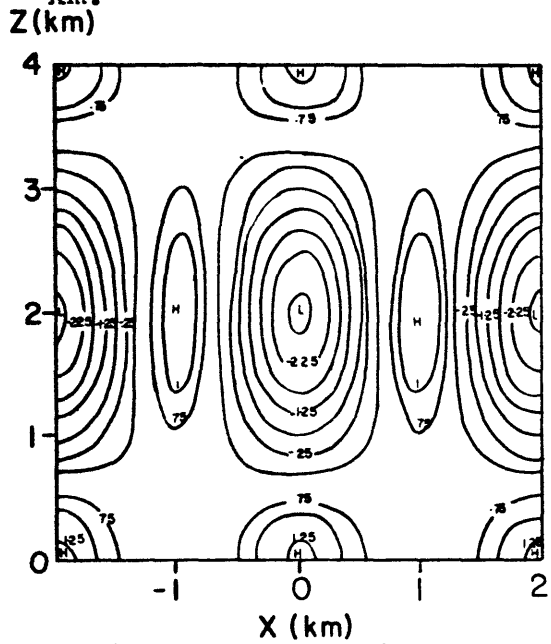


Fig. 3.17. Vertical section of non-dimensional perturbation pressure induced by kinetic energy forcing. The contours are in units of 10^{-5}.

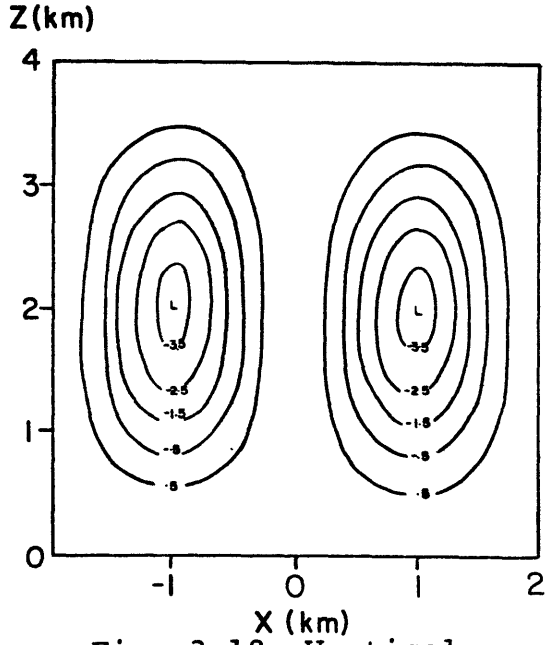


Fig. 3.18. Vertical section of non-dimensional pressure induced by vorticity forcing. The contours are in units of 10^{-5}.

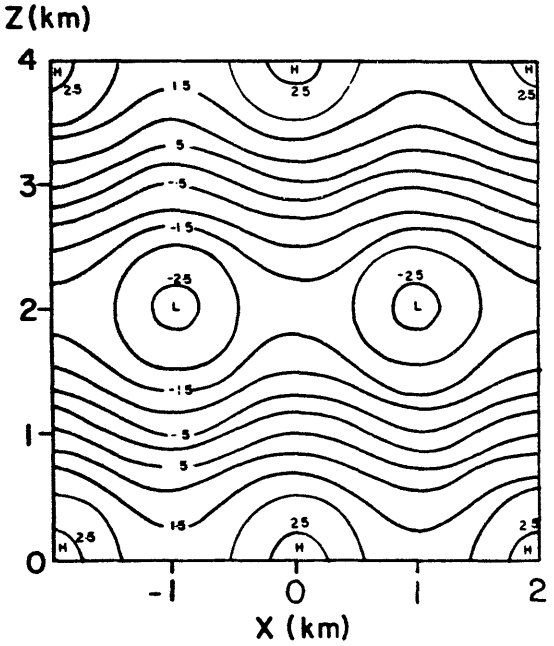


Fig. 3.19. Vertical section of dynamic perturbation pressure. The contours are in units of 10^{-5}.

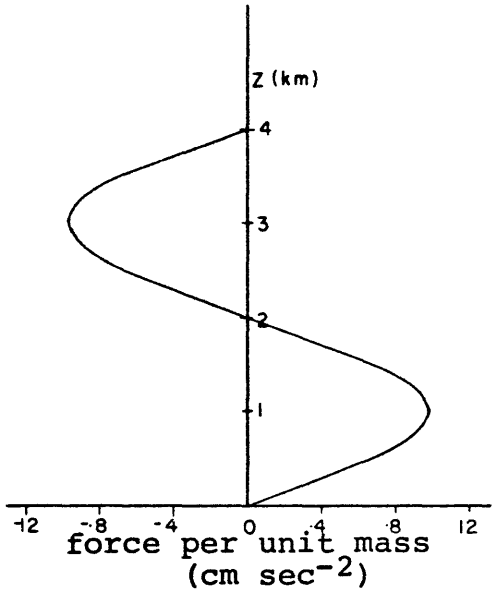


Fig. 3.20. Vertical perturbation pressure force induced by dynamic forcing at the central axis.

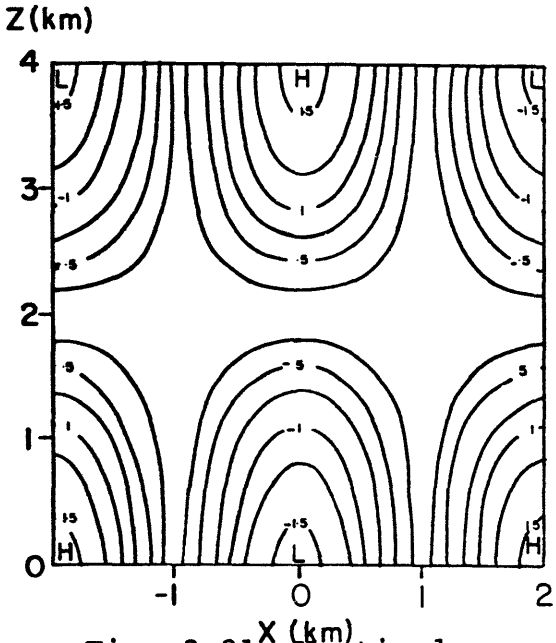


Fig. 3.21. Vertical section of non-dimensional buoyancy perturbation pressure for $S_z=2\times10^{-5}m^{-1}$. The contours are in units of 10^{-5}. H=4 km, L_1=1 km.

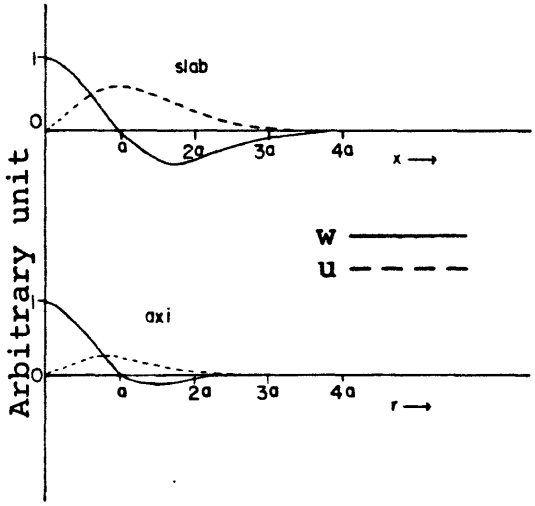


Fig. 3.22. Comparison of horizontal profiles for u and w in the case of axi- and slab-geometry. a is the radius of the updraft.

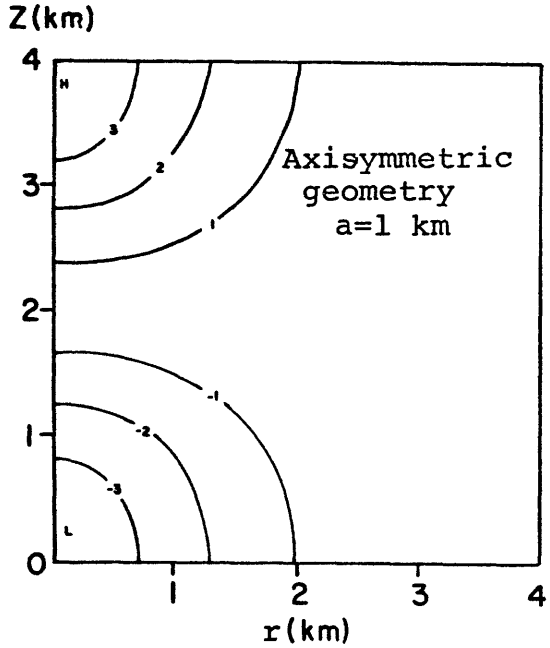


Fig. 3.23. Vertical section of non-dimensional perturbation pressure induced by buoyancy forcing. The contours are in units of 10^{-5}.

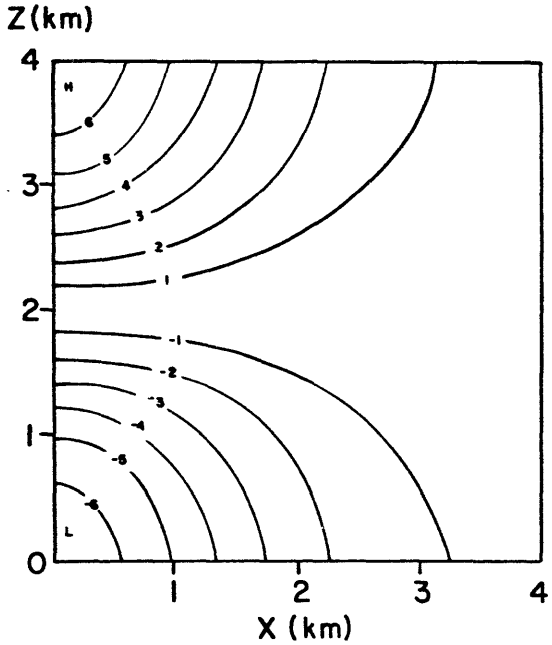


Fig. 3.24. Same as Fig. 3.23 except for slab-symmetric geometry.

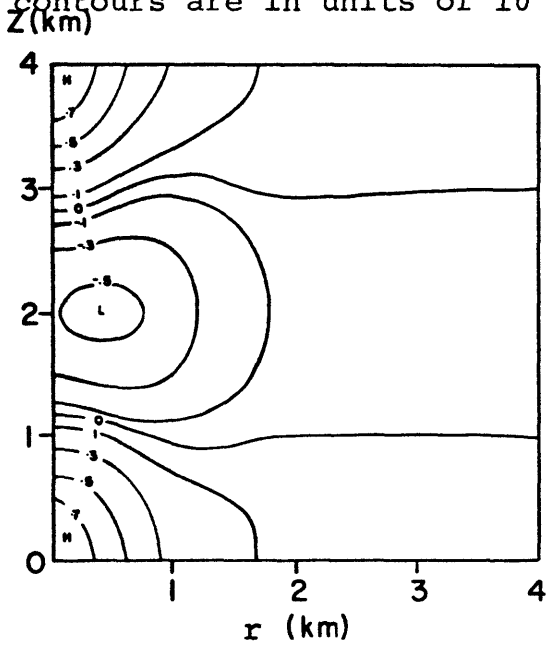


Fig. 3.25. Vertical section of non-dimensional perturbation pressure induced by dynamic forcing for axi-symmetric geometry. The contours are in units of 10^{-5}. Cloud radius a=1 km.

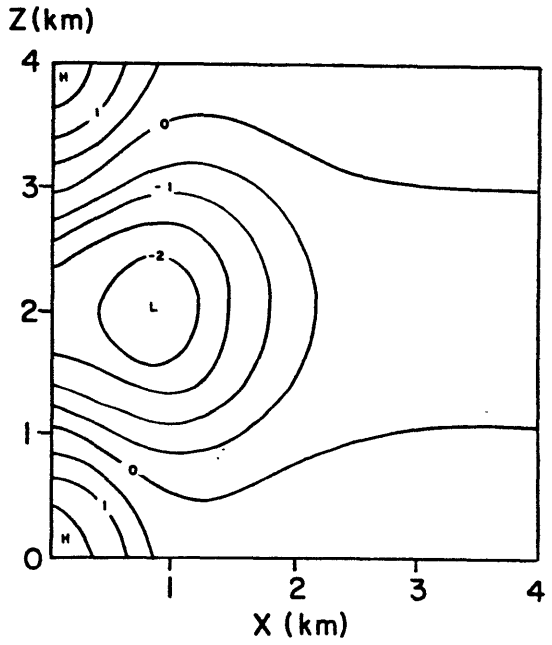


Fig. 3.26. Same as Fig. 3.25 except for slab-symmetric geometry.

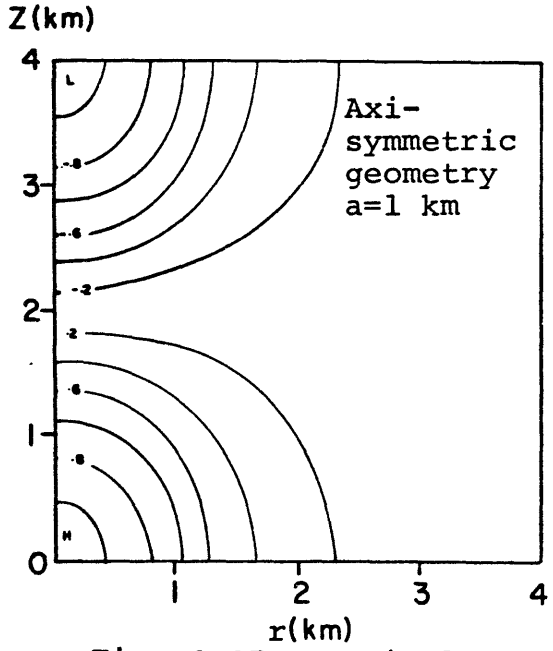


Fig. 3.27. Vertical section of non-dimensional pressure induced by drag forcing. The contours are in units of 10^{-5}.

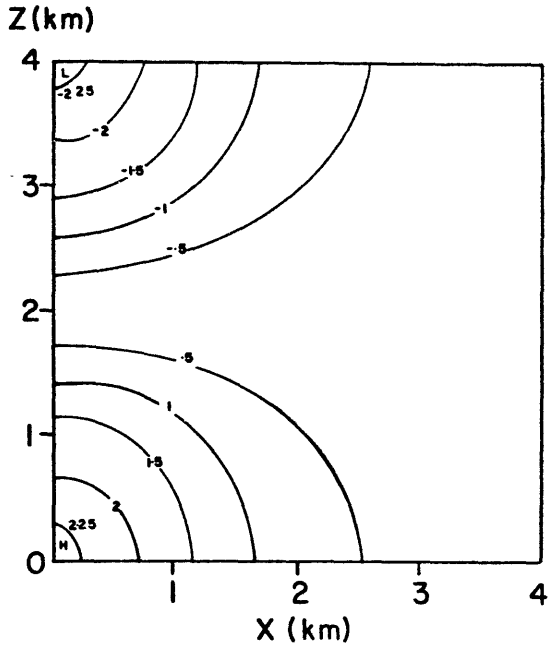


Fig. 3.28. Same as Fig. 3.27 except for slab-symmetric geometry.

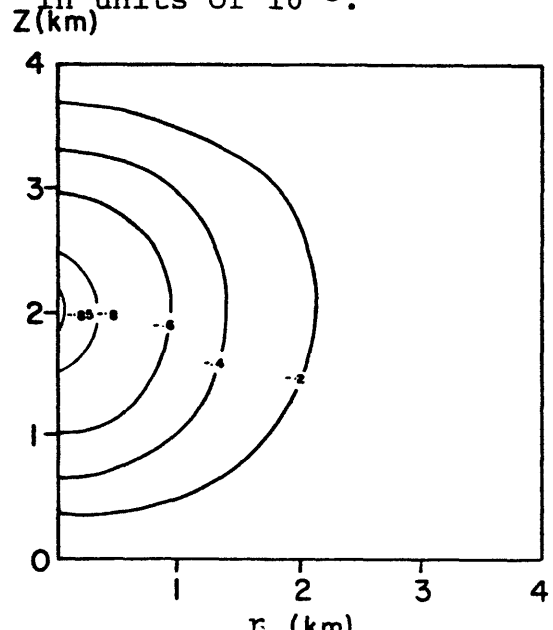


Fig. 3.29. Vertical section of vertical buoyancy perturbation pressure gradient force for axi-symmetry geometry. The contours are in units of cm sec^{-2}. Cloud radius =1 km.

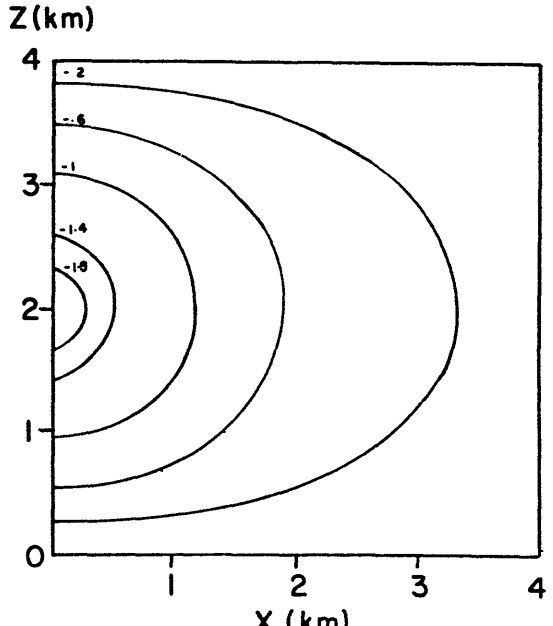


Fig. 3.30. Vertical section of vertical buoyancy perturbation pressure gradient force for slab-symmetric geometry. The contours are in units of cm sec^{-2}. Cloud radius =1 km.

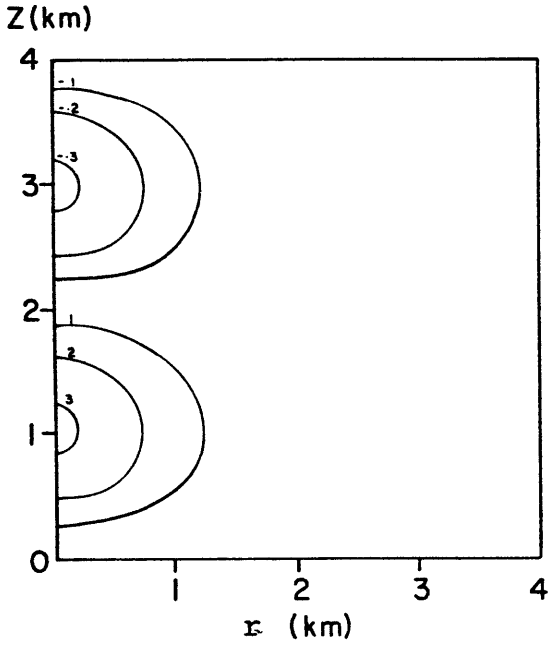


Fig. 3.31. Same as Fig. 3.29 except for vertical dynamic perturbation pressure gradient force.

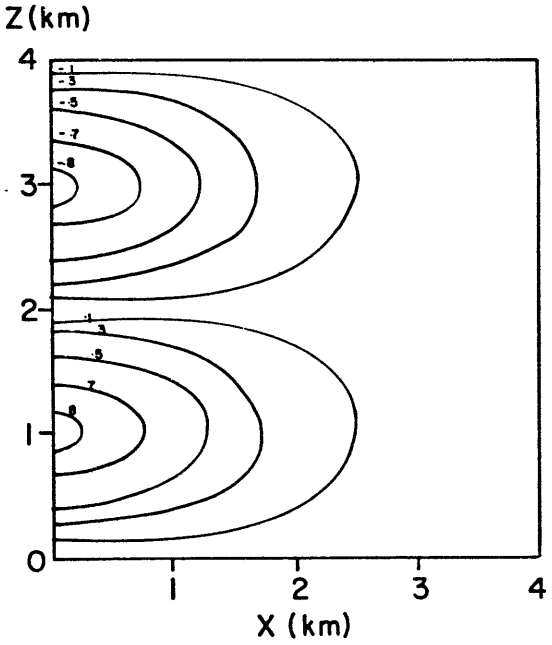


Fig. 3.32. Same as Fig. 3.30 except for vertical dynamic perturbation pressure gradient force.

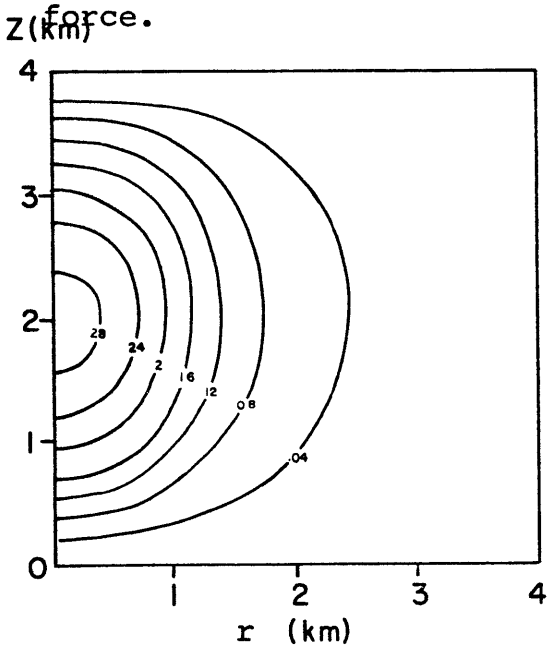


Fig. 3.33. Same as Fig. 3.29 except for vertical drag perturbation pressure gradient force.

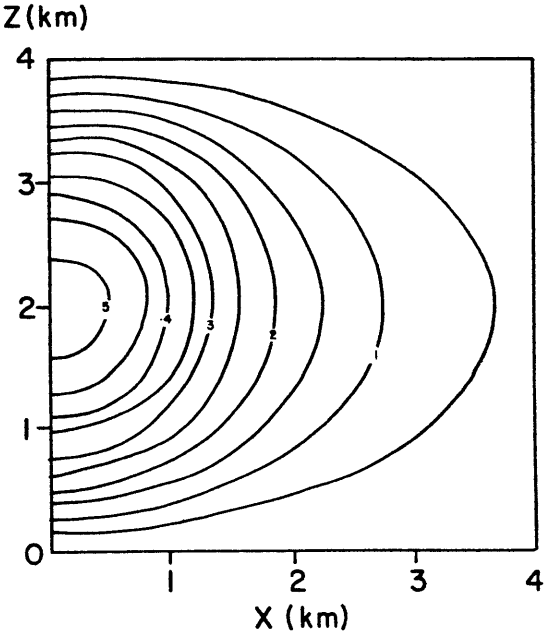


Fig. 3.34. Same as Fig. 3.30 except for vertical drag perturbation pressure gradient force.

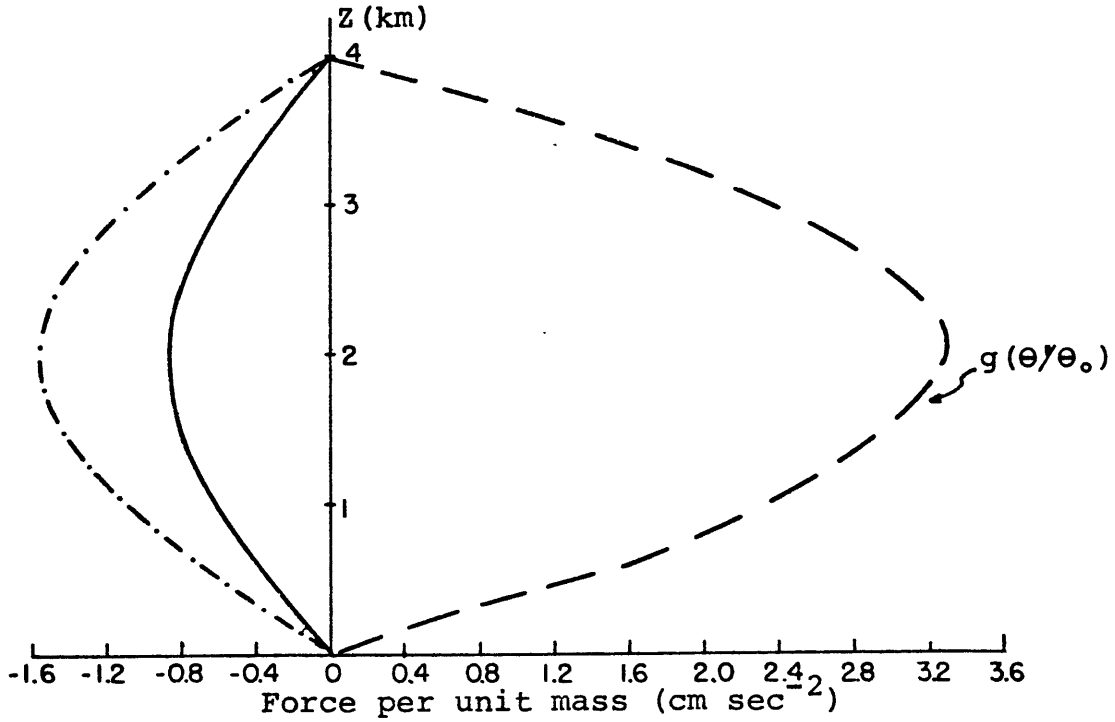


Fig. 3.35. Buoyancy and buoyancy pressure force at the central axis.
Buoyancy— — —, buoyancy pressure force ————(axi),-.-.-.-.-.-.(slab).

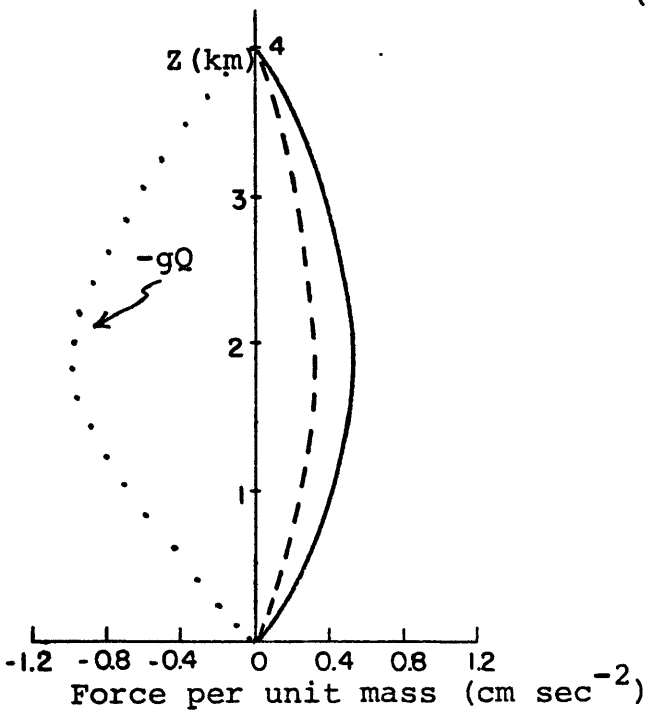


Fig. 3.36. Drag and drag pressure force at the central axis. Drag ...., drag pressure force— — — (axi),————(slab).

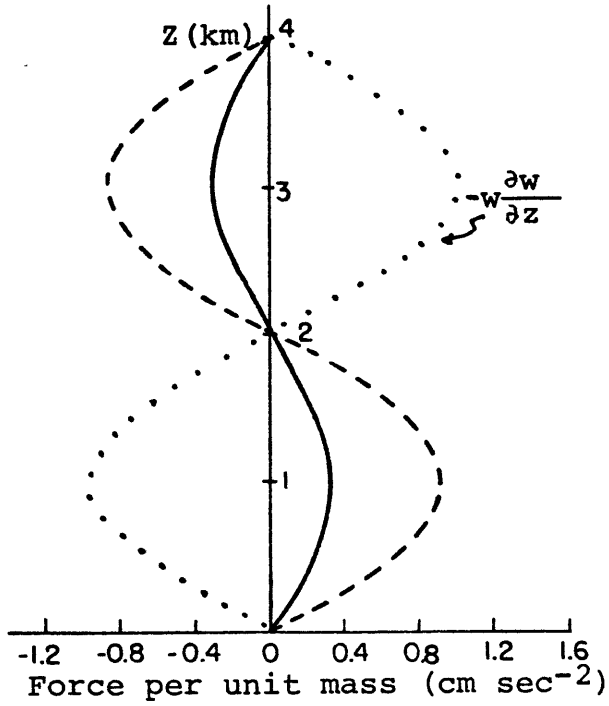


Fig. 3.37. Vertical advection and dynamic pressure force at the central axis. Dynamic pressure force——(axi), — — —(slab).

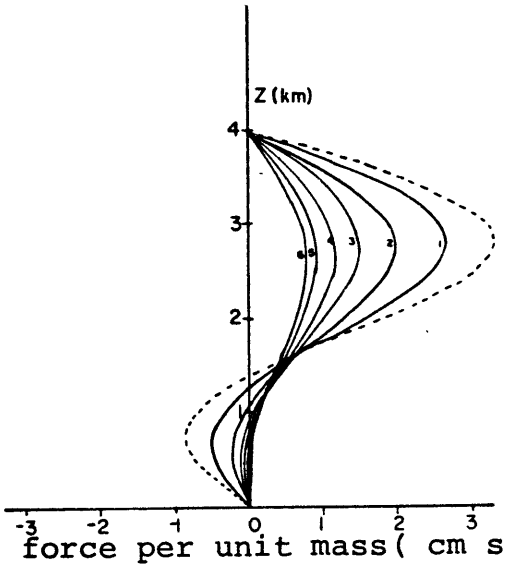


Fig. 3.38. Effect of perturbation pressure force on negative buoyancy. Buoyancy $g\theta'/\theta_o$ — — —. $g\theta'/\theta_o - C_p\theta_o\frac{\partial \pi'}{\partial z}$: curves 1-6 are for a cloud radius of 0.5,1, 1.5,2,2.5,and 3 km respectively.

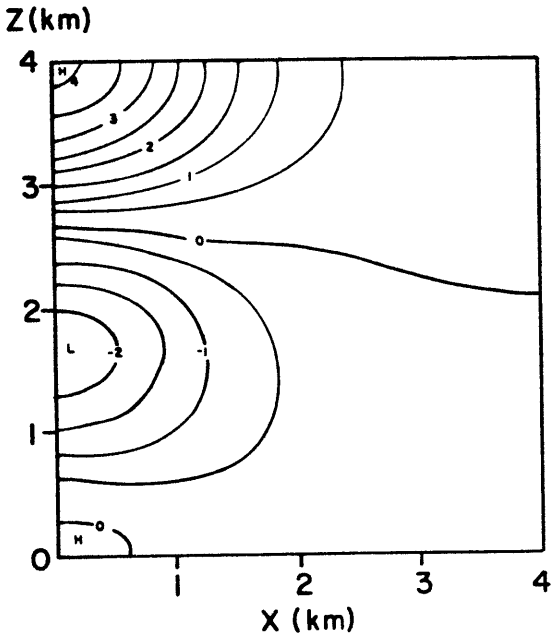


Fig. 3.39. Vertical section of non-dimensional perturbation pressure induced by buoyancy forcing in eq.(3.49). The contours are in units of 10^{-5}.

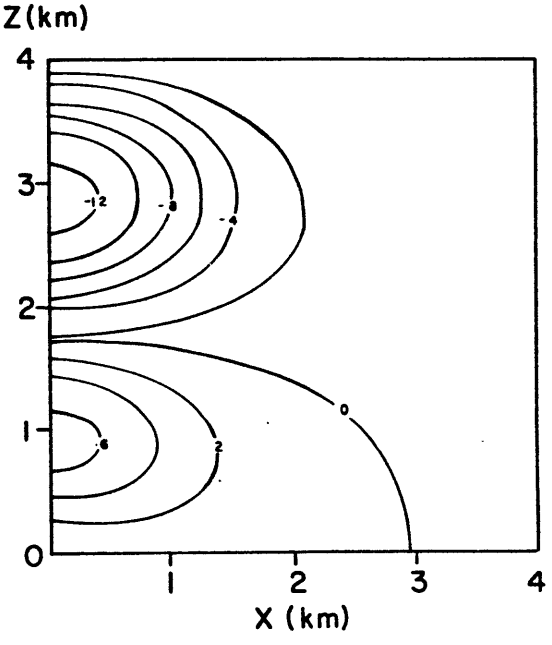


Fig. 3.40. Vertical section of vertical pressure gradient force induced by forcing in eq.(3.49) in cm sec^{-2}.

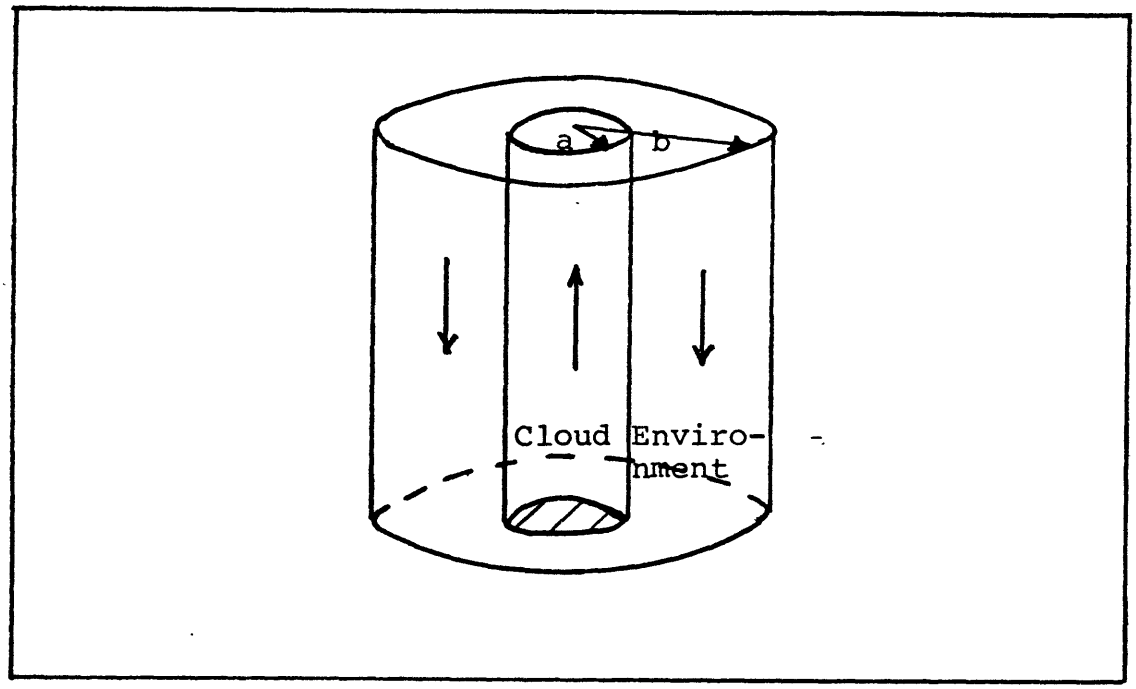


Fig. 4.1. Basic configuration of the two-cylinder model.

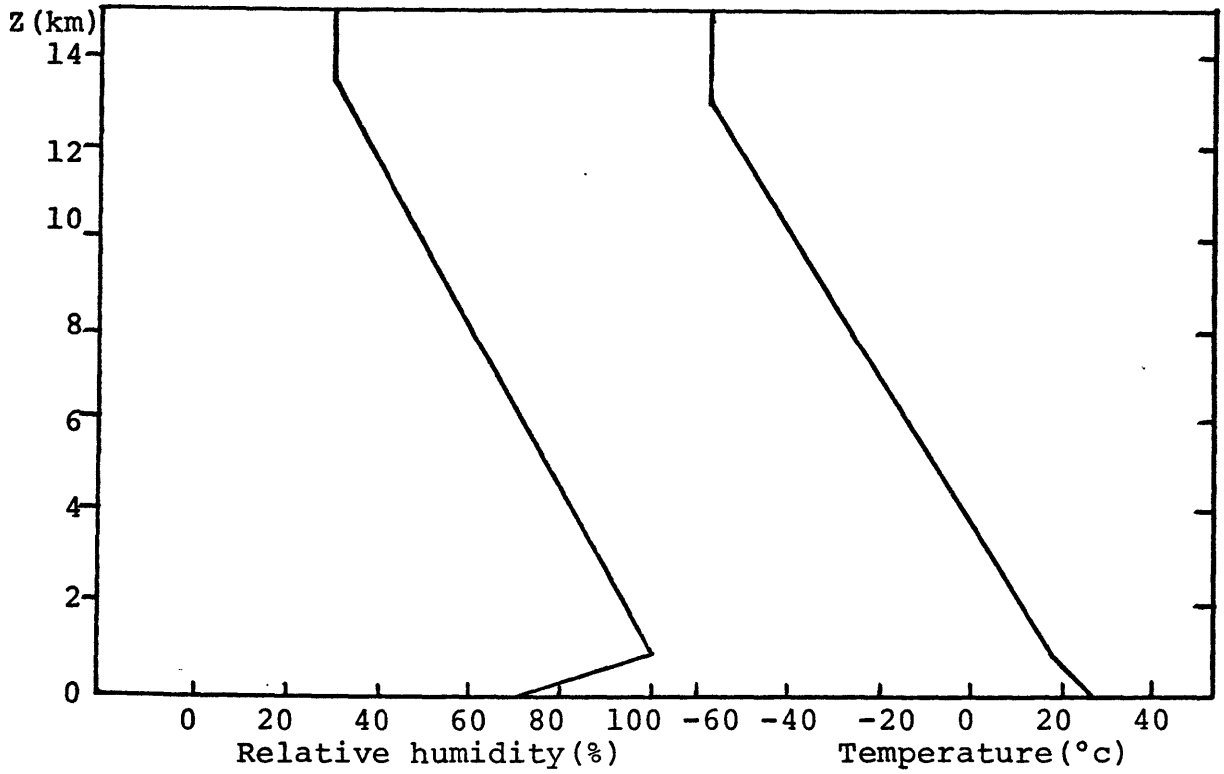


Fig. 4.2. Idealized sounding used to represent the base state atmosphere.

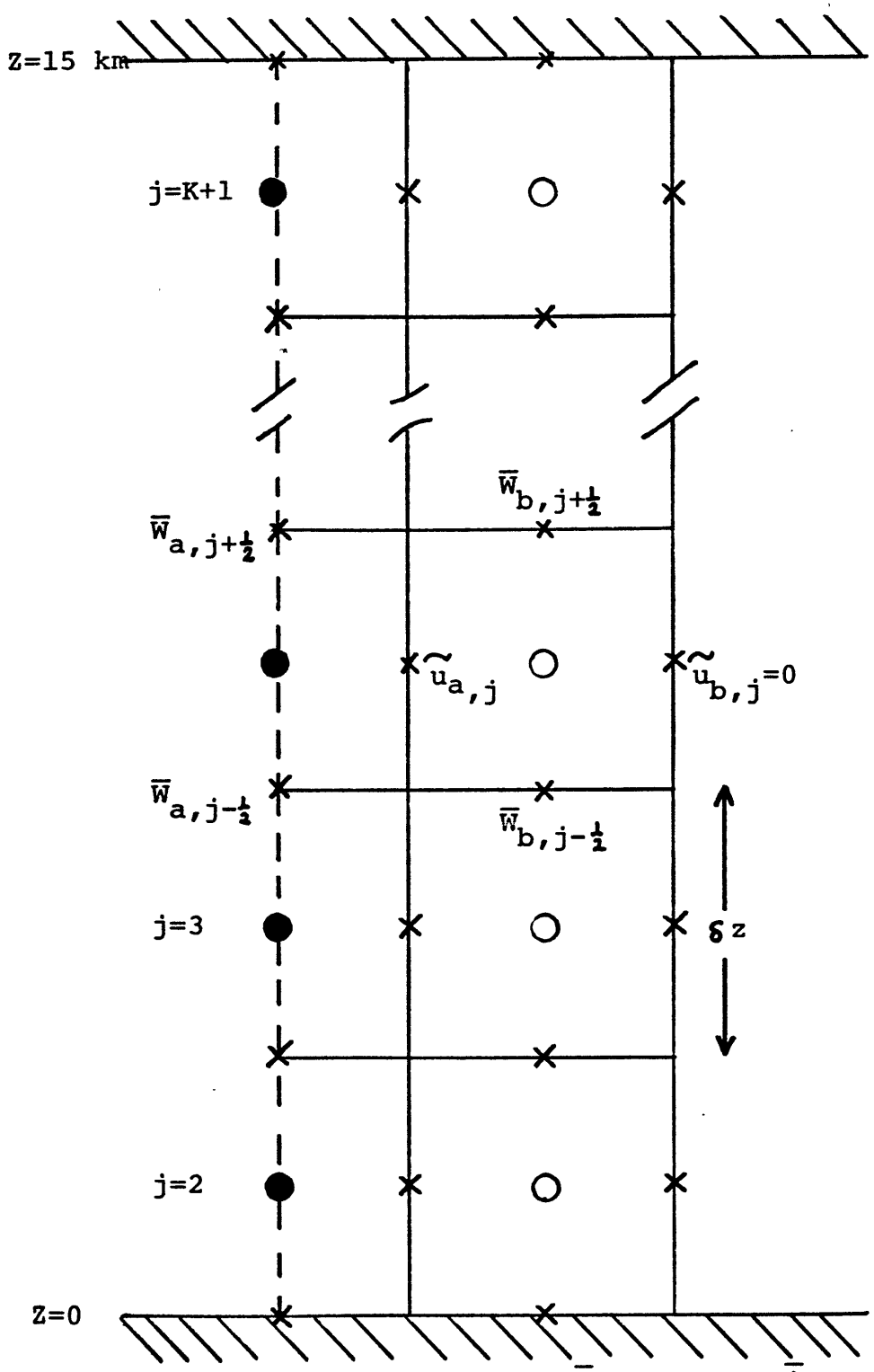


Fig. 4.3. The staggered-grid system.

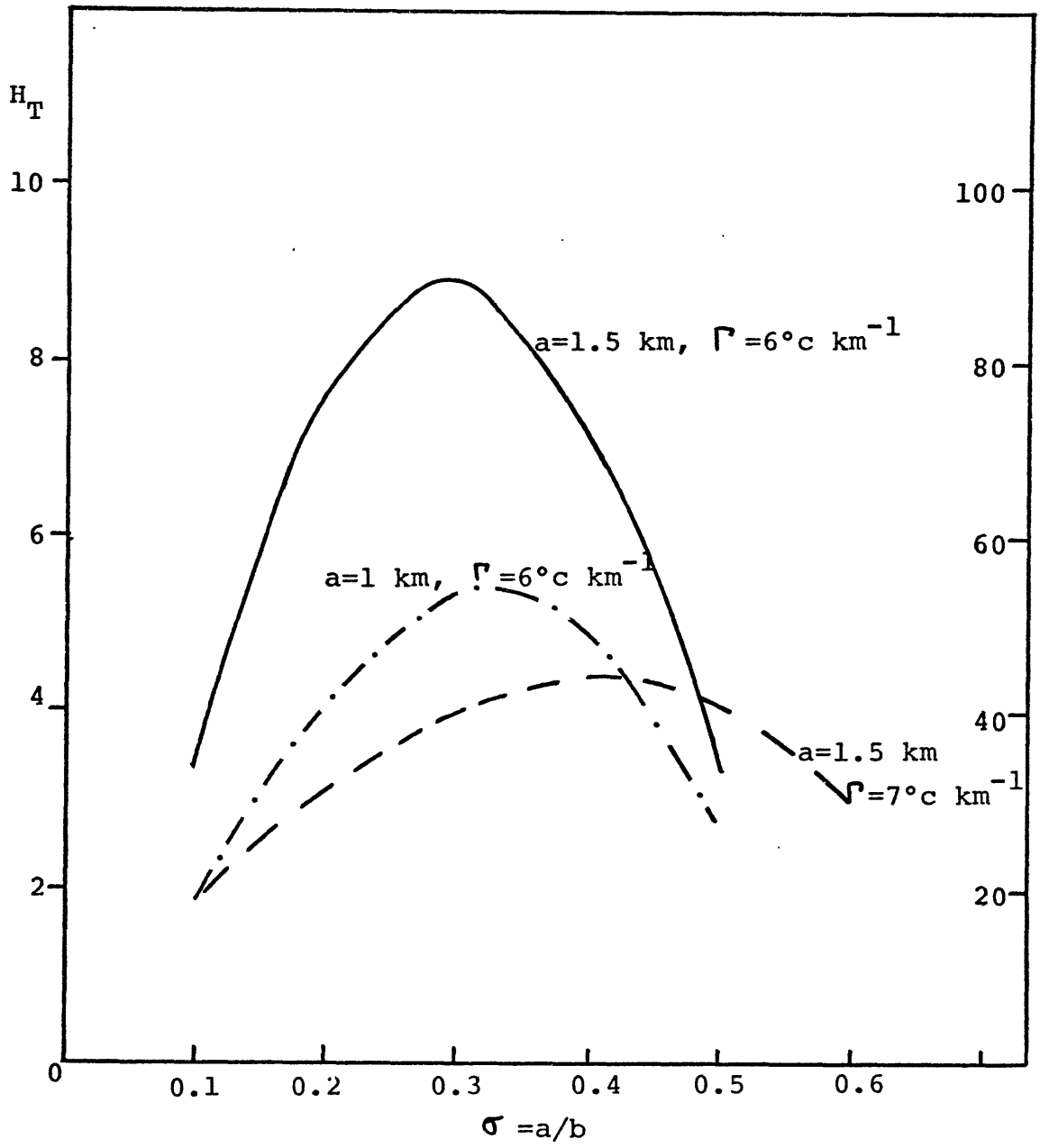


Fig. 4.4. Relation of σ and heat transport H_T.
The scale on the right is for Γ = 7°c km^{-1}.

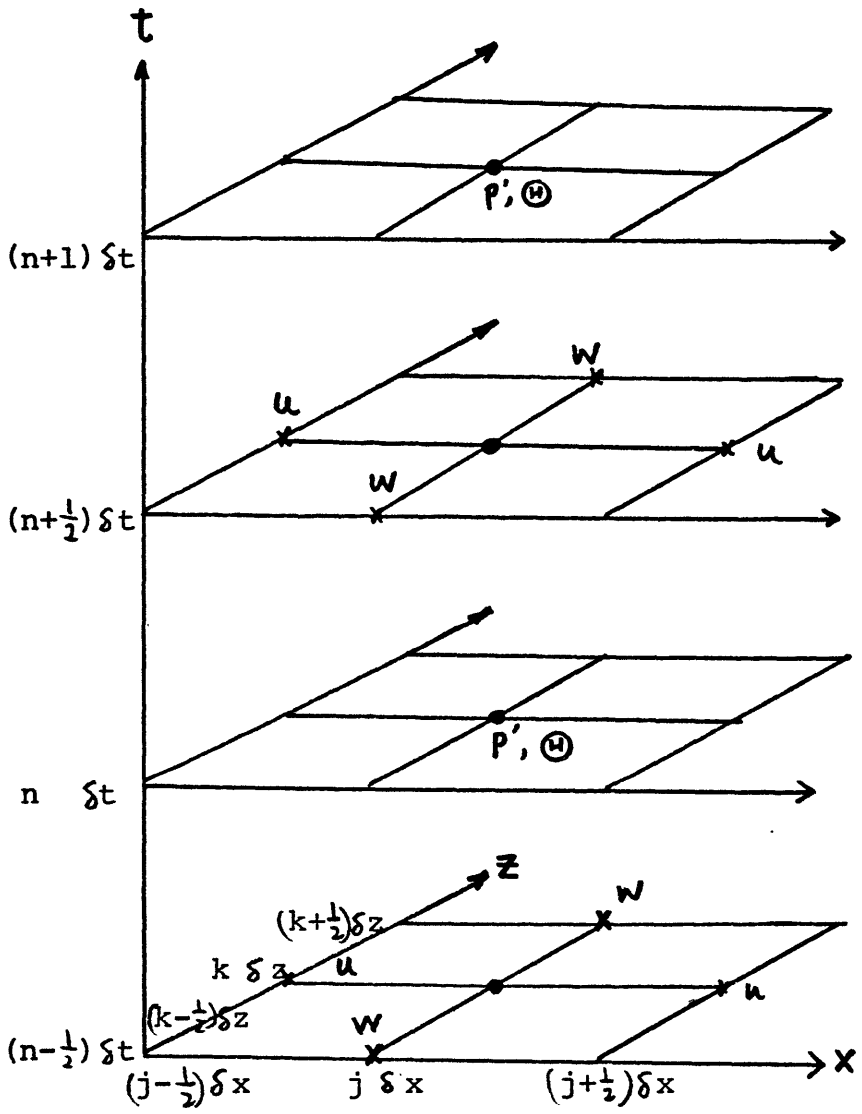


Fig. B1. The grid system for stability analysis of internal gravity wave motion.

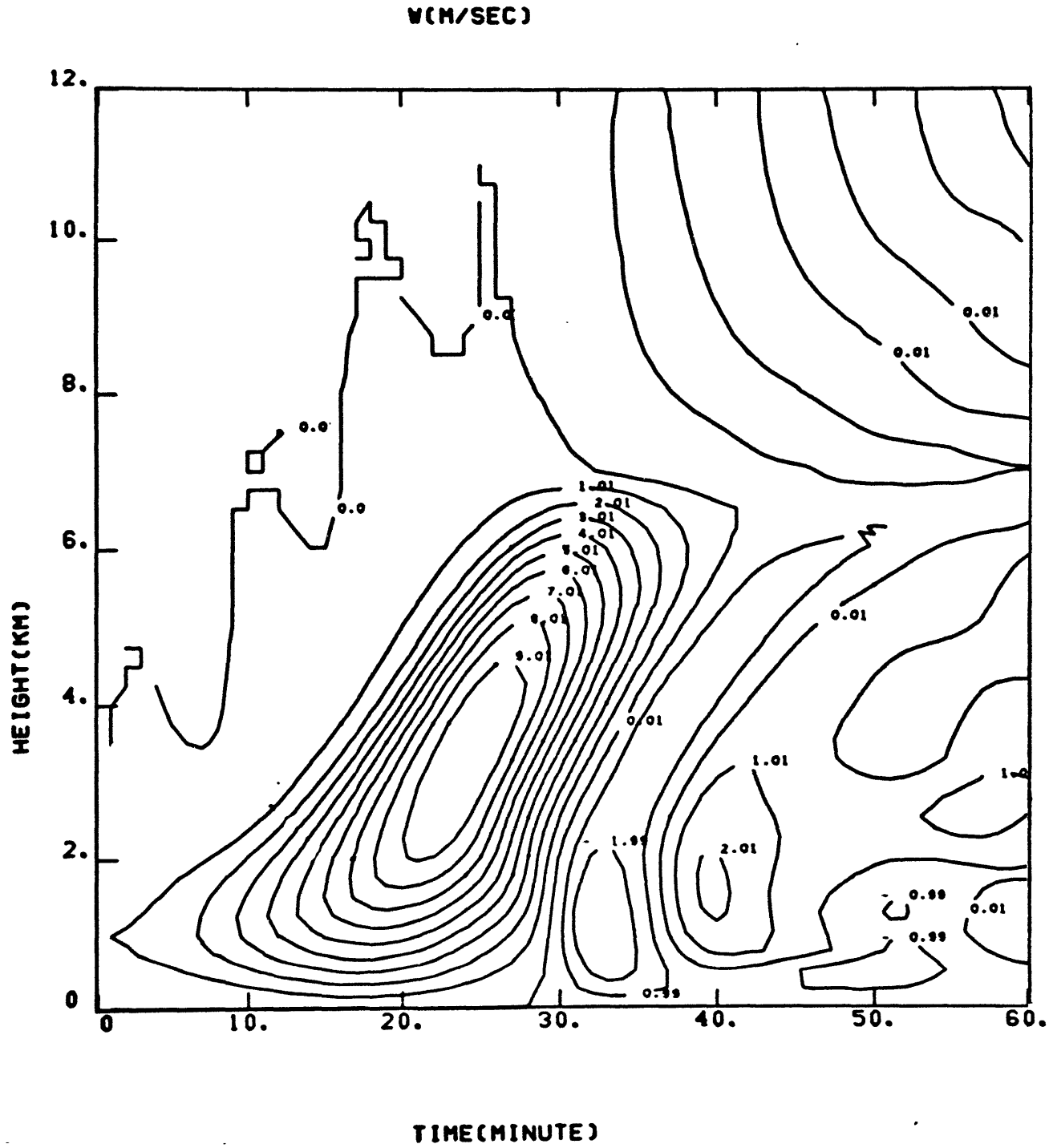


Fig. 5.1. Time-height cross-section of vertical velocity $\bar{W}_a$ in the inner cylinder for experiment E1. The contour interval is 1 m sec^{-1}.

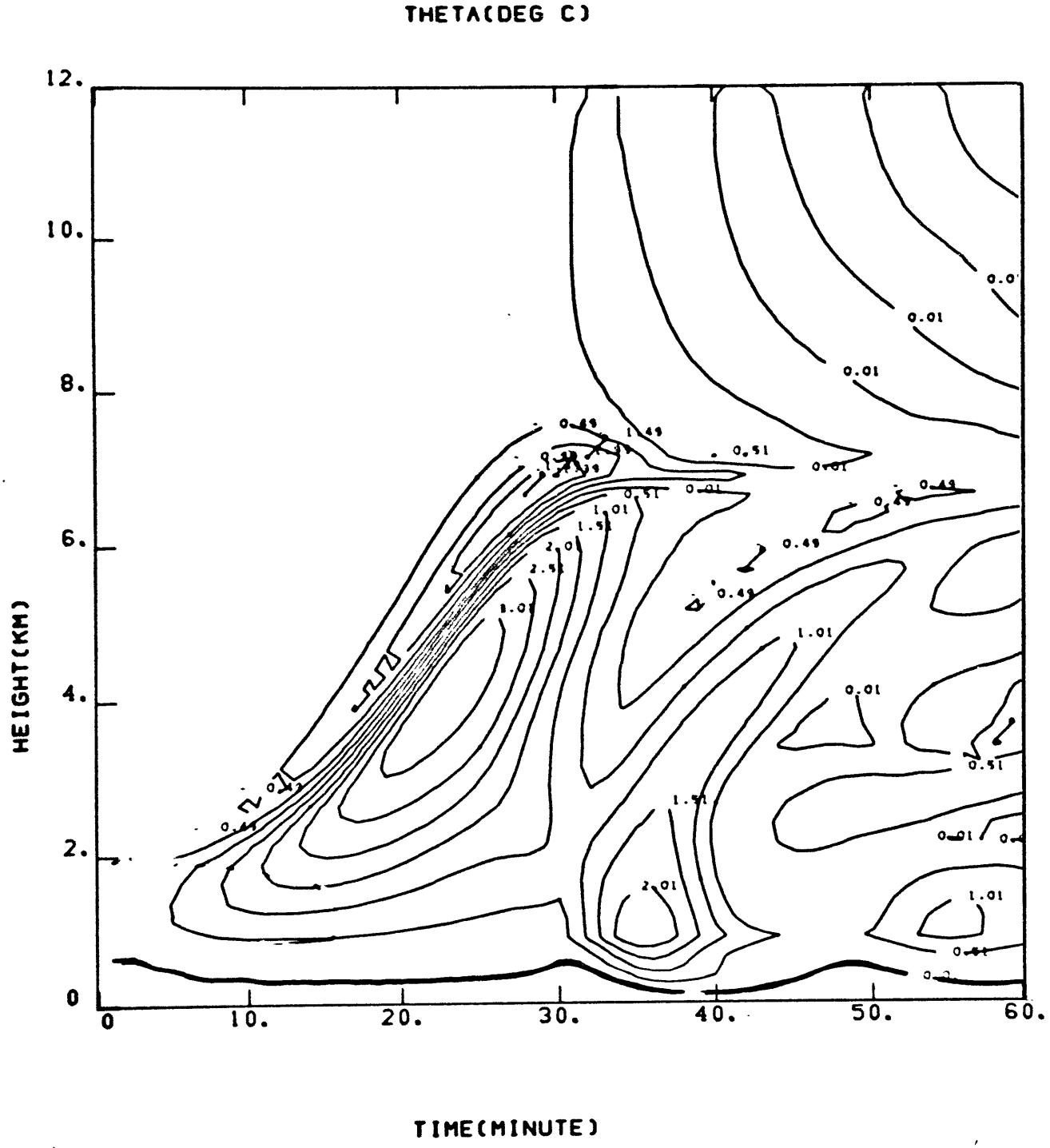


Fig. 5.2. Same as Fig. 5.1 except for potential temperature deviation $\bar{\theta}'_a$. The contour interval is 1°K.

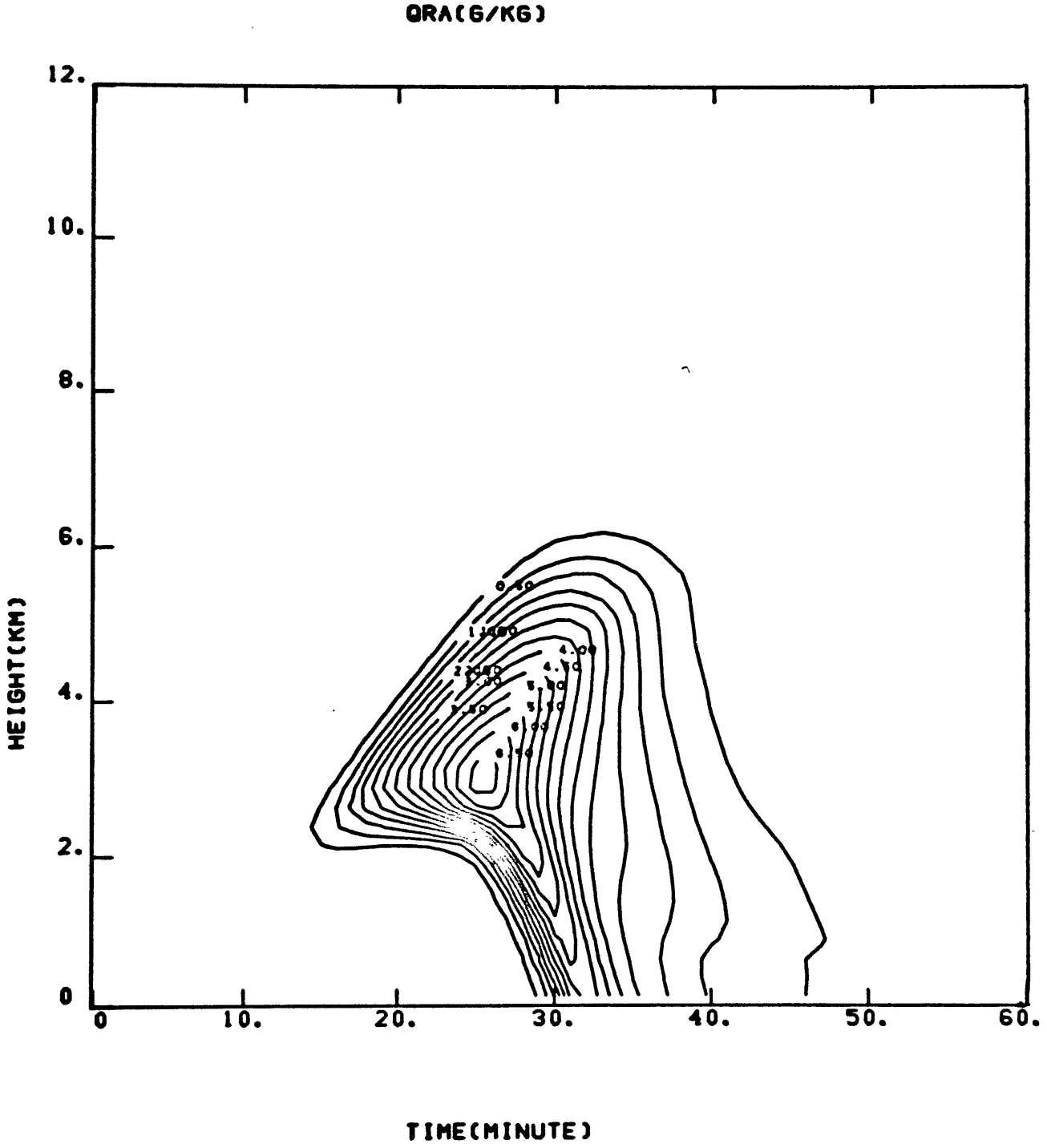


Fig. 5.3. Same as Fig. 5.1 except for rain water content $\bar{q}_{ra}$. The contour interval is 0.5 g kg^{-1}.

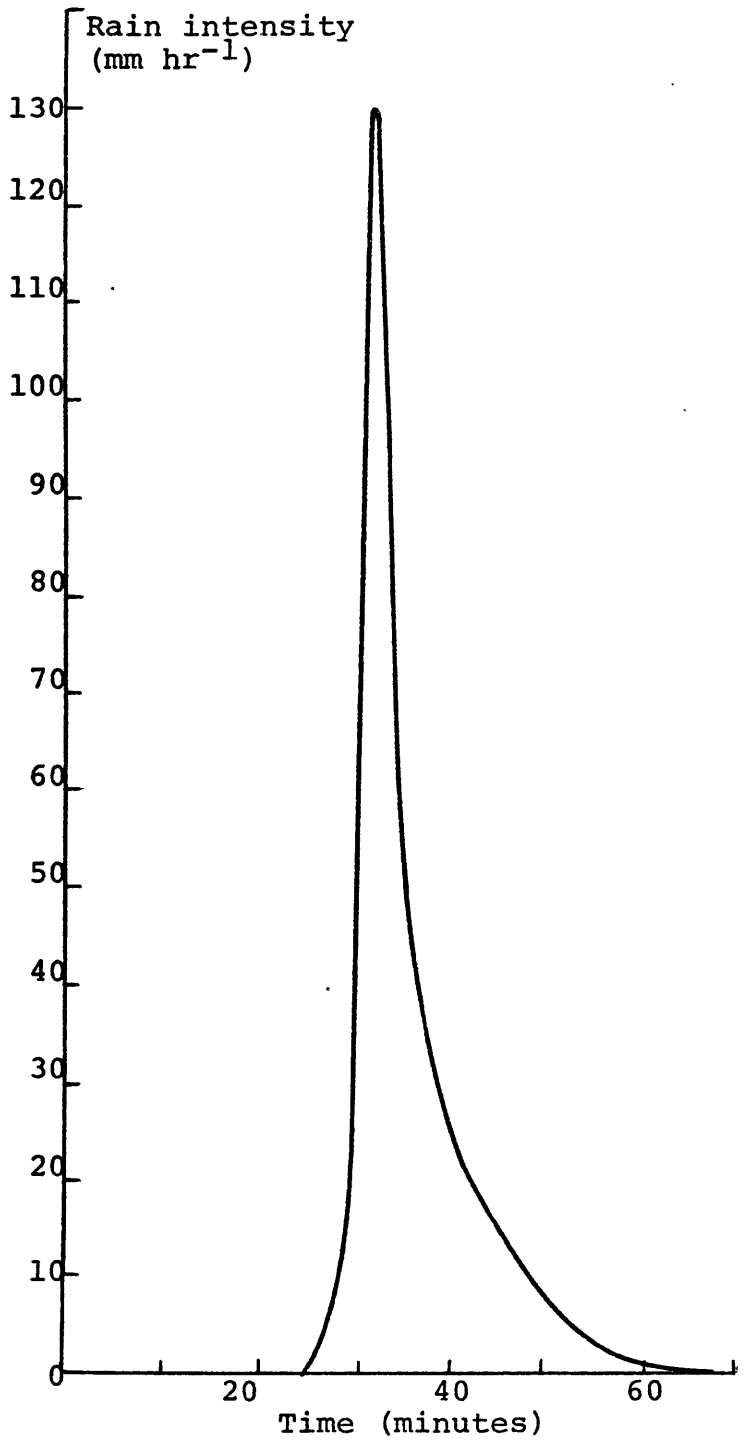


Fig. 5.4. Time variation of surface rainfall intensity in the inner cylinder for experiment E1.

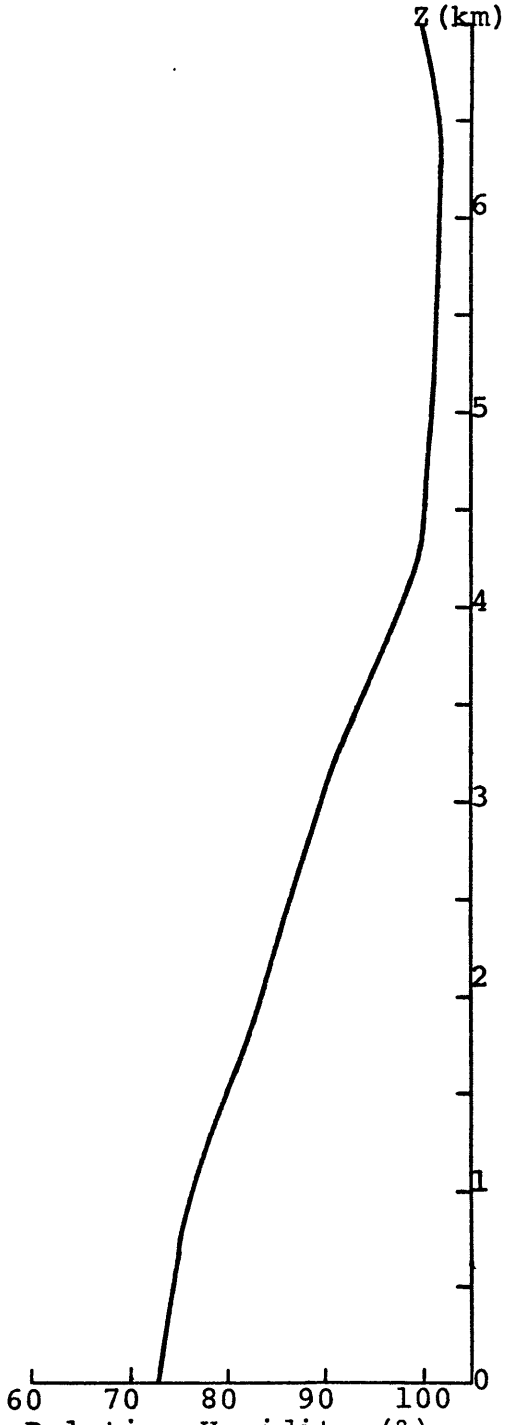


Fig. 5.5. Vertical distribution of relative humidity in the inner cylinder for E1 at 35 minutes.

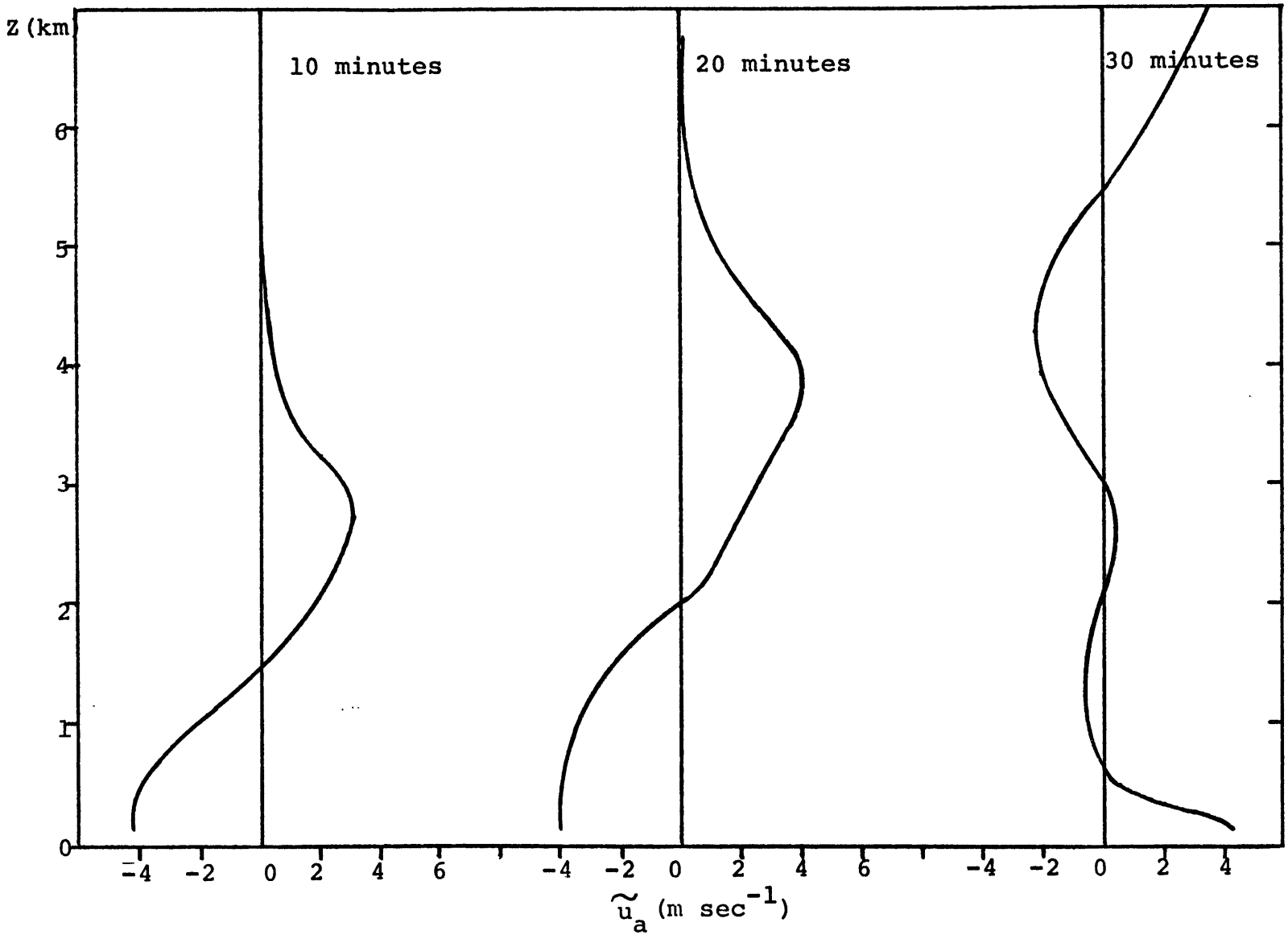


Fig. 5.6. Radial velocity at the edge of the inner cylinder at 10, 20, and 30 minutes for experiment E1.

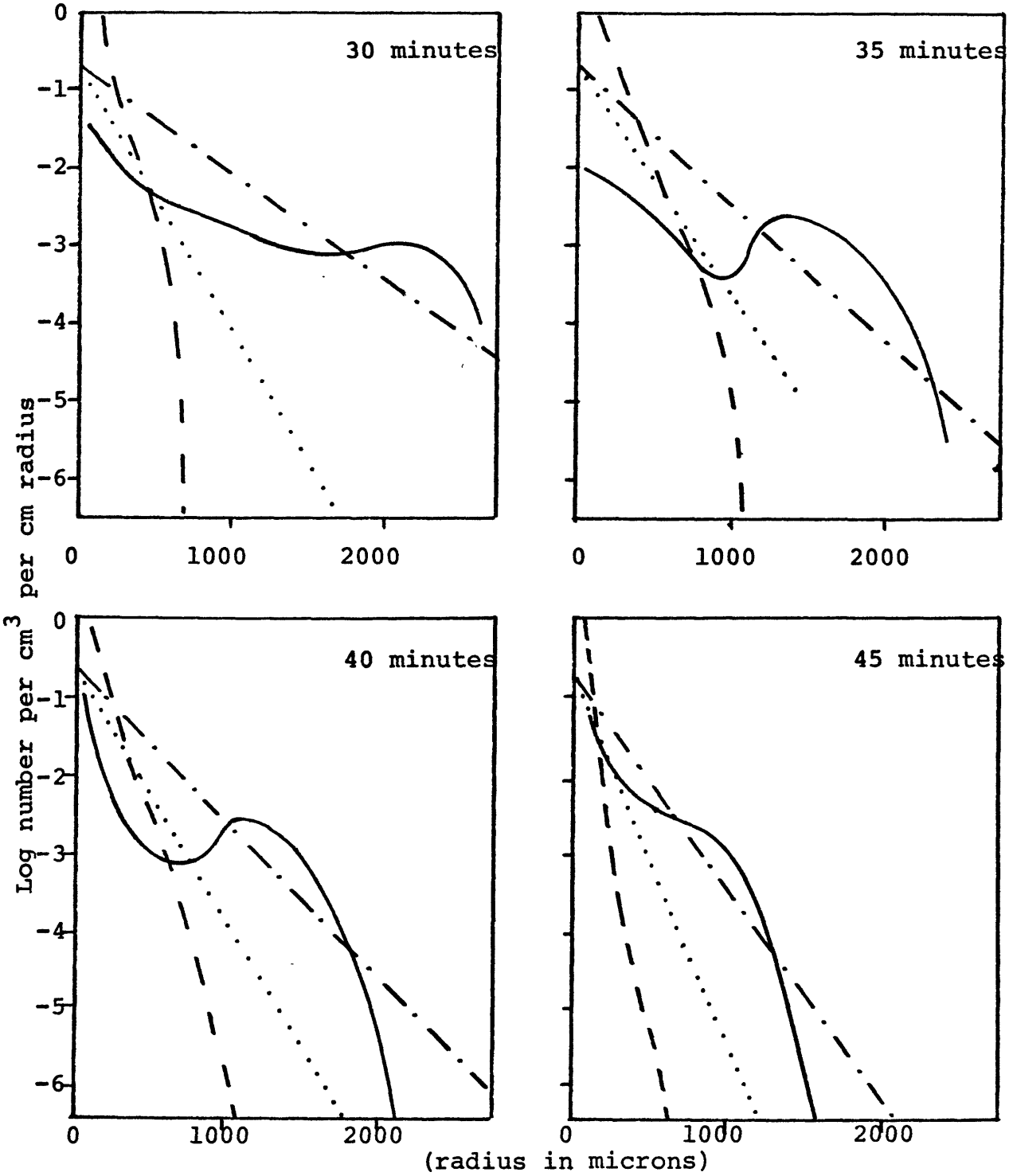


Fig. 5.7. Rainfall spectra in the inner cylinder near the cloud base(875 m)————, and the cloud top (6125 m)— — ——— at 30,35,40,and 50 minutes for E1. The diagonal lines are Marshall-Palmer spectra with the same rain water content. — .— .— MP spectra at 875 m, ... MP spectra at 6125 m.

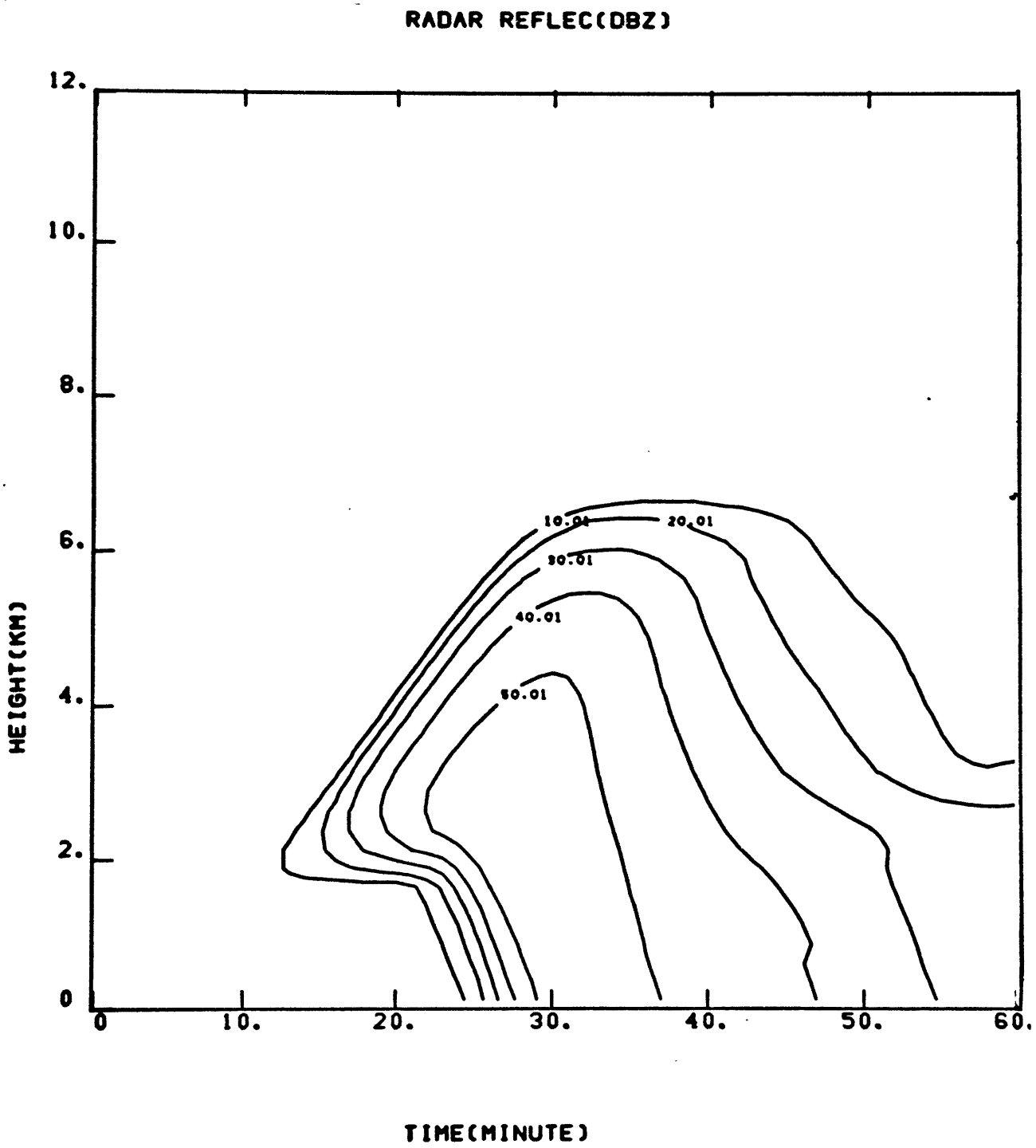


Fig. 5.8. Same as Fig. 5.1 except for radar reflectivities. The contour interval is 10 dbz.

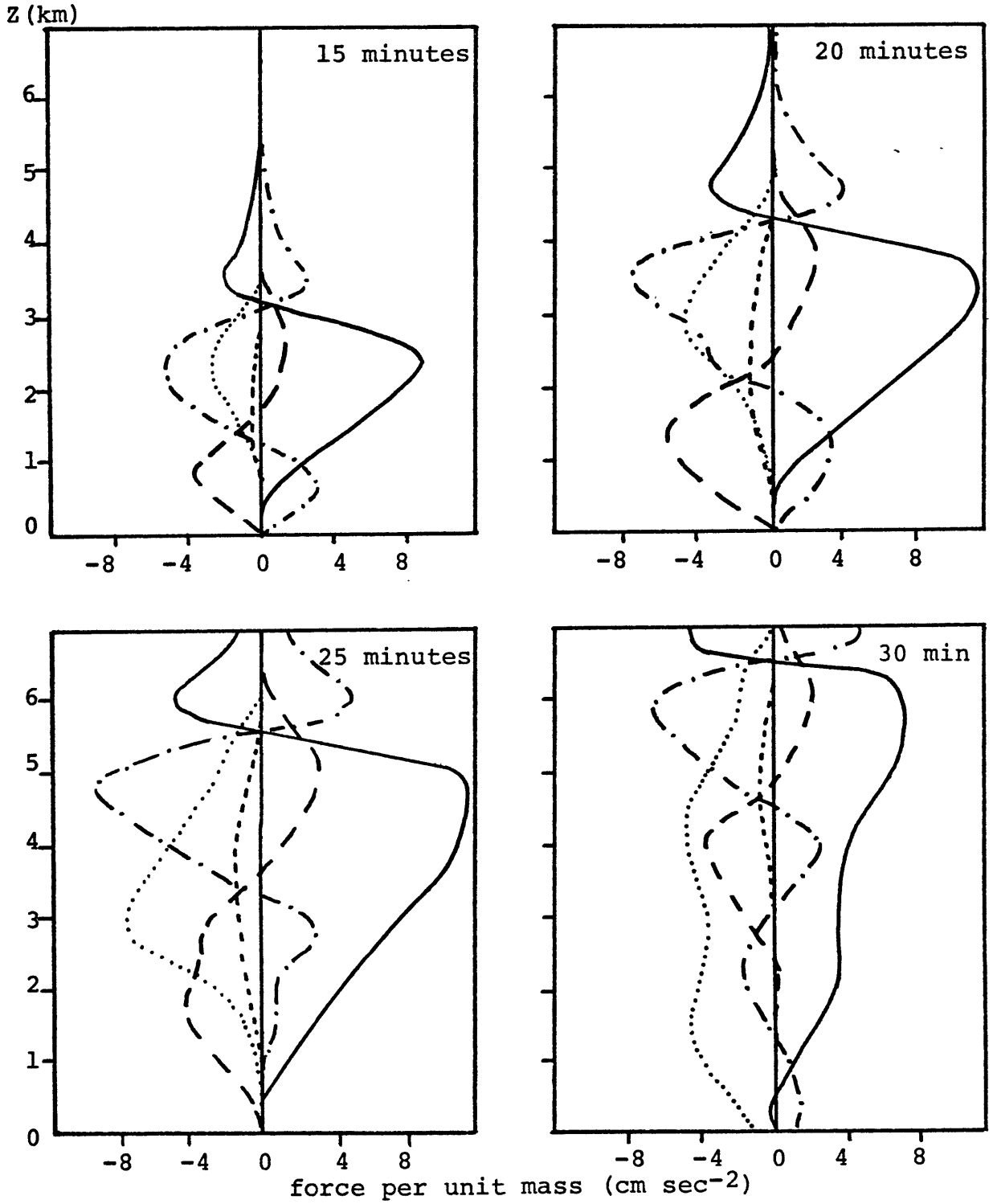


Fig. 5.9. Analysis of forces in the vertical momentum equation (4.23) in the inner cylinder at 15,20,25,and 30 minutes for experiment E1. Buoyancy————, drag ....., turbulent entrainment -------, dynamic entrainment and vertical advection — — —, perturbation pressure gradient force -.-.-.-.

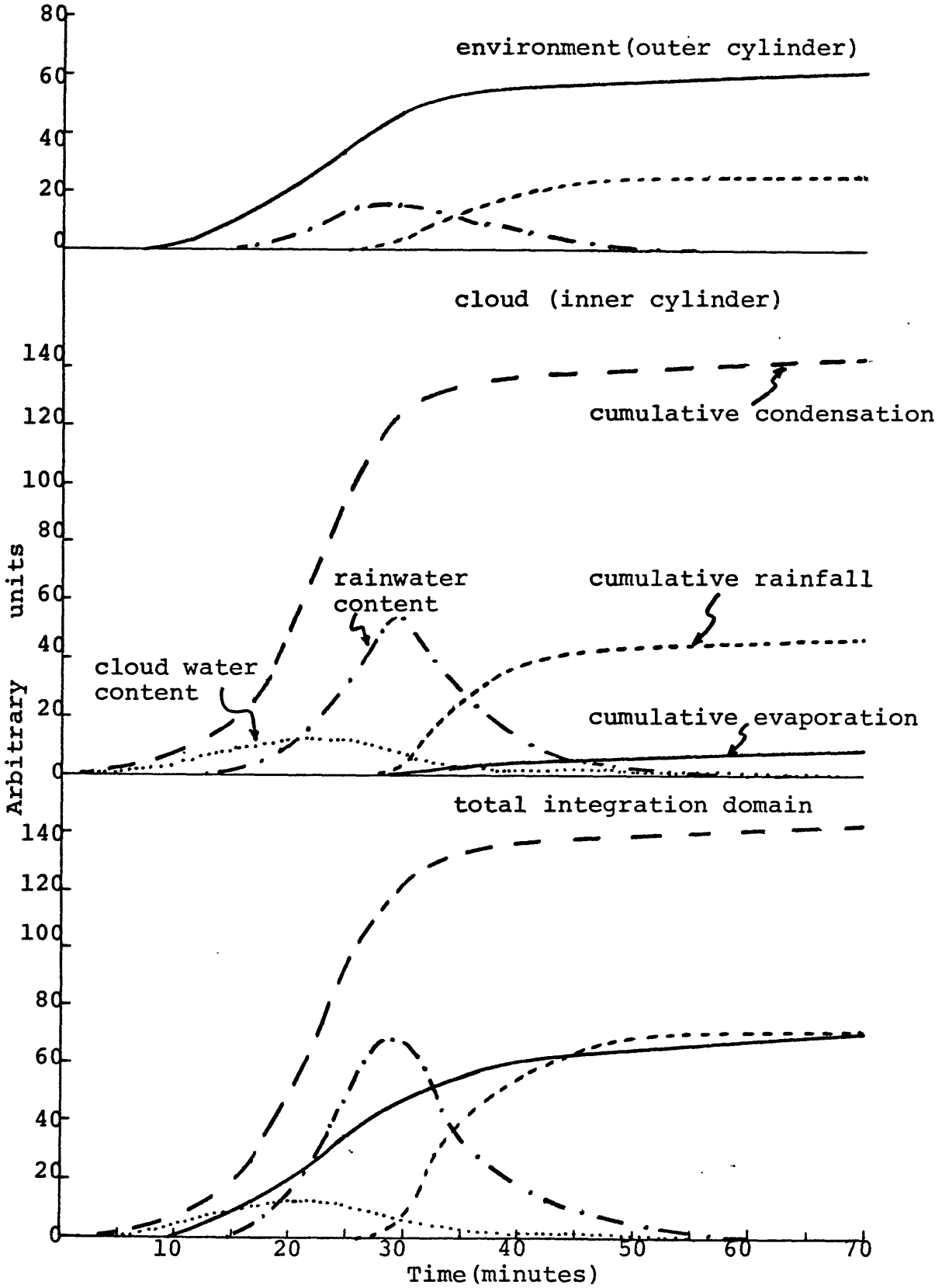


Fig. 5.10. Analysis of water budget in the environment, the cloud column, and the whole integration domain for experiment E1.

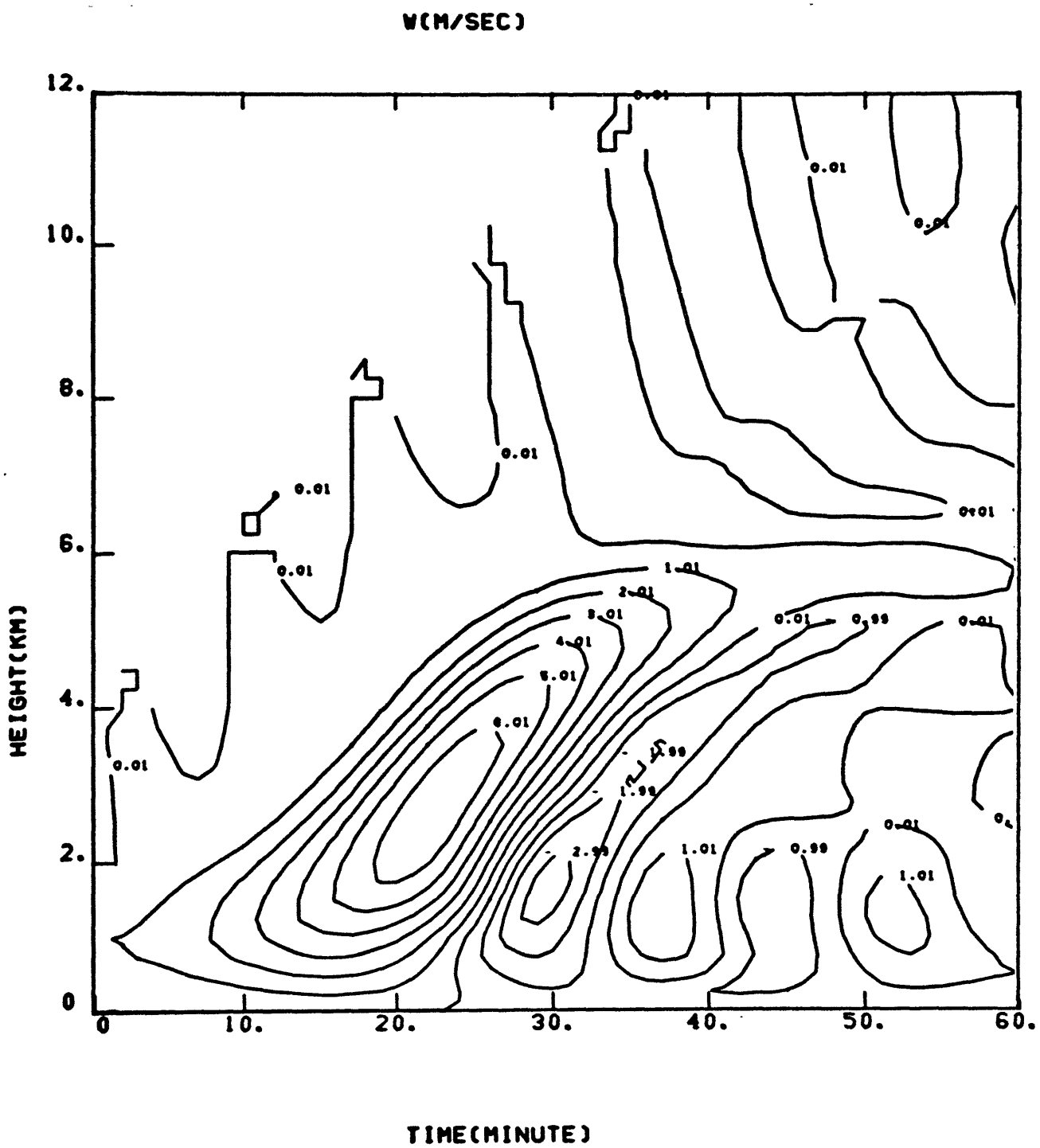


Fig. 5.11. Same as Fig. 5.1 except for experiment E2.

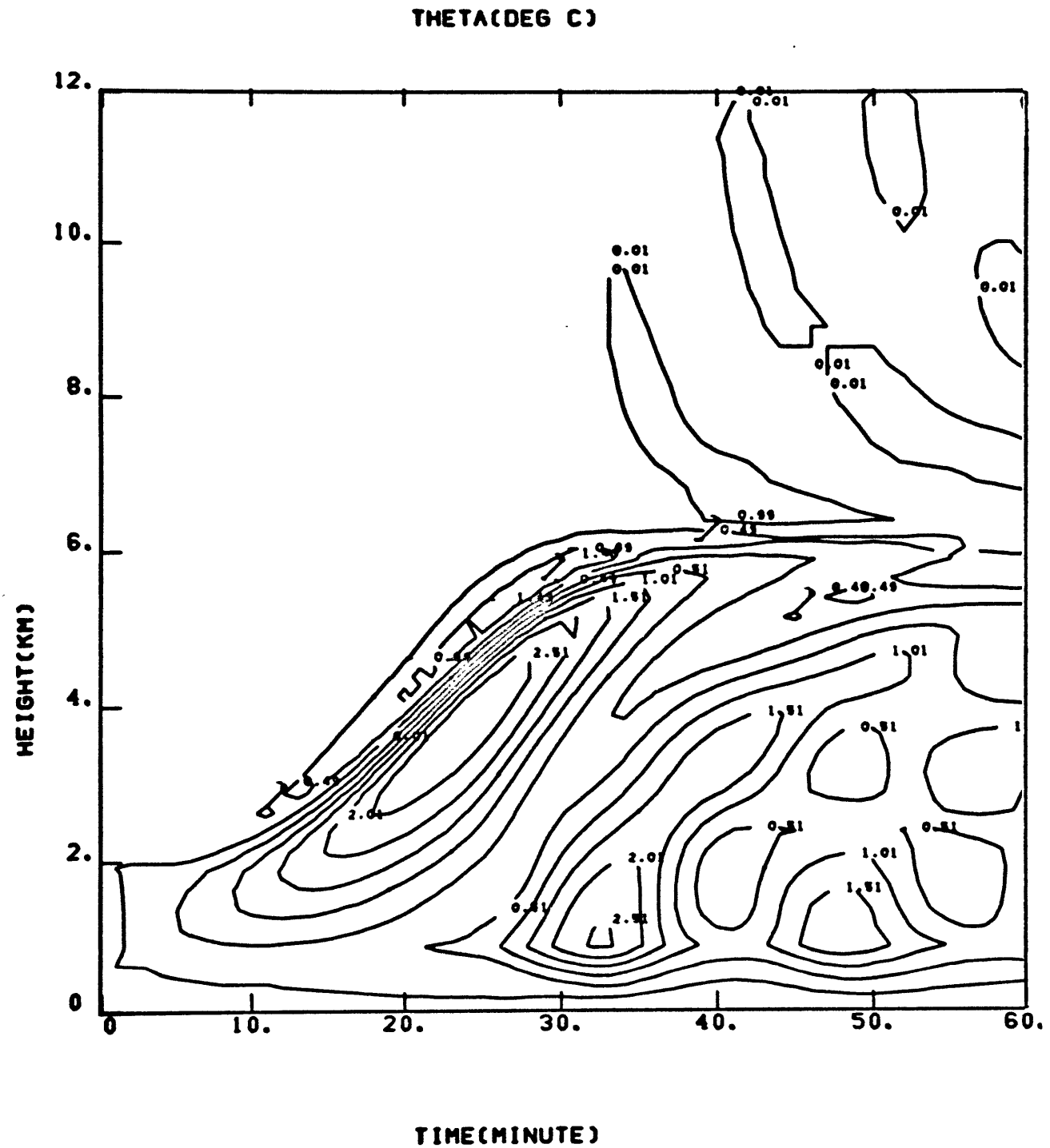


Fig. 5.12. Same as Fig. 5.2 except for experiment E2.

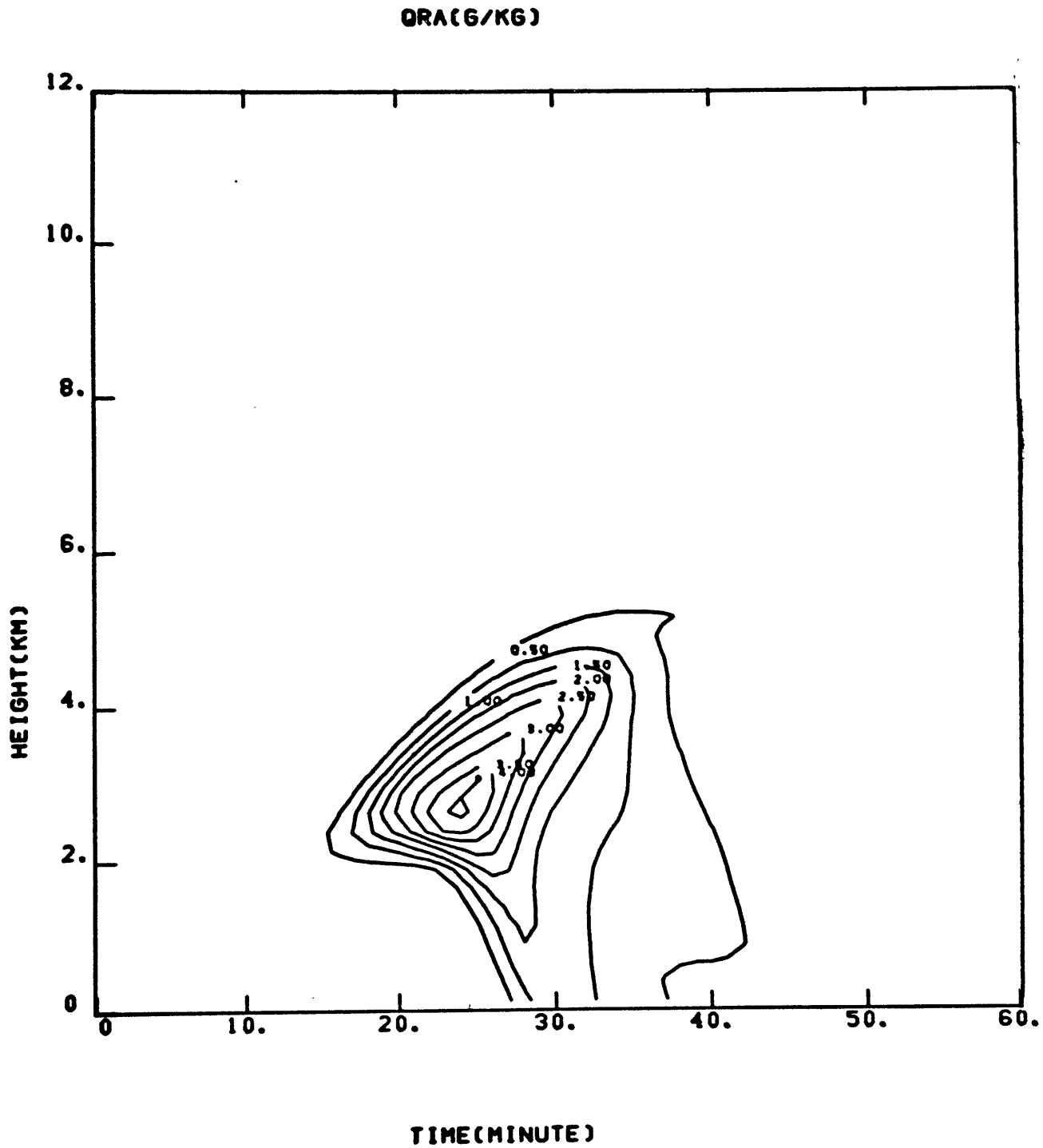


Fig. 5.13. Same as Fig. 5.3 except for experiment E2.

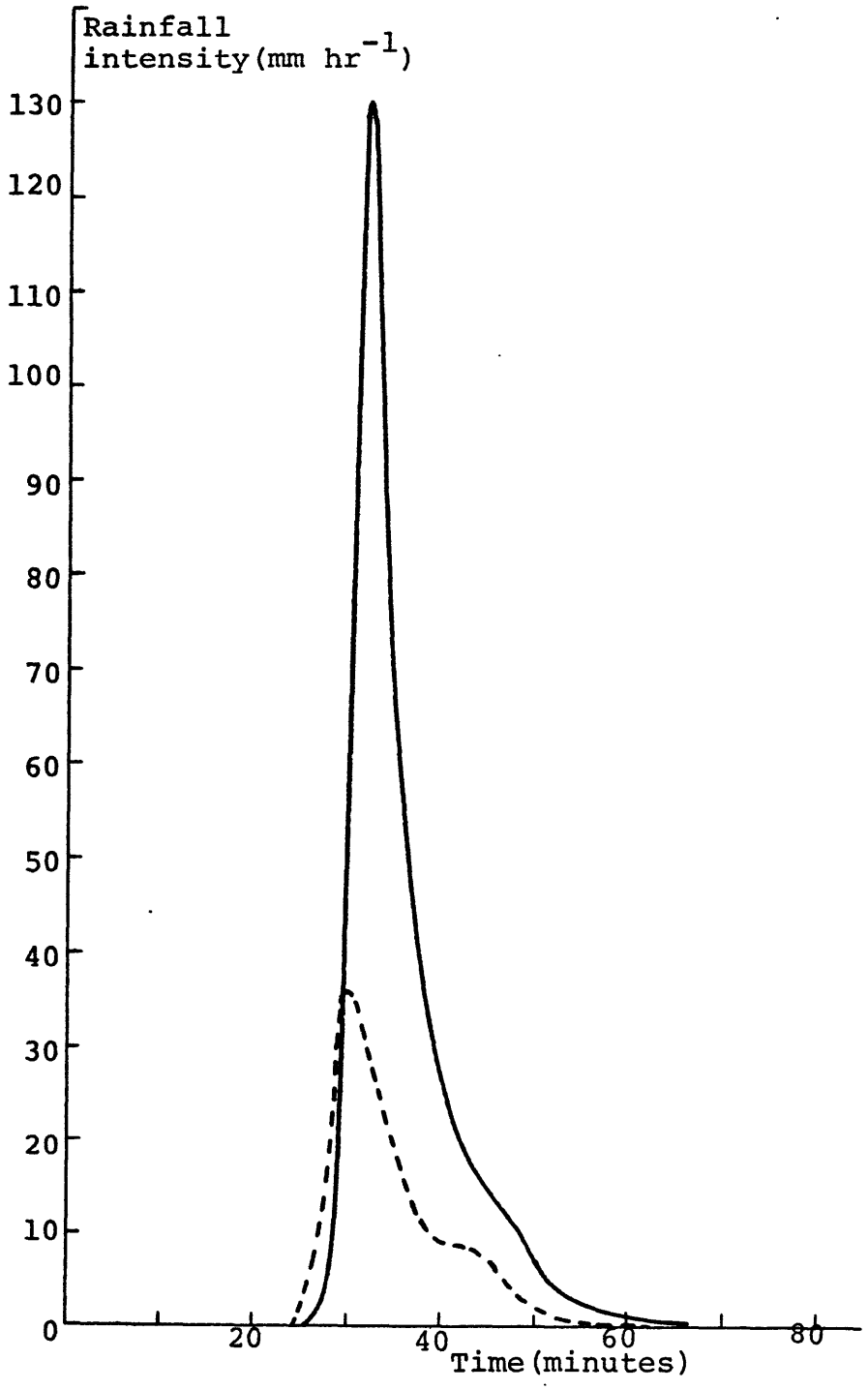


Fig. 5.14. Comparison of surface rainfall intensity for experiments E1 and E2.
E1————, E2 - - - - -.

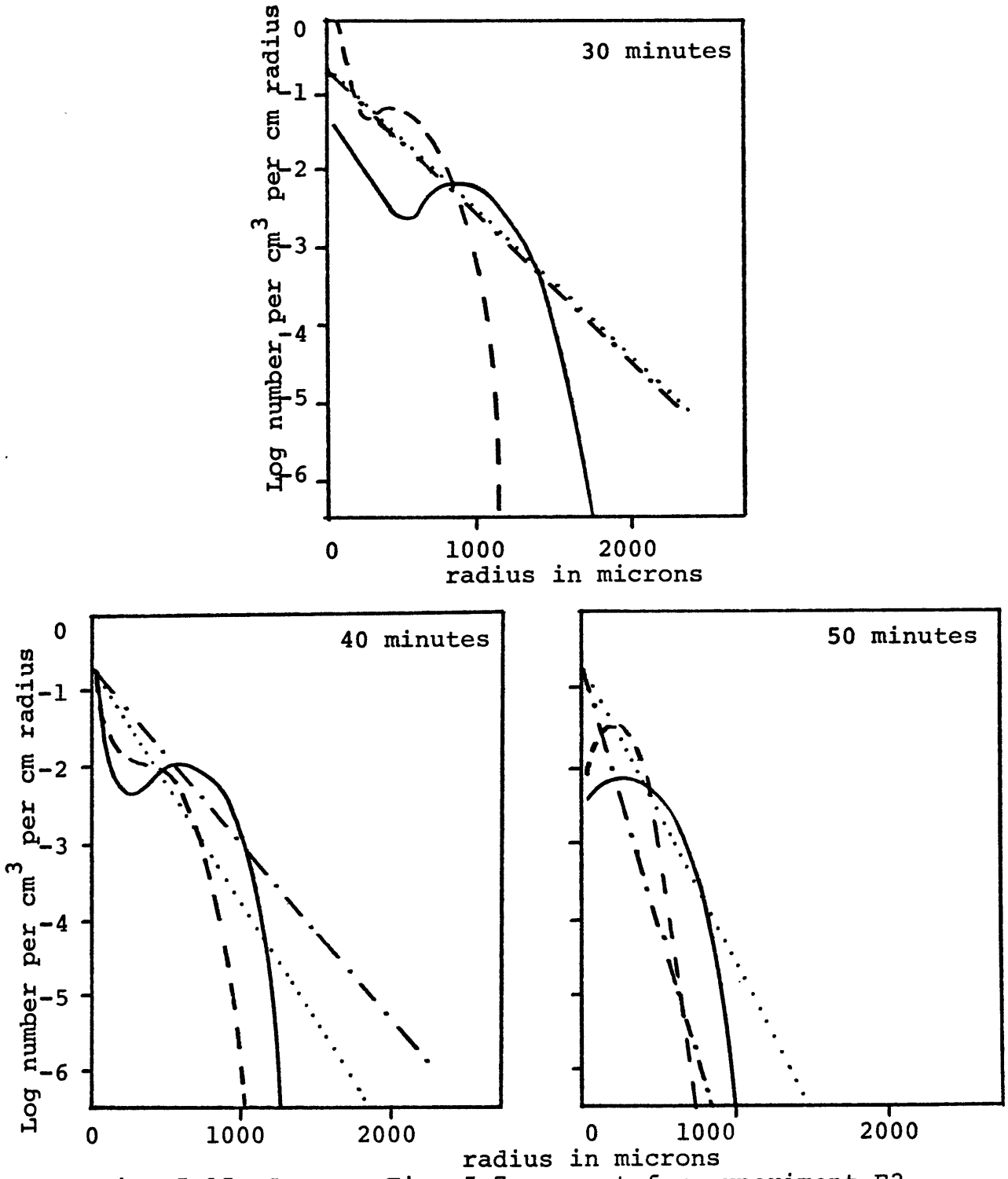


Fig. 5.15. Same as Fig. 5.7. except for experiment E2.

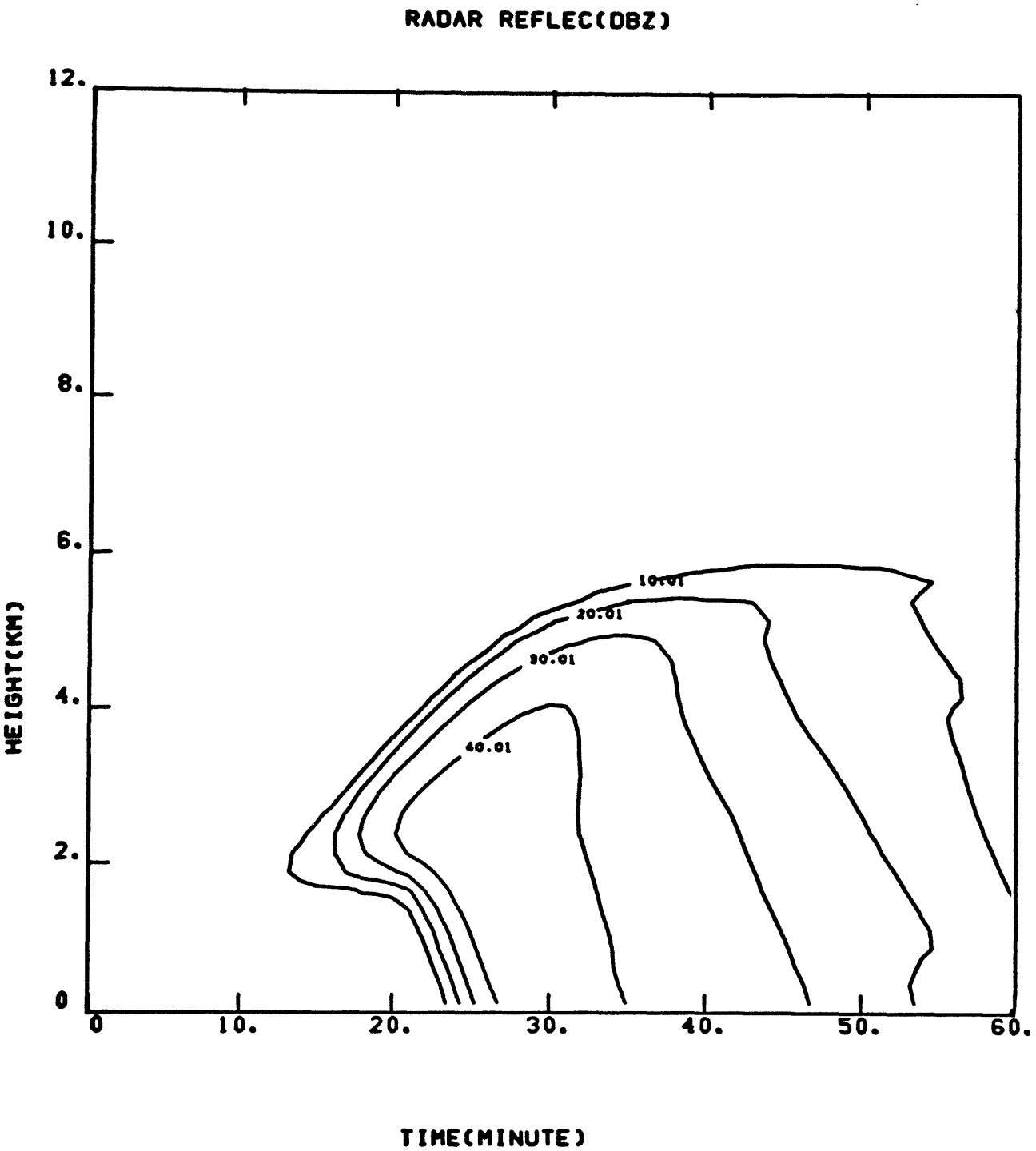


Fig. 5.16. Same as Fig. 5.8 except for experiment E2.

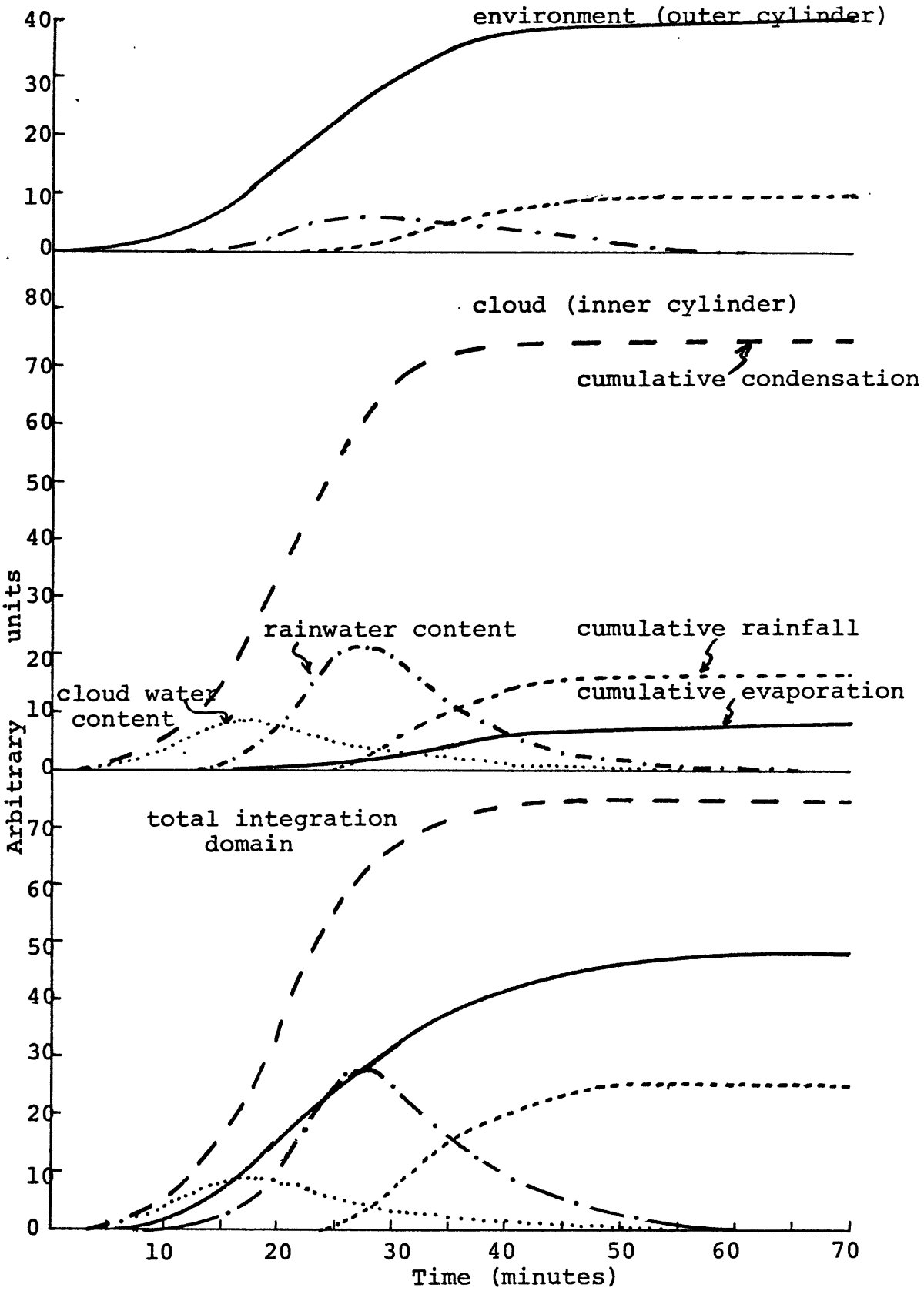


Fig. 5.17. Same as Fig. 5.10 except for experiment E2.

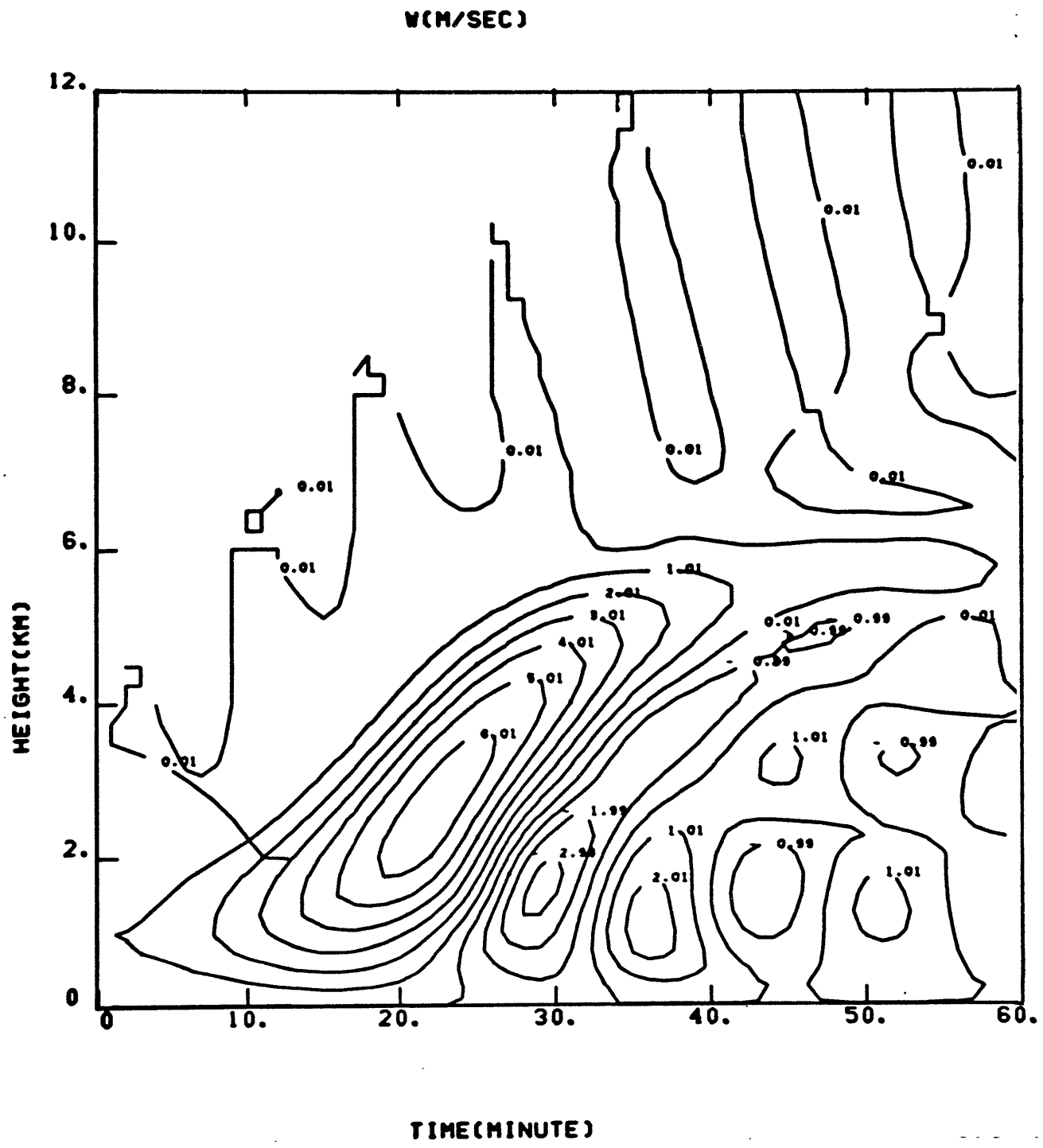


Fig. 5.18. Same as Fig. 5.1 except for experiment E3.

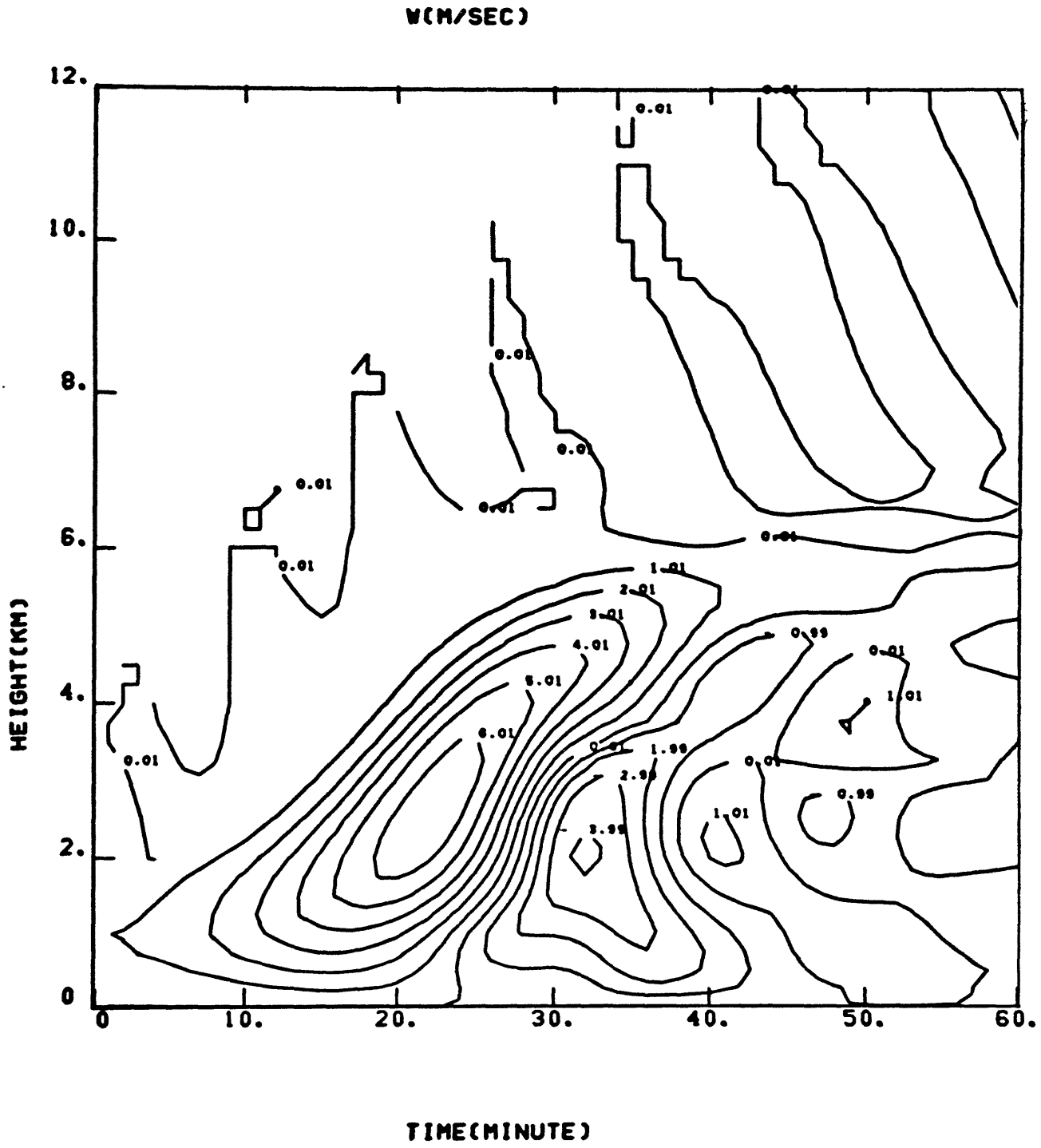


Fig. 5.19. Same as Fig. 5.1 except for experiment E4.

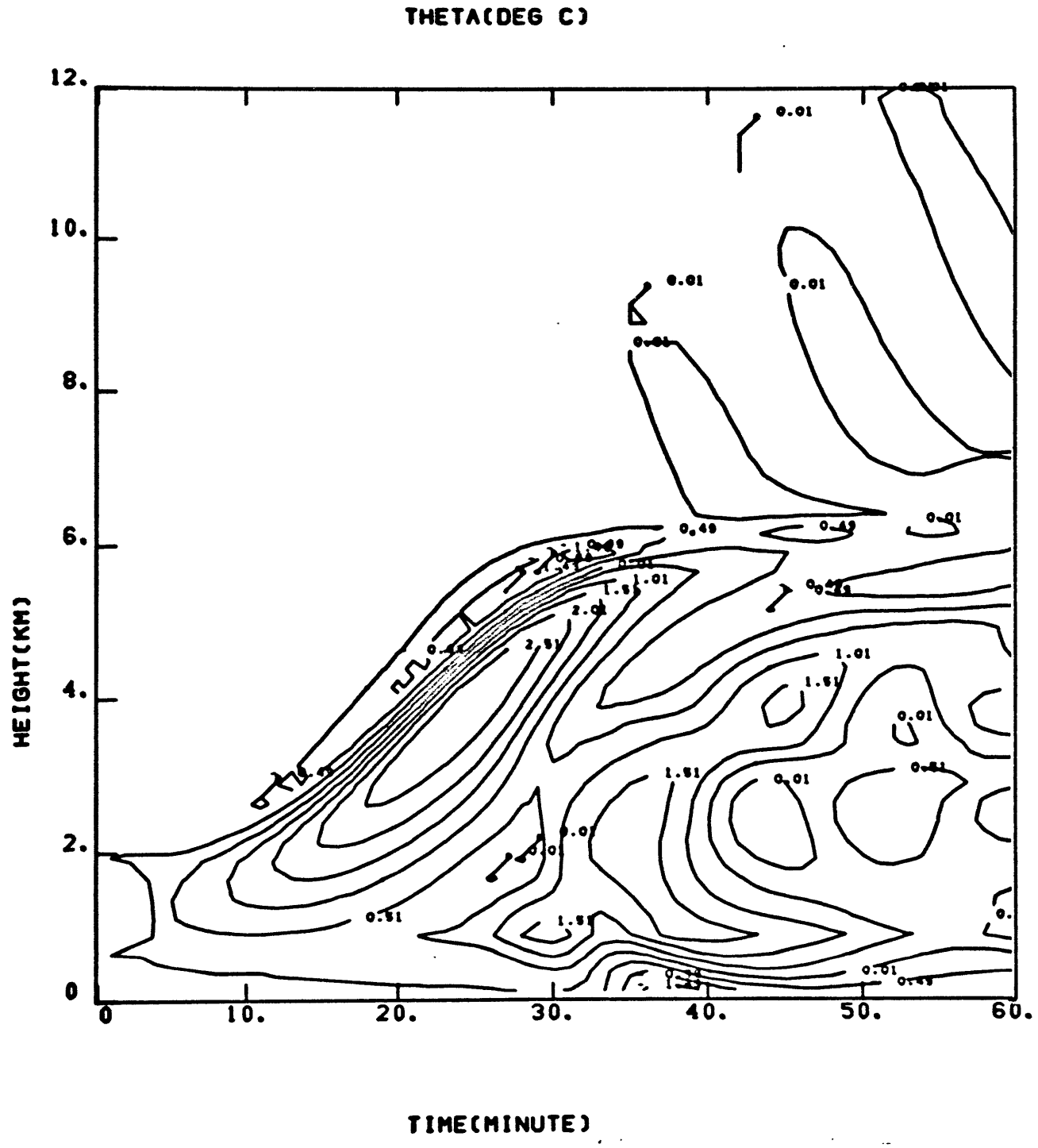


Fig. 5.20. Same as Fig. 5.2 except for experiment E4.

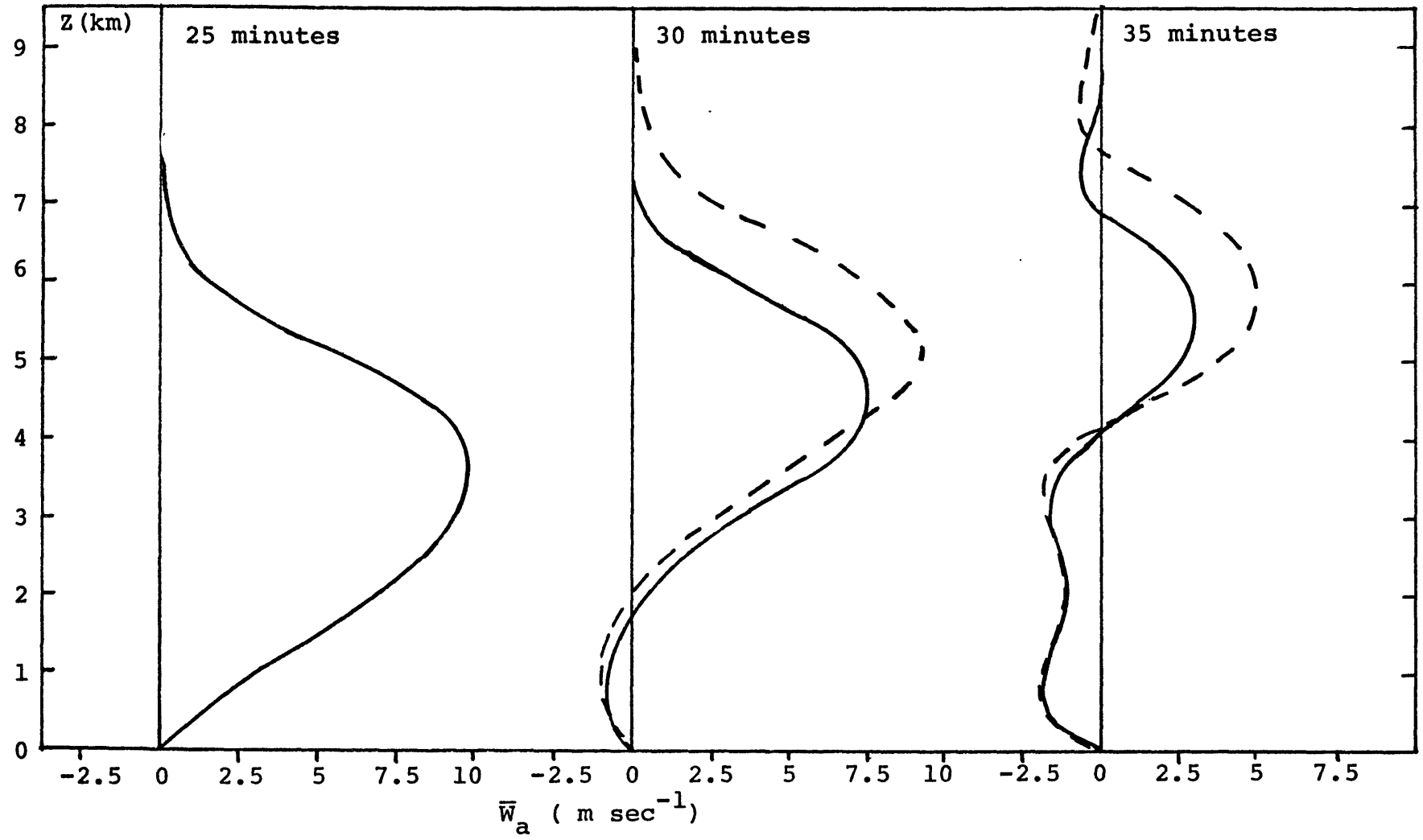


Fig. 5.21. Comparison of the vertical velocity in the inner cylinder for the case with (E5) and without(E1) the ice phase.
With ice phase— — —, without ice phase————————.

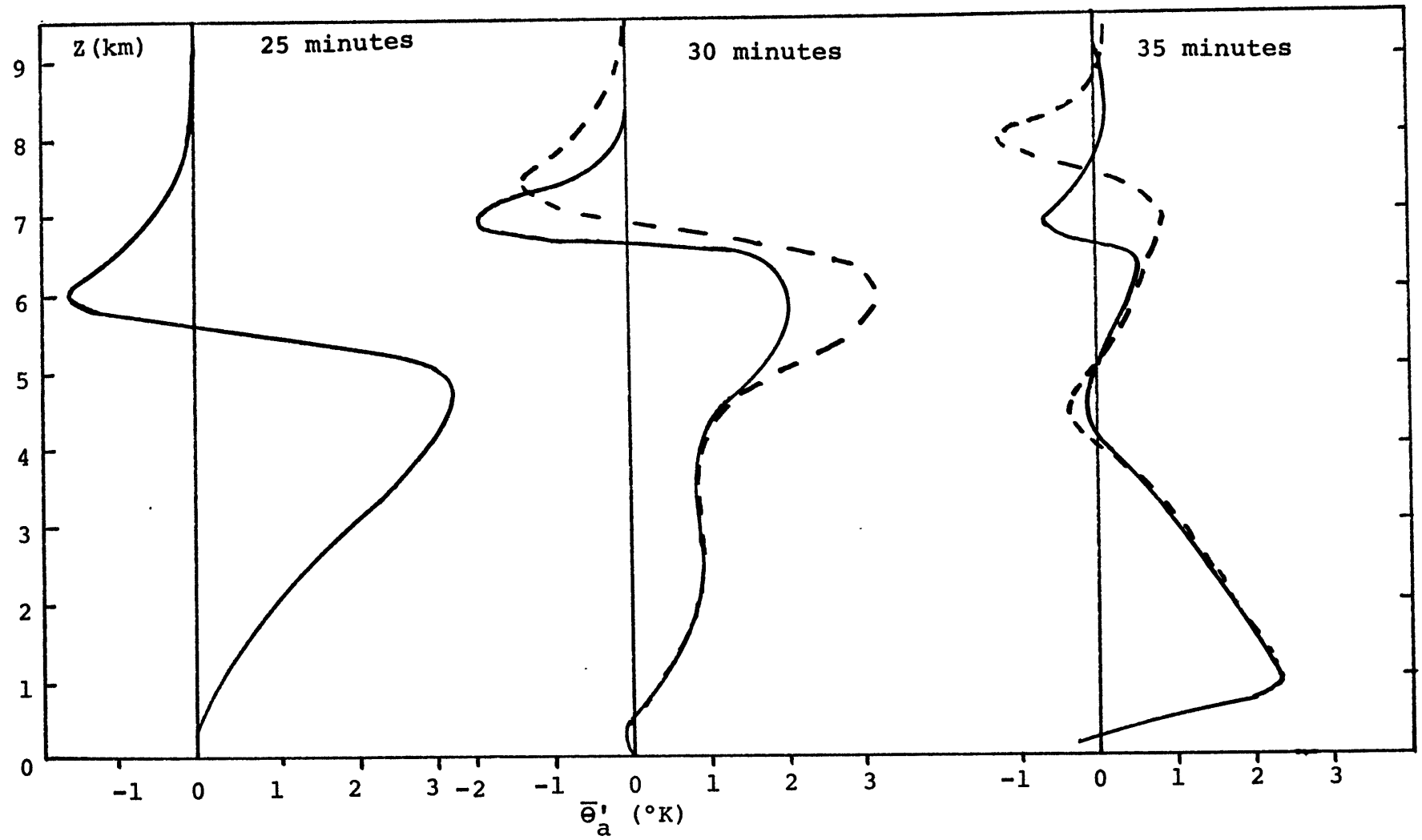


Fig. 5.22. Comparison of the the potential temperature deviation in the inner cylinder for the case with (E5) and without (E1) the ice phase.
With ice phase— — —, without ice phase————.

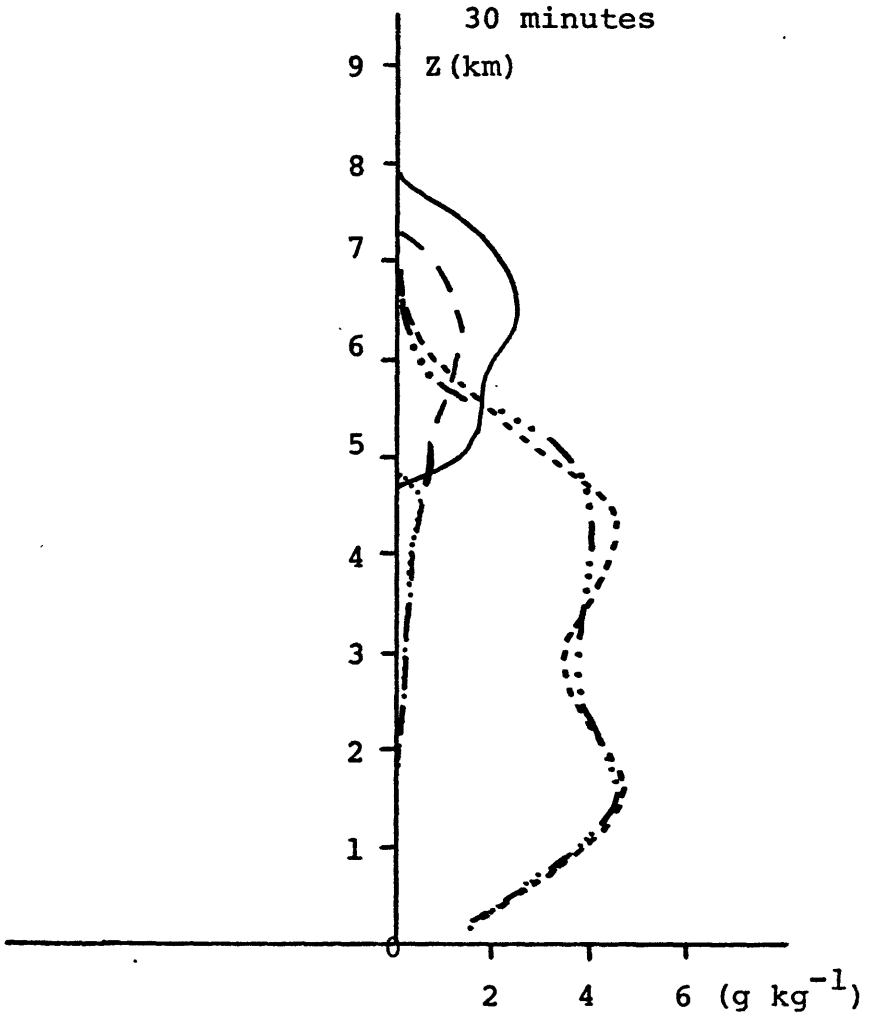


Fig. 5.23. Comparison of cloud, cloud ice, and rain water content in the inner cylinder at 30 minutes for E5 and E1.
Experiment E5, cloud ice———, cloud water .....,
rainwater -...-...-...
Experiment E1, cloud water — — —,
rain water - - - - .

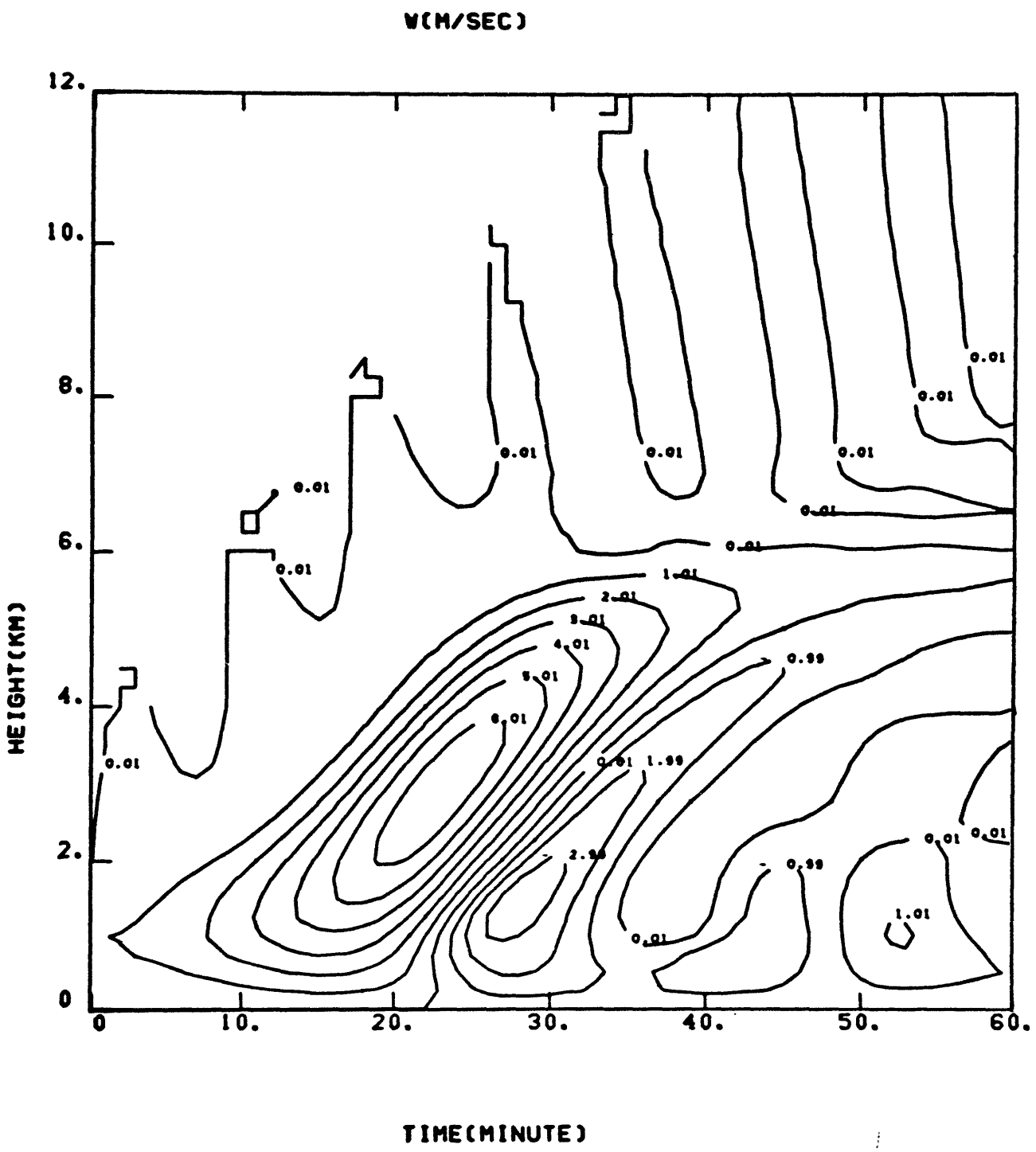


Fig. 5.24. Same as Fig. 5.1 except for experiment E6.

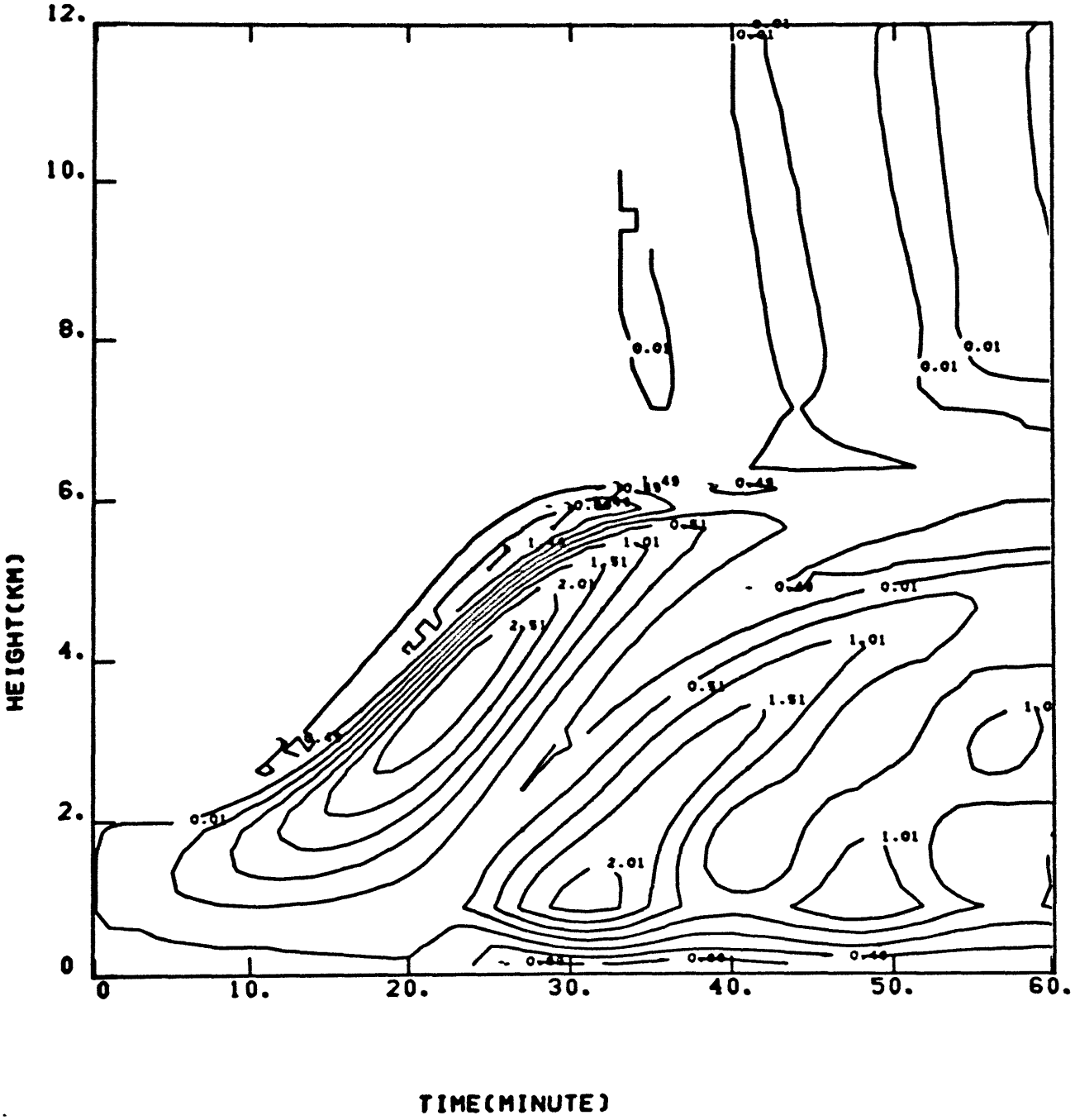


Fig. 5.25. Same as Fig. 5.2 except for experiment E6.

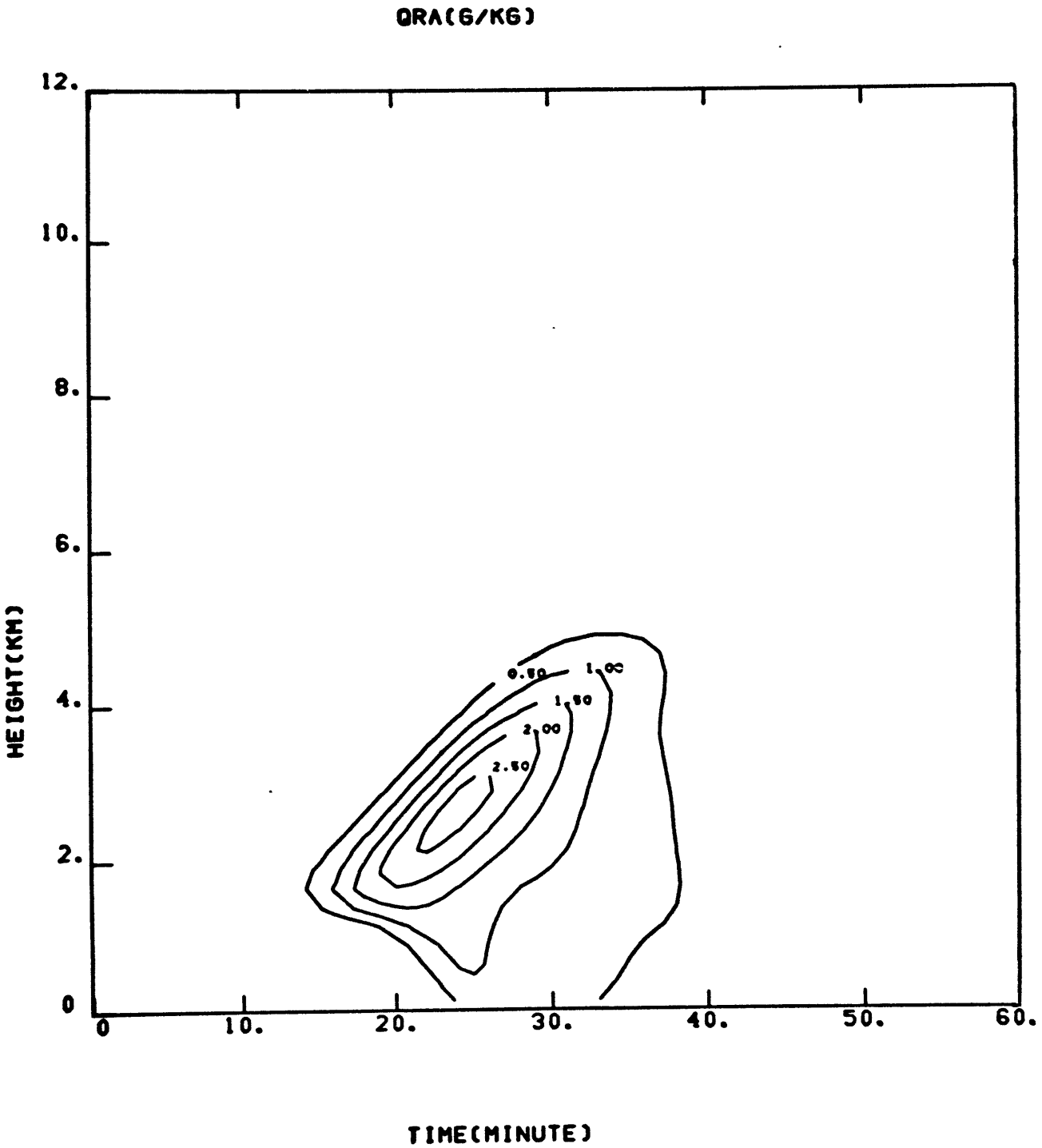


Fig. 5.26. Same as Fig. 5.3 except for experiment E6.

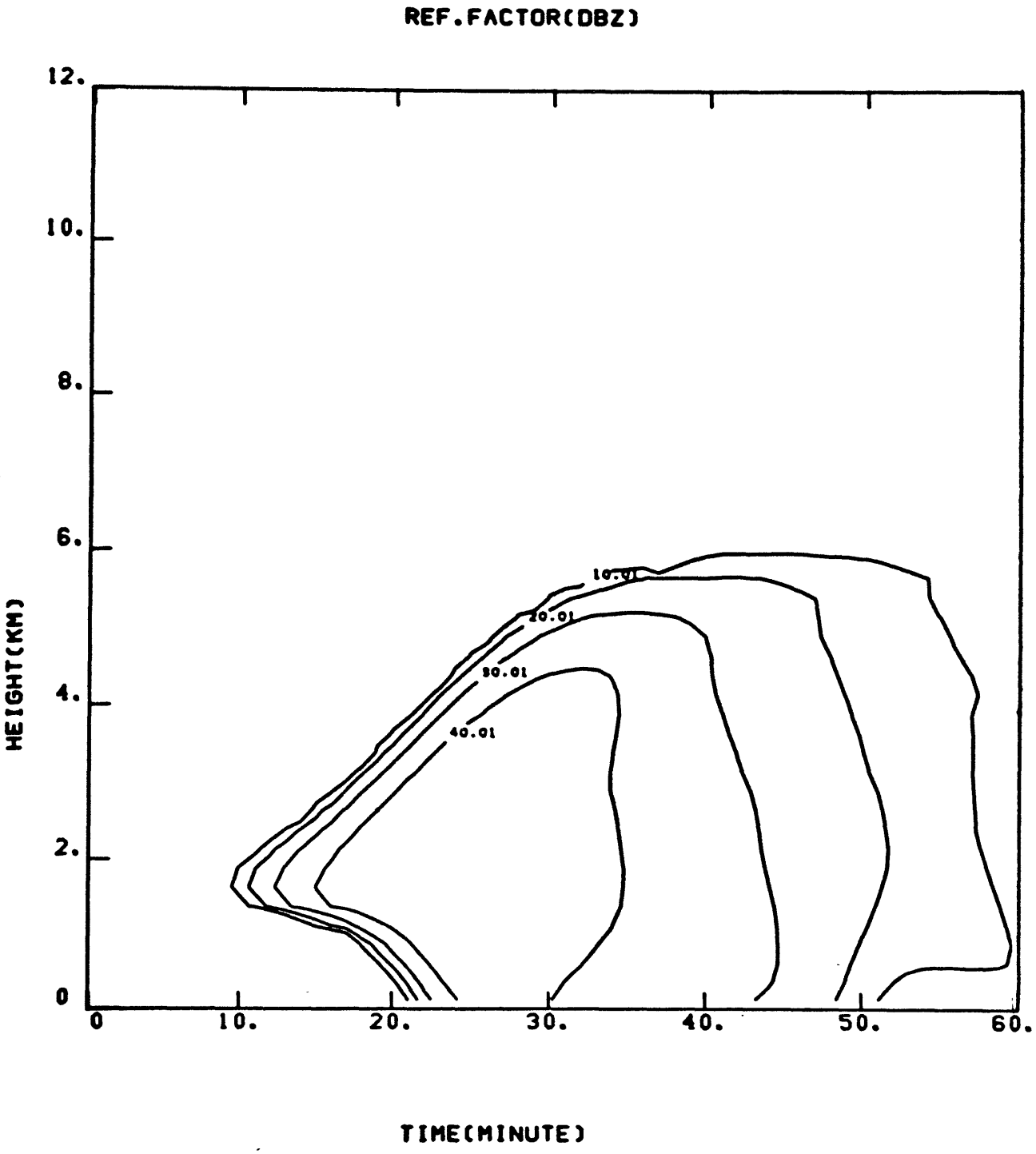


Fig. 5.27. Same as Fig. 5.8 except for experiment E6.

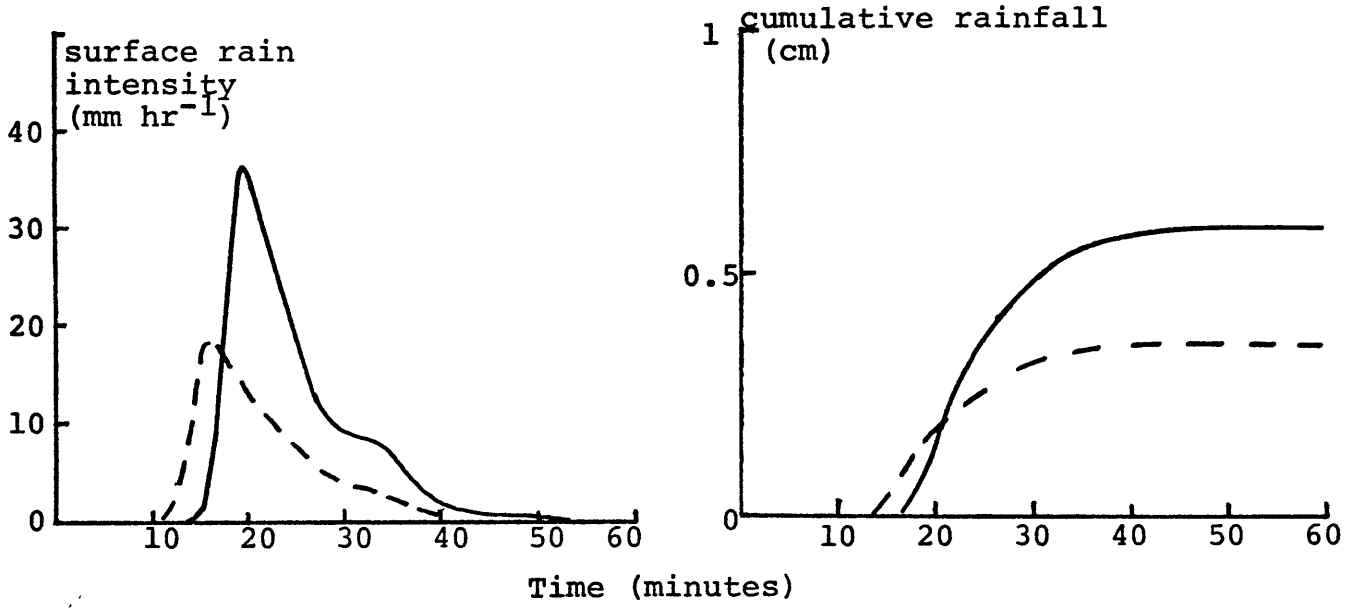


Fig. 5.28. Comparison of rain intensity and cumulative rainfall for model P———————— , and model K— — — — — — — microphysical parameterization.

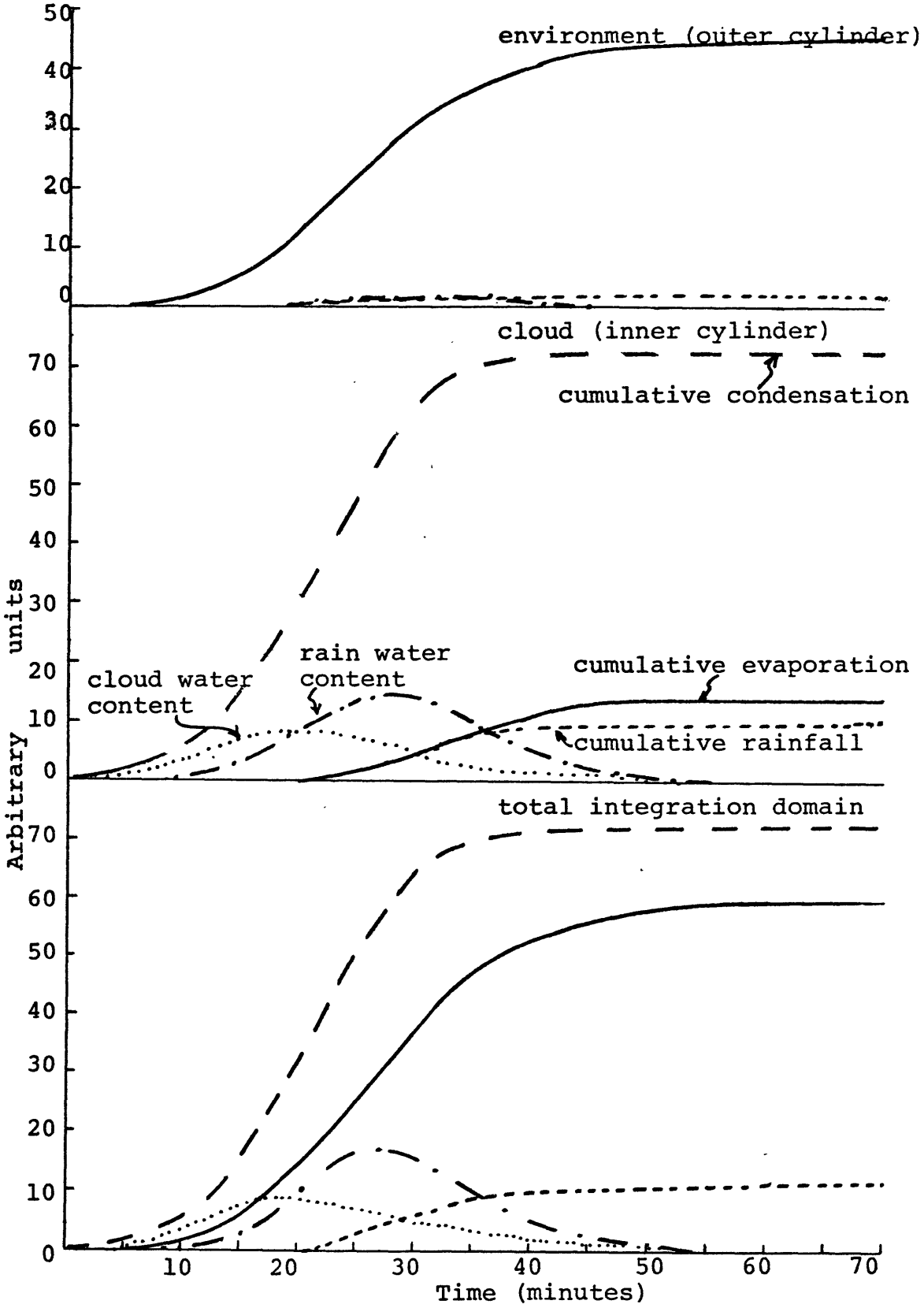


Fig. 5.29. Same as Fig. 5.10 except for experiment E6.

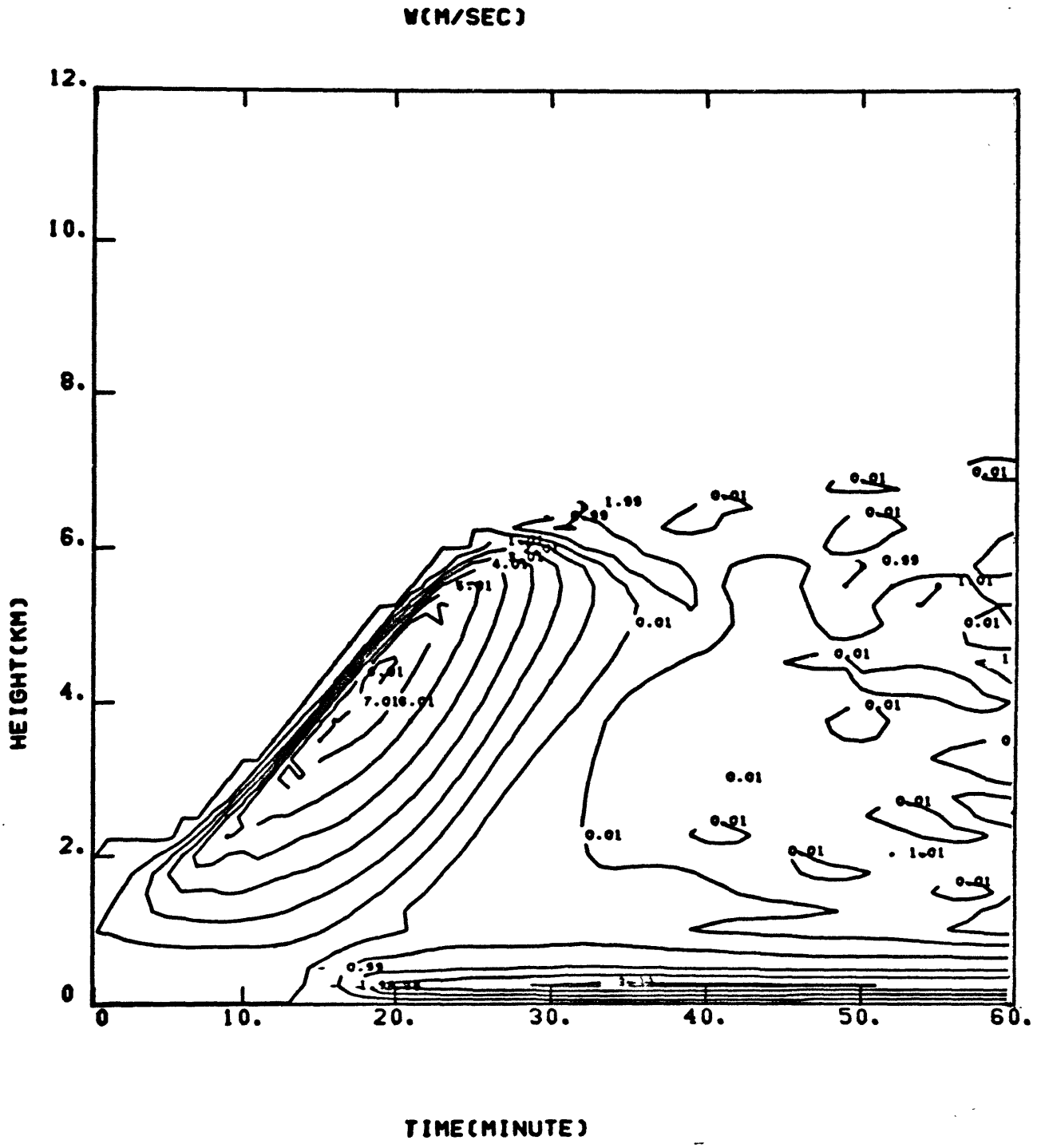


Fig. 5.30. Same as Fig. 5.1 except for experiment E7.

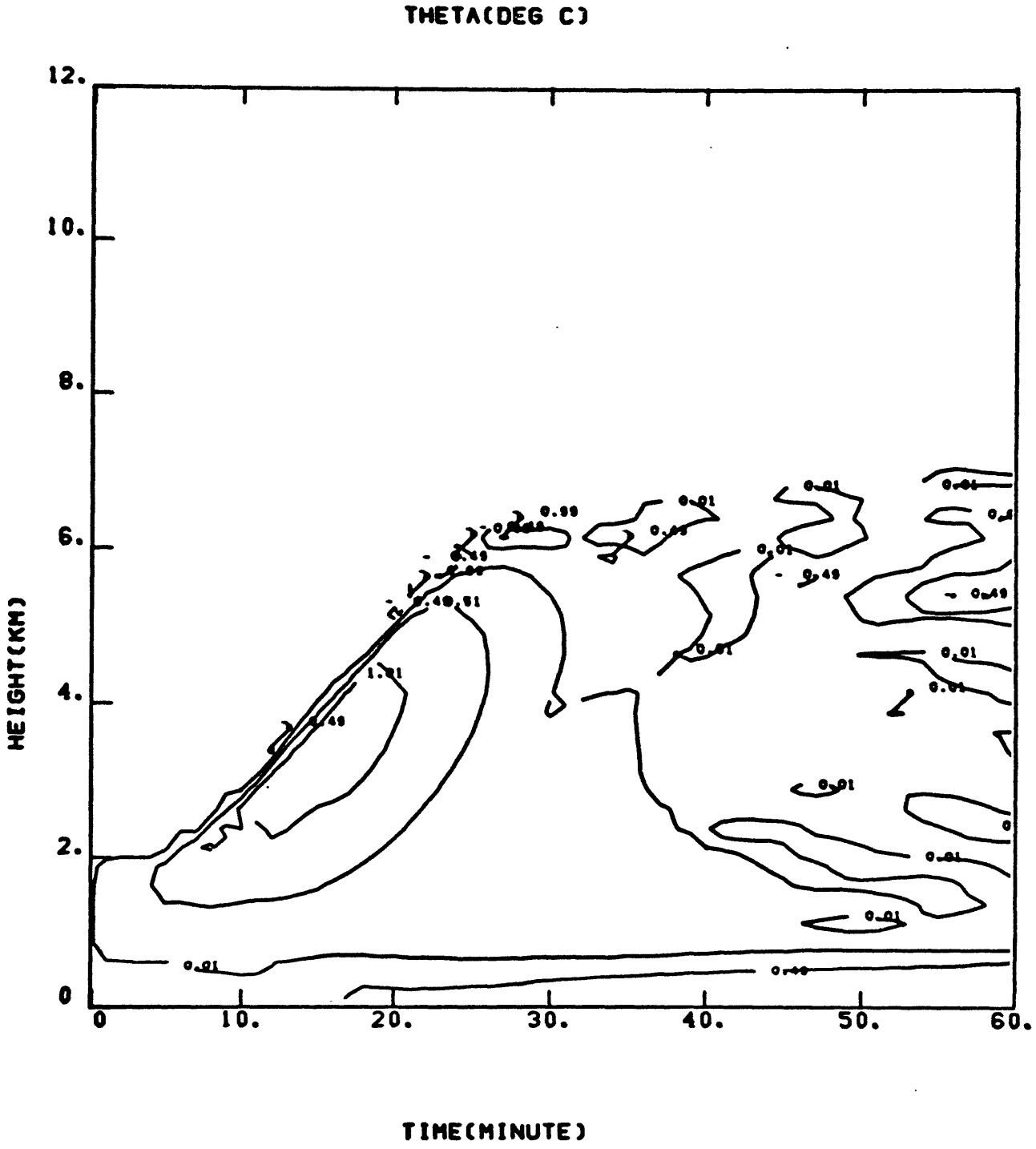


Fig. 5.31. Same as Fig. 5.2 except for experiment E7.

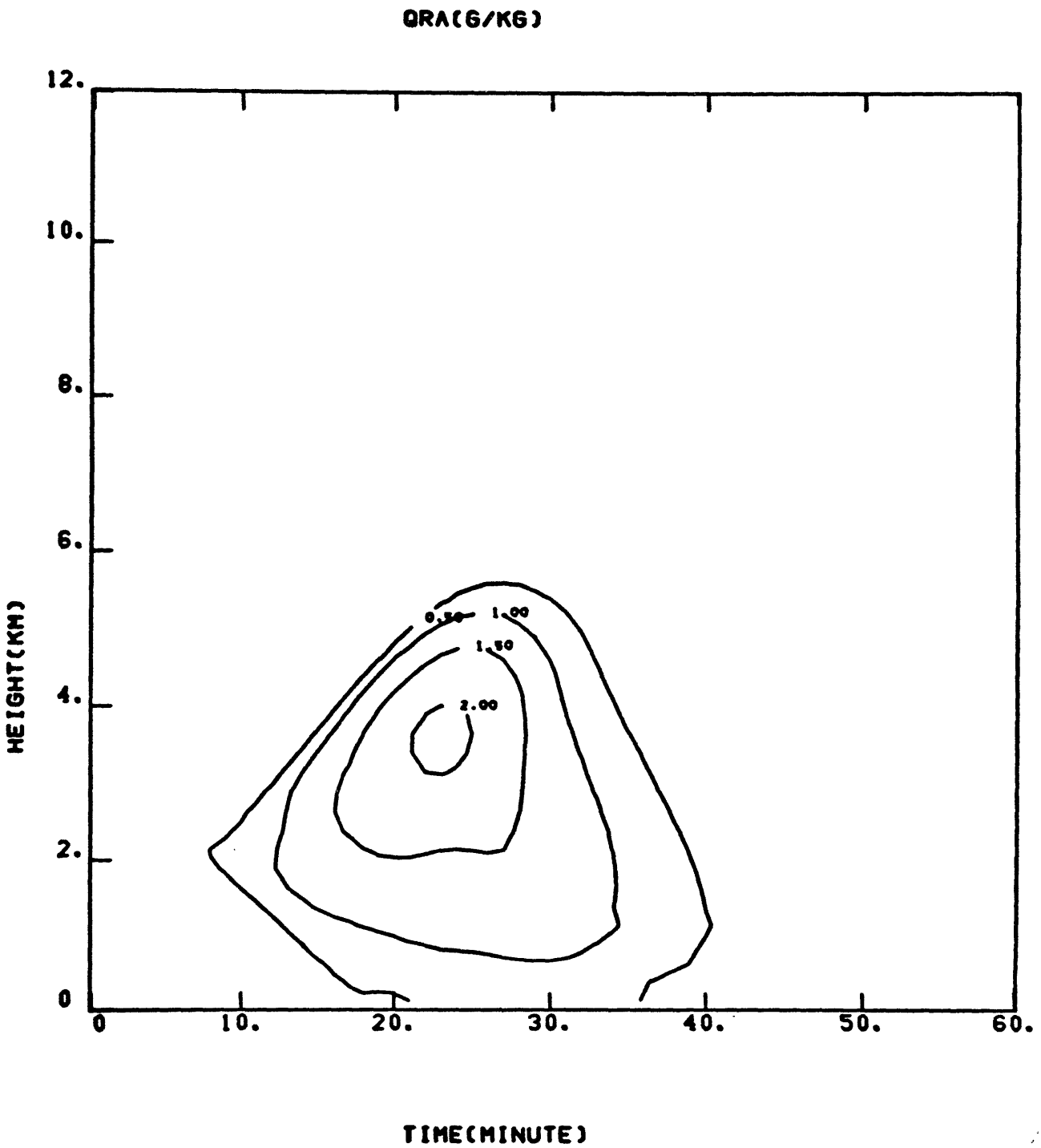


Fig. 5.32. Same as Fig. 5.8 except for experiment E7.

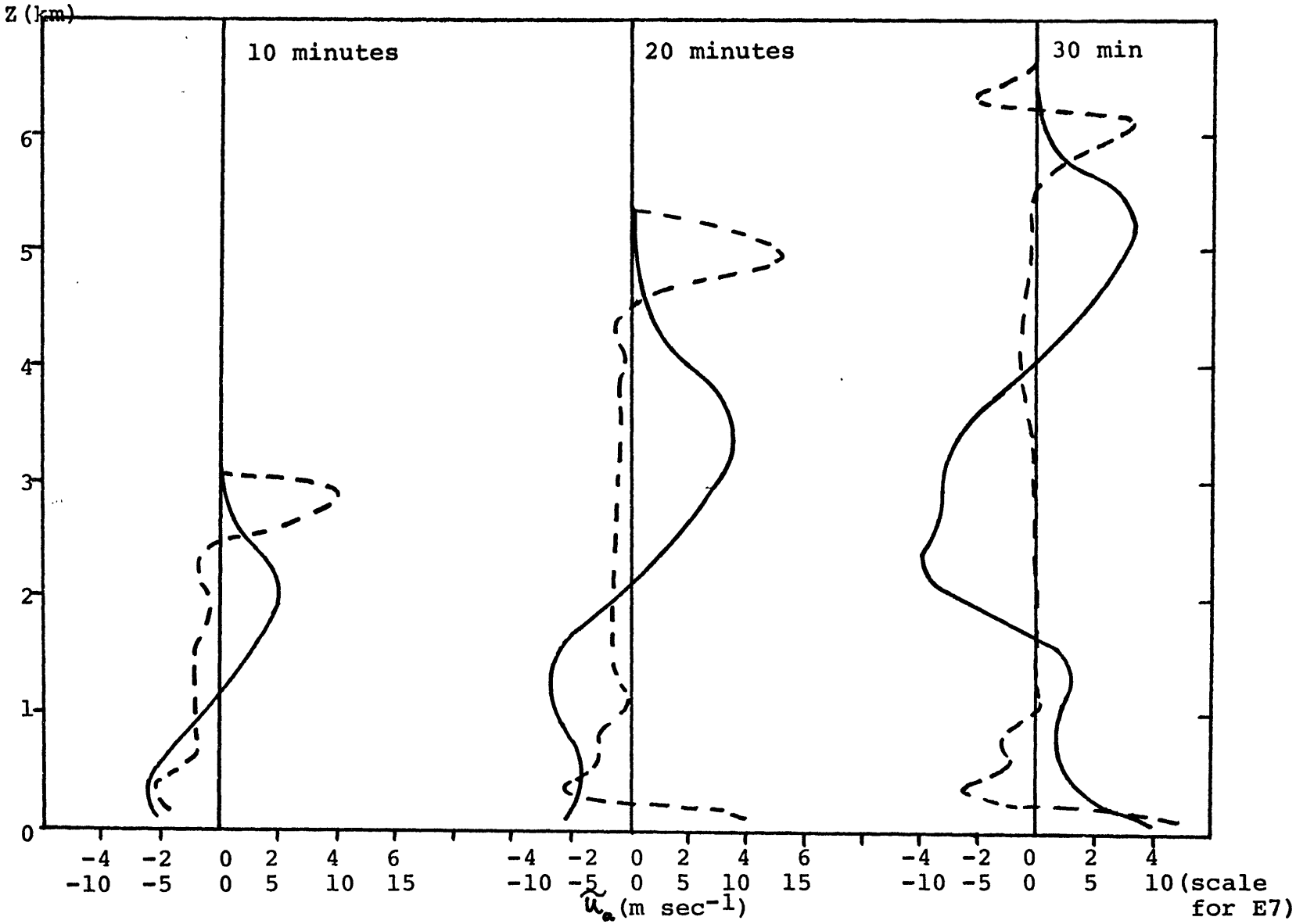
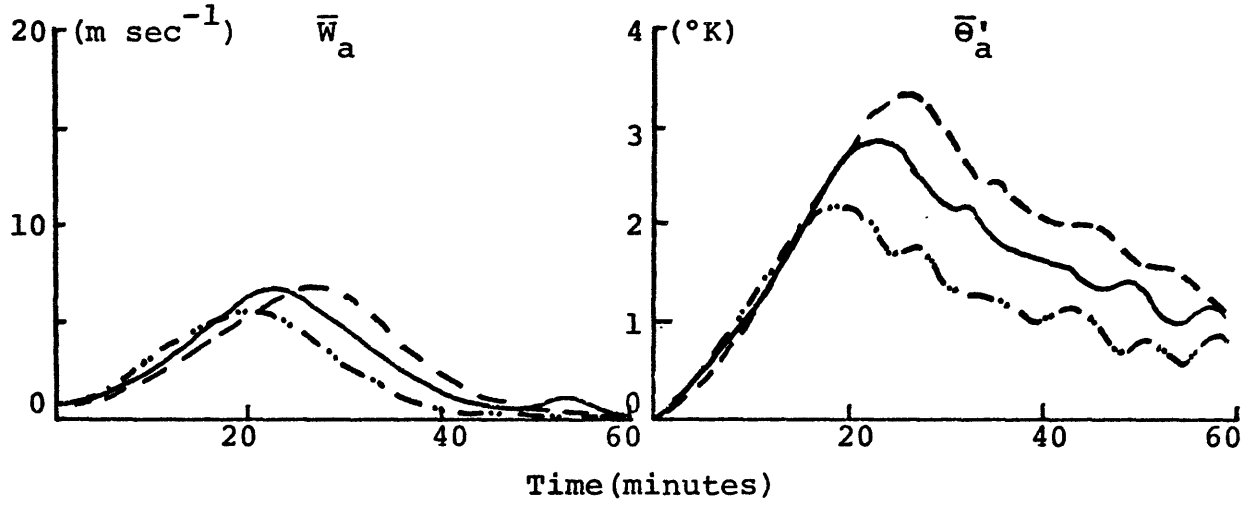


Fig. 5.33. Comparison of radial velocity at the edge of the inner cylinder at 10,20,and 30 minutes for experiments E6 and E7.
E6————————'E7- - - - - - - -·



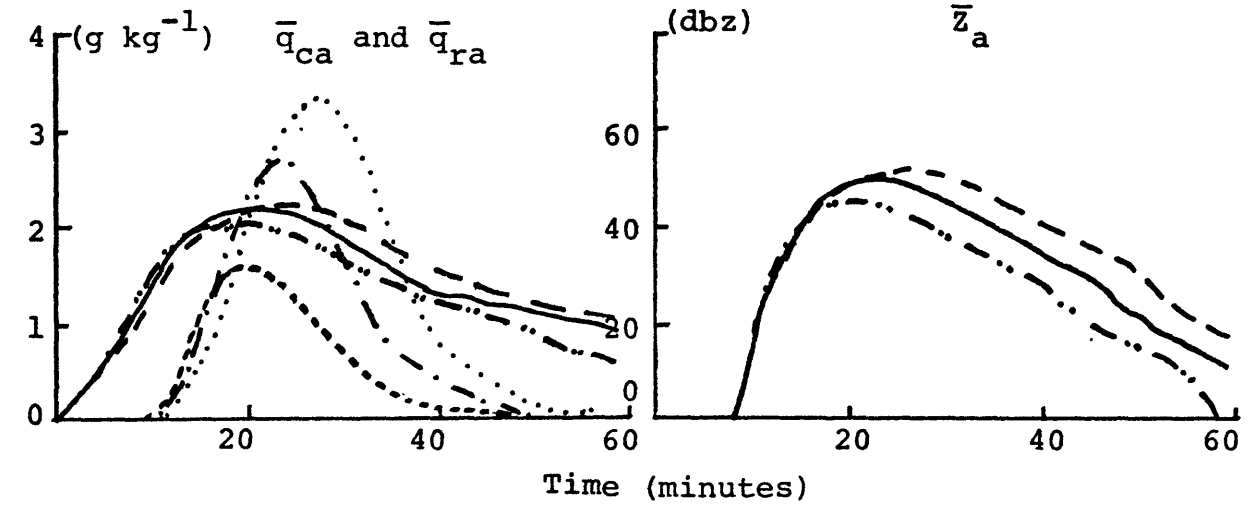


Fig. 5.34. Effect of varying the cloud radius on maximum $\bar{W}_a, \bar{\theta}'_a, \bar{q}_{ca}, \bar{q}_{ra}, \bar{Z}_a$, rainfall intensity, and cumulative rainfall in the inner cylinder.
For $\bar{q}_{ra}$, a=1 km - - ——, a=1.5 km -.-.-.-, a=2 km....
For all other variables, a=1 km -..-..-, a=1.5km———,
a=2km — — —.

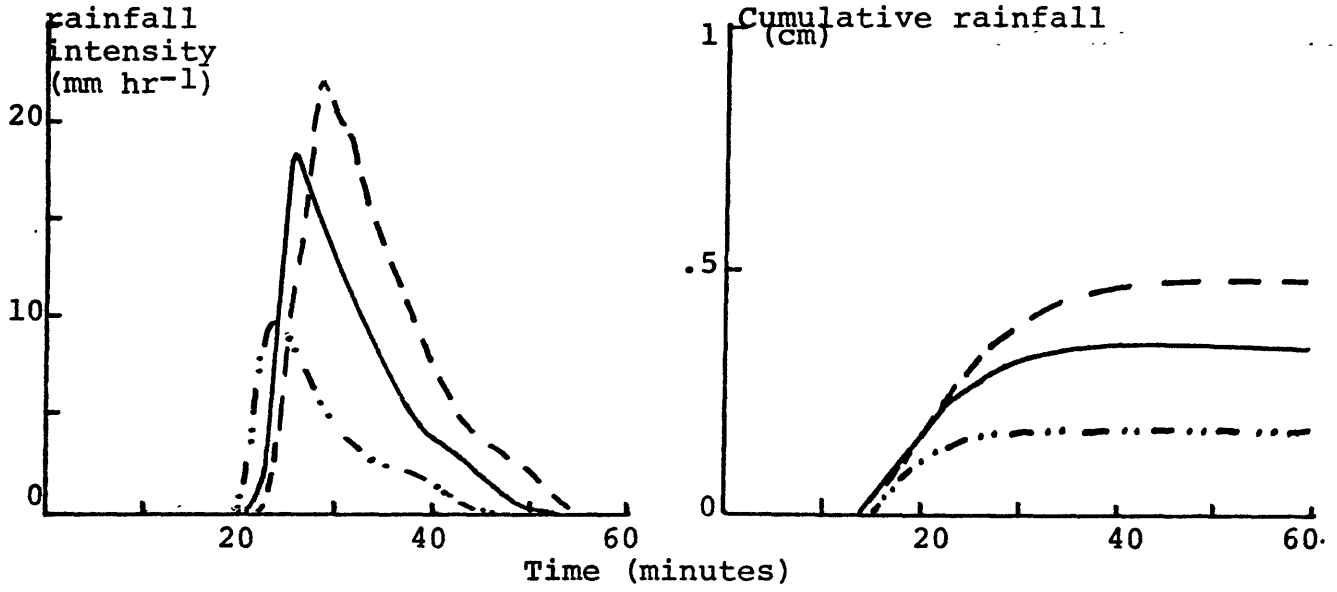
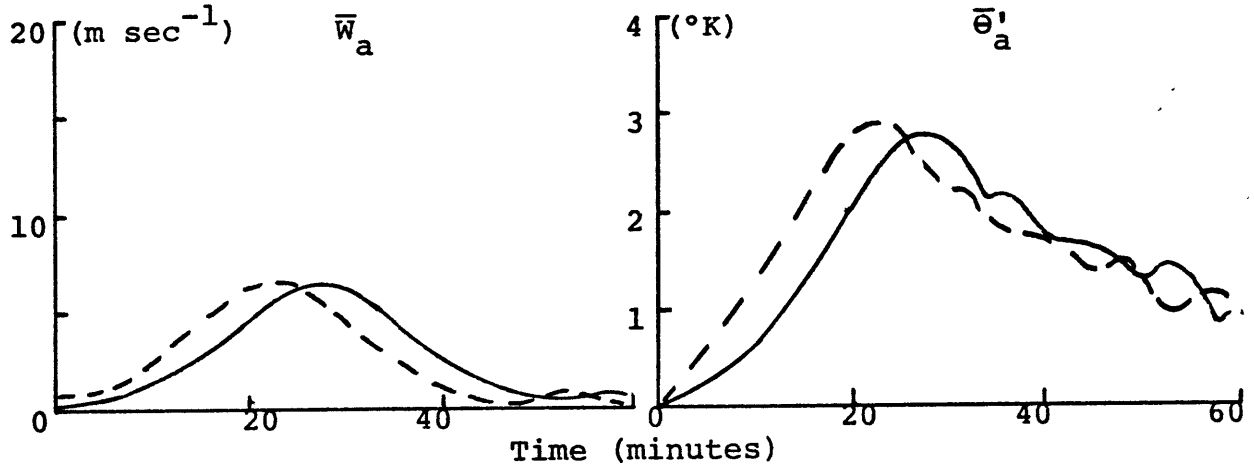

rainfall intensity (mm hr-1)
20
10
0
20
40
60
Time (minutes)
Cumulative rainfall (cm)
1
.5
0
20
40
60

Fig. 5.34. Cont.



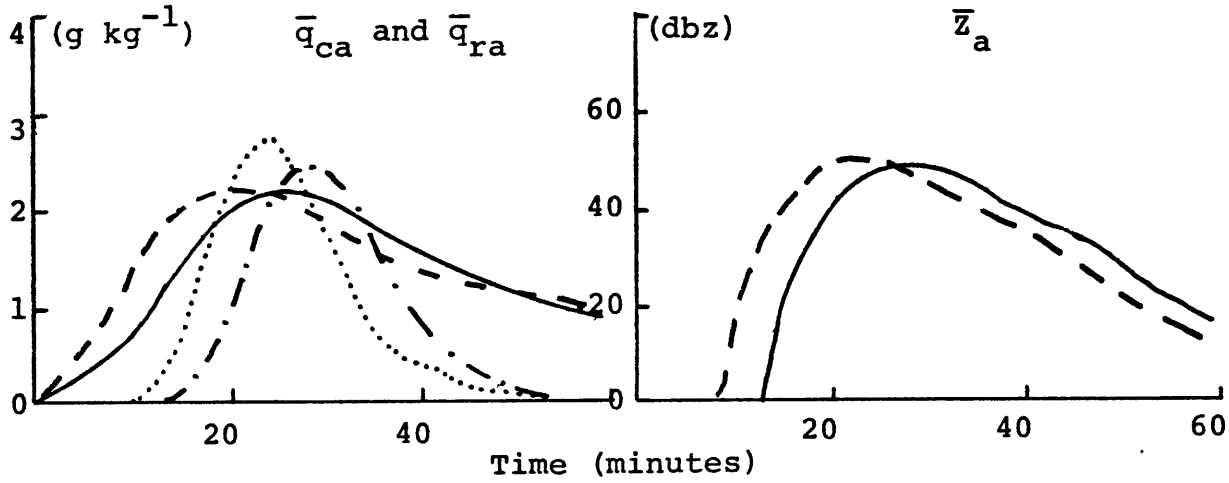
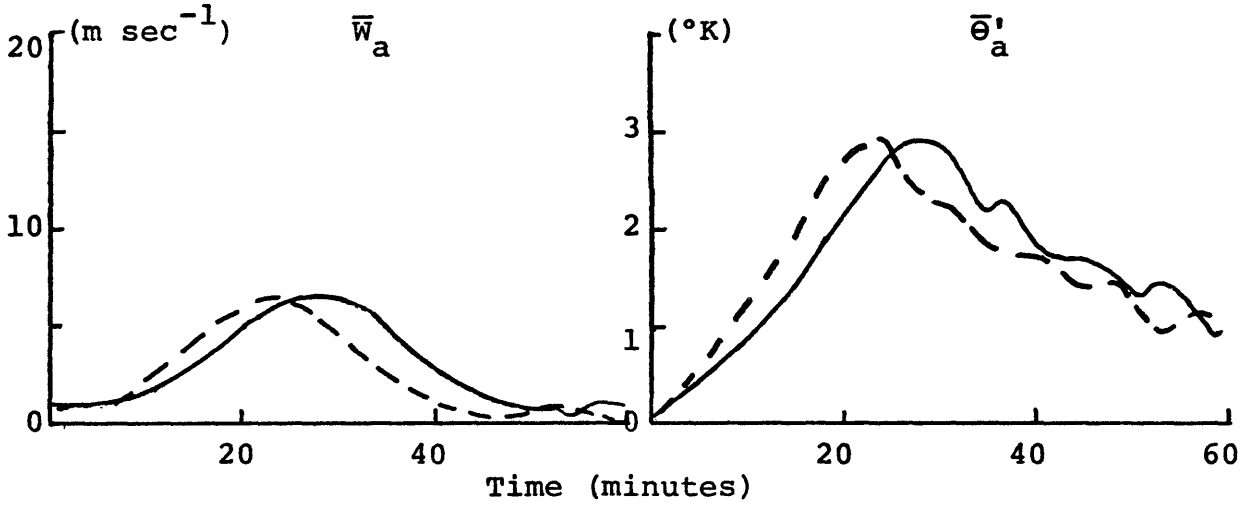


Fig. 5.35. Effect of varying the amplitude of velocity impulse W_o on maximum $\bar{W}_a$, $\bar{\Theta}'_a$, $\bar{q}_{ca}$, $\bar{q}_{ra}$, and $\bar{Z}_a$ in the inner cylinder.
For $\bar{q}_{ra}$, W_o= 1 m sec^{-1} ....., W_o=0.2 m sec^{-1} -.-.-.
For all other variables, W_o=1 m sec^{-1} — — —,
W_o=0.2 m sec^{-1} ————.



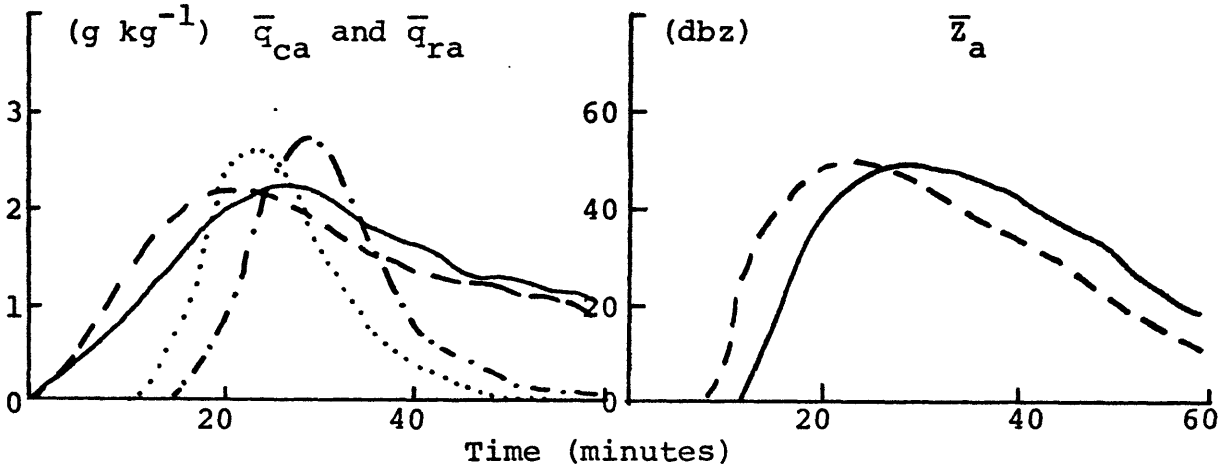


Fig. 5.36. Effect of humidity impulse on maximum $\bar{W}_a$, $\bar{\theta}'_a$, $\bar{q}_{ca}$, $\bar{q}_{ra}$, and $\bar{Z}_a$ in the inner cylinder. For $\bar{q}_{ra}$, no humidity impulse -.-.-.-, with humidity impulse ..... For all other variables, no humidity impulse ————, with humidity impulse — — —.

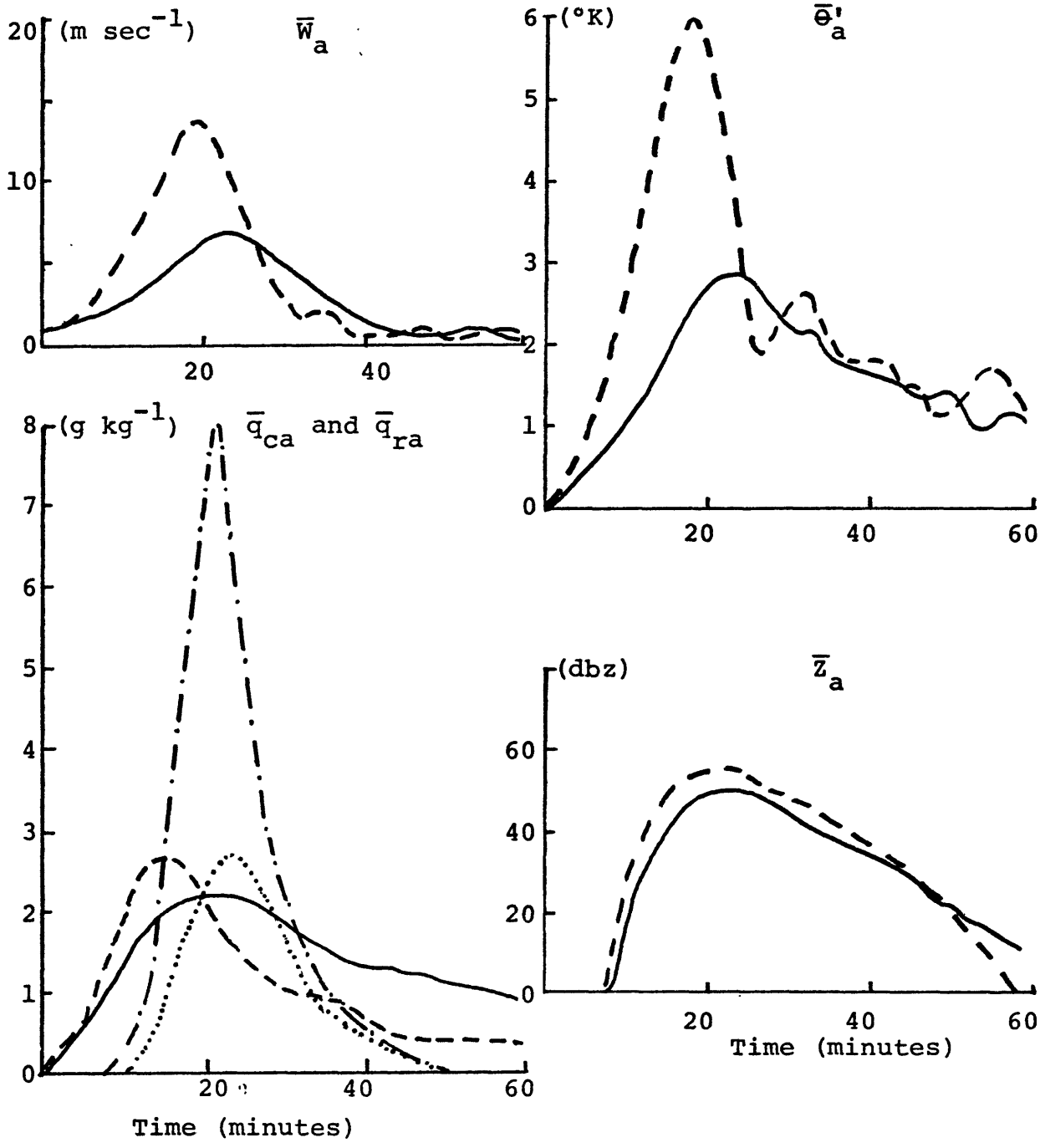
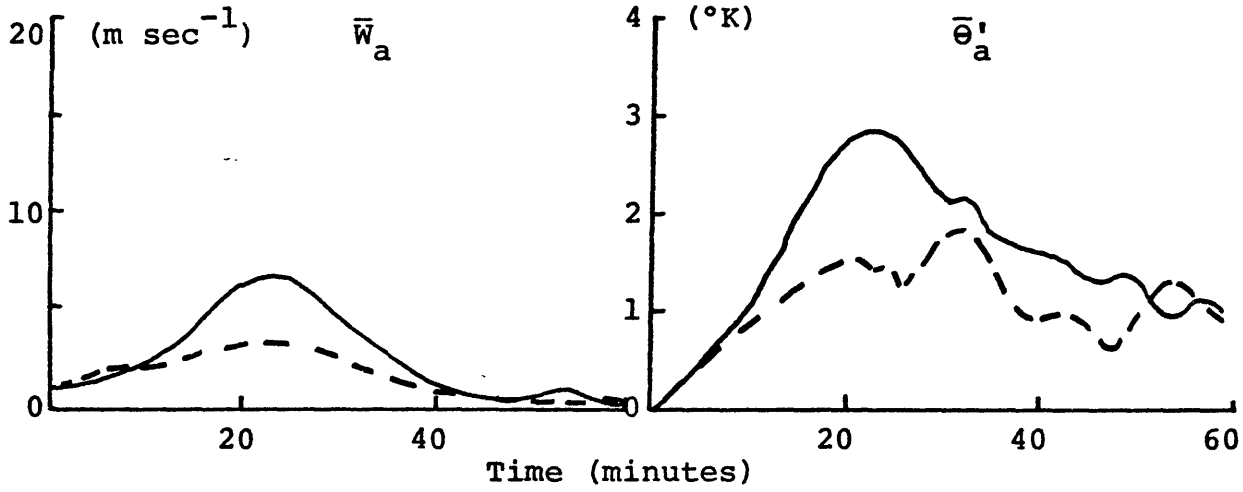


Fig. 5.37. Effect of environmental temperature lapse rate Γ on maximum $\bar{w}_a, \bar{\theta}'_a, \bar{q}_{ca}, \bar{q}_{ra}$, and $\bar{z}_a$ in the inner cylinder. For $\bar{q}_{ra}$, Γ =7°c km^{-1} -.-.-., Γ =6 °c km^{-1} ..... For all other variables, Γ =7°c km^{-1} — — —, Γ =6°c km^{-1} ————.



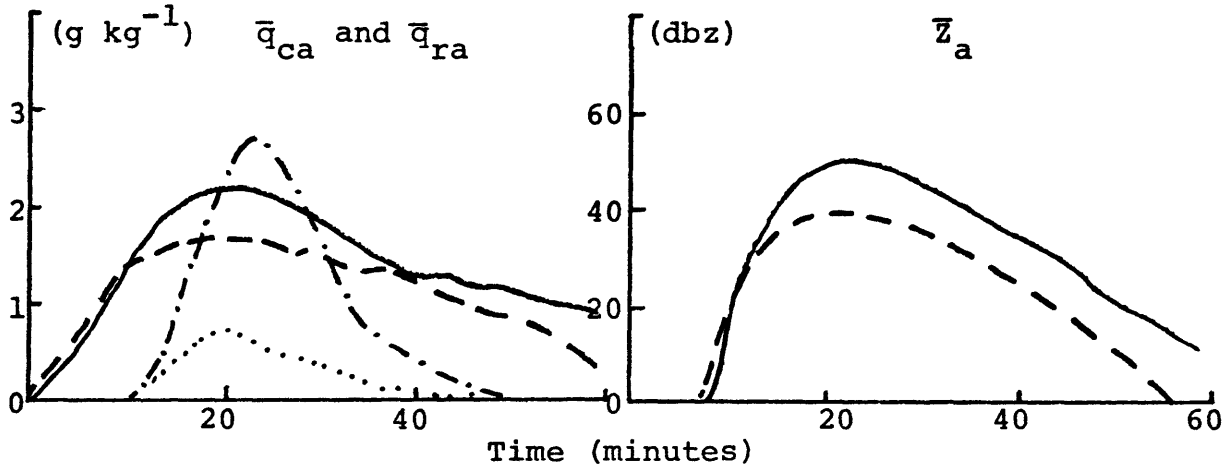
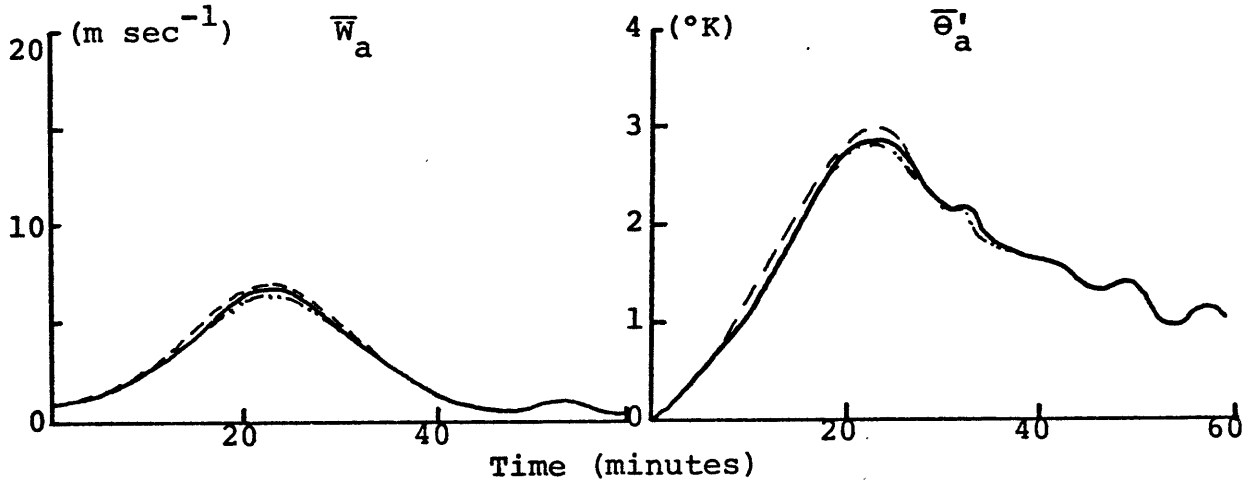


Fig. 5.38. Effect of varying the environmental humidity stratification on maximum $\bar{W}_a$, $\bar{\theta}'_a$, $\bar{q}_{ca}$, $\bar{q}_{ra}$, and $\bar{Z}_a$ in the inner cylinder.
For $\bar{q}_{ra}$, humidity as in idealized sounding -.-.-.,
humidity as in E13 .....
For all other variables, humidity as in idealized sounding ————, humidity as in E13 -- -- --.



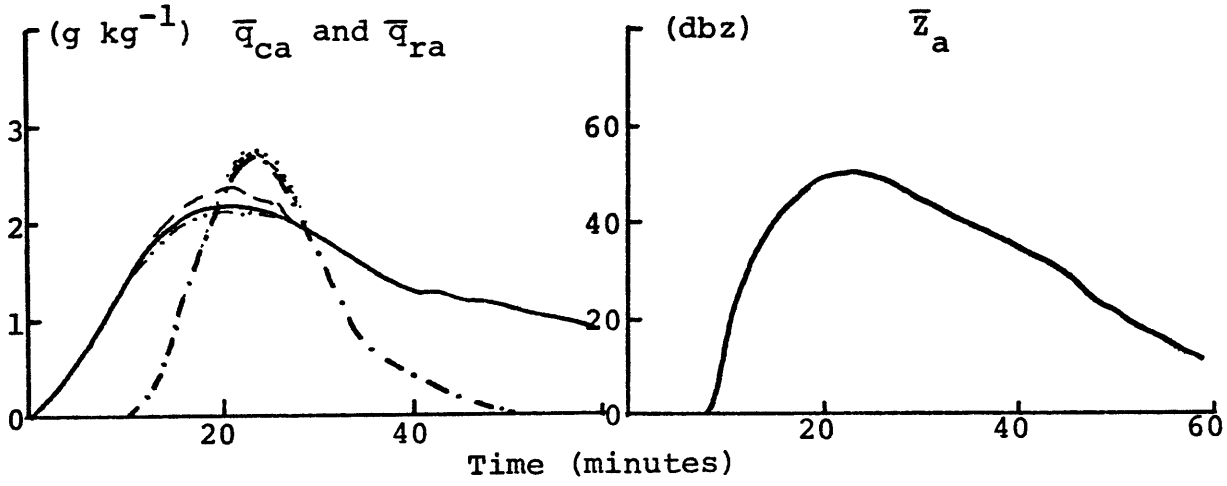
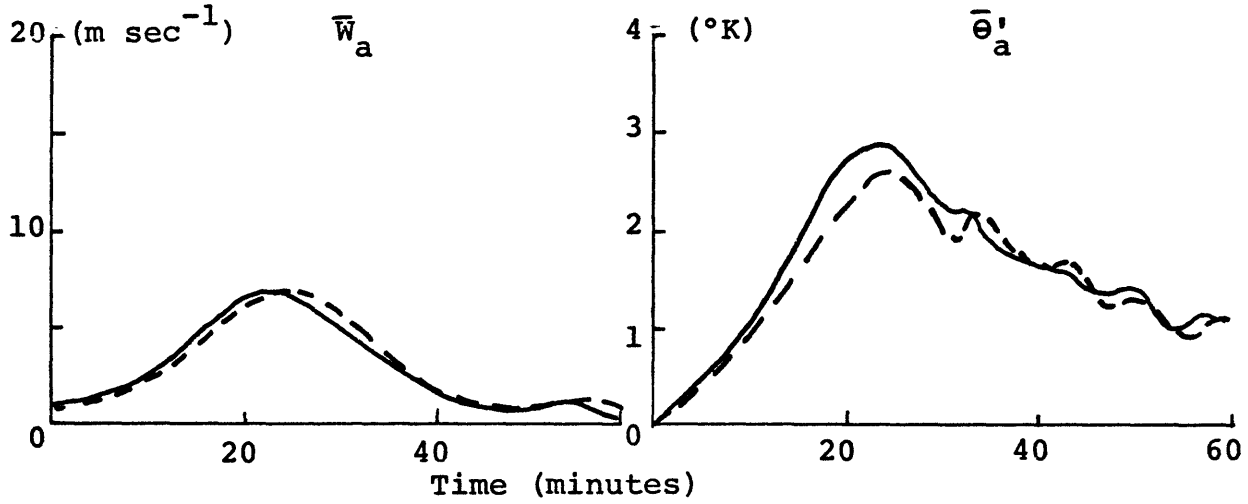


Fig. 5.39. Effect of varying the time step δt on maximum $\overline{W}_a$, $\overline{\Theta}'_a$, $\overline{q}_{ca}$, $\overline{q}_{ra}$, and $\overline{Z}_a$ in the inner cylinder.
For $\overline{q}_{ra}$, δt =5 sec -.-.-., δt =10 sec - - -, δt = 20 sec .....
For all other variables, δt =5 sec -..-..-.., δt = 10 sec ————, δt =20 sec — — —.



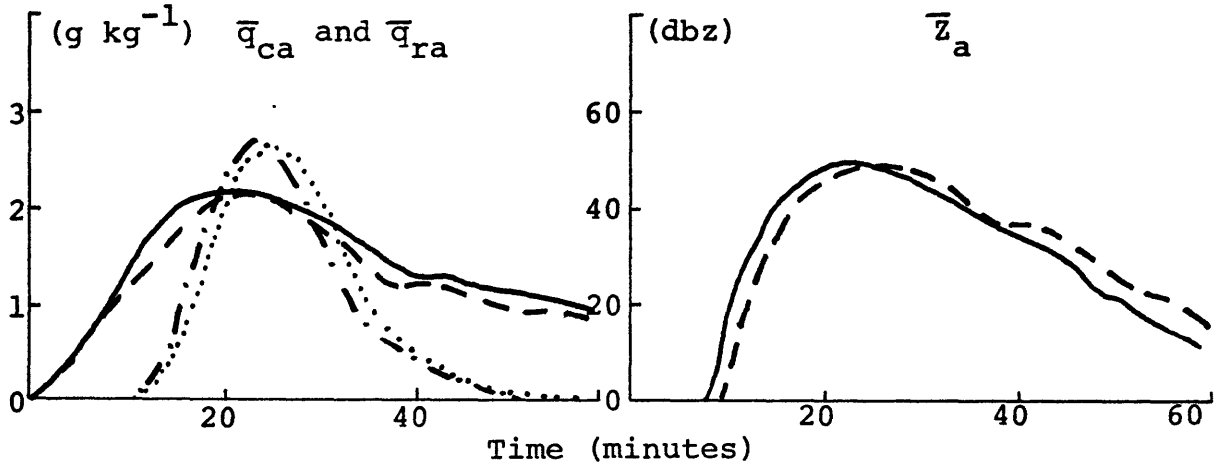


Fig. 5.40. Effect of varying the space increment δz on maximum $\bar{W}_a, \bar{\theta}'_a, \bar{q}_{ca}, \bar{q}_{ra}$, and $\bar{Z}_a$ in the inner cylinder.
For $\bar{q}_{ra}$, δz =500 m ....., δz =250 m-.-.-.-.
For all other variables, δz =500 m— — —,
δz = 250 m————.

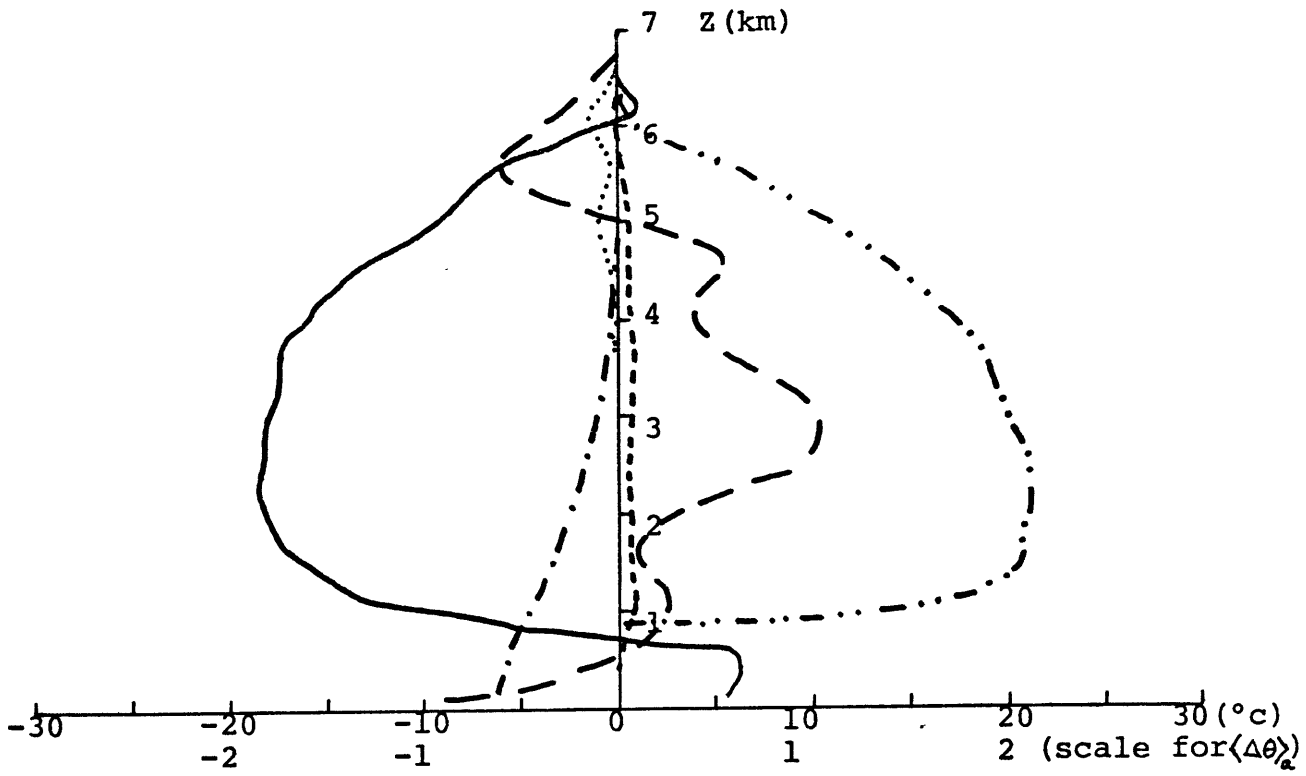


Fig. 6.1. Factors contributing to the temperature change in the cloud for a cloud life-time of one hour.
$\langle -\bar{w}_a \frac{\partial \bar{\theta}_a}{\partial z} \rangle_a$, ----- $\langle \epsilon_\theta \rangle_a$, -.-.-. $-\frac{L}{c_p \bar{\pi}_a} \langle E_r \rangle_a$, — — — $\langle \Delta\theta \rangle_a$,
-..-..- $\frac{L}{c_p \bar{\pi}_a} \langle c \rangle_a$, ... $-\frac{L}{c_p \bar{\pi}_a} \langle E_c \rangle_a$.

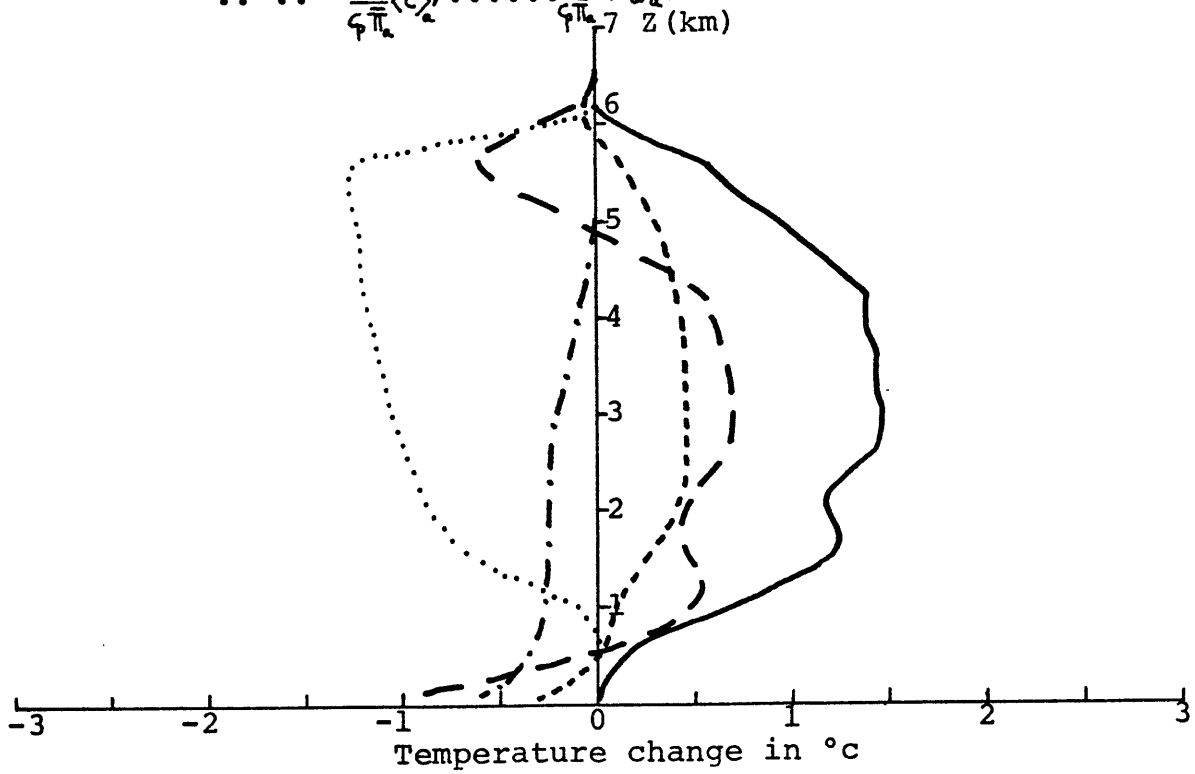


Fig. 6.2. Factors contributing to the temperature change in the environment for a cloud life-time of one hour.
$\langle -\bar{w}_b \frac{\partial \bar{\theta}_b}{\partial z} \rangle_b$, ----- $\langle \epsilon_\theta \rangle_b$, -.-.-. $-\frac{L}{c_p \bar{\pi}_b} \langle E_r \rangle_b$, — — — $\langle \Delta\theta \rangle_b$,
..... $-\frac{L}{c_p \bar{\pi}_b} \langle E_c \rangle_b$

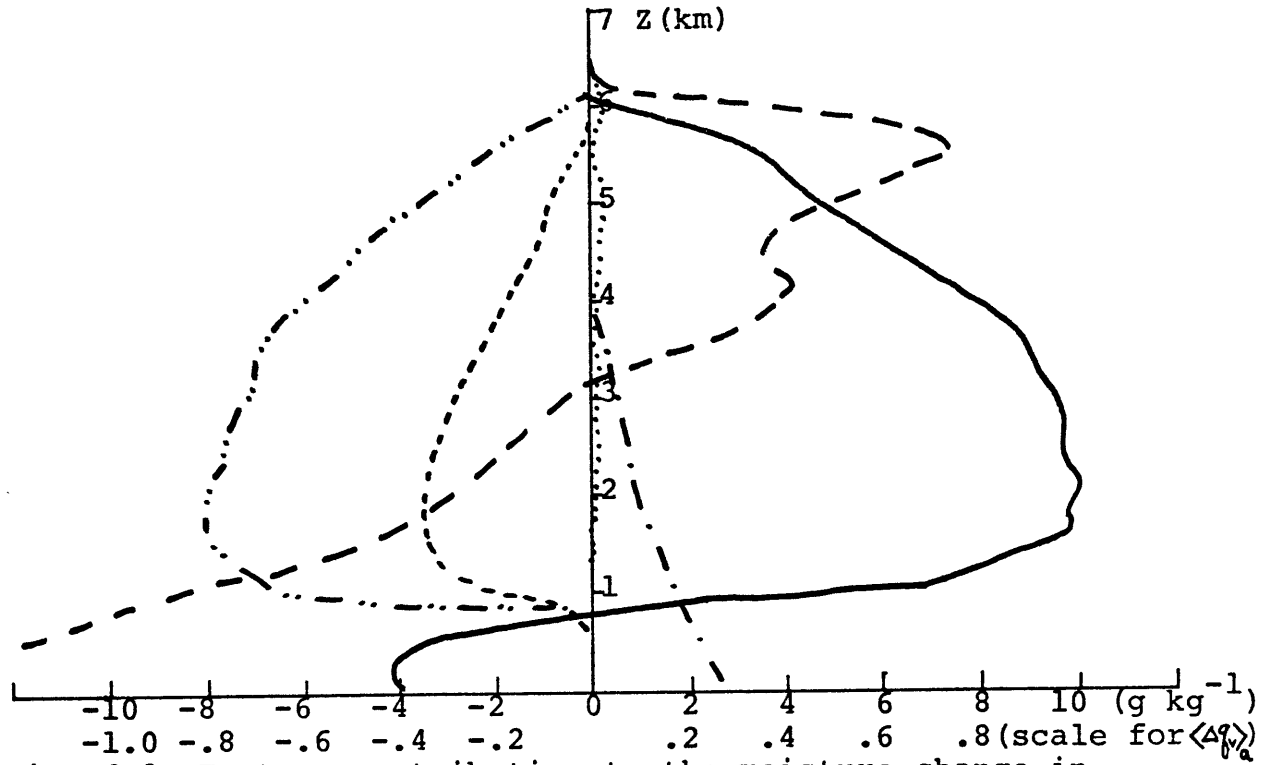


Fig. 6.3. Factors contributing to the moisture change in the cloud for a cloud life-time of one hour.
$\langle -\bar{w}_a \frac{\partial \bar{q}_{va}}{\partial z} \rangle$ ----- $\langle \epsilon_{q_v} \rangle_a$, -.-.- $\langle E_r \rangle_a$, — — — $\langle \Delta q_{fv} \rangle_a$,
-..-..- $\langle c \rangle_a$, ... $\langle E_c \rangle_a$.

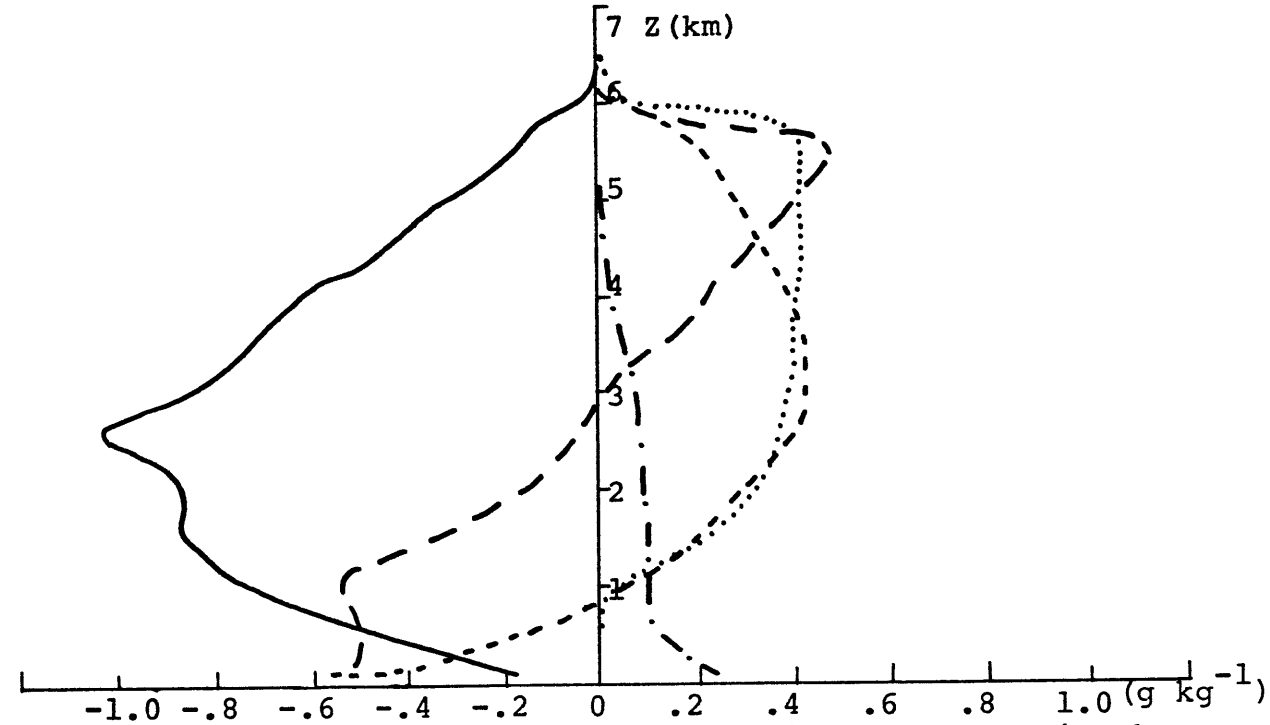


Fig. 6.4. Factors contributing to the moisture change in the environment for a cloud life-time of one hour.
$\langle -\bar{w}_b \frac{\partial q_{vb}}{\partial z} \rangle_b$, ----- $\langle \epsilon_{q_v} \rangle_b$, -.-.- $\langle E_r \rangle_b$, — — — $\langle \Delta q_{fv} \rangle_b$,
. . . . . $\langle E_c \rangle_b$.

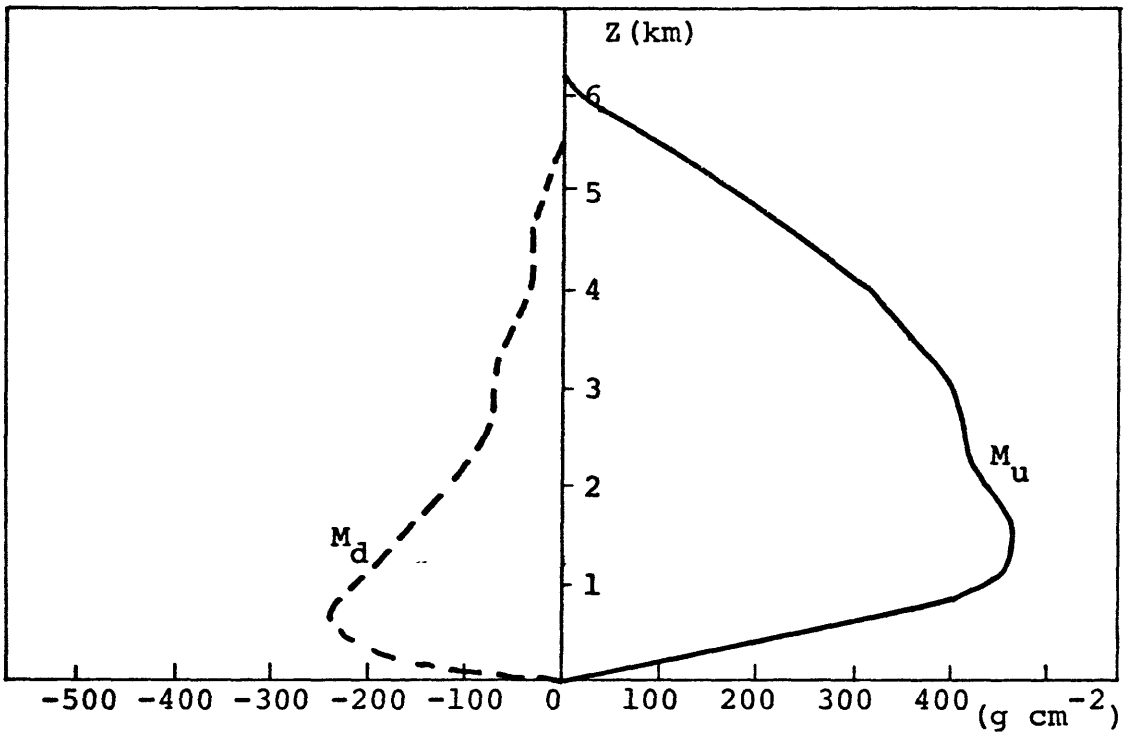


Fig. 6.5. Mass flux per unit area integrated over a cloud life-time of one hour.

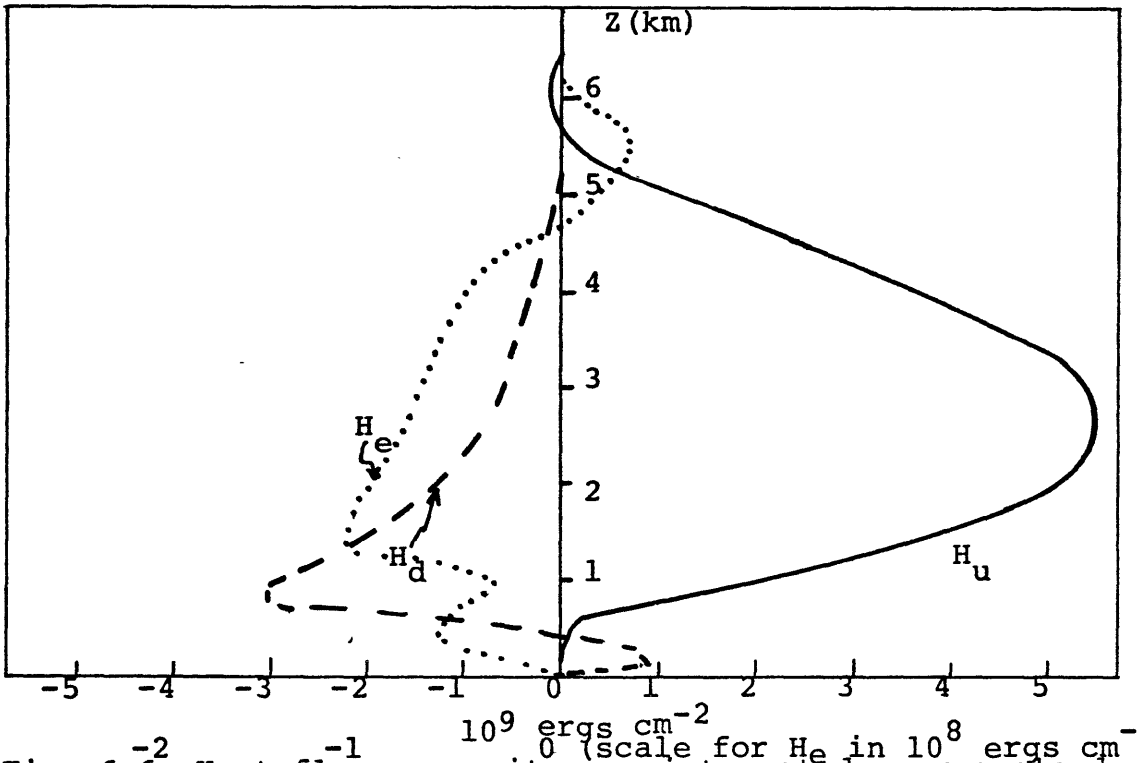


Fig. 6.6. Heat flux per unit area integrated over a cloud life-time of one hour.

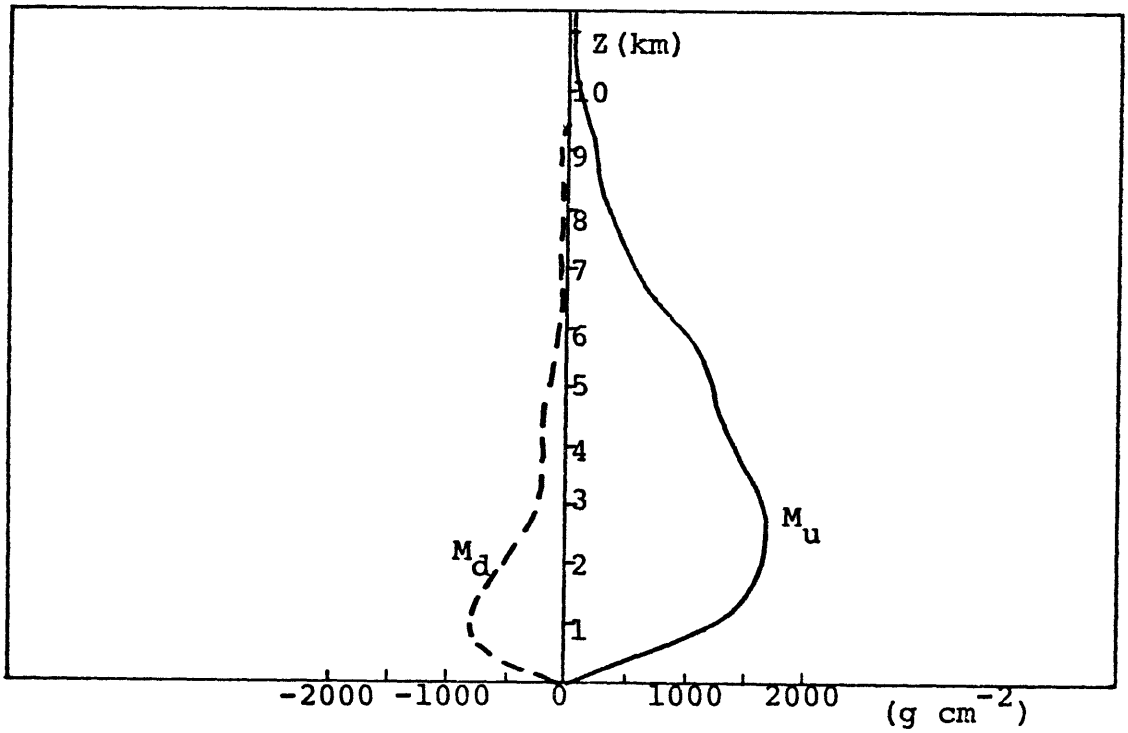


Fig. 6.7. Average monthly mass transport by cumulus clouds at Boston for the month of July.

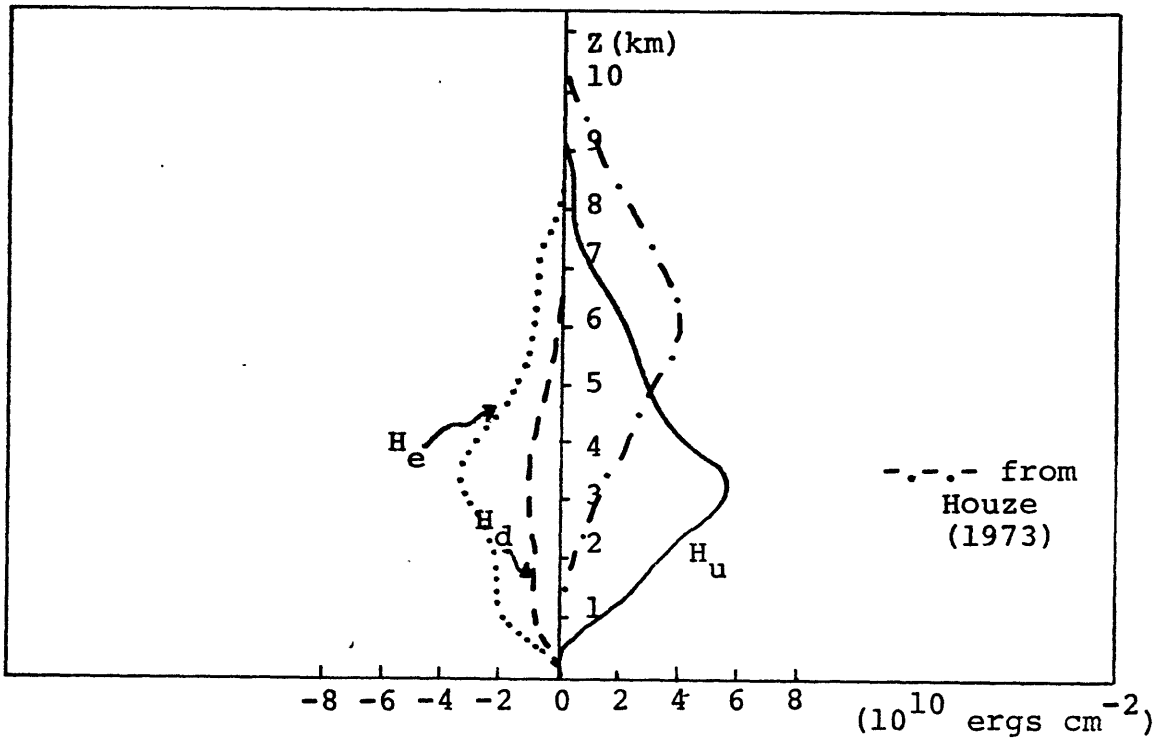


Fig. 6.8. Average monthly sensible heat transport by cumulus clouds at Boston for the month of July. The scale for H_e is in 10^9 ergs cm^{-2}.

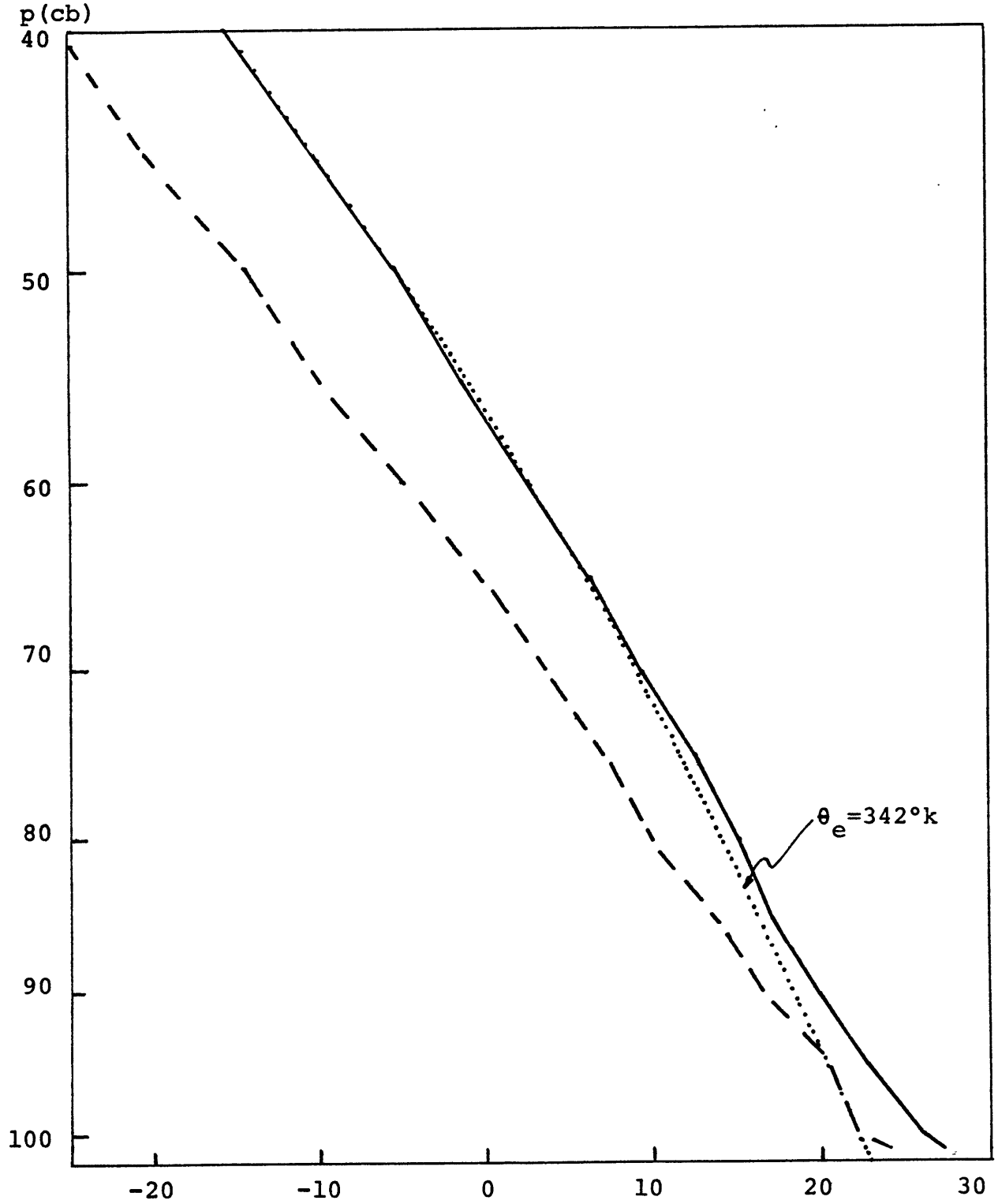


Fig. 6.9. Monthly mean sounding for Majuro, Marshall Islands in July, 1975. Sounding taken at 0000 GMT.

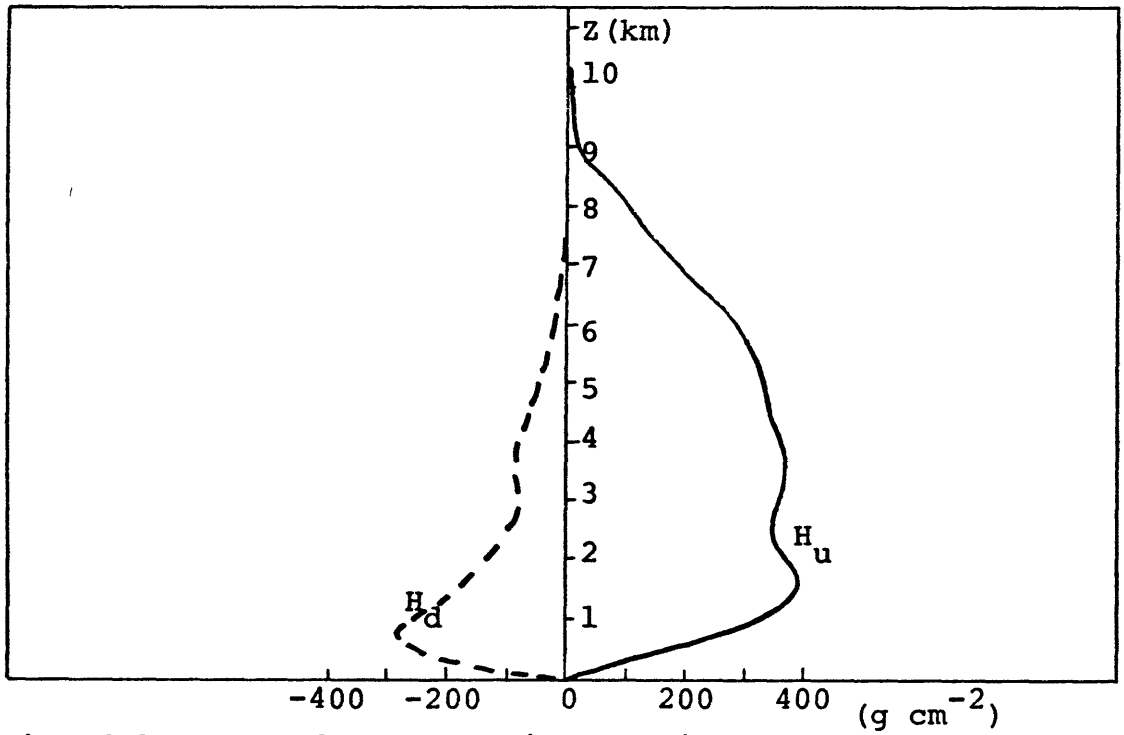


Fig. 6.10. Mass flux per unit area integrated over a cloud life-time of one hour with the sounding in fig. 6.9.

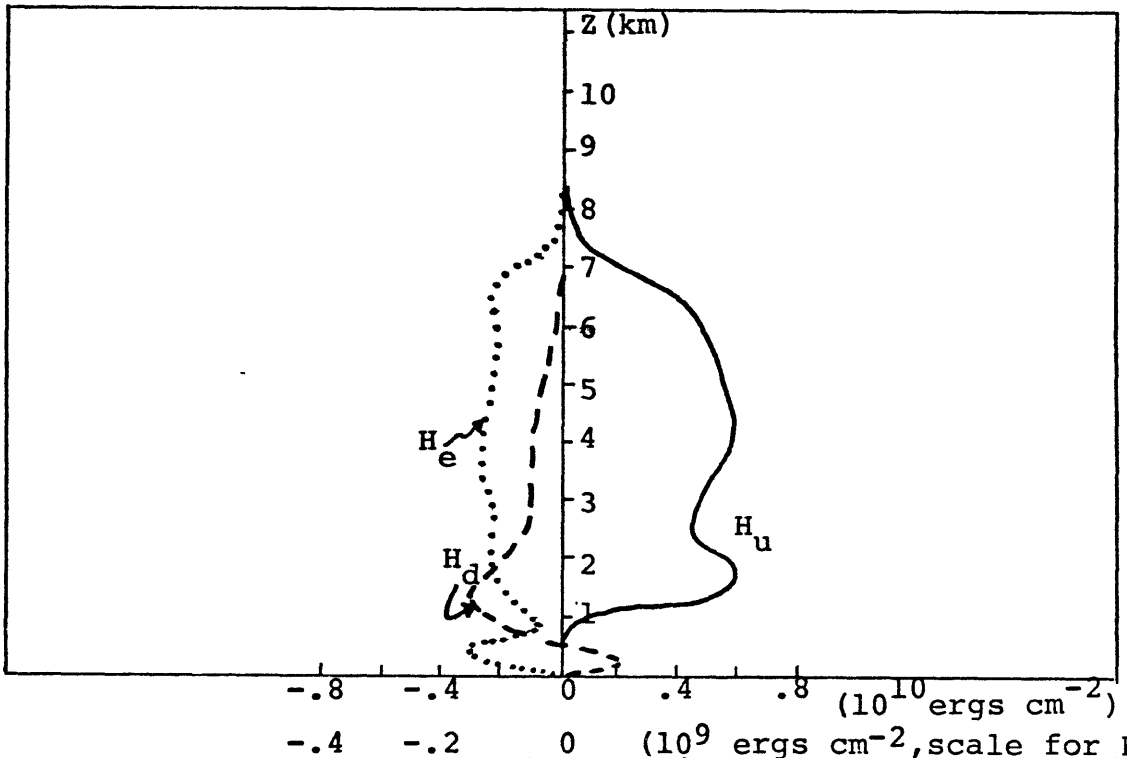


Fig. 6.11. Heat flux per unit area integrated over a cloud life-time of one hour with the sounding in fig. 6.9.

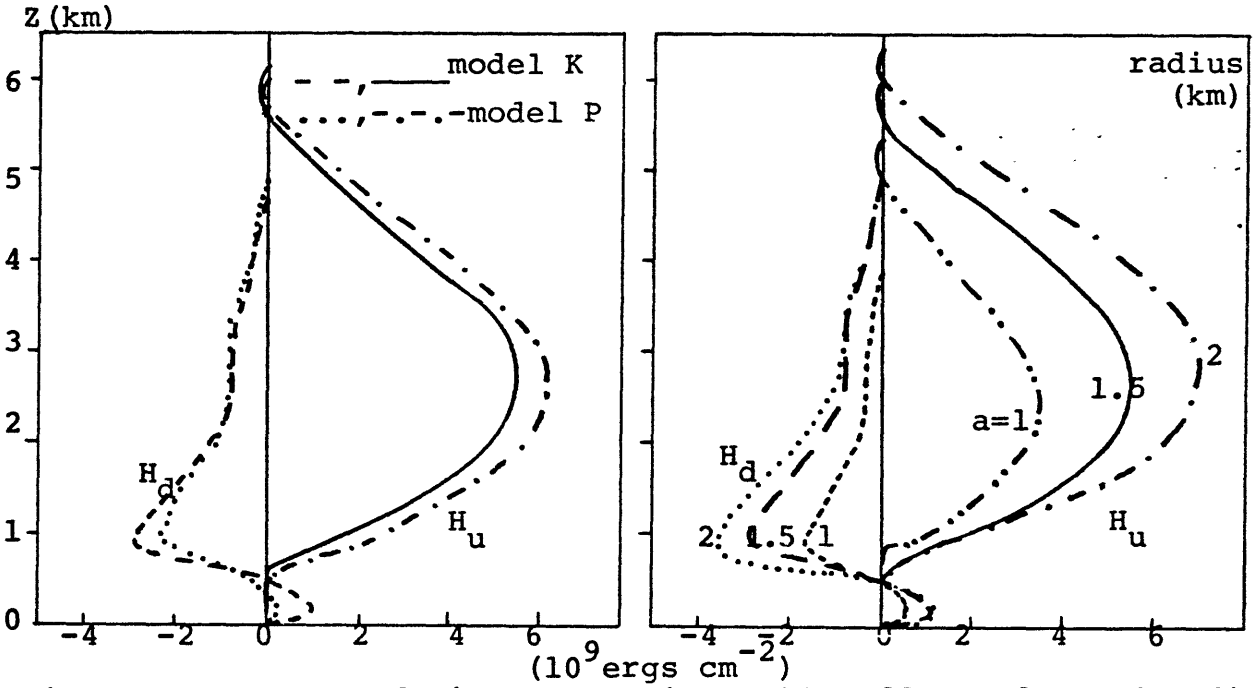


Fig. 6.12. Effect of microphysical parameterization on time-integrated heat flux for a cloud life-time of 70 min.

Fig. 6.13. Effect of cloud radius on time-integrated heat flux for a cloud life-time of 70 min.

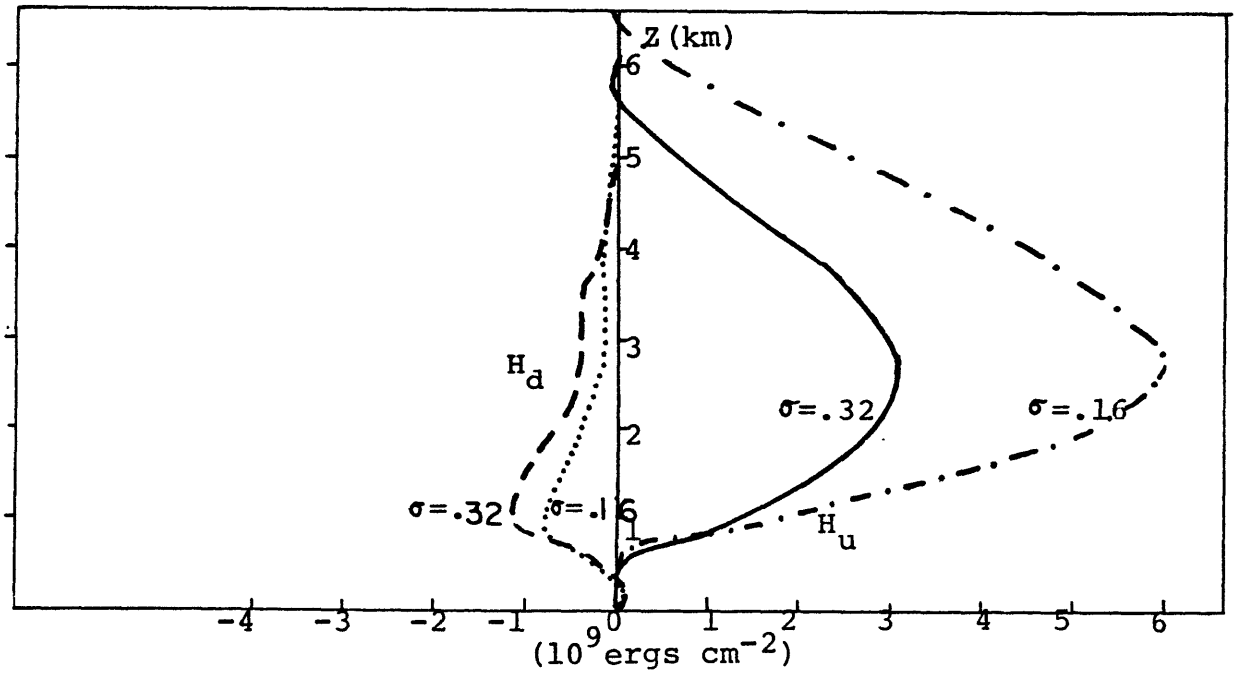


Fig. 6.14. Effect of radii ratio σ, on time-integrated heat flux for a cloud life-time of 70 min. Model P microphysics used.

APPENDIX 2.1

Condensation and evaporation of cloud droplets

Consider an air parcel with potential temperature θ^*, non-dimensional pressure π, vapor and cloud mixing ratio q_v^* and q_c^*. The calculation of condensation and evaporation for cloud droplets is described by the following procedure.

I. The saturation mixing ratio q_s^* corresponding to a temperature $T^* = \pi\theta^*$ is evaluated from Teten's (1938) formula

$$q_s^* = \frac{3.8}{P} \times 10^{7.5(T-273)/(T-36)} \tag{1}$$

where P is the pressure in mb.

II. $\delta M = q_v^* - q_s^*$ is then calculated. The air is supersaturated if $\delta M > 0$. However only part of δM, δM_1, is condensed; the release of latent heat increases the temperature and the saturation mixing ratio and a residue δM_2 remains in vapor form. Thus,

$$\delta M_2 = \delta M - \delta M_1 \tag{2}$$

The change in potential temperature from condensation is

$$\delta\theta = \frac{L_v}{c_p \pi} \delta M_1 \tag{3}$$

and δM_2 is related to $\delta\theta$ by the Clausius-Claperon equation as

$$\delta M_2 = \frac{L_v}{R_v}\frac{q_s^*}{\pi\theta^{*2}}\delta\theta \tag{4}$$

Eliminating δM_2 and $\delta\theta$ from (2), (3) and (4) gives

$$\delta M_1 = \frac{q_v^* - q_s^*}{\left[1+\frac{L^2}{C_p R_v}\frac{q_s^*}{(\pi\theta^*)^2}\right]} \tag{5}$$

The adjustment for cloud and vapor becomes

$$\begin{aligned} q_v &= q_v^* - \delta M_1 \\ q_c &= q_c^* + \delta M_1 \end{aligned} \tag{6}$$

III. In the event that $\delta M < 0$ and $q_c^* > 0$, the air is subsaturated and evaporation of cloud occurs. The same procedure in step II applies if cloud is present in sufficient quantity to saturate the air. Otherwise all cloud water will be evaporated and further evaporation from raindrops and wet graupel particles is necessary. The adjustment in this case is:

$$\begin{aligned} q_v &= q_v^* + q_c^* \\ q_c &= 0 \end{aligned} \tag{7}$$

APPENDIX 2.2

This appendix describes the method in determining the modes of growth and the calculation of the melting of graupel particles.

I. Growth modes

Under equilibrium conditions and neglecting the collection of cloud ice, two modes of growth for graupel particles are possible.

(a) Dry growth

The ambient temperature, water content, and heat transfer rate are such that the graupel is at a temperature below 0^{o}c. The surface of the graupel is dry; its temperature is greater than that of the ambient air, and all collected water drops freeze.

(b) wet growth

The surface temperature of the graupel is 0^{o}c. Heat transfer by conduction and convection, evaporation and deposition is unable to get rid of the heat added through freezing of supercooled water present on the surface of the graupel. The surface is therefore wet and part of the graupel remains unfrozen.

II. Determination of growth modes and melting

The growth modes are determined from the mass and heat transfer equations as follows:

Let $\rho_0 \hat{q}_r$ be the graupel content of the category with median radius R. $\rho_0 \hat{q}_r$ has a water portion $\rho_0 \hat{q}_{rw}$ and ice portion $\rho_0 \hat{q}_{ri}$.

The rate of growth of graupel is influenced by collection of supercooled water drops and by evaporation and deposition given as:

$$\frac{d}{dt}(\rho_0 \hat{q}_r) = \left.\frac{d}{dt}(\rho_0 \hat{q}_r)\right|_{\text{collection}} + \left.\frac{d}{dt}(\rho_0 \hat{q}_r)\right|_{\text{depo./evp.}} \quad (1)$$

where

$$\left.\frac{d}{dt}(\rho_0 \hat{q}_r)\right|_{\substack{\text{depo./}\\ \text{evp.}}} = \hat{N}(R)\, 2\pi R\,(2 + 0.844 \times Re^{1/2})\, D(\rho_{vc} - \rho_{vs}) \quad (2)$$

$$\left.\frac{d}{dt}(\rho_0 \hat{q}_r)\right|_{\text{collection}} = \hat{N}(R) \sum_{R>R'} \pi (R+R')^2 E(R,R')[V(R) - V(R')]\rho_0 q_r \quad (3)$$

Under equilibrium condition, the heat transfer from freezing of supercooled water drops, $\left(\frac{dQ}{dt}\right)_f$, on the surface of the graupel is balanced by heat transfers from evaporation and deposition, $\left(\frac{dQ}{dt}\right)_{\text{depo./evp.}}$, conduction and convection $\left(\frac{dQ}{dt}\right)_K$, and the sensible heat required to bring the temperature of the collected water to the surface temperature of the graupel $\left(\frac{dQ}{dt}\right)_{SH}$. Hence

$$\left(\frac{dQ}{dt}\right)_f = \left(\frac{dQ}{dt}\right)_{\text{depo./evp}} + \left(\frac{dQ}{dt}\right)_K + \left(\frac{dQ}{dt}\right)_{SH} \quad (4)$$

Following English (1973)

$$\left(\frac{dQ}{dt}\right)_{\substack{\text{depo.}/\\ \text{evp.}}} = \hat{N}(R)\,2\pi R\,(2 + 0.6\,Sc^{1/3}\,Re^{1/2})\,L_v\,D\,(\rho_{vs} - \rho_{vc}) \qquad (5)$$

$$\left(\frac{dQ}{dt}\right)_K = \hat{N}(R)\,2\pi R\,(2 + 0.6\,Pr^{1/3}\,Re^{1/2})\,K\,(T_s - T_c) \qquad (6)$$

$$\left(\frac{dQ}{dt}\right)_{SH} = C_w \left(\frac{d}{dt}(\rho_0 \hat{q}_r)\right)_{\text{collection}} (T_s - T_c) \qquad (7)$$

where Sc is the Schmidt number; Pr the Prandtl number; Cw the specific heat of water; T_s= and T_c are respectively the temperature at the surface of the graupel and the ambient cloud temperature.

Computation proceeds by first assuming a dry growth mode such that:

$$\left(\frac{dQ}{dt}\right)_f = L_f \left[\frac{d}{dt}(\rho_0 \hat{q}_r) + \frac{\rho_0 \hat{q}_{rw}}{\delta t}\right] \qquad (8)$$

where L_f is the latent heat of fusion and δt the time step. The last term of (8) represents the freezing of the water portion present on the graupel other than by collection. The term is not included in English (1973).

Using (4) and (8), T_s can be obtained by iteration. If T_s is below 0°c, the growth is indeed dry , otherwise wet growth must have occured. In the latter case, (4) is used to solve for $\left(\frac{dQ}{dt}\right)_f$ assuming T_s=0°c.

Then the rate of change of the ice portion is

$$\frac{d}{dt}(\rho_0 \hat{q}_{ri}) = \frac{1}{L_f}\left(\frac{dQ}{dt}\right)_f \tag{9}$$

which can be positive or negative depending on whether freezing or melting has taken place.

The ice portion $\rho_0 \hat{q}_{ri}$ can be calculated from (9). Transfer of graupel particles into rain drops is made when $\rho_0 \hat{q}_{ri} \leq 0$.

APPENDIX 2.3

This appendix describes comparison of numerical methods in computing the spectral transfer term $\delta R \frac{\partial}{\partial R}(\rho_0 q_r \frac{\dot{R}}{\delta R})$. It will be shown that the technique by Egan and Mahoney (1971) eliminates much of the numerical spreading caused by finite differencing.

I. Finite difference formulation (FD)

The upstream finite difference analog of the spectral transfer term for the m^{th} category at grid point j is

$$\left[\delta R \frac{\partial}{\partial R}(\rho_0 q_r \frac{\dot{R}}{\delta R})\right]_{m,j} = \frac{}{\delta R_{mj}} \begin{cases} (\rho_0 q_r)_{mj} \frac{\dot{R}_m}{\delta R_m} - (\rho_0 q_r)_{m-1,j} \frac{\dot{R}_{m-1}}{\delta R_{m-1}} ; \text{if } \dot{R}_m \geq 0. \\ (\rho_0 q_r)_{m+1,j} \frac{\dot{R}_{m+1}}{\delta R_{m+1}} - (\rho_0 q_r)_{mj} \frac{\dot{R}_m}{\delta R_m} ; \text{if } \dot{R}_m < 0. \end{cases} \quad (1)$$

II. Egan and Mahoney method (EM)

Application of the EM method involves calculation of the first and second moments of the hydrometeor water distribution after transfer has been made into and out of a particular category. The first moment represents the center of mass and the second moment is taken to be a measure of the horizontal spread. A new rectangular distribution is then reconstructed having the same hydrometeor water content and identical first and second moments as those computed.

Fig. A1 illustrates the computation using this procedure. In the figure, the hydrometeor water is assumed to distribute

linearly in the category which is transformed to a coordinate with 0 at the center and a value of 0.5 and -0.5 at the ends of the range interval. All length scales in a category are normalized to its range δR_m .

Let $(\rho_0 q_v)^n_{mj}$, F^n_{mj} , R^n_{mj} be the water content, center of mass, and spread of the distribution for the m^{th} category at a grid point j and time step n. The change of radius, $\dot{R}_m$, in a time step advances the center of mass by a distance σ given by

$$\sigma = \frac{\dot{R}_m \delta t}{\delta R_m} \qquad (2)$$

(σ is assumed positive in this example. The case for negative σ can be obtained using the same reasoning). A portioning parametar $P^n_{mj} = (F^n_{mj} + \sigma + \frac{R^n_{mj}}{2} - 0.5) / R^n_{mj}$ is then calculated. For $P^n_{mj} \leq 0$, none of the water is transferred. For $P^n_{mj} \geq 1$ all the water is transferred into the upper category. For $1 > P^n_{mj} > 0$, an amount $P^n_{mj} (\rho_0 q_v)^n_{mj}$ is transferred to category m+1 and $(1 - P^n_{mj})(\rho_0 q_v)^n_{mj}$ remains. The water transferred to an upper category will have a center of mass at $0.5 \left(P^n_{mj} R^n_{mj} \frac{\delta R_{m+1}}{\delta R_m} - 1 \right)$ relative to the center of the $m+1^{th}$ category and a spread equal to $P^n_{mj} R^n_{mj} \frac{\delta R_m}{\delta R_{m+1}}$. For the water remaining, its center of mass and spread are respectively

$$(1 - R^n_{mj} + P^n_{mj} R^n_{mj})/2 \qquad \text{and}$$

$$(1 - P_{mj}^{n}) R_{mj}^{n}$$

For the general case of transfer into and out of a category and the changes in center of mass and spread caused by advection from different grid points, the following sequence of computation is adopted:

(a) A tentative center of mass F_{mj}^{*} and spread R_{mj}^{*} is computed based only on the microphysical processes. Thus

$$(\rho_0 q_r)_{mj}^{n+1} F_{mj}^{*} = (\rho_0 q_r)_r F_r + (\rho_0 q_r)_a F_a + Q F_{mj}^{n} \tag{3}$$

$$(\rho_0 q_r)_{mj}^{n+1} R_{mj}^{*2} = (\rho_0 q_r)_r [R_r^2 + 12(F_{mj}^{*} - F_r)^2] + (\rho_0 q_r)_a [R_a^2 + 12(F_{mj}^{*} - F_a)^2] + Q [R_{mj}^{n\,2} + 12(F_{mj}^{*} - F_{mj}^{n})^2] \tag{4}$$

where subscripts r and a denote quantities remaining and newly transferred. Q represents the source of hydrometeors by the microphysical processes in a time step.

(b) Changes in the center of mass and spread by advection

are then made,

$$(\rho_0 q_r)_{mj}^{n+1} \; F_{mj}^{n+1} = \left[(\rho_0 q_r)_{mj}^{n} - T_{mj}\right] F_{mj}^{*} + \sum_{\ell} I_{m\ell}^{n} \, F_{m\ell}^{*} \qquad (5)$$

$$(\rho_0 q_r)_{mj}^{n+1} \; (R_{mj}^{2})^{n+1} = \left[(\rho_0 q_r)_{mj}^{n} - T_{mj}^{n}\right]\left[R_{mj}^{*2} + 12\left(F_{mj}^{*} - F_{mj}^{n+1}\right)^2\right]$$

$$+ \sum_{\ell} I_{m\ell}^{n} \left[R_{m\ell}^{*2} + 12\left(F_{m\ell}^{*} - F_{mj}^{n+1}\right)^2\right] \qquad (6)$$

where T_{mj}^{n} is the water transferred out of grid point j and $I_{m\ell}^{n}$ is the transfer into grid point j from grid point ℓ.

III. Results

The FD and EM methods are compared in a one-dimensional model described in section 2.2. In these computations, values of 10^{-3} sec and 0.5 g m^{-3} are assigned to K and a, respectively, but a unit coalescence efficiency is assumed. The results depicted in figs. A2-A5 show that precipitation develops earlier in the FD model. The rainfall maximum occurs 3 minutes earlier and the peak is 3.2 mm hr^{-1} less than that computed by the EM technique. Fig. A4 indicates the presence of large drops at 16 minutes near the cloud base by finite differencing. As a result the radar reflectivity factor has a larger magnitude initally. Since continuous supply of liquid water by condensation is not allowed in the computations, the earlier

depletion of hydrometeor water by rainout resulted in a smaller reflectivity factor and narrower distribution at a later time.

A second order finite difference method by Crowley (1971) has also been tested in computing the spectral transfer term and the results are similar to the upstream differencing method. A point to note is that hydrometeor water is automatically transferred to an upper category in each time step by the FD method. Since large drops are crucial for the formation of the precipitation drop-size spectrum, an artificial spreading is not acceptable for the computation of the evolution of the drop-size spectra.

The Egan and Mahoney technique eliminates much numerical spreading by explicit calculation of the moments of the distribution. The method is therefore superior in this aspect of the computation although a large volume of calculation is required.

APPENDIX 3.1

DERIVATION OF GREEN'S FUNCTION

The derivation of the Green's function for the solution of the perturbation pressure is outlined in this appendix. The procedure for the axi-symmetric case appears in section I while the slab-symmetric case forms the subject of section II. The method of integration is in III.

I. Axi-symmetric case

Let the region of interest be $0 \leq r \leq b$, $0 \leq z \leq H$, and let $G^k(\xi,r)$ be the Green's function for the k^{th} harmonic. Since Π_k satisfies an equation of form

$$\frac{1}{\xi}\frac{d}{d\xi}\left(\xi\frac{d\Pi_k}{d\xi}\right) - (kn)^2\Pi_k = F_k = \frac{2}{H}\int_0^H \mathcal{F}\cos(kn\zeta)\,d\zeta \qquad (1)$$

we multiply (1) by $\xi G^k(\xi,r)$ and integrate by parts from $\xi=0$ to b to obtain

$$b\,\Pi_{k\xi}(b)\,G^k(b,r) - \Pi_k(b)\,b\,G^k_\xi(b,r) - 0.\,\Pi_{k\xi}(0)\,G^k(0,r)$$
$$+ \Pi_k(0).0.G^k_\xi(0,r) + \int_0^b (\xi G^k_\xi)_\xi\,\Pi_k\,d\xi - \int_0^b (kn)^2\xi\,\Pi_k G^k(\xi,r)\,d\xi$$
$$= \int_0^b G^k(\xi,r)\,\xi\,F_k\,d\xi \qquad (2)$$

(the derivation of any function Q with respect to ξ is denoted by Q_ξ).

As $\Pi_{k\xi}(0) = \Pi_k(b) = 0$, the Green's function is chosen to satisfy the following conditions

$$(\xi G^k_\xi)_\xi - (kn)^2 \xi G^k = \delta(\xi - r) \tag{3a}$$

$$G^k(b,r) = 0 \tag{3b}$$

$G^k_\xi(0,r)$ is finite (3c)

$G^k(\xi,r)$ is continuous at $\xi = r$ (3d)

$$(\xi G^k)_\xi \Big|_{r=r_-}^{r=r_+} = 1 \tag{3e}$$

We write down the solution of (3a) as follows:

$$G^k = A_k I_o(kn\xi) + B_k K_o(kn\xi) \quad , 0 \leq \xi < r;$$

$$G^k = C_k I_o(kn\xi) + D_k K_o(kn\xi) \quad , r < \xi \leq b.$$

where I_o and k_o are respectively the modified Bessel functions of the first and second kind.

The four coefficients as determined by the 4 conditions (3a)-(3e) are

$$A_k = \left[I_0(k_n r)\, K_0(k_n b) - I_0(k_n b)\, K_0(k_n r) \right] / I_0(k_n b) \qquad (4a)$$

$$B_k = 0 \qquad (4b)$$

$$C_k = I_0(k_n r)\, K_0(k_n b) / I_0(k_n b) \qquad (4c)$$

$$D_k = - I_0(k_n r) \qquad (4d)$$

Thus the Green's function is given by

$$G^k(\xi, r) = \left[I_0(k_n \xi) / I_0(k_n b) \right] \left[I_0(k_n r)\, K_0(k_n b) - I_0(k_n b)\, K_0(k_n r) \right],$$

for $0 \leq \xi < r$; (5a)

$$G^k(\xi, r) = \left[I_0(k_n r) / I_0(k_n b) \right] \left[I_0(k_n \xi)\, K_0(k_n b) - I_0(k_n b)\, K_0(k_n \xi) \right]$$

for $r < \xi \leq b$. (5b)

Using the asymptotic behavior of $I_0(r)$ and $K_0(r)$, we find for

$b \to \infty$ $\qquad G^k(\xi, r) = - I_0(k_n \xi)\, K_0(k_n r)$, for $0 \leq \xi < r$ (6a)

$$G^k(\xi, r) = - I_0(k_n r)\, K_0(k_n \xi), \quad \text{for } r < \xi \leq \infty \qquad (6b)$$

T_k is determined from

$$T_k(r) = \int_0^\infty G^k(\xi, r)\, \xi\, F_k(\xi)\, d\xi \tag{7}$$

II. Slab-symmetric case

The procedure for obtaining the Green's function is completely analogous to that of the axi-symmetric case. The domain is now defined by $0 \leq x \leq b$, $0 \leq z \leq H$. The Green's function satisfies

$$G^k_{\xi\xi} - (kn)^2 G^k = \delta(\xi - x) \tag{8a}$$

$$G^k(b, x) = 0 \tag{8b}$$

$$G^k_\xi(0, x) = 0 \tag{8c}$$

$G^k(\xi, x)$ is continuous at $\xi = x$ (8d)

$$G^k_\xi \Big|_{x=x_+}^{x=x_-} = 1 \tag{8e}$$

The solution of (8a) is given as

$$G^k = \frac{1}{kn} \frac{\sinh[kn(x-b)]}{\cosh(knb)} \cosh(kn\xi), \quad \text{for } 0 \leq \xi < x. \tag{9a}$$

$$G^k = \frac{1}{k_n} \frac{\cosh(k_n x)\,\sinh[k_n(\xi-b)]}{\cosh(k_n b)}, \quad \text{for } x < \xi \leq b. \tag{9b}$$

As $b \to \infty$, the Green's function becomes:

$$G^k = -\frac{1}{k_n} e^{-k_n x} \cosh(k_n \xi), \quad \text{for } 0 \leq \xi < x \tag{10a}$$

$$G^k = -\frac{1}{k_n} e^{-k_n \xi} \cosh(k_n x), \quad \text{for } x < \xi \leq \infty \tag{10b}$$

and

$$\Pi_k(x) = \int_0^\infty F_k(\xi)\, G^k(\xi, x)\, d\xi \tag{11}$$

III. Method of integration

The integrals in (7) and (11) can be evaluated in closed form for the top-hat profile used to represent the drag forcing. For the Gaussian profiles in the buoyancy and dynamic terms, closed form solutions have not been found and numerical integration methods are used. The method is a combination of Romberg extrapolation and Gaussian Hermite quadrature. These are available in the form of two scientific subroutines, namely QAF and QLF, in the SLMATH library supported by the Information Processing Center at M.I.T.

APPENDIX 4.1

STABILITY ANALYSIS FOR INTERNAL GRAVITY WAVE MOTION

The linearized gravity wave equations similar to those given by Ogura and Charney (1962) are

$$\begin{aligned} \hat{u}_t &= -p_x' \\ \hat{w}_t &= -p_z' + g\,\textcircled{H} \\ p_{xx}' + p_{zz}' &= g\,\textcircled{H}_z \\ \textcircled{H}_t &= -\hat{w}\,S \end{aligned} \tag{1}$$

where $\hat{u}=\rho_0 u$, $\hat{w}=\rho_0 w$, $\textcircled{H} = \rho_0 \theta'/\theta_0$, $S=\frac{\partial \ln\theta_0}{\partial z}$, and $p=p_0+p'$. ρ_0, θ_0, and p_0 are the base state density, potential temperature, and pressure for a dry atmosphere.

Using staggered time and space differences as is illustrated in fig. B1, the finite difference analog of (1) becomes

$$\hat{u}_{j+1/2\,k}^{\,n+1/2} = \hat{u}_{j+1/2\,k}^{\,n-1/2} - \frac{\delta t}{\delta x}\left(p_{j+1,k}'^{\,n} - p_{jk}'^{\,n}\right)$$

$$\hat{w}_{j\,k+1/2}^{\,n+1/2} = \hat{w}_{j\,k+1/2}^{\,n-1/2} - \frac{\delta t}{\delta z}\left(p_{j\,k+1}'^{\,n} - p_{jk}'^{\,n}\right) + \frac{g}{2}\left(\textcircled{H}_{j\,k+1}^{\,n} + \textcircled{H}_{jk}^{\,n}\right)\delta t$$

$$\Theta_{jk}^{n+1} = \Theta_{jk}^{n} - \frac{\delta t}{2}\left(\hat{w}_{jk+1/2}^{n+1/2} + \hat{w}_{jk-1/2}^{n+1/2}\right)S \qquad (2)$$

$$\frac{p_{j+1k}^{n+1} - 2p_{jk}^{n+1} + p_{j-1k}^{n+1}}{\delta x^2} + \frac{p_{jk+1}^{n+1} - 2p_{jk}^{n+1} + p_{jk-1}^{n+1}}{\delta z^2} = \frac{g}{2\delta z}\left(\Theta_{jk+1}^{n+1} - \Theta_{jk-1}^{n+1}\right)$$

Let the solution to $\hat{u}$, $\hat{w}$, Θ , p' be of form

$$f_{jk}^{n} = \tilde{f}^{n}\, e^{i(l j\delta x + m k\delta z)}$$

where l,m are wave numbers and $x=j\delta x$, $z=k\delta z$, $t=n\delta t$.

Substituting the wave solution into (2) yields:

$$\tilde{u}^{n+1/2} = \tilde{u}^{n-1/2} - \frac{\delta t}{\delta x}\tilde{p}^{n}\, 2i \sin\left(\delta x \frac{l}{2}\right)$$

$$\tilde{w}^{n+1/2} = \tilde{w}^{n-1/2} - \frac{\delta t}{\delta z}\tilde{p}^{n}\, 2i \sin\left(\delta z \frac{m}{2}\right) + g\delta t \cos\left(\frac{m\delta z}{2}\right)\tilde{\Theta}^{n}$$

$$\tilde{\Theta}^{n+1} = \tilde{\Theta}^{n} - \delta t\, S\, \tilde{w}^{n+1/2} \cos\left(\frac{m}{2}\delta z\right)$$

$$\tilde{p}^{n+1} = \frac{-ig}{2\delta z} \frac{\sin\left(\frac{m}{2}\delta z\right)\cos\left(\frac{m}{2}\delta z\right)\tilde{\Theta}^{n+1}}{\left[\frac{\sin^2\left(\frac{l}{2}\delta x\right)}{\delta x^2} + \frac{\sin^2\left(\frac{m}{2}\delta z\right)}{\delta z^2}\right]}$$

which simplifies to

$$\begin{aligned}
\tilde{u}^{n+1/2} &= \tilde{u}^{n-1/2} - A\tilde{p}^{n} \\
\tilde{w}^{n+1/2} &= \tilde{w}^{n-1/2} - B\tilde{p}^{n} + C\tilde{\Theta}^{n} \\
\tilde{\Theta}^{n+1} &= \tilde{\Theta}^{n} - D\tilde{w}^{n+1/2} \\
&= \tilde{\Theta}^{n}(1-CD) - D\tilde{w}^{n-1/2} + BD\tilde{p}^{n} \\
\tilde{p}^{n+1} &= \tilde{\Theta}^{n} E(1-CD) - DE\tilde{w}^{n-1/2} + BDE\tilde{p}^{n}
\end{aligned} \tag{3}$$

where A= $2i\frac{\delta t}{\delta x}\sin\left(\frac{l}{2}\delta x\right)$

B= $2i\frac{\delta t}{\delta z}\sin\left(\frac{m}{2}\delta z\right)$

C= $q\,\delta t\cos\left(\frac{m}{2}\delta z\right)$

D= $\delta t\, S\cos\left(\frac{m}{2}\delta z\right)$

E= $\dfrac{-iq\sin\left(\frac{m}{2}\delta z\right)\cos\left(\frac{m}{2}\delta z\right)}{2\delta z\left[\frac{\sin^2\left(\frac{l}{2}\delta x\right)}{\delta x^2}+\frac{\sin^2\left(\frac{m}{2}\delta z\right)}{\delta z^2}\right]}$

In matrix notation (3) becomes

$$\begin{pmatrix} \tilde{u} \\ \tilde{w} \\ \tilde{\Theta} \\ \tilde{p} \end{pmatrix}^{n+1} = \begin{pmatrix} 1 & 0 & 0 & -A \\ 0 & 1 & C & -B \\ 0 & -D & 1-CD & BD \\ 0 & -DE & E(1-CD) & BDE \end{pmatrix} \begin{pmatrix} \tilde{u} \\ \tilde{w} \\ \tilde{\Theta} \\ \tilde{p} \end{pmatrix}^{n} \tag{4}$$

In (4) $\tilde{u}^{n-\frac{1}{2}}$, $\tilde{w}^{n-\frac{1}{2}}$ are therein renamed $\tilde{u}^{n}$, $\tilde{w}^{n}$.

The characteristic equation of the coefficient matrix can be readily shown as:

$$-\lambda(1-\lambda)\left[(1-\lambda)^2-(1-\lambda)\sigma+\sigma\right]=0$$

where σ = CD-BDE

$$= g\delta t^2 S\cos^2\left(\frac{m}{2}\delta z\right)-\frac{g\delta t^2 S\sin^2\left(\frac{m}{2}\delta z\right)\cos^2\left(\frac{m}{2}\delta z\right)}{\delta z^2\left[\frac{\sin^2\left(\frac{l}{2}\delta x\right)}{\delta x^2}+\frac{\sin^2\left(\frac{m}{2}\delta z\right)}{\delta z^2}\right]}$$

For simplicity, we assume $\delta x = \delta z$,

thus $$\sigma = \frac{g\delta t^2 S\sin^2\left(\frac{l}{2}\delta x\right)\cos^2\left(\frac{m}{2}\delta z\right)}{\sin^2\left(\frac{l}{2}\delta x\right)+\sin^2\left(\frac{m}{2}\delta z\right)}$$

and $\sigma > 0$ for $S > 0$.

The eigenvalues are respectively

$$\lambda_1 = 0$$

$$\lambda_2 = 1$$

$$\lambda_{3,4} = 1-\frac{\sigma\pm\sqrt{\sigma^2-4\sigma}}{2}$$

In the event that $\sigma^2 < 4\sigma$, that is $\sigma < 4$

$$\lambda_{3,4} = 1-\frac{\sigma\pm i\sqrt{4\sigma-\sigma^2}}{2}$$

$$|\lambda_{3,4}|^2 = (1-\sigma/2)^2+\tfrac{1}{4}(4\sigma-\sigma^2)$$

$$= 1$$

Therefore the stability criteria for internal gravity waves is

$$g\delta t^2 S\left[\frac{\sin^2\left(\frac{l}{2}\delta x\right)\cos^2\left(\frac{m}{2}\delta z\right)}{\sin^2\left(\frac{l}{2}\delta x\right)+\sin^2\left(\frac{m}{2}\delta z\right)}\right] < 4$$

If we maximize with respect to m such that $\cos^2\left(\frac{m}{2}\delta z\right)=1$, and $\sin^2\left(\frac{m}{2}\delta z\right)=0$, the above stability criteria becomes

$$\delta t < \frac{2}{\sqrt{gS}}$$

A typical value for S in the atmosphere is $10^{-5}m^{-1}$. Hence δt is of the order of 100 sec for stable solutions.

APPENDIX 4.2

FINITE DIFFERENCE EQUATIONS AND SEQUENCE OF COMPUTATION

Sequence of computation

Let A_j be the value of a variable A at time $t=n\delta t$ and $z=j\delta z$ with reference to the grid mesh in fig. 4.3. The sequence of computations at the j^{th} grid cell is typically

(1) Predict $\overline{w_a}^{n+1/2}$ from $\overline{w_a}^{n-1/2}$, $\overline{w_b}^{n-1/2}$, $\overline{\pi'}^{n}$, $\overline{B_a}^{n}$, and $\overline{Q_a}^{n}$ according to (4.23).

(2) calculate $\overline{w_b}^{n+1/2}$ from (4.24) and $\widetilde{u_a}^{n+1/2}$ from (4.15).

(3) Determine $\widetilde{w}^{n}$, $\widetilde{\theta}^{n}$, $\widetilde{q_v}^{n}$, $\widetilde{q_c}^{n}$, $\widehat{q_c}^{n}$, $\widetilde{q_r}^{n}$, $\widehat{q_r}^{n}$ from (4.20).

(4) A first guess $\overline{q_v}^{*}$, $\overline{q_c}^{*}$, $\overline{\hat{q}_c}^{*}$, $\overline{q_r}^{*}$, $\overline{\hat{q}_r}^{*}$, $\overline{\theta'}^{*}$ are calculated from $\overline{w}^{n+1/2}$, $\widetilde{u}^{n+1/2}$, $\widetilde{q_v}^{n}$, $\widetilde{q_c}^{n}$, $\widehat{q_c}^{n}$, $\widetilde{q_r}^{n}$, $\widehat{q_r}^{n}$, $\widetilde{\theta'}^{n}$, $\overline{q_v}^{n}$, $\overline{q_c}^{n}$, $\overline{\hat{q}_c}^{n}$, $\overline{q_r}^{n}$, $\overline{\eta_r}^{n}$, $\overline{\Phi_v}^{n}$, $\overline{\Phi_c}^{n}$, $\overline{\hat{\Phi}_c}^{n}$, $\overline{\Phi_r}^{n}$, $\overline{\hat{\Phi}_r}^{n}$, and $\overline{SS}^{n}$ using (4.25) and (4.26) but neglecting the terms where phase changes occur. For model P microphysics, the computation of the spectral shifting terms and the changes in moments of the rain and graupel spectrum is accomplished by the Egan and Mahoney (E&M) technique discussed in Chapter 2.

(5) Adjustments of the potential temperature and water substances from the first guess values in step (4) are made for the processes of evaporation, condensation, deposition, freezing and melting. The saturation vapor pressure is calculated from $\overline{\pi'}^{n}$ and $\overline{\theta'}^{*}$. Changes in the moments of the rain and graupel spectrum are again computed by the E&M

method for model P microphysics.

(6) $\overline{\pi}'^{,n+1}$ is diagnosed from (4.34), (4.35), and (4.37) using $\overline{\omega}^{n+1/2}$, $\overline{Q}^{n+1}$, and $\overline{B}^{n+1}$ obtained from steps (1) and (5).

Finite difference equations

The finite difference equations from (4.23), (4.24), (4.15), $\overline{q_{ra}}$ in (4.25), and (4.26) are written out explicitly. The equations for the other variables can be obtained in a like manner.

Referring to the j^{th} cell in fig. 4.3, the velocities are computed from

$$\overline{w}_{aj+1/2}^{n+1/2} = \overline{w}_{aj+1/2}^{n-1/2} - \delta t \frac{z}{a} \tilde{u}_{aj+1/2}^{n-1/2} \tilde{w}_{aj+1/2}^{n-1/2}$$

$$- \delta t \frac{2\alpha^2}{a} \left| \overline{w}_{aj+1/2}^{n-1/2} - \overline{w}_{bj+1/2}^{n-1/2} \right| \left(\overline{w}_{aj+1/2}^{n-1/2} - \overline{w}_{bj+1/2}^{n-1/2} \right)$$

$$- \frac{\delta t}{\delta z} \frac{1}{\rho_{oj}} \left[\rho_{oj+1} \overline{w}_{aj+1}^{**} \overline{w}_{aj+1/2}^{n} - \rho_{oj} \overline{w}_{aj}^{**} \overline{w}_{aj-1/2}^{n} \right]$$

$$- \frac{\delta t}{\delta z} c_p \theta_{oj} \left(\overline{\pi}'^{n}_{aj+1} - \overline{\pi}'^{n}_{aj} \right) + g \delta t \, \overline{B}_{aj+1/2}^{n-1/2} \qquad (1)$$

$$- \delta t \, g \, \overline{Q}_{aj+1/2}^{n-1/2}$$

where

$$\tilde{u}_{aj+1/2}^{n-1/2} = 0.5 \left(\tilde{u}_{aj}^{n-1/2} + \tilde{u}_{aj+1}^{n-1/2} \right)$$

$$\overline{B}_{aj+1/2}^{n-1/2} = 0.5 \left(\overline{B}_{aj}^{n-1/2} + \overline{B}_{aj+1}^{n-1/2} \right)$$

$$\overline{Q}_{aj+1/2}^{n-1/2} = 0.5 \left(\overline{Q}_{aj}^{n-1/2} + \overline{Q}_{aj+1}^{n-1/2} \right)$$

$$\overline{w}_{aj+1}^{**} = \overline{w}_{aj+1/2}^{n} \quad \text{if} \quad \overline{w}_{aj+1/2}^{n} \geq 0$$

$$= \overline{w}_{aj+3/2}^{n} \quad \text{if} \quad \overline{w}_{aj+1/2}^{n} < 0$$

$$\overline{w}_{aj}^{**} = \overline{w}_{aj-1/2}^{n} \quad \text{if} \quad \overline{w}_{aj-1/2}^{n} \geq 0$$

$$= \overline{w}_{aj+1/2}^{n} \quad \text{if} \quad \overline{w}_{aj-1/2}^{n} < 0$$

for j=2,....., K+1

where K is the number of grid cells.

$$\overline{w}_{oj+1/2}^{n+1/2} = -\frac{\sigma^2}{(1-\sigma^2)} \overline{w}_{aj+1/2}^{n+1/2} \tag{2}$$

$$\tilde{u}_{aj}^{n+1/2} = -\frac{a}{2\delta z} \frac{1}{\rho_{oj}} \left(\rho_{oj+1/2} \overline{w}_{aj+1/2}^{n+1/2} - \rho_{oj-1/2} \overline{w}_{aj-1/2}^{n+1/2}\right) \tag{3}$$

The rain mixing ratio in (4.25) can be calculated as

$$\overline{q_{ra}}_j^{n+1} = \overline{q_{ra}}_j^{n} - \delta t \frac{2}{a} \tilde{u}_{aj}^{n+1/2} \tilde{q}_{raj}^{n+1/2}$$

$$- \frac{\delta t}{\delta z} \frac{1}{\rho_{oj}} \left[\rho_{oj+1/2} \overline{q_{ra}}_{j+1/2}^{**} \left(V + \overline{w_a}\right)_{j+1/2}^{n+1/2} - \rho_{oj-1/2} \overline{q_{ra}}_{j-1/2}^{**} \left(V + \overline{w_a}\right)_{j-1/2}^{n+1/2}\right]$$

$$+ \delta t \, \overline{\Phi}_{rj}^{n} \tag{4}$$

where

$$\overline{q_{ra}}_{j+1/2}^{**} = \overline{q_{ra}}_{j}^{n} \quad \text{if} \quad \left(V + \overline{w_a}\right)_{j+1/2}^{n+1/2} \geq 0$$

$$= \overline{q_{ra}}_{j+1}^{n} \quad \text{if} \quad \left(V + \overline{w_a}\right)_{j+1/2}^{n+1/2} < 0$$

$$\bar{q}^{**}_{ra\,j-1/2} = \bar{q}^{n}_{ra\,j-1} \quad \text{if} \quad (V+\bar{w}_a^{n+1/2})_{j-1/2} \geq 0$$

$$= \bar{q}^{n}_{ra\,j} \quad \text{if} \quad (V+\bar{w}_a^{n+1/2})_{j-1/2} < 0$$

The k^{th} mode pressure equation (4.35) is solved by a method in Richtmyer (1967). The finite difference equation for (5).

$$\frac{\partial}{\partial \zeta}\left(\rho_0 \theta_0 \frac{\partial \pi_k}{\partial \zeta}\right) - \rho_0 \theta_0 \mu_k^2 \pi_k = F_k \quad , \tag{5}$$

which is a generalized form of (4.35) with generalized boundary condition,

$$\frac{\partial \pi_k}{\partial \zeta} = 0 \qquad \text{at} \quad z = H$$

$$\text{and} \qquad \frac{\partial \pi_k}{\partial \zeta} = \phi \qquad \text{at} \quad z = 0 \tag{6}$$

can be written as

$$-A_j \pi_{k\,j+1} + B_j \pi_{kj} - C_j \pi_{k\,j-1} = D_j \tag{7}$$

where $A_j =$ 1

$$C_j = (\rho_0 \theta_0)_{j-1/2} / (\rho_0 \theta_0)_{j+1/2}$$

$$B_j = [1 + C_j + (\rho_0 \theta_0)_j / (\rho_0 \theta_0)_{j+1/2}\, \delta z^2 / \mu_k^2]$$

$$D_j = -\delta z\, F_{kj} / (\rho_0 \theta_0)_{j+1/2} \tag{8}$$

The boundary condition in (6) gives

$$\pi_{k,\,K+1} = \pi_{k,\,K+2} \tag{9a}$$

$$\pi_{k,2} - \pi_{k,1} = \phi\, \Delta z \tag{9b}$$

where cell 1 and cell K+2 are fictitions cells outside the integration domain.

Now let

$$\Pi_{k,j} = \Pi_{k,j+1} E_j + F_j \tag{10}$$

comparing (10) and (9b) gives

$$E_1 = 1, \quad F_1 = -\phi \delta z \tag{11}$$

using (10) and (7) and eliminating $\Pi_{k,j-1}$, the expressions for E_j and F_j result.

$$\left.\begin{aligned} E_j &= 1/(B_j - C_j E_{j-1}) \qquad (12) \\ F_j &= E_j (P_j + C_j F_{j-1}) \qquad (13) \end{aligned}\right\} \quad j = 2, \ldots, K+1$$

Combining (10) and (9b), the equation for $\Pi_{k,K+1}$ is

$$\Pi_{k,K+1} = F_{K+1}/(1 - E_{K+1}) \tag{14}$$

Finally $\Pi_{k,j}$ can be calculated from (10) by sweeping backward from j=K to j=2.

LIST OF SYMBOLS

a	autoconversion threshold also radius of inner cylinder
b	radius of outer cylinder
B	buoyancy
C_D	drag coefficient of graupel in air
C_p	specific heat of air at constant pressure
D	coefficient of molecular duffusion of water vapor in air
e	partial pressure of water vapor
e_s	saturation vapor pressure with respect to water
e_i	saturation vapor pressure with respect to ice
E	collection efficiency between water drops
$\hat{E}$	collection efficiency between graupel and water drops
E_1	collision efficiency
E_2	coalescence efficiency
f	dimensionless factor
g	acceleration due to gravity
F	fraction of drops frozen
$f(x)$	number density distribution function of an x mass drop
H	vertical scale of cloud
K	autoconversion rate
L_f	latent heat of fusion of water
L_s	latent heat of sublimation of water
L_v	latent heat of vaporization of water
L_1	horizontal scale of cloud in X direction
L_2	horizontal scale of cloud in Y direction
$\widetilde{N}$	number of collisions
$\widetilde{N}_s$	number of separations
$N(R)$	number density of rain particles of radius R
$\hat{N}(R)$	number density of graupel particles of radius R
P_r	Prandtl number= $\mu C_p/\kappa$
$\hat{Q}$	amplitude of drag forcing
q_c	mixing ratio of cloud water
$\hat{q}_c$	mixing ratio of cloud ice
q_r	mixing ratio of rain water
$\hat{q}_r$	mixing ratio of graupel
q_v	mixing ratio of water vapor
q_v'	deviation of water vapor mixing ratio from the base state
Q	mixing ratio of all water substance
Re	Reynolds number = $2RV/\nu$

R_s radius of curvature
r radius of cloud droplets and cloud ice
R radius of rain and graupel particles
r_s radius of satellites
$\dot{R}$ rate of change of radius
R_v gas constant of water vapor
S supersaturation with respect to water, e/e_s
S_c Schmidt number ($2R\nu$)
S_i supersaturation with respect to ice= e/e_i
T air temperature
T_o temperature of base state atmosphere
$\vec{u}$ three-dimensional vector velocity (u,v,w)
$\vec{u}_H$ horizontal vector velocity (u,v)
u x component of horizontal velocity
v y component of horizontal velocity, also volume of a water drop
U the relative velocity between drops of radius R and R'
V terminal velocity of rain and graupel particles. V is negative when the rain or graupel particles fall toward the ground
V_o terminal velocity of median volume diameter drop in model K microphysics. V_o is negative when the rain or graupel particles fall toward the ground
$\hat{W}$ amplitude of vertical velocity
$X(R)$ mass of a water drop of radius R
Z radar reflectivity factor
∇ three-dimensional gradient operator
∇_H horizontal gradient operator
δR range of radius in a particular category
δR_m range of radius in category m
δt time step
δz space increment
Γ temperature lapse rate
κ thermal conductivity of air
χ numerical factor in heat transfer coefficient
μ microns, also dynamic viscosity
ν kinematic viscosity
Φ collection kernel
$\vec{\omega}$ vorticity
π' perturbation non-dimensional pressure
π'_m dynamic perturbation pressure
π'_B drag perturbation pressure
π'_θ buoyancy perturbation pressure
ρ_o air density of base state atmosphere
ρ_g density of graupel
ρ_{vc} vapor density in the air stream
ρ_{vs} vapor density at surface of a graupel particle
ρ_w density of water drops

Ψ breakup kernel
σ^* surface tension of water drops
σ radii ratio a/b
θ_o potential temperature of base state atmosphere
θ' potential temperature deviation
$\hat{\theta}$ amplitude of buoyancy forcing

BIOGRAPHICAL NOTE

The author was born on July 24,1946 in Hong Kong. His youth was spent on the island where he received his high school education. After graduation in 1965, he joined the Hong Kong Royal Observatory as an observer and engaged in the tracking of meteorological satellites. In 1967, he entered Vincennes University in Indiana on a Lions' Club Scholarship. He transferred to M.I.T. in 1969 and received his S.B. degree in the Department of Earth and Planetary Sciences in 1971. He has been with the Department of Meteorology since then and obtained his S.M. degree in 1973.

He is a member of Sigma Xi and a student member of the American Meteorological Society. He is co-author of a paper with Dr. Pauline Austin entitled ' A Kinematic Cumulus Cell Model' which was presented at the Cloud Physics Conference at Tucson , Arizona in October, 1974.

REFERENCES

Arakawa, A., and W.H. Schubert, 1974: Interaction of a cumulus cloud ensemble with the large-scale environment, Part 1, J. Atmos. Sci.,31, 674-701.

Arnason, G.,R.S. Greenfield,and E.A. Newburg, 1968: A numerical experiment in dry and moist convection including the rain stage. J. Atmos. Sci.,25,404-415.

Asai, T., 1965: A numerical study of the air-mass transformation over the Japan Sea in winter. J. Meteor. Soc. Japan, 43,1-15.

Asai, T., and A. Kasahara, 1967: A theoretical study of the compensating downward motions associated with cumulus clouds, J.Atoms. Sci., 24, 487-496.

Austin, J.M., 1948: A note on cumulus growth in a non-saturated environment. J. Meteor., 5, 103-107.

Austin, P. M., and R.A. Houze, Jr., 1972: Analysis of the structure of precipitation patterns in New England. J. Appl. Meteor., 11, 926-935.

_____, _____, 1973: A technique for computing vertical transports by precipitating cumuli. J. Atoms. Sci., 30, 1100-1111.

Barnes, S.L., 1970: Some aspects of a severe right-moving thunderstorm deduced from mesonetwork rawinsonde observations. J. Atmos. Sci.,27,634-648.

_____, 1971: Reply to ' Comments on " Some aspects of a severe right-moving thunderstorm deduced from mesonetwork rawinsonde observations"'. J. Atmos. Sci., 28,653-654.

Berry, E.X., 1967: Cloud droplet growth by collection. J. Atmos. Sci., 24, 688-701.

_____, 1968: Modification of the warm rain process. Proc. First Natl. Conf. Wea. Modification, Boston, Amer., Meteor. Soc., 81-85.

_____, and R.L. Reinhardt, 1973: Modeling of condensation and collection within clouds. Final Report to the National Science Foundation on grant GA-21350, 70 pp.

Best, A.C., 1950: Empirical formulae for the terminal velocity of water drops falling through the atmosphere. Q.J.R.M.S. 76, 302-311.

Betts, A.K.,1973: A relationship between stratification, cloud depth, and permitted cloud radii. J.Appl.Meteor., 12 890-893.

Bjerknes, J.,1938: Saturated-adiabatic ascent of air through dry-adiabatically descending environment. Q.J.R.M.S., 64,325-330.

Bleeker W. and M.J. Andre,1950: Convective phenomena in the atmosphere. J. Meteor., 7, 195-209.

Braham, R.R.,Jr., 1952: The water and energy budgets of the thunderstorm and their relationship to thunderstorm development. J.Meteor., 9, 227-242.

_____, L.J.Battan and H.R.Byers, 1957: Artificial nucleation of cumulus clouds. Meteor. Monogr.,2,No.11, 47-85.

Brazier-Smith, P.R., S.G.Jennings, and J.Latham, 1972: The interaction of falling water drops:coalescence. Proc.R.Soc.,A326, 393-408.

_____,_____,_____, 1973: Raindrop interactions and rainfall rates within clouds. Q.J.R.M.S.,99,260-272.

Byers, H.R.,and Braham,R.R., Jr., 1949: The Thunderstorm, U.S. Govt. Printing Office, Washington, D.C.

Byers,H.R.,1965: Elements of Cloud Physics. University of Chicago Press, 191pp.

Charney, J.G., 1971: Tropical cyclogensis and the formation of the Intertropical Convergence Front. In Lectures in Appl.Math., Vol.,13,Amer.Math.Soc.,355-368.

Charney, J.G. and A.Eliassen, 1964: On the growth of the hurricane depression. J.Atmos.Sci.,21,68-75.

Clark,T.L.,1973: Numerical modeling of the dynamics and microphysics of warm cumulus convection. J.Atmos.Sci.,30,857-878.

Cooper,W.A., 1975: Reply to 'Comments on"A possible mechanism for contact nucleation"'. J.Atmos.Sci., 32, 2371-2373.

Cotton, W.R., 1972: Numerical simulation of precipitation development in supercooled cumuli. Part 2, Mon. Weather Rev.,100, 764-784.

_____, 1975: On parameterization of turbulent transport in cumulus clouds. J.Atmos.Sci.,32, 548-564.

Crowley,W.P.,1968:Numerical advection experiments. Mon. Weather Rev.,96,1-11.

Danielsen,E.F., R.Bleck, and D.A. Morris, 1972: Hail growth by stochastic collection in a cumulus model. J. Atmos. Sci., 29,135-155.

Davies-Jones,R., 1974: Discussion of measurements inside high-speed thunderstorm updrafts. J. Appl.Meteor.,13,710-717.

_____, and J.H.Henderson, 1975: Updraft properties deduced statistically from rawin soundings. Pure and Appl. Geophysics,113,787-802.

_____, and N.B.Ward, 1971: Comments on "Some aspects of a severe right-moving thunderstorm deduced from mesonetwork rawinsonnde observations". J.Atmos.Sci., 28 652-653.

Das, P.,1964: Role of condensed water in the life cycle of a convective cloud. J.Atmos.Sci., 21,404-418.

_____, and M.C.Subba Rao, 1972: The unsaturated downdraft. Indian J. of Meteor. and Geophysics, 23(2), 135-144.

Egan, B.A. and J.R. Mahoney, 1972: Numerical modeling of advection and diffusion of urban area-source pollutants. J.Appl. Meteor.,11, 312-322.

English,M.,1973: The growth of large hail. Scientific report MW-78, Stormy Weather Group, McGill University,Canada.82pp.

Fitzgerald,J.W.,1973: Dependence of the supersaturation spectrum of CCN on aerosol size distribution and composition. J.Atmos. Sci.,32,628-634.

Fukuta, N., 1975: Comments on "A possible mechanism for contact nucleation". J.Atmos.Sci., 32,2371-2373.

Gordon, N.,1976: Research paper. M.I.T. 30pp.

Holton, J.R.,1972: An Introduction to Dynamic Meteorology. Academic Press, New York. 319 pp.

_____, 1973: A one-dimensional cumulus model including pressure perturbations. Mon. Weather Rev.,101,201-205.

Houze, R.A.,Jr.,1972: Development and application of a method for computing cumulus transports. Ph.D. Dissertation,MIT.

_____, 1973: A climatological study of vertical transports by cumulus-scale convection. J.Atmos.Sci.,30,1112-1123.

_____, and C.A. Leary, 1976: Comparison of convective mass and heat transports in tropical easterly waves computed by two methods. J.Atmos.Sci.,33,424-429.

Jordan, C.L.,1958: Mean soundings for West Indies area. J. Meteor.,15, 91-97.

Johnson, R.H., 1976: The role of convective-scale precipitation downdraft in cumulus and synoptic-scale interactions. J. Atmos. Sci.,33,1890-1910.

Kamburova, P. and F.H. Ludlam,1966: Rainfall evaporation in downdraft. Q.J.R.M.S.,92,510-518.

Kessler, E., 1969: On the distribution and continuity of water substance in atmospheric circulation. Meteor. Monogr.,10,No. 32, 84pp.

Komabayasi, M., T. Gonda,and K. Isono, 1964: Life-time of water drops before breaking and size distribution of fragment droplets. J.Meteor. Soc. Japan,42,330-340.

Kuo, H.L., 1962: On the controlling influences of eddy diffusion on thermal convection. J. Atmos. Sci.,19,236-243.

Lee, J. L., 1971 : A numerical study of shallow convection. Report no. 19 to National Sci. Foundation under grant GA-13818. Dept. of Meteorology, Penn. State University.

Leighton, H.G., and R.R. Rogers,1974: Droplet growth by condensation and coalescence in a strong updraft. J. Atmos. Sci.,31,271-279.

Levine,J., 1959: Spherical vortex of bubble-like motion in cumulus clouds. J. Meteor., 16, 653-662.

List, R., and Gillespie, D.T., 1976: Evolution of raindrop spectra with collision-induced breakup. J. Atmos. Sci., 33, 2007-2013.

Lopez, R.E.,1973: Cumulus convection and large-scale circulations II. Cumulus and mesoscale interactions. Mon. Weather Rev., 101, 856-870.

Macklin, W.C.,1963: Heat transfer by hailstones. Q.J.R.M.S., 89, 360-369.

_____, and I.H. Bailey, 1968: The collection efficiencies of hailstones. Q.J.R.M.S., 94, 393-396.

Malkus, J.S., 1954: Some results of a trade cumulus cloud investigation. J.Meteor, 11, 220-237.

_____, C.Ronne and M.Chaffee, 1961: Cloud Patterns in hurricane Daisy. Tellus, 13,8-30.

Marwitz, J.D.,1973: Trajectories within the weak echo regions of hailstorms. J.Appl. Meteor., 12,1174-1182.

Mason, B.J., and J.B. Andrews,1960: Dropsize distributions from various types of rains. Q.J.R.M.S.,86,301-314.

Mason, B.J.1971: The physics of Clouds. Clarendon Press, Oxford, 671 pp.

McTaggart-Cowan, J.D. and R.List, 1975: Collision and breakup of water drops at terminal velocity. J.Atmos.Sci., 32, 1401-1411.

Molenkamp, C.R.,1968: Accuracy of finite-difference methods applied to the advection equation. J.Appl.Meteor., 7,160-167.

Murray, F.W.,1970: Numerical models of a tropical cumulus cloud with bilateral and axial symmetry. Mon. Weathers Rev., 98,14-28.

_____, 1971: Humidity augmentation as the initial impulse in a a numerical cloud model. Mon.Weather Rev.,99,37-48.

_____, and L.R.Koenig, 1972: Numerical experiments on the relation between microphysics and dynamics in cumulus convection. Mon. Weather Rev.,100,717-732.

Nelson, L.D.,1971: A numerical study on the initiation of of warm rain. J.Atmos Sci., 28, 752-762.

Nitta, T.,1975: Observational determination of cloud mass flux distributions. J.Atmos.Sci., 32, 73-91.

_____, 1977: Response of cumulus updraft and downdraft to GATE A/B scale motion system. Trop.Meteor.Paper, 18, U.C.L.A.,60 pp.

Ogura, Y., 1962: Convection of isolated masses of buoyant fluid:a numerical calculation. J.Atmos.Sci., 19,492-502.

_____, and J.G.Charney, 1960: A numerical model of thermal convection in the atmosphere. Proceeding of International Symposium of Numerical Weather Prediction, Meteor.Soc. Japan,431-452.

_____, and H.-R. Cho,1973: Diagnostic determination of cumulus cloud population from observed large-scale variables. J.Atmos.Sci.,30,1276-1286.

_____, and N.A.Phillips,1962: A scale analysis of deep and shallow convection in the atmosphere.J.Atmos.Sci.,19,173-179.

_____, and T.Takahashi,1971: Numerical simulation of the life cycle of a thunderstorm cell. Mon.Weather Rev.,99,895-911.

_____,_____,1973: The development of warm rain in a cumulus model. J.Atmos.Sci.,30,262-277.

Orville,H.D.,1968:Ambient wind effects on the initiation and development of cumulus clouds over mountains.J.Atmos.Sci., 25,385-403.

____,and L.J.Sloan,1971:Effects of higher order advection techniques on a numerical cloud model.Mon.Wea.Rev.,98,7-13.

Richtmyer R.D. and K.W. Morton,1967: Difference methods for initial-value problems. Interscience Publishers.405pp.

Sanders, F,1975: Comments on anelastic pressure fields. MIT synoptic meteorology class notes.

Saunders,P.M.,1965: Some characteristics of tropical marine showers. J.Atmos.Sci.,22, 167-175.

Schlesinger,R.E.,1973a: A numberical model of deep moist convection. I, Comparative experiments for variable ambient moisture and wind Shear. J.Atmos.Sci.,30, 835-856.

_____, 1973b: A numerical model of deep moist convection, II, A Proto-type experiment and variations upon it. J.Atmos.Sci., 30, 1374-1391.

_____,1975: A three-dimensional model of an isolated deep convection cloud: preliminary results. J.Atmos.Sci.,32,934-957.

Scott, B.C. and P.V.Hobbs, 1977: A theoretical study of the evolution of mixed-phase cumulus clouds. To appear in J.Atmos.Sci.,34(5).

Silverman,B.A. and M.Glass,1973: A numerical simulation of warm cumulus clouds: I, Parameterized VS. non-parameterized microphysics. J.Atmos.Sci.,30,1620-1637.

Simpson,J. and V. Wiggert,1969: Models of precipitating cumulus tower. Mon.Weather Rev., 97, 471-489.

_____,_____, 1971: 1968 Florida cumulus seeding experiment: Numerical model and results. Mon.Weather Rev., 99,87-118.

Soong,S.-T., and Y.Ogura, 1973: A comparison between axi-symmetric and slab-symmetric cumulus cloud models. J.Atmos.Sci.,30,879-893.

_____,_____,1976:A determination of the trade-wind cumuli population using BOMEX data and an axisymmetric cloud model. J.Atmos.Sci.,33,992-1007.

Spengler, J.D., and Gokhale,N.R., 1973: Drop impaction. J.Appl.Meteor., 12,316-321.

Squires,P., and J.S.Turner, 1962: An entraining jet model for cumulonimbus updraughts. Tellus, 14,422-434.

Srivastava,R.C.,1971: Size distribution of raindrops generated by their breakup and coalescence. J.Atmos.,Sci.,28,410-415.

Stommel,H.,1947: Entainment of air into a cumulus cloud. J. Meteor ., 4,91-94.

Takeda,T.,1971: Numerical simulation of precipitating convective cloud: The formation of a"long-lasting" cloud. J.Atmos.Sci., 28, 356-376.

Tracton,M.S., 1973: The role of cumulus convection in the development of extratropical cyclones. Mon.Weather Rev., 101, 573-593.

Vali, G., 1968: Ice nuclei relevant to formation of hail. Sci., Report. MW-58, Stormy Weather Group, McGill Unversity, Canada. 51 pp.

Van Thullenar,C.F., 1960: Pressure difference between a cumulus cloud and its environment. Cumulus Dynamics: Proc. of first conf, on cumulus convection, ed. C.E. Anderson, Pergamonon Press, New York, 19-22.

Warner,J., 1970: The microstructure of cumulus cloud, Part III. The nature of the updraft. J.Atmos.Sci., 27, 282-688.

Whelpdale,D.M., and R.List, 1971: The coalescence process in raindrop growth. J.Geophy.Res., 76, 2836-2856.

Wilhelmson, R., 1974: The life cycle of a thunderstorm in three-dimensions. J.Atmos.Sci., 31, 1629-1651.

_____, and Y. Ogura, 1972: The pressure perturbation and the numerical modelling of a cloud. J.Atmos.Sci., 29 1295-1307.

Yanai, M., S. Esbensen, and J-H. Chu, 1973: Determination of bulk properties of tropical cloud clusters from large-scale heat and moisture budgets. J.Atmos.Sci., 30, 611-627.

Young, J.A., 1972: A simple model relati anelastic pressure and buoyancy. Dynamics of the Tropical Atmosphere, 525-528 , NCAR, Boulder, Colorado.

Young, K.C., 1974a: The role of contact nucleation in ice phase initiation in clouds. J.Atmos.Sci., 31, 768-776.

_____, 1974b: A numerical simulation of wintertime, orographic precipitation. I, description of model microphysics and numerical technique. J.Atmos.Sci., 31, 1735-1748.

_____, 1975: The evolution of drop spectra due of condensation, coalescence and breakup. J.Atmos.Sci., 32, 965-973.